Imperial College London

Department of Chemical Engineering

A thesis submitted for the degree of

Doctor of Philosophy

Screening, developing and testing Metal-Organic Frameworks for industrially relevant CO/N_2 separation

Arwyn Evans

September 2019

Abstract

The demands to reduce the energy consumption and expenditure of industrial chemical separation processes provide great opportunities to develop and apply new technology and materials. As carbon monoxide (CO) is not a natural resource, its requirement for purification is important for its utilisation as a large-scale chemical reagent. Nitrogen (N_2) impurity from the syngas source poses difficult separation challenges, which current CO purification technologies are trying to overcome to reduce capital and operating costs. Adsorption separation is an avenue that has the ability to improve the efficiency of this challenging separation, with metal-organic frameworks (MOFs) highlighted as a class of porous materials to achieve this. However, the number of studies on CO separation using MOFs that mimic industrial conditions remain scarce.

This thesis presents an in-depth study of MOFs for CO/N_2 separation with an industrial outlook, using tailored screening, design, synthesis, characterisation and testing of MOFs. An initial testing screening procedure found two MOFs to be the best performing for CO/N_2 separation; Ni-MOF-74 and Co-MOF-74. Further in-depth testing was performed on these MOFs, studying the effect of N_2 and CO_2 impurity levels and recyclability under dynamic conditions. Dynamic testing of related structures provided greater insight into the role of the MOFs metal sites and porosity. These dynamic measurements also contributed useful kinetic data for future development of process scale modelling. Using the knowledge gained from the preliminary screening and in-depth testing, the CO/N_2 separation performance of M-MOF-74 was enhanced by post-synthesis chemical modification (*i.e.* addition of Cu^+ sites). Overall, this thesis assesses and improves the industrial viability of MOFs for CO/N_2 separation.

Publications

A Evans, R Luebke, C Petit, “The use of metal–organic frameworks for CO purification,” Journal of Materials Chemistry A, **6**, (2018), 10570-10594

A Evans, M Cummings, R Luebke, M Brown, S Favero, M Attfield, F Siperstein, D Fairen-Jimenez, K Hellgardt, R Purves, D Law, C Petit, “Screening Metal-Organic Frameworks for dynamic CO/N_2 separation using complementary adsorption measurement techniques,” Industrial & Engineering Chemistry Research, **58**, (2019), 18336-18344

A Evans, M Cummings, D Decarolis, D Gianolio, S Shahid, G Law, M Attfield, D Law, C Petit, “Optimisation of Cu^+ impregnation of MOF-74 to improve CO/N_2 and CO/CO_2 separations,” accepted by RSC Advances

J Thompson, G Marinick, J Osio-Norgaard, A Evans, R Street, C Petit, G Whiting, “3D-Printed Multi-functional Composites for Carbon Dioxide Removal Through Temperature Swing Adsorption,” ACS Applied Material Interfaces, **11**, (2019), 43337-43343

M Cummings, A Evans, D Decarolis, C Petit, F Siperstein, M Attfield, “Studies into the CO hysteresis of Cu analogues of the hexagonal pore MOFs,” in preparation

M Cummings, A Evans, M Brown, C Petit, F Siperstein, M Attfield, “Role of the Metal Centre, Pore Diameter and Metal Coordination in the Separation of CO/N_2,” in preparation

Declaration of Originality

I hereby declare that this thesis is my own work, and any work performed by others has been clearly indicated and acknowledged. References to published work have been appropriately cited.

Copyright declaration

The copyright of this thesis rests with the author. Unless otherwise indicated, its contents are licensed under a Creative Commons Attribution-Non Commercial 4.0 International Licence (CC BY-NC).

Under this licence, you may copy and redistribute the material in any medium or format. You may also create and distribute modified versions of the work. This is on the condition that: you credit the author and do not use it, or any derivative works, for a commercial purpose.

When reusing or sharing this work, ensure you make the licence terms clear to others by naming the licence and linking to the licence text. Where a work has been adapted, you should indicate that the work has been changed and describe those changes.

Please seek permission from the copyright holder for uses of this work that are not included in this licence or permitted under UK Copyright Law.

Acknowledgements

I would like to sincerely thank my supervisor Dr. Camille Petit for all her support and supervision these last four years. Camille has always gone over and beyond her means, as both an academic supervisor and mentor, and for that I am very grateful for. Thank you also taking me on as a student in the first place, and for providing wonderful opportunities such as the international conferences to present my work and meet leading academics.

I would like to thank all members of the Petit group past and present, who have made my time at Imperial very enjoyable along with new friends made at Imperial. I would like to extend special thanks to Dr. Ryan Luebke and Dr. Salman Shahid, from whom I learnt a lot from, and showed great patience while training and discussing ideas. I would also like to thank Prof. Klaus Hellgardt and Dr. Fessehaye Zemichael for their assistance and guidance throughout my studies.

I would like to acknowledge the funding from BP-ICAM and EPSRC who funded the project and made this research possible. I would like to thank all members who have participated on the BP-ICAM project, and special thanks goes to Dr. Les Bolton and Dr. Dave Law for their technical input and continued support throughout the whole project. Thank you also to Dr Donato Decaloris for all his work at Diamond, and Matt Cummings for the synthesis and testing, and who has also been brilliantly responsive to any queries I have, no matter how big or small.

Finally, I would like to thank Mam, Dad and Emrys for their immense love and support, not only during these last four years, but for all the preceding years as well. Thank you for all you have provided, and I hope to continue making you all proud. Thank you to all of my family, and to Khun Yay, to whom I would like to dedicate this thesis to. Thank you for all the joy and happiness you provided us all as a family.

Table of Contents

Chapter 1 Introduction 18

1.1 Motivation 18

1.2 Thesis content 19

1.3 References 21

Chapter 2 Literature Review 22

2.1 Introduction 22

2.2 Carbon monoxide production 22

2.2.1 CO industrial uses 24

2.2.2 Routes to CO production 26

2.2.3 Industrial routes to CO separation and purification 27

2.2.4 CO purification techniques under development 28

2.3 Adsorption theory 30

2.4 Adsorbent materials 32

2.4.1 Activated carbons 32

2.4.2 Activated alumina 33

2.4.3 Zeolites 33

2.5 Metal-organic frameworks 37

2.5.1 Overview of CO purification mechanisms in MOFs 37

2.5.2 CO adsorption through CO-metal binding 38

2.5.3 CO adsorption through CO-metal binding and conformational change 45

2.5.4 CO adsorption through CO-metal binding enhanced by spin state transition 46

2.5.5 CO adsorption through chemical modification of the MOF 50

2.5.6 CO purification via size exclusion based separation 52

2.5.7 Current challenges and outlook in the use of MOFs for CO purification 54

2.6 Conclusions and Research Gaps 59

2.7 Research Objectives 61

2.7.1 RO 1: To screen MOFs for CO/N_2 separation 62

2.7.2 RO 2: To test the dynamic performance of the best performing MOFs for CO/N_2 separation 62

2.7.3 RO 3: To collect kinetic and thermodynamic data relevant for CO/N_2 separation 62

2.7.4 RO 4: To design, synthesize and test new MOFs for CO/N_2 separation based on the knowledge collected 63

2.8 References 64

Chapter 3 Dynamic adsorption measurement techniques 74

3.1 Introduction 74

3.2 Flux response technology 74

3.2.1 Background 74

3.2.2 Dynamic capacity measurements theory 75

3.2.3 Dynamic capacity measurements experimental 80

3.3 Breakthrough column analysis 81

3.3.1 Background 81
3.3.2 Dynamic separation and breakthrough capacity measurements 83
3.3.3 Diffusivity measurements 90
3.4 References 95
Chapter 4 Characterisation techniques 99
4.1 MOF structure 99
4.1.1 Textural parameters: N_2 sorption isotherms at -196 °C 99
4.1.2 Crystalline structure- X-ray diffraction 102
4.1.3 Electronic structure: X-ray absorption fine structure 104
4.2 MOF chemistry 107
4.2.1 Bulk chemistry: Diffuse reflectance infrared Fourier transform spectroscopy 107
4.2.2 Bulk chemistry: Inductively coupled plasma mass spectrometry 108
4.2.3 Surface chemistry: X-ray photoelectron spectroscopy 109
4.2.4 Thermal analysis: Thermogravimetric analysis 111
4.2.5 Thermal analysis: Temperature programmed desorption 111
4.3 References 113
Chapter 5 Preliminary MOF screening 114
5.1 Introduction 114
5.2 Materials synthesis 115
5.2.1 Cu-Zeolite Y 117
5.2.2 CuTDPAT 117
5.2.3 HKUST-1 118
5.2.4 MOF-505 118
5.2.5 PCN-12 118
5.2.6 Fe-MIL-100 120
5.2.7 Cr-MIL-101 120
5.2.8 Cu-MFU-4L 121
5.2.9 Cu-MOF-74 122
5.2.10 Ni-MOF-74 123
5.2.11 Co-MOF-74 123
5.2.12 Ni_2Cl_2(BBTA) 124
5.2.13 Co_2Cl_2(BBTA) 124
5.2.14 Ni_2Cl_2(BTDD) 125
5.2.15 Co_2Cl_2(BTDD) 125
5.3 Materials characterisation 127
5.4 Materials testing 127
5.4.1 Equilibrium testing 127
5.4.2 Dynamic testing 131
5.5 Results and discussion 131
5.5.1 Materials characterisation 131
5.5.2 Equilibrium adsorption 135
5.5.3 Dynamic adsorption 143

5.6 Conclusions 145
5.7 References 147
Chapter 6 CO/N_2 dynamic separation studies 150
6.1 Introduction 150
6.2 Materials synthesis 152
6.3 Materials testing 152
6.4 Results and discussion 152
6.4.1 Equimolar $CO:N_2$ breakthrough analysis 152
6.4.2 Varying $CO:N_2$ compositions analysis 156
6.4.3 1-D hexagonal pored MOF structure comparison 160
6.5 Conclusions 163
6.6 References 165
Chapter 7 Stability and impurity testing for CO/N_2 separation 166
7.1 Introduction 166
7.2 Materials synthesis 168
7.3 Materials characterisation 168
7.4 Materials testing 168
7.4.1 Equilibrium testing 169
7.4.2 Dynamic testing 169
7.5 Results and Discussion 170
7.5.1 Thermal analysis of the MOF structural integrity 170
7.5.2 CO desorption temperature analysis 170
7.5.3 Cyclic testing and post-CO adsorption characterisation 172
7.5.4 CO/CO_2 separation 173
7.5.5 $CO/N_2/CO_2$ separation 176
7.6 Conclusions 177
7.7 References 179
Chapter 8 Thermodynamic and kinetic data 181
8.1 Introduction 181
8.2 Materials synthesis 183
8.3 Materials characterisation 183
8.4 Materials testing 183
8.4.1 Equilibrium testing 183
8.4.2 Dynamic testing 185
8.5 Results and discussion 185
8.5.1 1-D hexagonal pored MOFs K_H and K_D 185
8.5.2 Cu-Cu paddlewheel MOFs K_H 188
8.6 Conclusions 190
8.7 References 192

Chapter 9 Cu impregnation of MOF-74 to improve CO/N_2 and CO/CO_2 separations 193

9.1 Introduction 193

9.2 Materials synthesis 195

9.3 Materials characterisation 196

9.4 Materials testing 196

9.4.1 Dynamic testing conditions using flux response technology 196

9.4.2 Dynamic testing conditions using breakthrough column 197

9.5 Results and discussion 197

9.5.1 Characterisation of Cu impregnated samples 197

9.5.2 Effect of Cu impregnation on CO adsorption 201

9.5.3 In-situ Cu@M-MOF-74 XAFS characterisation 204

9.5.4 In-situ Cu@M-MOF-74 DRIFTS characterization 209

9.5.5 Dynamic CO/N_2 and CO/CO_2 separation testing 211

9.6 Conclusions 213

9.7 References 215

Chapter 10 Conclusions and Outlook 218

10.1 Conclusions 218

10.2 Future work 220

10.2.1 To perform post-synthesis modification with MOFs with greater porosity 220

10.2.2 To develop MOF formulation for an adsorbent bed and to measure their material properties 221

10.2.3 To develop an experimental breakthrough set-up to test different adsorption separation processes 221

Appendices 222

Appendix 1 222

Appendix 2 224

Appendix 3 225

Appendix 4 228

Appendix 5 231

Appendix 6 232

Rights and Permissions 236

Table of Figures

Figure 2-1. Schematic of syngas production process and CO purification steps. The colour code distinguishes between chemicals to be recovered and used (in green) and impurities (red). 23

Figure 2-2. Overview of the different separation mechanisms utilised for CO sorption and purification in MOFs: (A) highly energetic CO-metal interactions (chemisorption or quasi-chemical sorption); (B) surface interactions through ligand functional groups; (C) CO-metal interactions promoting conformational change; (D) size exclusion based separation. Green octahedrons denotes metal cluster. Grey cylinders denote organic ligands. Blue spheres denotes the targeted adsorbate. 31

Figure 2-3. CO adsorption on M-MOF-74 dominated by CO-metal binding. (A) First coordination sphere of M-MOF-74 analogues for M^{2+} ions with M-CO distances (Å) and M-C-O angles (°) labelled; (B) Relationship between M-CO distance (open black diamonds) and isosteric heat of CO adsorption (Qst, blue circles) of M-MOF-74 metal centre. Ideal Adsorbed Solution Theory (IAST) selectivities of M-MOF-74 for: (C) CO/N_2 and (D) CO/H_2 mixtures at varying compositions at 25 °C and 1 bar.[97] Reprinted (adapted) with permission from ACS Publications. Copyright 2014 American Chemical Society. 42

Figure 2-4. CO separation through CO-metal binding and conformational change using $Cu(AIP)(H_2O)$: Coordination environment of: (A) solvated Cu-Cu paddlewheel units and (C) desolvated Cu-Cu paddlewheel unit. Porous structures illustrated with Connolly surfaces: (B) as-synthesized $Cu(AIP)(H_2O)$ and (D) dried $Cu(AIP)(H_2O)$. Atom colors: Cu, green; C, grey; N, blue; O, red. Hydrogen atoms and azide groups emitted for clarity. (E) $Cu(AIP)(H_2O)$ CO sorption isotherm (adsorption- solid circles, desorption- open circles) at -153 °C.[109] 45

Figure 2-5. CO separation through CO-metal binding and conformational change using Fe-BTTri. Ideal Adsorbed Solution Theory (IAST) selectivities of Fe-BTTri for: (A) CO/H_2 (purple), CO/N_2 (blue), CO/CH_4 (black); (B) CO/CO_2 (green at 25 °C, light green at 45 °C) mixtures at 25 °C and 1 bar, unless stated otherwise. (C) Cyclic CO adsorption (blue circles) and desorption (red circles profiles of Fe-BTTri with Cycle 1 capacity used as reference percentage capacity. Adsorption recorded at 25 °C and 0.01 bar and desorption was performed at 150 °C under dynamic vacuum.[111] Reprinted (adapted) with permission from ACS publications. Copyright 2016 American Chemical Society. 47

Figure 2-6. CO adsorption through CO-metal binding and conformational change using $Fe_2Cl_2(BBTA)$. (A) Schematic of cooperative spin transition mechanism of $Fe_2Cl_2(BBTA)$ at low pressure (< 0.1 bar) before isotherm step region, Fe^{2+} high-spin to low-spin state conversion with increasing pressure (0.15-0.3 bar) and full conversion to low-spin state beyond the step pressure. Atom/ion colors: C, grey; Cl, green; N, blue; O, red; high-spin Fe^{2+}, orange; low-spin Fe^{2+}, purple. Hydrogen atoms emitted for clarity. (B) CO adsorption isotherm of $Fe_2Cl_2(BBTA)$ at 25 °C with steps 1-3 shown in corresponding purple and green regions.[110] 48

Figure 2-7. CO adsorption through chemical modification of the MOF. Schematic of Fe-MIL-100 and Cu impregnated Fe-MIL-100, CO and N_2 adsorption isotherms, and IAST selectivities for equimolar CO/N_2 at 25 °C.[85] 51

Figure 3-1. Schematic of the experimental configuration of flux response technology for an (a) electric Wheatstone bridge assembly and (b) pneumatic Wheatstone bridge assembly. 76

Figure 3-2. Schematic of flux response technology instrument for dynamic CO adsorption measurements. MFC = Mass-flow controller; BPR = Back-pressure regulator; DPT = Differential pressure transducer. 76

Figure 3-3. Flux response technology experimental profile of Co-MOF-74 (50:50 *v:v* CO:N_2) at 25 °C and 1 bar. 77

Figure 3-4. Example single component breakthrough curve profile of adsorbates exhibiting fast (green) and slow (red) sorption kinetics. 82

Figure 3-5. Example binary breakthrough curve profile of adsorbates with high (green) and low (blue) affinity to the adsorbate with differing breakthrough times (t_{b1} and t_{b2}). 82

Figure 3-6. Schematic of breakthrough column. 85

Figure 3-7. Schematic of breakthrough adsorption column instrument for CO/N_2 separation measurements. *a* = adsorbates, MFC = Mass-flow controller; BPR = Back-pressure regulator; MS = Mass spectrometer. 88

Figure 3-8. Images of the breakthrough adsorption column instrument for CO/N_2 separation measurements. (a) Front-view image displaying the column, back-pressure regulators, gauges and switches. (b) Side-view image displaying the mass-flow controllers and inlet gases. (c) Side-view image displaying power supply and the tubing from the inlet to the four-port switch valves to the outlet. 88

Figure 3-9. Calibration curves of the mass-spectrometer ionic conductivity signals relative to the inlet gas adsorbate flow rates of CO (left) and N_2 (right). 89

Figure 3-10. Desorption profiles of CO adsorbate with He inert carrier gas (15 mL min^{-1}) for $K_{D,\,CO}$ calculation at 25 °C through using the ZLC method. 94

Figure 4-1. A schematic representation of Bragg's law with X-ray diffraction. 103

Figure 4-2. Ni-edge X-ray absorption fine structure spectrum of Ni-MOF-74. 105

Figure 4-3. Schematic of a Diffuse reflectance infrared Fourier transform spectroscopy experimental set-up. 108

Figure 5-1. Structures of Cu-Cu paddlewheel MOFs: (a) CuTDPAT,[24] (b) HKUST-1,[25] (c) MOF-505[26] and (d) PCN-12.[26] 119

Figure 5-2. Structures of mesoporous MOFs: (a) Fe-MIL-100[29] and (b) Cr-MIL-100.[30] 121

Figure 5-3. Structure of Cu-MFU-4L.[33] 122

Figure 5-4. Structures of 1-D hexagonal pored MOFs: (a) M-MOF-74, M_2(BBTA) and (c) M_2(BTDD). Images produced by Mr Matthew Cummings (University of Manchester) 126

Figure 5-5. X-ray diffraction patterns of (a) HKUST-1 and (b) Ni-MOF-74. The simulated diffraction pattern of each structure is added on each panel for comparison, shown in black at the bottom of the panel. 132

Figure 5-6. N_2 sorption isotherms at -196 °C of the: (a) Cu-Cu paddlewheel MOFs, (b) Cu^+-based MOF and mesoporous MOFs, (c) 1-D hexagonal pored M-MOF-74 structures and (d) 1-D hexagonal pored M_2Cl_2(BBTA) and M_2Cl_2(BTDD) structures. The isotherm for Cu-Zeolite Y is added on each panel for comparison. 133

Figure 5-7. CO equilibrium sorption isotherms at 25 °C up to 20 bar using gravimetric gas sorption analysis of the: (a) Cu-Cu paddlewheel MOFs, (b) Cu^+-based MOF and mesoporous MOFs, (c) 1-D hexagonal pored M-MOF-74 structures and (d) 1-D hexagonal pored M_2Cl_2(BBTA) and M_2Cl_2(BTDD) structures. The isotherm for Cu-Zeolite Y is added on each panel for comparison. 136

Figure 5-8. N_2 equilibrium sorption isotherms at 25 °C up to 20 bar using gravimetric gas sorption analysis of the: (a) Cu-Cu paddlewheel MOFs, (b) Cu^+-based MOF and mesoporous MOFs, (c) 1-D hexagonal pored M-MOF-74 structures and (d) 1-D hexagonal pored M_2Cl_2(BBTA) and M_2Cl_2(BTDD) structures. The isotherm for Cu-Zeolite Y is added on each panel for comparison. 137

Figure 5-9. CO/N_2 (50:50 *v:v*) IAST selectivity at 25 °C up to 20 bar calculated from the CO and N_2 pure single component isotherms of: (a) Cu-Cu paddlewheel MOFs, (b) Cu^+-based MOF and mesoporous MOFs, (c) 1-D hexagonal pored M-MOF-74 structures and (d) 1-D hexagonal pored M_2Cl_2(BBTA) and M_2Cl_2(BTDD) structures. The isotherm for Cu-Zeolite Y is added on each panel for comparison. 138

Figure 6-1. CO and N_2 breakthrough curves of Cu-Zeolite Y, Co-MOF-74 and Ni-MOF-74 for a 50:50 *v:v* CO:N_2 binary gas mixture measured on a breakthrough adsorption column instrument at 25 °C and 1 bar. 153

Figure 6-2. (a) CO and (b) N_2 breakthrough curves of a binary mixture (5:95, 30:70, 50:50, 70:30, 95:5 *v:v* CO:N_2 inlet feed concentration) for Co-MOF-74 at 25 °C and 1 bar. (c) CO and (d) N_2 breakthrough curves of a binary mixture (5:95, 30:70, 50:50, 70:30, 95:5 *v:v* CO:N_2 inlet feed concentration) for Ni-MOF-74 at 25 °C and 1 bar. (e) The CO and N_2 breakthrough capacities of Co-MOF-74 (circles) and Ni-MOF-74 (triangles) at varying inlet feed concentrations. The Cu-Zeolite Y breakthrough capacities at 50:50 *v:v* CO:N_2 are shown on the figure. (f) The separation factor (squares) and CO/N_2 equilibrium ideal selectivity (triangles) of Co-MOF-74 at varying inlet feed concentrations. 157

Figure 6-3. (a) CO and N_2 breakthrough curves, (b) CO breakthrough capacities and CO/N_2 ideal equilibrium selectivities of Cu-Zeolite Y, Co-MOF-74, Ni-MOF-74, Co_2Cl_2(BBTA), Ni_2Cl_2(BBTA), Co_2Cl_2(BTDD) and Ni_2Cl_2(BTDD) for a 50:50 *v:v* CO:N_2 binary gas mixture measured on a breakthrough adsorption column instrument at 25 °C and 1 bar. 161

Figure 7-1. Variable-temperature X-ray diffraction patterns of (a) Ni-MOF-74 and (b) Co-MOF-74 from room temperature up to 500 °C. (c) Temperature Programmed CO desorption curve of Co-MOF-74 and Ni-MOF-74. (d) Thermogravimetric curve of Co-MOF-74 and Ni-MOF-74 under N_2 atmosphere. (e) Cyclic CO and N_2 breakthrough capacities of Co-MOF-74 (circles) and Ni-MOF-74 (triangles) for 50:50

v:v $CO:N_2$ feed mixture at 25 °C and 1 bar. Thermal regeneration was performed in between adsorption cycles by heating for 2 h at 190 °C and 180 °C for Ni-MOF-74 and Co-MOF-74, respectively. (f) X-ray diffraction patterns and textural parameters of simulated M-MOF-74, as-synthesized and post-CO adsorption tested Co-MOF-74 (20 cycles) and Ni-MOF-74 (12 cycles). 171

Figure 7-2. CO, N_2 and CO_2 equilibrium adsorption isotherms of (a) Ni-MOF-74 and (b) Co-MOF-74 at 25 °C up to 1 bar using volumetric gas sorption analysis. 173

Figure 7-3. CO breakthrough capacities and CO/X (X = CO_2, N_2) ideal equilibrium selectivities of (a) Co-MOF-74 and (b) Ni-MOF-74 at 50% (top), 95% (middle) and 99% (bottom) CO inlet feed concentration of $CO:CO_2$, $CO:N_2$ and $CO:N_2:CO_2$ gas mixtures measured on a breakthrough adsorption column instrument at 25 °C and 1 bar. 174

Figure 8-1. (a) CO and (b) N_2 equilibrium adsorption isotherms of HKUST-1 and Co-MOF-74 at 25 °C up to 1 bar with their corresponding Henry's law constant values labelled. 184

Figure 8-2. (a) CO and (b) N_2 Henry's law constant values as an inverse function of temperature over a range of 10-40 °C for Ni-MOF-74, Co-MOF-74, Ni_2Cl_2(BBTA), Co_2Cl_2(BBTA), Ni_2Cl_2(BTDD) and Co_2Cl_2(BTDD). 186

Figure 8-3. The 1-D hexagonal pored MOFs (a) CO Henry's law constant (25 °C) and CO Q_{st} values as a function of CO/N_2 (50:50 *v:v*) IAST selectivity. (b) CO Henry's law constant (at 25 °C) and $Q_{st, CO}$ values as function of metal density. (c) CO Henry's law constant (25 °C) and CO diffusivity coefficients (25 °C) values as a function of $Q_{st, CO}$. (d) N_2 diffusivity coefficient values as a function of BET surface area. 1 point (circle, triangle or square) represents one 1-D hexagonal pored MOF structure. 187

Figure 8-4. (a) CO and (b) N_2 Henry's law constant values as an inverse function of temperature over a range of 10-40 °C for HKUST-1, CuTDPAT, MOF-505 and PCN-12. 189

Figure 8-5. (a) CO and N_2 Henry's law constant values (25 °C) as a function of BET surface area and (b) CO/N_2 IAST selectivity as a function of N_2 Q_{st}. 1 point (circle, triangle or square) represents one 1-D hexagonal pored MOF structure. 190

Figure 9-1. Characterisation of the Cu-impregnated MOFs: (a) X-ray diffraction patterns of simulated MOF-74, Ni-MOF-74, 2-Cu@Ni-MOF-74, 4-Cu@Ni-MOF-74 and 7-Cu@Ni-MOF-74. (b) N_2 sorption isotherms at -196 °C of Ni-MOF-74, 2-Cu@Ni-MOF-74, 4-Cu@Ni-MOF-74 and 7-Cu@Ni-MOF-74. The textural parameters derived from the isotherms are shown on the table. (c) Cu 2*p* spectra of 4-Cu@Ni-MOF-74. The deconvoluted Cu peaks and energy levels are shown alongside the characteristic Cu^{2+} satellites. 199

Figure 9-2. Dynamic CO capacities (50:50 *v:v* $CO:N_2$) measured at 25 °C and 1 bar on the FRT set-up. Thermal activation and Cu reduction was performed for 6 h at 250 °C with flowing 10% CO (in He) unless stated otherwise. The dynamic CO capacity per mol of metal was calculated using the measured values on the FRT and the Cu loading obtained from the ICP-MS analysis. (a) Dynamic CO capacities at varied Cu loadings using equimolar $CuCl_2:Cu(HCO_2)_2$ salt precursors. (b) Dynamic CO capacities using different Cu salts for impregnation. (c) Dynamic CO capacities using $CuCl_2:Cu(HCO_2)_2$ salts with

thermal activation and Cu reduction performed using He or CO atmosphere. (d) Dynamic CO capacities of Cu@Ni-MOF-74 and Cu@Co-MOF-74 at varied Cu loadings using equimolar $CuCl_2$:$Cu(HCO_2)_2$ salt precursors. 202

Figure 9-3. Study of the MOF activation and Cu reduction procedure of 4-Cu@Ni-MOF-74: (a) Cu-edge XANES spectra. Arrow 1 = Cu^{2+} peak; Arrow 2 = Cu^{+} peak. (b) Linear Combination Fit analysis of Cu species. (c) Ni-edge XANES spectra. (d) Ni-O bond lengths obtained by the EXAFS fit during the activation and Cu reduction procedure and analysis (shaded). 205

Figure 9-4. Study of CO adsorption upon 4-Cu@Ni-MOF-74: (a) Cu-edge XANES spectra. (b) Ni-edge XANES spectra. 209

Figure 9-5. *In-situ* DRIFTS measurement of chemisorbed CO on Ni-MOF-74, Cu-MOF-74 and 4-Cu@Ni-MOF-74 at 25 °C and 1 bar. Each spectrum has been background corrected with respect to the instrument and sample holder. 210

Figure 9-6. Breakthrough curves of Ni-MOF-74 and 4-Cu@Ni-MOF-74 for 50:50 v:v binary gas mixtures on a breakthrough adsorption column at 25 °C and 1 bar: (a) CO:N_2 mixture and (b) CO:CO_2 mixture. (*CO* Q_{BT} = CO breakthrough capacity, $S_{CO/X}$ = CO/X ideal selectivity at equilibrium where X = N_2, CO_2) 212

Table of Tables

Table 2-1. Chemical reactions associated with syngas and/or CO usage and production. 25

Table 2-2. Summary table of adsorbents reported so far for CO adsorption and CO/X separation (X = CH_4, N_2, CO_2 and H_2) at varying temperature and 1 bar. 34

Table 2-3. Benefits and limitations of various existing and proposed CO purification technologies. 36

Table 2-4. Summary table of MOFs reported to date for CO adsorption and CO/*X* separation (*X*: CH_4, N_2, CO_2, H_2) at varying temperature and 1 bar. 39

Table 5-1. Metal density and textural parameters derived from N_2 sorption isotherms at -196 °C of the Cu-Zeolite Y and MOFs. (S_{BET} = BET surface area, V_{tot} = total pore volume, V_{mic} = micropore volume and V_{mes} = mesopore volume). 134

Table 5-2. Summary of CO and N_2 equilibrium adsorption capacities, CO/N_2 IAST selectivity values (50:50 *v:v* CO:N_2) and dynamic CO uptake change values (50:50 *v:v* CO:N_2, obtained using the FRT instrument) at 25 °C and specified pressure. 139

Table 5-3. CO and N_2 Q_{st} values of MOFs at low loading. 140

Table 8-1. Henry's law constants, diffusivity coefficent values, metal densities and textural parameters of 1-D hexagonal pored and Cu-Cu paddlewheel MOFs at 25 °C. (S_{BET} = BET surface area, Q_{st} = isosteric enthalpy of adsorption, K_H = Henry's law constant and K_D = diffusivity coefficient). 186

Table 9-1. Metal loading quantities and textural parameters derived from the elemental analysis (XPS and ICP-MS) and N_2 sorption isotherms at -196 °C for the synthesized and Cu impregnated MOFs. The MOFs were loaded with equimolar solutions of $Cu(II)Cl_2$:$Cu(II)(HCOO)_2$. (S_{BET} = BET surface area, V_{tot} = total pore volume, V_{mic} = micropore volume and V_{mes} = mesopore volume). 198

Abbreviations

AC	Activated carbon	IL	Ionic liquid
ATR	Autothermal Reforming	IR	Infrared
BET	Brunauer–Emmett–Teller	IUPAC	International Union of Pure and Applied Chemistry
BPR	Back pressure regulator	MeOH	Methanol
DCM	Dichloromethane	MFC	Mass flow controller
DMA	*N,N*-Dimethylacetamide	MOF	Metal-organic framework
DMF	*N,N*-Dimethylformamide	MS	Mass spectrometry
DPT	Differential pressure transducer	POX	Partial oxidation
DRIFTS	Diffuse reflectance infrared Fourier transform spectroscopy	PSA	Pressure-swing adsorption
EDAX	Energy Dispersive Analysis of X-rays	PTSA	Pressure-temperature-swing adsorption
EtOH	Ethanol	SMR	Steam-methane reformation
EXAFS	Extended X-ray absorption fine structure	TGA	Thermogravimetric analysis
FRT	Flux response technology	THF	Tetrahydrofuran
FTIR	Fourier Transform Infrared Spectroscopy	TPD	Temperature programmed desorption
H_2BBTA	1H,5H-benzo(1,2-d:4,5-d')bistriazole)	TSA	Temperature-swing adsorption
H_2BDC	Benzene-1,4-dicarboxylic acid	VSA	Vacuum-swing adsorption
H_2BTDD	Bis(1H-1,2,3-triazolo[4,5-b],[4',5'-i])dibenzo[1,4] dioxin	VTSA	Vacuum-temperature-swing adsorption
H_3BTC	benzene-1,3,5-tricarboxylic acid	VTXRD	Variable temperature X-ray diffraction
H_4BPTC	Biphenyl-3,3′,5,5′-tetracarboxylic acid	XAFS	X-ray absorption fine structure
H_4DOBDC	2,5-dihydroxyterephthalic acid	XANES	X-ray absorption near edge structure
IAST	Ideal Adsorbed Solution Theory	XPS	X-ray photoelectron spectroscopy
ICP-MS	Inductively coupled plasma mass spectrometry	XRD	X-ray diffraction
IGA	Intellectual gravimetric analyser	ZLC	Zero length column

Chapter 1 Introduction

1.1 Motivation

The capital and operating costs of chemical separations contribute significantly to the overall industrial expenditure. For instance, separation processes account for 10-15% of global energy consumption.[1] Improvements upon production and purification of synthetic industrial chemical reagents can therefore provide large economic and environmental benefits. Due to the similar chemical and physical properties of carbon monoxide (CO) and nitrogen (N_2), CO purification from N_2 impurity is particularly challenging and therefore energy and cost intensive.[2] Adsorption separation provides a possible energy-saving alternative.[3] While porous adsorbents such as activated carbons and zeolites have exhibited CO adsorption capacity and selectivity,[4] their CO/N_2 separation performance for industrial implementation does not challenge the current technology for CO purification performance, *i.e.* cryogenic distillation.[2,5-7]

Metal-organic frameworks (MOFs) are a class of materials that have emerged as effective adsorbents for gas separation owing to their high surface area and the versatility of their structure and chemistry.[8-11] Through exploiting their metal interactions with CO,[12] highly selective CO/N_2 separation can be achieved that surpasses the performance of activated carbons and zeolites.[4] However, identifying and taking advantage of the MOFs chemical and physical properties that controls CO/N_2 separation is required in order for MOFs to compete with the existing technology. Furthermore, comprehensive testing of the MOFs under dynamic conditions is required to understand how they would perform in an industrial setting. The systematic screening study of MOF properties, dynamic testing of promising

MOFs in industrial conditions and the development of novel MOFs for enhancing CO/N_2 separation represent the motivation of the work discussed in this thesis.

1.2 Thesis content

- Chapter 1 provides further background and motivation for the project.
- Chapter 2 presents the importance of CO as a chemical reagent in industry and provides a literature review of the current technologies for CO purification. It covers the theory of molecular separation *via* adsorption and how it can be employed for CO/N_2 separation. The chapter provides a literature review of the studies on MOFs for CO adsorption and CO/N_2 separation. This chapter highlights the knowledge gaps and presents the research objectives established from these areas.
- Chapter 3 presents the background, theory and experimental procedures of the dynamic sorption testing techniques used in the thesis. The chapter explains the motivation for choosing these techniques. It also describes the modifications of the apparatus to extract further kinetic information.
- Chapter 4 presents the theory and experimental procedures of the characterisation techniques used throughout the thesis, and an explanation of why these techniques were chosen.
- Chapter 5 presents the MOF synthesis procedures and the preliminary screening of the MOFs for CO/N_2 separation through equilibrium and dynamic sorption testing. The chapter discusses the MOF properties that govern CO/N_2 separation.
- Chapter 6 presents an in-depth dynamic sorption study for CO/N_2 separation for the best performing MOFs identified in Chapter 5. The chapter studies the effect of N_2 impurity in an industrial stream, and the effect of varying the MOF metal density and porosity upon CO/N_2 separation.

- Chapter 7 presents the CO/N_2 separation cyclability and effect of CO_2 impurity in $CO/N_2/CO_2$ separation of the best performing MOFs identified in Chapters 5 and 6. The tests performed here provide an outlook on the industrial viability of the MOFs for implementation in a separation process.
- Chapter 8 provides kinetic and thermodynamic data of the MOFs. The data from this chapter is key for developing a process scale design of a CO/N_2 separation.
- Chapter 9 presents the design, synthesis and development of new MOF-based systems to enhance the CO/N_2 separation performance using the knowledge gained from the previous chapters. This was done *via* impregnation of Cu sites within the MOF structures.
- Chapter 10 presents a summary of the findings and a discussion of the potential future work.

1.3 References

1 Sholl, D. S. & Lively, R. P. Seven chemical separations: to change the world: purifying mixtures without using heat would lower global energy use, emissions and pollution--and open up new routes to resources. *Nature* **532**, 435-438, (2016).

2 Dutta, N. N. & Patil, G. S. Developments in CO separation. *Gas Separation & Purification* **9**, 277-283, (1995).

3 Yang, R. T. *Gas Separation by Adsorption Processes*. (Imperial College Press, 1997).

4 Evans, A., Luebke, R. & Petit, C. The use of metal–organic frameworks for CO purification. *Journal of Materials Chemistry A* **6**, 10570-10594, (2018).

5 Mosa, T. & Taylor, G. T. *Method and apparatus for the manufacture of high purity carbon monoxide*, US Pat., 8,703,089, (2014).

6 Mosa, T. & Taylor, G. T. *Method and apparatus for the manufacture of high purity carbon monoxide*, US Pat., 9,567,226, (2017).

7 Haase, D. J. & Walker, D. G. The COSORB Process. *Chemical Engineering Progress* **5**, 74-77, (1974).

8 Sumida, K. *et al.* Carbon Dioxide Capture in Metal–Organic Frameworks. *Chemical Reviews* **112**, 724-781, (2012).

9 Kuppler, R. J. *et al.* Potential applications of metal-organic frameworks. *Coordination Chemistry Reviews* **253**, 3042-3066, (2009).

10 Li, J.-R., Kuppler, R. J. & Zhou, H.-C. Selective gas adsorption and separation in metal–organic frameworks. *Chemical Society Reviews* **38**, 1477-1504, (2009).

11 Czaja, A. U., Trukhan, N. & Müller, U. Industrial applications of metal–organic frameworks. *Chemical Society Reviews* **38**, 1284-1293, (2009).

12 Khan, N. A. & Jhung, S. H. Adsorptive removal and separation of chemicals with metal-organic frameworks: Contribution of π-complexation. *Journal of Hazardous Materials* **325**, 198-213, (2017).

Chapter 2 Literature Review

Aspects of the literature review in this chapter have been published in Journal of Materials Chemistry A.[1]

2.1 Introduction

In this chapter, a general introduction to the production routes and applications of CO as an industrial reagent is provided. The current approaches used to purify CO are reviewed, before detailing more recent research contributions towards the development of adsorbents for challenging CO/N_2 separation as an energy and cost efficient alternative to thermal separations and absorption technologies. All the classes of adsorbents studied are reviewed, before discussing in detail the CO adsorption studies using metal-organic frameworks (MOFs). The CO adsorption mechanisms and provide are reviewed and an industrial outlook for CO separation on the reported studies is provided, with particular emphasis on kinetic data and cyclability as these provide useful information for scale-up from lab tests to industrial use. From these key findings and knowledge gaps identified, established research objectives for the study of using MOFs for dynamic CO/N_2 separation were established.

2.2 Carbon monoxide production

Separation processes contribute 40-70% of capital and operating costs within industry, and account for an estimated 10-15% of global energy consumption.[2] Nearly all products require some form of separation during manufacture. Given the scale and energy-intensive nature of separation processes, even a small technological

improvement can have a large impact from a cost and sustainability viewpoint. In this regard, the emergence of 'non-traditional' separation techniques along with the development of novel materials can provide alternative solutions to existing industrial separation processes.

One specific area that could benefit from such development and represents the topic of this study is carbon monoxide (CO) purification, especially with respect to synthesis gas (syngas) production. Syngas is the major source of CO and H_2 in industry and is obtained through partial oxidation or steam reformation of carbonaceous feedstocks - biomass or fossil fuels. Syngas production and separation (*i.e.* CO/H_2 separation along with removal of impurities) is required to obtain CO for industrial use.[3,4] The current industrial route towards CO purification involves a combination of cryogenic distillation, acid gas removal and dehydration (Figure 2-1).

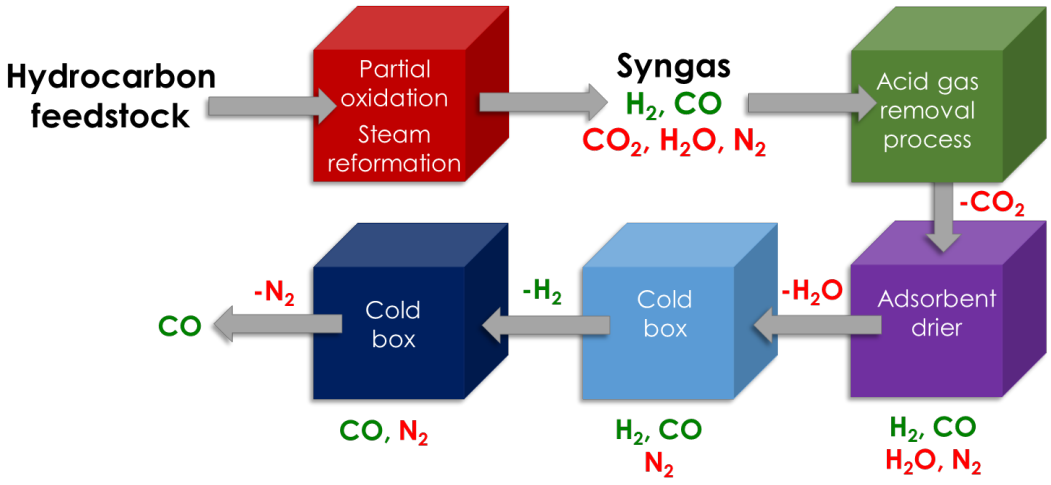


Figure 2-1. Schematic of syngas production process and CO purification steps. The colour code distinguishes between chemicals to be recovered and used (in green) and impurities (red).

The use of CO as a reagent, in various industrial processes, often requires an excess of 99 mol% purity;[5-7] to achieve such high purity incurs significant cost and often requires additional separation steps or a completely revised purification process. From

these separation processes, separating N_2 from CO is the most challenging. Current technologies such as cryogenic distillation can reach this target as long as the N_2 concentration remains low (< 1 mol%).[8] Yet, the similar chemical and physical properties of CO and N_2 make for a difficult separation, with high operating expenditure and energy costs due to the requirement for multiple heat exchangers and distillation columns. In this context, absorption using designer solvents or adsorption using porous materials (such as zeolites, activated carbons or metal-organic frameworks) are among the solutions explored as energy efficient alternatives.[9-14] These various options are discussed in this review with emphasis on the development and use of MOFs for CO separation owing to their promising performance so far.

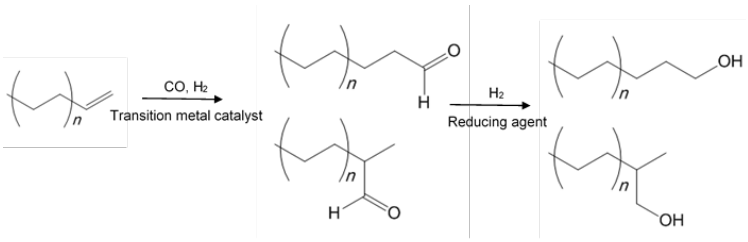
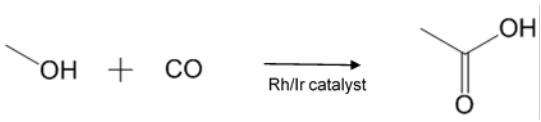
Overall, this review proposes a critical assessment of current advancements in the field of MOFs for CO purification and CO/N_2 separation, and provides insight into desirable properties to include in future materials designed for this targeted application.

2.2.1 *CO industrial uses*

As shown in Table 2-1, there are numerous large-scale industrial processes in which CO is a key input for synthesis of higher value compounds.[8,15,16] The Fisher Tropsch process for liquid fuel production is probably the most well-known example where syngas, hence CO, is used (Eq 2-1**,** Table 2-1).[17] Methanol is primarily produced from syngas feedstocks (Eq 2-2, Table 2-1). Another important process requiring pure CO is hydroformylation, which uses a homogenous catalytic reaction to convert CO and alkenes into aldehydes (Eq 2-3**,** Table 2-1).[18] The resultant aldehyde products can be further hydrogenated to produce alcohols that are eventually converted into plasticisers and detergents. Since the introduction of commercial scale

hydroformylation (also known as the oxo process) in 1948, the total consumption of products based on this process has risen to millions of metric tonnes per year.[19]

Table 2-1. Chemical reactions associated with syngas and/or CO usage and production.

Syngas/CO usage routes		
Fischer-Tropsch process	$(2n+1)H_2 + n\,CO \rightarrow C_nH_{(2n+2)} + n\,H_2O$	(2-1)
Methanol production	$2H_2 + CO \rightarrow CH_3OH$	(2-2)
Hydroformylation (followed by hydrogenation)		(2-3)
Phosgene production	$CO + Cl_2 \xrightarrow{Activated\ carbon} COCl_2$	(2-4)
Acetic acid production (Monsanto/CATIVA process)		(2-5)
Syngas/CO production routes		
Steam-methane reformation	$CH_4 + H_2O \rightarrow CO + 3H_2$	(2-6)
Water-gas shift	$CH_4 + 2\,H_2O \rightarrow CO_2 + 4H_2$	(2-7)
Water-gas shift	$CO + H_2O \rightarrow CO_2 + H_2$	(2-8)
General Partial Oxidation	$C_xH_y + x\,O_2/2 \rightarrow x\,CO + y\,H_2/2$	(2-9)
Methane Partial Oxidation	$2\,CH_4 + O_2 \rightarrow 2\,CO + 4H_2$	(2-10)
Autothermal Reformation	$4\,CH_4 + O_2 + 2\,H_2O \rightarrow 4\,CO + 10\,H_2$	(2-11)
Autothermal Reformation	$2\,CH_4 + O_2 + CO_2 + \rightarrow 3\,CO + 3\,H_2 + H_2O$	(2-12)

CO is also utilised as a reagent during the industrial synthesis of phosgene[20] (Eq 2-4**,** Table 2-1). Phosgene is produced when a pure stream of CO and Cl_2 gas is passed over a bed of catalytic activated carbon. Phosgene is an important industrial reagent used in the production of isocyanates, a precursor to numerous polymers including polyurethane foam which has a global consumption of 17 million metric tonnes per annum.[21]

The production of acetic acid through the carbonylation of methanol in the rhodium-catalysed Monsanto process also uses CO as a reagent (Eq 2-5, Table 2-1).[18] After the inception of the Monsanto process in 1970, an alternative and more environmentally friendly process – CATIVA process – with greater efficiency was discovered in the 1990s.[22] The final product in these processes, acetic acid, is a chemical reagent widely used as a solvent and as a precursor for numerous useful products including the polymers polyvinyl acetate and cellulose acetate. A study on the acetic acid world market in 2014 reported that 12.9 million metric tons was consumed annually,[23] emphasising further the requirement for large-scale CO production and purification in industry. As can be seen in Table 2-1, some reactions (Eq 2-4 and 2-5) do not directly involve syngas, but rather require a pure stream of CO. Hence, processes must be in place to provide pure CO streams.

2.2.2 *Routes to CO production*

CO chemical feedstocks originate from syngas, which is produced synthetically from carbon containing feedstocks such as natural gas, coal or biomass. Although predominantly composed of H_2 and CO, syngas also contains impurities such as CO_2 and H_2O (steam) which are generated during syngas production, and N_2, CO_2 and CH_4 which originate from the reactant feed stream.[24]

A number of industrial processes can be used to generate syngas resulting in a wide range of H_2:CO ratios depending on the foreseen application. Steam-methane reformation (SMR) is one example, (Eq 2-6**,** Table 2-1). While it is possible to use the resulting H_2:CO composition commercially,[25] lower temperature water-gas shift (WGS) reactions are often used to enrich the H_2 composition (Eq 2-7**,** Table 2-1) or to completely oxidise CO to CO_2 (Eq 2-8, Table 2-1). Other commercial routes to syngas

production include Partial Oxidation (POX) and Autothermal Reforming (ATR) (Eq 2-9 and Eq 2-10, Table 2-1). A hybrid of SMR and POX, Autothermal Reforming (ATR), generates syngas from hydrocarbon feedstocks combined with either O_2 and steam (Eq 2-11**,** Table 2-1) or O_2 and CO_2 (Eq 2-12**,** Table 2-1).

When pure CO streams are desired, a variety of separation processes can be implemented. Given the composition of typical syngas streams, CO separation from H_2 remains the most significant separation procedure. In addition, CO/CO_2, CO/N_2, CO/CH_4 separation and water removal processes are often required to remove further impurities.[8] CO purification and separation is the topic of the next section.

2.2.3 *Industrial routes to CO separation and purification*

2.2.3.1 Cryogenic distillation

The most common method for CO purification is through cryogenic distillation,[8,26-28] which has been implemented to obtain high purity H_2 and CO.[29-31] During syngas purification, CO_2, H_2O, and CH_4 are relatively easily condensed and are removed using low temperatures and moderate pressures *via* acid gas removal systems, drying units and gas scrubbers respectively. The resulting stream contains H_2, CO, and a variable concentration of N_2, ranging from trace amounts to percent levels depending on the hydrocarbon feedstock. Further cooling and/or compression liquefies the N_2 and CO components allowing for removal of high purity H_2 gas. If there is a small enough fraction of N_2, the CO can be used directly. If the content of N_2 is too large for the desired application, further processing is required to sufficiently reduce the residual N_2. This is often accomplished through an additional cryogenic distillation step involving multiple heat exchangers and distillation columns, significantly increasing the overall energy and process costs.

2.2.3.2 Absorption

An alternative to cryogenic distillation are separation processes utilising absorption mechanisms. The absorption routes explored in literature and industry rely on the interactions between CO molecules and transition metal ions, particularly Cu^+. These interactions involve σ-bond formation between the filled σ-orbital of the carbon electrons and the empty *d* or *p*-orbital of the metal. Back-donation from the filled metal *d*-orbital to the empty carbon π*-orbital enhances the strength of M-CO interactions. This complexation results in selective affinity to CO; the reversible nature of the interactions make this approach suitable for CO extraction and recovery. The COSORB™ process is an example of a copper-based absorption process used on an industrial-scale.[32-34] This process purifies mixed gas streams binding to CO, forming a cuprous aluminium chloride ($CuAlCl_4$)-toluene based complex.[20] CO molecules reversibly coordinate to Cu^+ ions, which enables extraction of CO from a mixed gas stream. The CO can later be desorbed allowing for recovery of CO with a purity greater than 98 mol%.[33] Despite no requirement for intensive pre-treatment, fundamental flaws still lie with this process. The presence of H_2O and H_2S, common impurities in industrial gas streams, result in harmful side reactions and the formation of HCl. Under the resulting acidic conditions, Cu^+ is vulnerable to oxidation/disproportionation which results in frequent and costly solvent renewals.

2.2.4 *CO purification techniques under development*

While COSORB and cryogenic distillation are industrially tested technologies used for CO purification, a number of studies have been reported in the literature that propose other competitive approaches for CO/N_2 separation. The materials involved in such processes include absorbents, membranes and adsorbents. To the best of our knowledge, none of these have been scaled to industrial size tests, but they claim to

address a number of the shortcomings of current commercial methods and are discussed below in the context of CO sorption/purification.

2.2.4.1 Ionic liquids

In addition to the COSORB absorption process, ionic liquids (ILs) have been identified as solvents capable of CO extraction.[35-37] A spectroscopic study by Repper *et al*. investigated CO absorption and separation using *in-situ* infrared spectroscopy, although this technique was unable to measure CO capacity.[38] The 1-hexyl-3-methylimidazolium (hmim) dibromocuprate IL proved to be best performing, recording 89% and 95% CO purity for 50:50 (*v:v*) CO:H_2 and CO:N_2 mixtures respectively, at 25 °C and 8 bar. The CO solubility of ILs has been investigated systematically, varying IL properties such as alkyl chain length, alkyl chain substituents and cation charge.[39-44] David *et al.* proposed an improvement to the COSORB process, using an imidazolium-based IL with a chloride ion to solubilise CuCl and improve the stability and availability of the Cu^+ ion.[44] This ionic liquid solubilised CO more readily than other ILs, however CO capacity still remains uncompetitive in comparison to current commercial CO purification processes. In addition, studies showed that imidazolium-based ILs are water sensitive and therefore not yet suitable for commercial use. Considering all the studies on ILs, only Repper *et al.* focussed specifically on mixed gas separation for CO or syngas purification.

2.2.4.2 Supported ionic liquid membranes

ILs have also been incorporated into nanofiltration membranes for use in gas separations. Most relevant studies on these nanofiltration membranes, or supported ionic liquid membrane (SILM) systems are reported in collaborative work by the Ortiz and Urtiaga groups which focus on separating the major components of syngas, *i.e.* CO and H_2, in both binary and multi-gas streams.[44-48] SILMs have been used to exploit

the large difference in diffusivity between H_2 and CO, resulting in greater H_2 permeability.[45,46] Although these studies primarily focus on H_2 recovery and H_2/CO separation, CO/N_2 separation has also been targeted.[44,47,48] Follow-up work from the same groups has improved CO solubility, capitalising on Cu-CO interactions with Cu-containing ILs.[44,47,48] One of the aforementioned studies focussed on simultaneously improving CO permeability and decreasing N_2 permeability.[44] While membrane performance has been the primary focus of Ortiz and Urtiaga's work, studies on CO transport properties and membrane stability have been performed by other groups.[49,50] In order for membranes to be considered suitable for industrial scale CO purification, the diffusion rate and stability must be improved from the level of performance reported to date.

2.3 Adsorption theory

Alongside absorption-based technologies, adsorption processes have been explored for CO purification and CO/N_2 separation. Adsorption refers to a process during which there is an enrichment of a chemical at an interface because of the fluid adhering through surface interactions.[51] As for any adsorbent, the sorption and separation mechanisms occurring depend on the physical and chemical properties of the porous sorbent materials. Adsorption can be classified depending on the strength of the surface interactions into physisorption and chemisorption. Described below and shown in Figure 2-2 are a number of mechanisms to consider:

- *Physisorption (physical adsorption)*: Physical interaction or affinity governed by the adsorbents surface characteristics, as well as the adsorbate's polarisability, dipole and quadrupole moment. These interactions enable reversible adsorbate-adsorbent interactions.

- *Chemisorption (chemical adsorption)*: Chemical interactions through highly energetic interactions which can yield higher selectivity and uptake than those reached *via* physisorption. An irreversible chemical bond is formed through strong intermolecular forces at the surface. Heat of adsorption values provide a measure of strength of binding between the adsorbate and adsorbent surface: physisorption (5-40 kJ mol^{-1}) or chemisorption (40-800 kJ mol^{-1}).

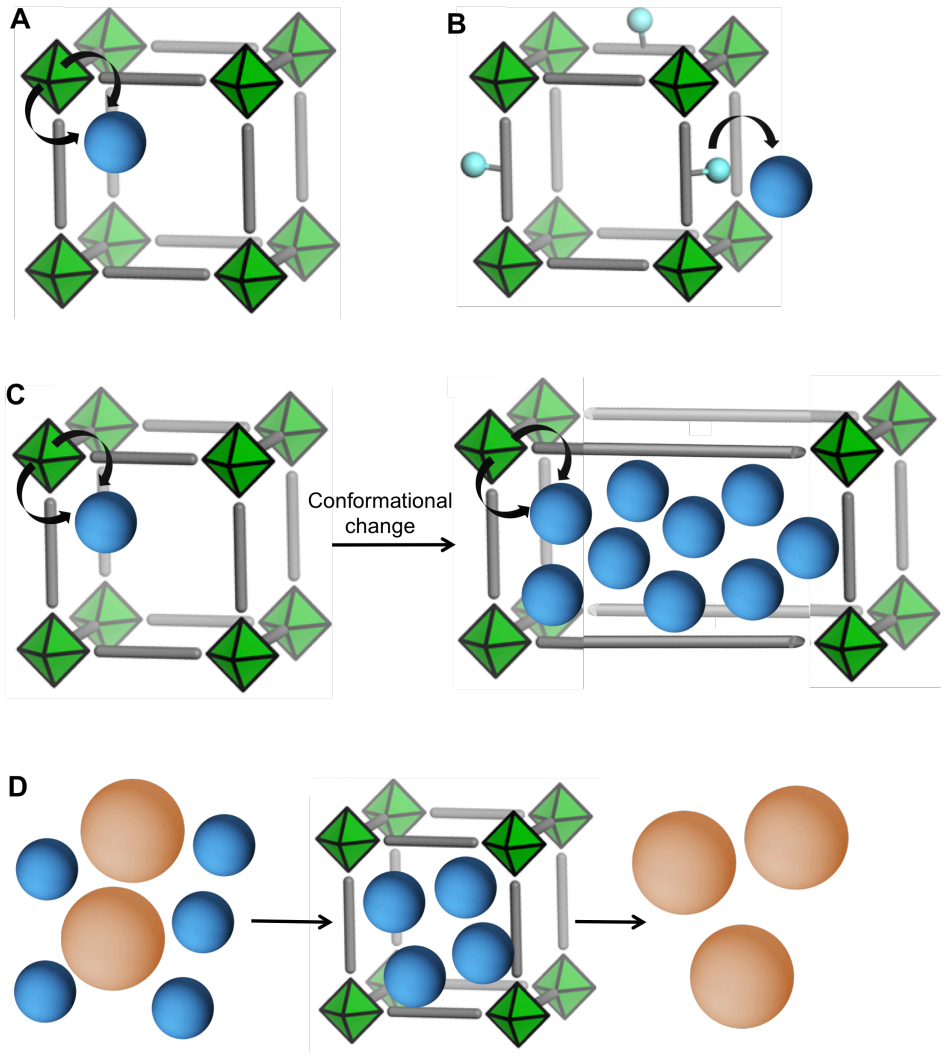


Figure 2-2. Overview of the different separation mechanisms utilised for CO sorption and purification in MOFs: (A) highly energetic CO-metal interactions (chemisorption or quasi-chemical sorption); (B) surface interactions through ligand functional groups; (C) CO-metal interactions promoting conformational change; (D) size exclusion based

separation. Green octahedrons denotes metal cluster. Grey cylinders denote organic ligands. Blue spheres denotes the targeted adsorbate.

- *Size exclusion based separation*: Size exclusion based separations (Figure 2-2D), also referred to as molecular sieving, require the kinetic diameters of the separated molecules to be similar to the pore sizes of the porous sorbent, therefore restricting the number of suitable adsorbents for a targeted separation. Here, the uptake and/or rate of adsorption of one or several of the components in the mixture becomes negligible since the internal surface area of the sorbent is inaccessible.

Once the adsorbent has been saturated, the adsorbate must be collected as a purified stream which is achieved by adsorbent regeneration.[52] Absorbent regeneration processes include: heating and purging the adsorbent bed to desorb the bound species (temperature-swing adsorption, TSA) and reducing the pressure of the bed and purging to remove the species (pressure-swing adsorption, PSA). Variations of these processes also exist at low pressure (vacuum-swing adsorption, VSA) or by using a combination of these methods (pressure-temperature-swing adsorption, PTSA and vacuum-temperature-swing adsorption, VTSA).

2.4 Adsorbent materials

A summary of literature reported CO adsorption studies is provided in Table 2-2, which shows key performance indicators including uptake, selectivity and heats of adsorption. These studies are further discussed below and are grouped based on the types of adsorbent investigated.

2.4.1 *Activated carbons*

Studies using commercially available activated carbons have targeted syngas separation, however the primary focus of most of these studies are H_2 recovery rather

than CO purification.[53-55] Commercialised activated carbons have been tested at an advanced stage for H_2 purification from syngas, using PSA units.[53,54] These same studies report both equilibrium adsorption measurements (CO, CO_2, H_2, CH_4 and N_2), and kinetic studies which are intended to replicate industrial conditions.[53-55] In addition to the commercial activated carbons, chemically modified equivalents have also been investigated. These modified activated carbons show greater promise than the aforementioned commercially available activated carbons for CO purification due to the impregnation of metals.[56-66] Of the various metals, Cu impregnation is the most prominent,[56-64] increasing the materials CO affinity and enhancing the potential for selective CO separation, as exemplified in a study with $CO/CO_2/N_2$ mixtures.[67]

2.4.2 *Activated alumina*

In order to be fully comprehensive in our review, the work on activated alumina is cited, as the adsorbent is used in a commercialised PSA system for CO.[68] The activated alumina was impregnated with Cu, in a similar manner to the techniques applied to activated carbon. No CO uptake or measures of selectivity were reported. Further CO adsorption studies of mesoporous alumina have also focussed on CO removal from incomplete combustion.[69]

2.4.3 *Zeolites*

In addition to activated carbons, zeolites have been proposed as materials suitable for CO purification. Metal cation-exchange involving alkali metals or alkaline earth metals has been shown to improve CO uptake and selectivity, a feature which is not possible with activated carbons unless metal impregnation is performed.[70-74] In the case of alkali metals, the equilibrium adsorption capacity decreases moving down the group toward heavier ions.

Table 2-2. Summary table of adsorbents reported so far for CO adsorption and CO/X separation (X = CH_4, N_2, CO_2 and H_2) at varying temperature and 1 bar.

Sorbent	*T* /°C	n_{CO} /mmol g^{-1}	CO ΔH_{ad} /-kJ mol^{-1}	n_{CH4} /mmol g^{-1}	CH_4 ΔH_{ad} /- kJ mol^{-1}	$S_{CO/CH4}$	N_{N2} /mmol g^{-1}	N_2 ΔH_{ad} /- kJ mol^{-1}	$S_{CO/N2}$	n_{CO2} /mmol g^{-1}	CO_2 ΔH_{ad} /- kJ mol^{-1}	$S_{CO/CO2}$	n_{H2} /mmol g^{-1}	H_2 ΔH_{ad} /- kJ mol^{-1}	$S_{CO/H2}$	S_{BET}†† /m^2 g^{-1}	Ref.
Activated carbons (ACs)																	
AC †	30	0.72	19.1	0.80	17.7	0.9*	0.30	11.8	2.4*	2.05	27.9	0.35*	0.03	3.2	24*		53
AC	30	0.45	22.6	0.95	22.7	0.47*	0.32	16.3	1.4*	1.98	29.1	0.2*	0.03	12.8	15*	481	54
AC	25	0.38	16.3	0.78	18.4	0.49*				1.80	20.9	0.21*	0.02	7.6	19*	859	55
AC supported CuCl	30	2.95		0.02		18	0.01		45	0.50		6				478	57
AC	30	0.25														1784	57
AC supported CuCl	25	2.30					0.04		80							472	62
AC	25	0.45					0.28		1.6*							1401	62
AC supported CuCl	25	2.30	25.0	0.33		5	0.01		20			2				652	63
AC	25	0.21														1170	63
AC supported CuCl	20	1.24														744	60
AC	20	0.33														1044	60
Zeolites																	
CuCl modified Zeolite 13X†††	30	3.41								2.05		1.66*					75
CuCl modified Zeolite Y†††	30	3.28		0.16		21*	0.12		27*	1.76		1.86*	0.04		82*		75
Zeolite Y Supported CuCl	30	2.70	28.5	0.08		25	0.02		65	0.98		2.8				329	64
Zeolite Y†††	30	0.66								5.05		0.13*					75
Na Zeolite X	30	1.11	26.1	0.76	21.5	1.51	0.42	21.5	2.79							721	73,74
Ca Zeolite X	30	1.91	33	1.45	25	1.32	1.07	27	1.80							704	74
Sr Zeolite X	30	1.90	31	1.12	22	1.63	0.80	25	2.37							622	74
Ba Zeolite X	30	1.26	30	0.94	22	1.34	0.53	23	2.39							565	74
Mg Zeolite X	30	0.80	17	0.63	21	1.27	0.40	19	2.00							711	74
Li Zeolite X	30	1.42	31.2	0.83	23.6	1.71	0.59	24.7	2.41							759	73
K Zeolite X	30	0.61	21.3	0.87	20.8	0.69	0.27	17.3	2.23							537	73
Rb Zeolite X	30	0.43	20.1	0.70	20.8	0.63	0.23	16.0	1.95							550	73
Cs Zeolite X	30	0.37	19.2	0.70	20.7	0.53	0.18	15.6	2.08							423	73
Zeolite 5A	25	1.15	25														76
Zeolite 13 X†††	30	0.53								4.43		0.12*					75
Zeolite 13X	25	0.48	36														76

n Amount adsorbed. CO ΔH_{ad} Enthalpy of Adsorption (units in –kJ mol^{-1}) at n_{CO} loading reported. CH_4, N_2, CO_2 and H_2 ΔH_{ad} Enthalpy of adsorption (units in –kJ mol^{-1}) reported at low loading
S Selectivity calculated using the Ideal Adsorbed Solution Theory by the author.* denotes Ideal Gas Selectivity calculated in this report from the equilibrium adsorption measurement values from the cited literature
† AC denotes Activated Carbon
†† BET denotes Brunauer–Emmett–Teller theory
††† Values recorded at 0.7 bar

This trend was attributed to the cation radius increasing down the group, thereby weakening the electrostatic interactions between polar CO and the metal ions.[73] It was found that exchanging zeolites with alkaline earth metals leads to greater uptakes than alkali metals.[74] These systematic studies highlighted the major impact the metal cation has upon CO adsorption in zeolites.

Zeolite Y, a topologically related analogue of Zeolite X, has also been tested and subjected to metal cation exchange.[64,77-79] A range of element types such as lanthanides, alkaline earth metals and transition metals have been studied for CO adsorption enhancement. While some investigations only used CO as a probe molecule to understand the zeolitic structure,[78] others have focussed on Cu incorporation specifically for CO adsorption.[64,75,80] Zeolites such as ZSM-5,[81] 4A, 5A,[82] and 10X [83] have also shown promise as candidates for CO adsorption or separation.

Overall, the data presented in literature show that zeolites perform better than activated carbons with regard to CO purification (Table 2-2). There is limited information exists on the kinetics of CO adsorption for these classes of sorbents, despite its relevance at an industrial scale. Yet, the performance of zeolites and activated carbons falls short of many metal-organic frameworks (MOFs) reported to date, as highlighted in several comparative studies.[76,84,85] The higher performance in terms of uptake and selectivity of MOFs is to a large extent related to their high density of CO binding sites, *i.e.* metal sites, compared to activated carbons or even zeolites. Chemical modification is restricted within zeolites to the types of metal cation exchange available, while such limitation does not exist with MOFs. The versatile nature of MOFs allows maximisation of CO uptake by manipulating the CO-metal interactions through appropriately choosing metal nodes having the strongest binding.

Table 2-3 summarises the advantages and disadvantages of implementing MOFs as an alternative to activated carbons or zeolites in adsorption separation systems.

Table 2-3. Benefits and limitations of various existing and proposed CO purification technologies.

Existing and proposed CO purification technologies		
Technology (Separation mechanism)	Benefits	Limitations
Distillation (Gas boiling temperatures)	Already commercialised on a large scale. High CO purity and recovery achieved.	High capital and operating costs at cryogenic temperatures. Problematic separating gases of similar boiling points.
Absorption/ COSORB™ process (Chemical and physical absorption)	High levels of CO extraction resulting in high purity. Most economic option for separating gases of similar boiling points and kinetic diameter (*i.e* CO/N_2)	Expensive and frequent solvent renewals required. Harmful side reactions in the presence of H_2O and H_2S.
Supported ionic liquid membranes (SILMs) (Solubility and chemical absorption)	High CO selectivity. Chemical tunability of ILs enables them to be potentially used for separating different types of CO-containing gas streams.	Low CO capacity and poor stability. Expensive cost of ionic liquids restricting commercialisation or large scale testing.
Adsorption - PSA, TSA, VSA* (Chemical and physical surface interactions)	Cost and energy-effective separation mechanism. High CO capacity and selectivity achievable with correct sorbent selection.	Slow cyclic heating-cooling steps during TSA and low working capacity unless an expensive and complicated VSA process is used. Dehydration or freezing required to remove undesired H_2O impurities that reduces capacity.
Proposed materials for CO adsorption		
Adsorbent	Benefits	Limitations
Activated Carbon	Low cost of adsorbent and widespread usage for a number of separations.	Typically low CO capacity due to the absence of reactive sites in unmodified activated carbons.
Zeolite	Adsorbent already tested at scale for a number of separations. Presence of metal sites allows enhanced CO uptake and selectivity. Metal–cation exchange improves performance. Robust at high temperatures.	Expensive (compared to activated carbons). Lower metal density, relative to MOFs, results in lower CO selectivity and uptake.
Metal-organic frameworks	Highly porous materials with high metal density available to achieve good CO selectivity and storage. Good tunability and versatility to adjust accordingly to types of CO separations.	Possible degradation of the structure at low temperature. Very expensive (compared to activated carbons and zeolites). Susceptible to degradation and irreversible binding to H_2O and H_2S.

*PSA – pressure-swing adsorption, TSA – temperature-swing adsorption, VSA – vacuum-swing adsorption

Table 2-3 also presents the pros and cons of adsorption based separation compared to other CO purification technologies.

An increasing number of studies have been reported on the use of MOFs for CO separation, with certain work focussing on CO/N_2 separation. The findings from these works are summarised and discussed in the following section.

2.5 Metal-organic frameworks

Metal-organic frameworks (MOFs), a class of coordination polymers composed of organic ligands coordinated to inorganic metal ions or clusters, have shown great promise in the area of gas storage and separations.[9,12,86-91] During synthesis, organic linkers, commonly carboxylate-based or imidazolate-based ligands, self-assemble with metal ions (or polynuclear metal clusters) to form organic-inorganic hybrid materials. There is a remarkable amount of diversity, tunability, and modularity in this class of materials as a result of the variety of inorganic building blocks and organic linkers available for MOF synthesis. In comparison to traditional solid state materials, MOFs modularity allows for a relative ease in modification of properties of the resultant material.[92-94] On-going research in this area continues to grow and reports of new compounds and applications are frequent. From the large range of applications of MOFs, the use of this class of materials for gas separation and purification continues to be a promising area of MOF research.[9,14,87,91,95]

2.5.1 *Overview of CO purification mechanisms in MOFs*

An overview of the MOFs reported for CO adsorption and CO/N_2 separation to date is provided in Table 2-4. In the case of CO gas separation, the most promising MOFs reported have energetics ranging from -16 kJ mol^{-1} to greater than -50 kJ mol^{-1} (see Section 2.5.2 and Table 2-4), which border between physisorption and chemisorption.

These interactions are referred to as quasi-chemical sorption which stems from coordinatively unsaturated metal sites; these interactions are beneficial for gas purification yielding higher purity streams. Gas separation through size exclusion has been reported for certain MOFs, although not as widely reported as MOFs containing quasi-chemisorbing unsaturated metal sites or separations using physisorption mechanisms.[9,96] As highlighted in Table 2-2 and Table 2-4, most MOFs identified in this review have greater surface area and porosity than activated carbons and zeolites, which provides greater potential for CO gas storage. The next sub-sections review studies where physisorption, chemisorption and/or size based separations are the dominant factors controlling the selective separation or adsorption of CO.

2.5.2 *CO adsorption through CO-metal binding*

MOFs containing unsaturated metal sites have a large influence on CO uptake and selectivity. These highly specific and energetic unsaturated metal sites enhance the surface area and electric field gradient, which originally only result in physisorbing surface interactions.[9] For a number of MOFs, CO adsorption at low to moderate pressure is dominated by chemisorption forces *via* binding between CO molecules and the unsaturated metal sites of the MOF. At higher pressures, the preferred highly energetic unsaturated metal sites become occupied with CO molecules and physisorption starts to dominate the adsorption process.

Table 2-4. Summary table of MOFs reported to date for CO adsorption and CO/*X* separation (*X*: CH_4, N_2, CO_2, H_2) at varying temperature and 1 bar.

Sorbent	*T* /°C	n_{CO} /mmol g^{-1}	CO ΔH_{ad} /- kJ mol^{-1}	n_{CH4} /mmol g^{-1}	CH_4 ΔH_{ad} /- kJ mol^{-1}	$S_{CO/CH4}$	n_{N2} /mmol g^{-1}	N_2 ΔH_{ad} /- kJ mol^{-1}	$S_{CO/N2}$	n_{CO2} /mmol g^{-1}	CO_2 ΔH_{ad} /- kJ mol^{-1}	$S_{CO/CO2}$	n_{H2} /mmol g^{-1}	H_2 ΔH_{ad} /- kJ mol^{-1}	$S_{CO/H2}$	S_{BET}† /m^2 g^{-1}	Ref.
CO-metal binding																	
Fe-MOF-74	25	6.02	40.2				0.6		68				0.01		507	1535††	97
Co-MOF-74	25	5.90	40.8						163				0.02		1040	1433††	97
Ni-MOF-74	25	5.74	36.0				0.85		216				0.02		1705	1574††	97
Mg-MOF-74	25	4.53	35.4				0.9		10				0.02		170	1957††	97
Mn-MOF-74	25	3.20	29.7				0.45		10				0.01		86	1797††	97
Rh-DUT-82	25	2.11	50.0													780	98
Zn-MOF-74	25	1.91	27.2				0.25		8				0.03		47	1105	97
HKUST-1	25	1.45	16.0	0.5	16	2.9*				5.2	26	0.28*				1663	99
Cr-MIL-101	25	1.30		0.30		2.5	0.15		5							1843	100
HKUST-1	25	1.20	17.3				0.08	13.1	15*	4.5	25.8	0.27*					101
Cr-MIL-101	25	1.05					0.22		35	0.75		4				2850	102
Cr-MIL-101	25	1.03					0.21		4.9*							3788	103
Cr-MIL-101	30	1.00		0.51	30.1	1.96	0.23	19.7	4.35	2.90	38.8	0.34				2471	84
Cr-MIL-101	22	0.90	16.5	0.30	21	3*				1.70	32	0.53*				2674	99
HKUST-1	22	0.77		0.96		0.8*	0.35		2.2*	5.02	28					965	104
Fe-MIL-100	25	0.50	38	0.25		8	0.22		10							1067	105
Fe-MIL-100	25	0.38	39.0				0.25		2							2042	85
Zr-UiO66-$(COOH)_2$	30	0.21	15.5	0.29	25	0.7*	0.10	19.5	2.1*	1.05	40	0.2*	0.02		10*	568††	106
Al-MIL-53l	30	0.18	16.4	0.53	18.3	0.5	0.14	15.9	1.3	2.05	26.4	0.13				1235	107
La(BTN)(DMF)	0	0.12					0.11		1.1	1.32		0.1					108
CO-metal binding and conformational change																	
Cu(aip)(H_2O)	-153	7.18	19.0				3.20		2.24*								109
CO-metal binding and spin state transition																	
Fe_2Cl_2(BBTA)	25	5.75	38				0.05			2.85			0.02			1055	110
Fe_2Cl_2(BTDD)	25	3.40	34.5													1897	110
Fe-BTTri	25	2.90†††	65.0	0.27†††		102	0.05 †††		250	1.85 †††		28	0.02 †††		1500	1630	111
Chemical modification of the MOF																	
Cu⁺ impregnated Fe-MIL-100	25	3.75		0.15		180	0.10		250							2023	105
Fe-MIL-100	25	0.50		0.25		8	0.22		10							1067	105
Cu⁺ impregnated Fe-MIL-100	30	3.30		0.20		100	0.01		900	0.30		11*				898	112
Fe-MIL-100	30	1.05								3.60						2458	112
Cu⁺ impregnated Fe-MIL-100	25	3.10								0.20		420				790	113
Fe-MIL-100	25	0.20								2.03						2200	113
Cu⁺ impregnated Cr-MIL-101	25	2.82					0.07		315	2.05		34				1030	102
Cr-MIL-101	25	1.05					0.22		35	0.75		4				2850	102
Cu⁺ impregnated Cr-MIL-101	25	2.42		0.25		25	0.1		1000							3615	100
Cr-MIL-101	25	1.30		0.30		2.5	0.15		5							1843	100

Cu⁺ impregnated Cr-MIL-101	25	2.26					0.05		32							2391	[103]
Cr-MIL-101	25	1.03					0.21		5							3788	[103]
Cu⁺ impregnated Fe-MIL-100	25	2.78					0.15		180							762	[85]
Fe-MIL-100	25	0.38	39.0				0.25		2							2042	[85]
Cu⁺/V impregnated Cr-MIL-101	25	1.29	52.5				0.20		170				0.07		641	1697	[114]
Cr-MIL-101	25	0.54	45.0				0.22		6				0.08		16	3189	[114]
NH_2-functionalised Ti-MIL-125	30	0.22	13.4	0.55	14.6	0.4*	0.13	11.7	1.7*	2.05	21.9	0.10*	0.14	23.3	1.6*		[115]
NO_2-$(OC_3H_5)_2$-$(OC_7H_7)_2$-functionalised MOF-5	25	0.21								1.60							[116]
MOF-5	25	0.17								0.76							[116]
Size exclusion based separation																	
MAMS-1	-160	0.60		0.55		1.1*							2.35		0.26*		[117]
Zn(ADC)(4,4'-Bpe)0.5·xG	-196	0.49					0.74		0.66*				2.83		0.17*	100	[118]
PCN-13	-196	0.41					0.49		0.84*				1.85		0.22*	150	[119]
ZIF-69	0	0.25								3.05		0.08					[120]
MOF-5	25	0.17								0.76							[116]
ZIF-95	25	0.12		0.21		0.57*	0.08		1.5*	0.80		0.09					
ZIF-100	25	0.12		0.22		0.55*	0.06		2*	0.88		0.06					
MOF-5	25	0.10	16.1													2449	[76]
MOF-177	25	0.05	19.8													3275	[76]
CO purification performance for structured and non-structured MOFs																	
Cr-MIL-101 (powder)	30	1.00	41.9	0.51	30.1	1.96	0.20	19.7	4.35	2.9	38.8	0.34				2471	[84]
Cr-MIL-101(granules)	30	0.52	41.2	0.28	21.2	1.81	0.18	15.8	4.14	1.62	39.1	0.34				1642	[84]
UTSA-16 extrudates	25	0.23		0.24		1.0*	0.15		1.5*	3.3		0.07*	0.02		11.5*	805	[121]

n Amount adsorbed. CO ΔH_{ad} Enthalpy of Adsorption (units in –kJ mol^{-1}) at n_{CO} loading reported. CH_4, N_2, CO_2 and H_2 ΔH_{ad} Enthalpy of adsorption (units in –kJ mol^{-1}) reported at low loading

S Selectivity calculated using the Ideal Adsorbed Solution Theory by the author

* denotes Ideal Gas Selectivity calculated in this report from the equilibrium adsorption measurement values from the cited literature

† BET denotes Brunauer–Emmett–Teller theory

†† Denotes Langmuir surface area

††† Values recorded at 0.3 bar

While higher pressure increases total CO uptake, there is a detrimental impact on CO selectivity as dispersion forces dominate and reduce the overall impact of previously dominant electrostatic interactions. As a consequence, high isosteric heats of adsorption are measured at low coverage and decrease progressively during adsorption as intermolecular CO-CO interactions become predominant. This category of MOFs for which CO adsorption predominantly occurs *via* binding to unsaturated metal sites includes: M-MOF-74, M-BTTri, M_2Cl_2(BBTA), M_2Cl_2(BTDD), HKUST-1, Cr-MIL-101, Fe-MIL-100 and Rh-DUT-82. More details are provided below for each of these MOFs, starting from the most studied ones.

M-MOF-74, also often referred to as CPO-27 or M_2(DOBDC), is a structure composed of the organic linker 2,5-dioxido-1,4-benzenedicarboxylate (DOBDC), which coordinates to divalent metal cations (Mg^{2+}, Ni^{2+}, Zn^{2+}, Fe^{2+}, Co^{2+}, Cu^{2+}) to form a MOF containing one-dimensional hexagonal pores.[122] Activated M-MOF-74 possesses unsaturated metal sites, which can preferentially bind to CO through synergistic π- and σ-bonding. The first study using Zn-MOF-74 for CO capture[123] reported a negligible dynamic adsorption capacity which was not quantified.

A more comprehensive study with a series of six M-MOF-74 analogues (M = Mg, Mn, Fe, Co, Ni, and Zn) was published later and combined both experimental results with density functional theory calculations to investigate the differences in capacity and binding modes of CO with the various metal centres.[97] The trend in terms of CO uptake followed the order: Zn < Mn < Mg < Ni < Co < Fe, which explained the minimal dynamic uptake previously reported with the original study of the Zn analogue.[123] A good agreement was found between the experimental and a computational study reporting crystallographic data of CO interacting with the metal centres.[124]

Ni-MOF-74 was discovered to have strongest interactions with CO based on the short M-C bond distance compared to the other analogues.[97,125,126] The trend followed that of the Irving Williams series, as shown Figure 2-3A. The shorter bond distance observed in Ni-MOF-74 was linked to the larger charge transfer and π-back-donation effect from Ni^{2+}. Back-donation is absent in both Mg- and Zn-MOF-74, as Mg^{2+} ions possess no *d* electrons for back-donation, and Zn^{2+} ions are unavailable to receive σ-donation as its 3d orbitals are full.

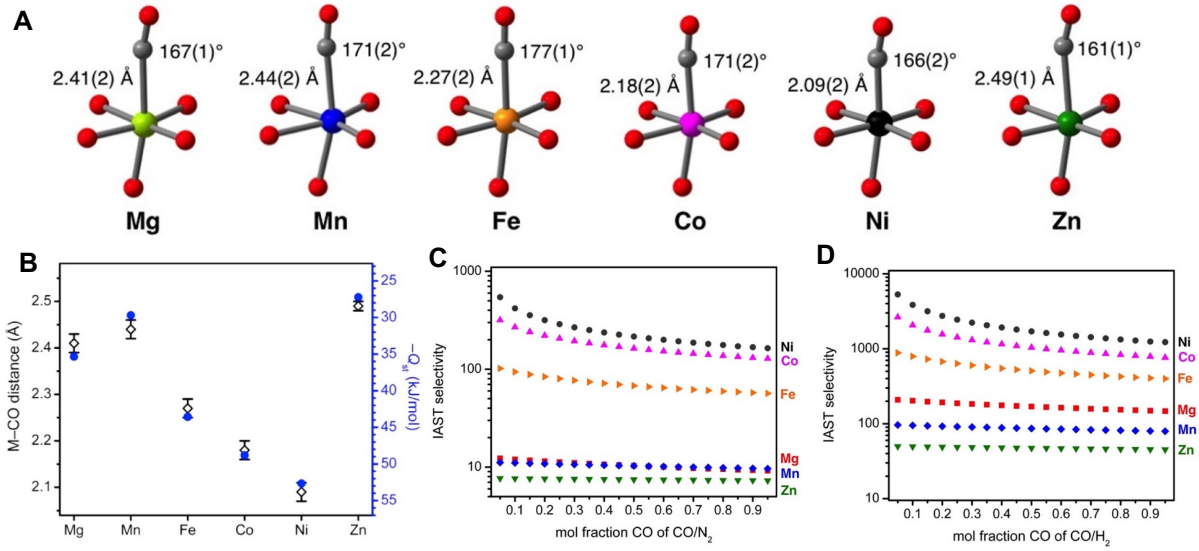


Figure 2-3. CO adsorption on M-MOF-74 dominated by CO-metal binding. (A) First coordination sphere of M-MOF-74 analogues for M^{2+} ions with M-CO distances (Å) and M-C-O angles (°) labelled; (B) Relationship between M-CO distance (open black diamonds) and isosteric heat of CO adsorption (Qst, blue circles) of M-MOF-74 metal centre. Ideal Adsorbed Solution Theory (IAST) selectivities of M-MOF-74 for: (C) CO/N_2 and (D) CO/H_2 mixtures at varying compositions at 25 °C and 1 bar.[97] Reprinted (adapted) with permission from ACS Publications. Copyright 2014 American Chemical Society.

Unlike the M-C bond distance, the C-O bond distance of the CO molecule was found unchanged for all M-MOF-74 analogues.[124] It was proposed that the structure deformation resulting from CO binding counteracts the C-O shortening from π-back-

donation expected from Ni-CO binding, as electron donation in the π* orbital weakens the C-O bond.[127] CO uptakes up to 6.04 mmol g^{-1} (at 25 °C and 1.2 bar) were measured for Ni-MOF-74,[97] representing the highest CO uptakes measured so far on MOFs, activated carbon and zeolites at near atmospheric pressure.

The isosteric heat of CO adsorption ranges from -52.7 kJ mol^{-1} for Ni-MOF-74 down to -27.2 kJ mol^{-1} for Zn-MOF-74. Ideal Adsorbed Solution Theory (IAST)[128,129] CO/N_2 selectivities of ~40 were calculated for Zn-MOF-74 and ~2000-5000 for Ni-MOF-74 (Figure 2-3C).[97] In the same study, CO/H_2 selectivities of ~8 and 155-500 were calculated for Zn-MOF-74 and Ni-MOF-74, respectively (Figure 2-3D). An experimental and computational study of M-MOF-74 exhibited different levels of CO/CO_2 selectivity between Mg-MOF-74 and the Ni- and Co-MOF-74 analogues.[130] CO_2 affinity to the unsaturated metal sites follows the order $Mg^{2+} > Ni^{2+} > Co^{2+}$, whereas the CO affinity for unsaturated metal sites follows the order of $Ni^{2+} > Co^{2+} \gg Mg^{2+}$. The Mg^{2+} sites that only form M-CO bonds does not have π backdonation because of the lack of valence electrons. These studies show that metal-CO binding strength is governed by the M^{2+} ion's ability to form π backdonation.

In addition to the M-MOF-74 series, experimental and modelling studies of CO adsorption on HKUST-1 ($Cu_3(BTC)_2$ where BTC = 1,3,5-benzenetricarboxylate) that possess Cu^{2+}-Cu^{2+} paddlewheel (referred to as "Cu-Cu paddlewheel" throughout) units have been carried out.[99,101,104,131] Activated HKUST-1 exhibits unsaturated Cu^{2+} metal centres which can be reduced to Cu^{+} *via* thermal treatment, supported by spectroscopic studies on the interactions from Cu^{+} binding to CO.[101,104,131-133] CO adsorption capacity between 0.77 and 1.45 mmol g^{-1} have been reported for HKUST-1 at 25 °C and 1 bar.[99,104] Experimental and computational studies have investigated

separations with various gas mixtures including CO/H_2 CO/N_2 and CO/CH_4 (Table 2-4).[99,101,131,94]

Like HKUST-1, Rh-DUT-82 (or $Rh_3(BTC)_2$ where BTC = 1,3,5-benzenetricarboxylate) is based on paddlewheel units and the unsaturated metal sites can bind CO molecules.[98] The CO uptake of this MOF has been investigated *via* both equilibrium measurement and breakthrough analysis. At 25 °C and 1 bar, Rh-DUT-82 recorded 2.11 mmol g^{-1} CO uptake, which is higher than capacities recorded for HKUST-1.

M-MIL-100 ($M_3(O)X(BTC)_2(H_2O)_2 \cdot nH_2O$ where M = Fe, Al, Cr, V; BTC = benzene-1,3,5-tricarboxylate and X = OH, F) and M-MIL-101 ($M_3(O)X(BDC)_3(H_2O)_2$ where M = Cr, Fe; BDC = benzene-1,4-dicarboxylate and X = OH, F) have also been tested for CO adsorption.[84,99,103,134] It was found that Cr-MIL-101 recorded low CO uptake at 1 bar because of weak Cr-CO interactions, and only significant CO adsorption was recorded at high pressure.[99] A topologically related MOF, Fe-MIL-100, also recorded low CO uptake (0.38 mmol g^{-1} at 25 °C and 1 bar) because of weak Fe-CO interactions.[85] The study focussed upon CO/N_2 separation and a low IAST selectivity of approximately 2 was calculated.

The CO equilibrium adsorption capacity (0.21 mmol g^{-1} uptake at 30 °C, 1 bar) of Zr-UiO-66-$(COOH)_2$ was presented in a study focussing on MOF formulation.[106] However, UiO-66-$(COOH)_2$ exhibited greater affinity to CO_2. Another example of a MOF involving CO-metal binding is La(BTN)(DMF), where BTN = 1,3,5-tri(6-hydroxycarbonylnaphthalen-2-yl)benzene.[108] The mechanism of CO adsorption on this MOF utilises the aromatic naphthalene rings to enhance adsorption strength.

Al-MIL-53 (Al(OH)(BDC) where BDC = benzene-1,4-dicarboxylate) was subject to sorption studies with a range of gases, including CO, CO_2, CH_4, N_2, O_2, and Ar for

selective CO_2 adsorption.[107] Al-MIL-53 has 1-D diamond shaped pores that exhibit a "breathing" effect and change conformation depending on the guest molecule or gas adsorbed.[135] Al-MIL-53 recorded low CO uptake, 0.18 mmol g^{-1} at 30 °C and 1 bar.

2.5.3 *CO adsorption through CO-metal binding and conformational change*

In this section, the CO-MOF interactions of MOFs, specifically CO-metal binding, leads to a structural deformation that further enhances CO adsorption. An example of such MOF is Cu(AIP)(H_2O), a Cu-Cu paddlewheel containing MOF composed of Cu^{2+} and 5-azidoisophthalate (AIP).[109] The Cu-Cu paddlewheels are arranged to form two-dimensional (2D) patterned layers (Figure 2-4A and B). Activation of the structure removes bound water molecules from the axial sites of the Cu-Cu paddlewheel unit which reversibly transforms the structure. This transformation narrows the pore channels and reduces the accessible pore volume from 38% to 25% of the unit cell (Figure 2-4C and D).

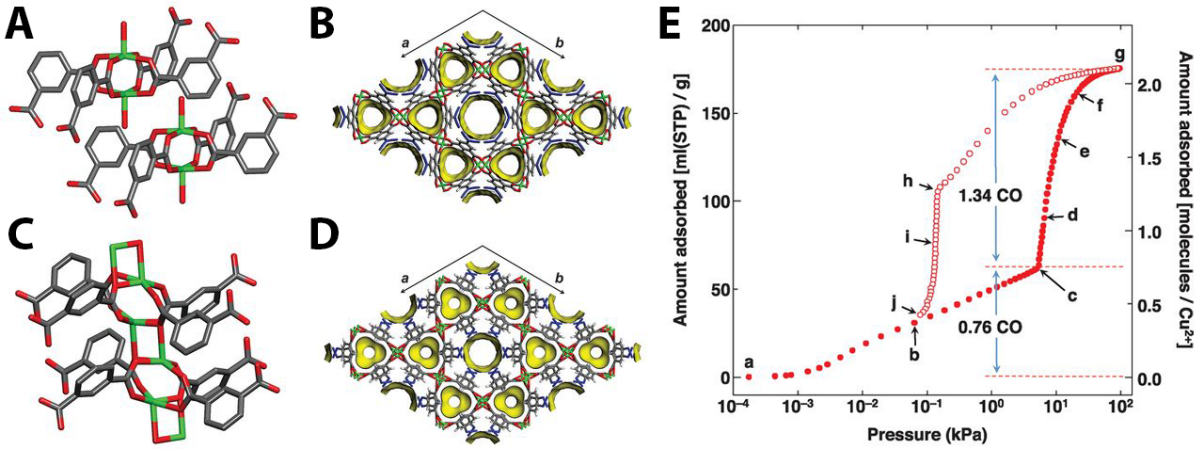


Figure 2-4. CO separation through CO-metal binding and conformational change using Cu(AIP)(H_2O): Coordination environment of: (A) solvated Cu-Cu paddlewheel units and (C) desolvated Cu-Cu paddlewheel unit. Porous structures illustrated with Connolly surfaces: (B) as-synthesized Cu(AIP)(H_2O) and (D) dried Cu(AIP)(H_2O). Atom colors: Cu, green; C, grey; N, blue; O, red. Hydrogen atoms and azide groups

emitted for clarity. (E) Cu(AIP)(H_2O) CO sorption isotherm (adsorption- solid circles, desorption- open circles) at -153 °C.[109]

It was found that physisorption of CO first occurs in the larger channels, followed by Cu^{2+}-CO bond formation on the paddlewheel units. The channel opens and initiates a reversible structural change allowing CO molecules to occupy the now accessible smaller channels. This "self-accelerating gas adsorption" is not observed for N_2 due to the weaker interactions between N_2 and the Cu centres which do not trigger the conformational change, thus resulting in a selective CO/N_2 separation at pressures above 0.1 bar. Cu(AIP)(H_2O) has Cu-Cu paddlewheel sites, similar to HKUST-1, which exhibited similar CO binding strength:-19 kJ mol^{-1} *vs* -17.3 kJ mol^{-1} respectively.[101,109] It is not until after its structural rearrangement, which induces self-accelerating adsorption as seen in Figure 2-4E, that significant CO uptake takes place: 2.58 mmol g^{-1} is adsorbed at 0.05 bar while 7.18 mmol g^{-1} is adsorbed at 0.8 bar, both at -153 °C. Note that the significantly higher CO uptake in this study is at cryogenic temperature, this cannot easily be compared to other MOFs CO adsorption measurements recorded at or near ambient temperature which are shown in Table 2-4.

2.5.4 *CO adsorption through CO-metal binding enhanced by spin state transition*

Another interesting structure for CO adsorption, Fe-BTTri (H_3BTTri = 1,3,5-tris(1H-1,2,3-triazol-5-yl)benzene), was reported by Reed *et al*. [111] CO-metal binding on this MOF involves a spin state transition mechanism through CO interactions with coordinatively unsaturated Fe^{2+} within the framework. Upon coordination of CO, a strong-field ligand, Fe^{2+}, switches from a square pyramidal high-spin state to an octahedral low-spin state. This MOF has shown to be particularly effective in scavenging trace amounts of CO. Infrared spectroscopy studies indicated π-back-

donation from the metal to the π* orbital of the CO. The CO sorption isotherms exhibits a steep initial rise at low pressure (> 0.01 bar) due to strong interactions with the Fe sites; isosteric heats of adsorption are estimated to be on the order of -65 kJ mol^{-1}, substantially higher than other reported MOF materials (Table 2-4). CO adsorption for Fe-BTTri has only been studied at low pressure, up to 1 bar.[111] CO uptake of 1.49 mmol g^{-1} at 0.1 bar and 2.7 mmol g^{-1} at 0.27 bar have been measured at 25 °C. This is due to the strong interactions between the low-spin state Fe^{2+} and CO. The strong interactions resulted in high IAST selectivities for CO/H_2, CO/N_2, and CO/CH_4 (10900, 1750, and 650, respectively) at 25 °C and 1 bar (Figure 2-5A and B), based on the H_2, N_2 and CH_4 isotherms collected. CO/CO_2 selectivity (~200) was not as high due the high affinity of Fe-BTTri to CO_2 (compared to H_2, CH_4 and N_2).

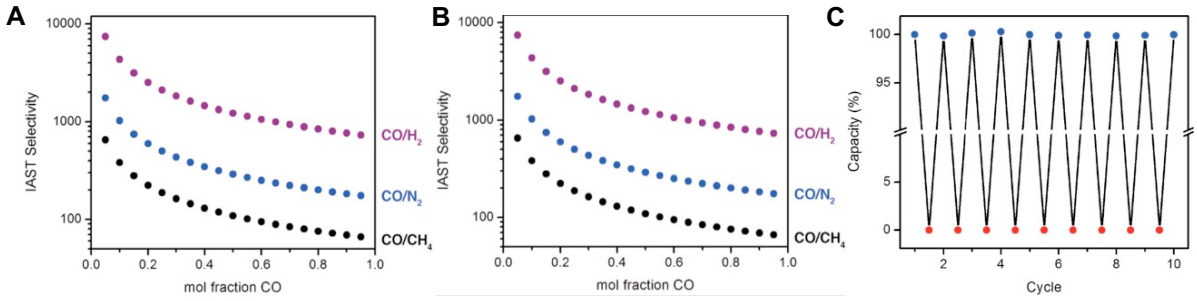


Figure 2-5. CO separation through CO-metal binding and conformational change using Fe-BTTri. Ideal Adsorbed Solution Theory (IAST) selectivities of Fe-BTTri for: (A) CO/H_2 (purple), CO/N_2 (blue), CO/CH_4 (black); (B) CO/CO_2 (green at 25 °C, light green at 45 °C) mixtures at 25 °C and 1 bar, unless stated otherwise. (C) Cyclic CO adsorption (blue circles) and desorption (red circles profiles of Fe-BTTri with Cycle 1 capacity used as reference percentage capacity. Adsorption recorded at 25 °C and 0.01 bar and desorption was performed at 150 °C under dynamic vacuum.[111] Reprinted (adapted) with permission from ACS publications. Copyright 2016 American Chemical Society.

The authors proposed that Fe-BTTri would be suited for purifying gases with low concentrations of CO, specifically targeting CO/H_2 separation due to the low H_2

uptake. IAST selectivity calculations of CO:H_2 streams at low concentrations of CO gave exceptionally high selectivity values (24,800 for 1% CO).[111]

Another study on Fe-based MOFs, Fe_2Cl_2(BBTA) and Fe_2Cl_2(BTDD) (H_2BBTA = 1H,5H-benzo(1,2-d:4,5-d′)bistriazole) and H_2BTDD=bis(1H-1,2,3-triazolo[4,5-b],[4′,5′-i])dibenzo[1,4]dioxin), also explored electronic and structural transitions through Fe-CO binding (Figure 2-6A).[110]

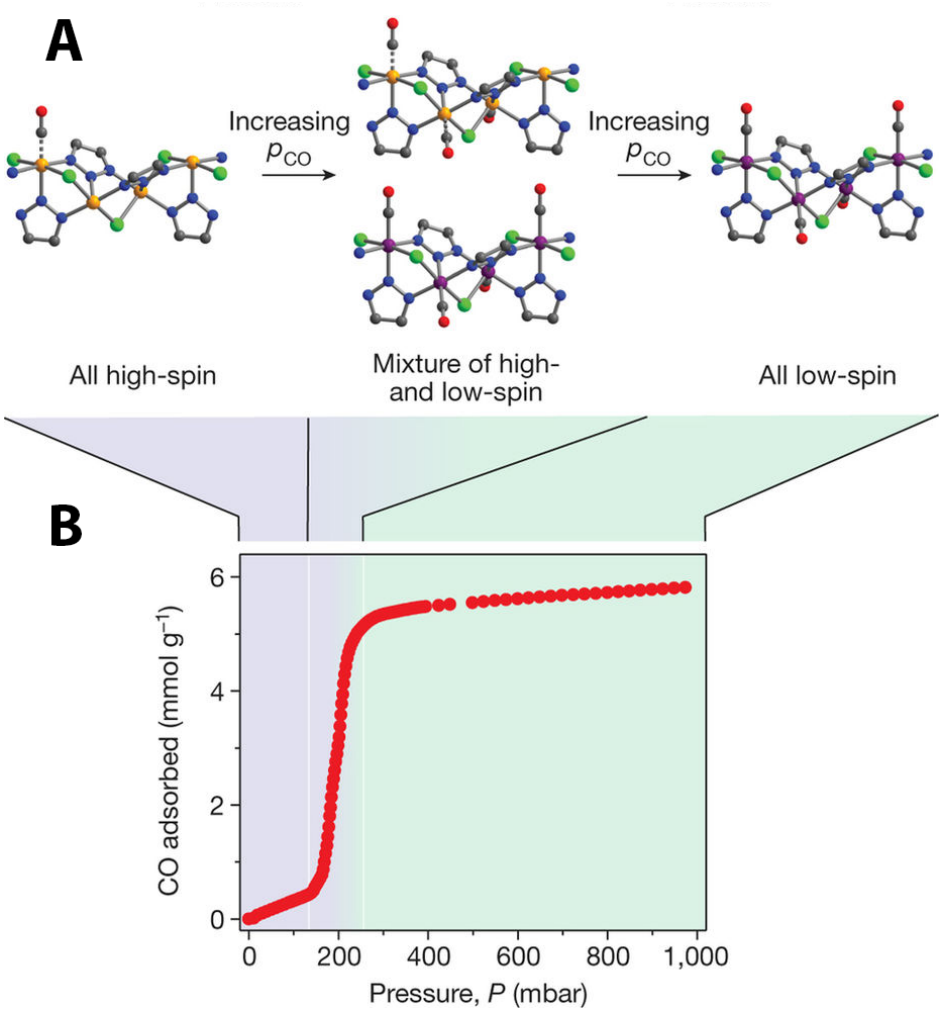


Figure 2-6. CO adsorption through CO-metal binding and conformational change using Fe_2Cl_2(BBTA). (A) Schematic of cooperative spin transition mechanism of Fe_2Cl_2(BBTA) at low pressure (< 0.1 bar) before isotherm step region, Fe^{2+} high-spin to low-spin state conversion with increasing pressure (0.15-0.3 bar) and full conversion to low-spin state beyond the step pressure. Atom/ion colors: C, grey; Cl, green; N, blue; O, red; high-spin Fe^{2+}, orange; low-spin Fe^{2+}, purple. Hydrogen atoms emitted

for clarity. (B) CO adsorption isotherm of Fe_2Cl_2(BBTA) at 25 °C with steps 1-3 shown in corresponding purple and green regions.[110]

These structures are isoreticular to the aforementioned M-MOF-74 analogues,[97] however they exhibit a cooperative spin transition ability upon CO adsorption. This coordinative feature of Fe_2Cl_2(BBTA) is not possible with Fe-BTTri because of its large distance between iron nodes.[111] A similar isotherm shape was observed with Cu(AIP)(H_2O),[109] and the spin-state and step-change is associated with the increase in CO pressure. The conversion from high to low spin state only takes place once the threshold pressure is reached, which activates the same high to low spin state transition throughout the structure which results in a steep uptake in CO adsorption (Figure 2-6A). CO adsorption of 0.45 mmol g^{-1} were measured at 25 °C and 0.15 bar, and 5.25 mmol g^{-1} uptake at 0.3 bar, producing near CO saturation after the step-change (Figure 2-6B). The pressure of that step increases with the temperature.

The work exploited that feature and proposed to use Fe_2Cl_2(BBTA) as a candidate for a 'non-standard' TSA processes with a relatively mild temperature swing (adsorption at 0.2 bar and 20 °C and desorption at 1 bar and 60 °C) conditions, with regeneration greater than 100 °C required for Ni- and Fe-MOF-74 for comparable working capacities.[97] CO molar selectivity calculations gave ~50 and ~125 for CO/N_2 and CO/H_2, respectively (for 50:50 *v:v* CO:X_2 ratios at 1 bar). Fe_2Cl_2(BTDD) was investigated to see how a different ligand would affect the electronic and structural change upon CO adsorption. Fe_2Cl_2(BTDD) exhibited the same step-change upon CO adsorption, however all step changes at the same temperature conditions were at higher pressure than for Fe_2Cl_2(BBTA). Hence, altering the triazolate ligand opens avenues to designing a desired MOF for a TSA system with a specified step change for CO gas separation.

2.5.5 *CO adsorption through chemical modification of the MOF*

While using unsaturated metal sites has been the most popular route for CO separation using MOFs to date, a number of studies have also been reported that have introduced additional preferential adsorption sites through metal impregnation[85,100,102,103,112,113] and/or ligand functionalisation (Figure 2-2B).[115,116,134]

Metal impregnation, similar to that reported with activated carbon,[62,63] has been performed on highly porous MOFs, *e.g.* M-MIL-100 and M-MIL-101.[85,100,102,103,112,113] For instance, Fe-MIL-100 and Cr-MIL-101 have been subject to post-synthesis modification using Cu-based impregnation and complexation to introduce Cu^+ sites. In the case of Cu impregnated Cr-MIL-101, the CO uptake more than doubled upon impregnation, rising from 1.03 to 2.26 mmol g^{-1} [103] and from 1.05 to 2.82 mmol g^{-1} [102] at 25 °C and 1 bar. CO/N_2 IAST selectivities dramatically increased after Cu impregnation in both studies, as did the CO/CO_2 selectivity in the latter study.[102] The introduction of Cu^+ sites increased the number of chemisorbing sites, while simultaneously decreasing the N_2 uptake due to the reduction of specific surface area. The Cu loading was optimised in order to maximise both of these beneficial effects. The Cu^+ sites reduced the accessibility of the Cr sites for CO_2 binding and increase the number of sites for π-complexation to CO.

In one Cu impregnation study on Fe-MIL-100, the CO uptake increased from 0.38 to 2.78 mmol g^{-1} (25 °C , 1 bar) after impregnation with Cu^+ (Figure 2-7).[85] CO/N_2 IAST selectivity was approximately 90 times higher than the original Fe-MIL-100.

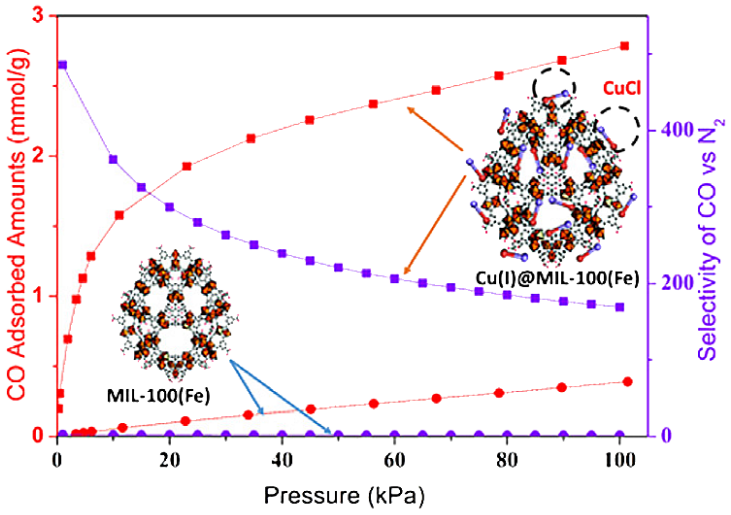


Figure 2-7. CO adsorption through chemical modification of the MOF. Schematic of Fe-MIL-100 and Cu impregnated Fe-MIL-100, CO and N_2 adsorption isotherms, and IAST selectivities for equimolar CO/N_2 at 25 °C.[85]

Another approach to enhancing CO gas separation has been through modification of the organic linker.[115,116] This route has been less explored for CO adsorption than the previous technique of Cu^+ impregnation and has resulted in less promising results. This is related to the weak dipole moment resulting in less pronounced enhancement in heats of adsorption from interactions with organic ligand functionalisation. For example, Ti-MIL-125 ($Ti_8O_8(OH)_4(BDC)_6$ where BDC = benzene-1,4-dicarboxylate) has been functionalised with amine groups and studies have been performed for syngas purification using a combination of single gas isotherms, column breakthrough and PSA experiments.[115]

Different functional groups (*i.e.* amino, bromo, chloro, nitro, methyl, allyloxy and benzyloxy) have been introduced using functionalised terephthalic acid in a number of multivariate MOF-5 analogues.[116] For the best performing material, MTV-MOF-5-EHI possess functional groups consisting of nitro, allyloxy and benzyloxy groups, and the CO capacity was increased from 0.17 to 0.21 mmol g^{-1} (25 °C, 1 bar).

2.5.6 *CO purification via size exclusion based separation*

In previous sections, the adsorption uptake and calculated IAST selectivities were based on different affinities to the chemical makeup of the MOF. In this section, the focus will be on MOFs for which separation is based on pore geometry, specifically small differences in aperture size, which under the right conditions can significantly enhance the ability to perform separations including CO purification (Figure 2-2D).

A molecular sieving or size exclusion effect has been highlighted in hydrated PCN-13, the 9,10-anthracenedicarboxylic acid based MOF-5 analogue, for O_2 and H_2 over CO.[119] Indeed this is consistent with the crystallographic pore size of PCN-13 of 3.50 Å, which would preclude adsorption of N_2 or CO (kinetic diameter 3.64 Å and 3.76 Å) and allow adsorption of H_2 or O_2 (kinetic diameter 2.89 Å and 3.46 Å). Thermal activation leads to dehydration of the MOF, thereby enhancing N_2 and CO uptakes and decreasing selectivity.

The adsorption and diffusion properties of USTA-16 ($KCo_3(C_6H_4O_7)$ $(C_6H_5O_7)$ $(H_2O)_2$) with CO were investigated in a systematic study.[121] The study focussed on H_2 recovery from steam methane reforming off-gases, including CO, CO_2, N_2 and CH_4. While never explicitly referring to the gas separation mechanism that is occurring, it is assumed that the main separation mechanism was kinetic and molecular size based separation. Multicomponent adsorption isotherms were simulated using IAST calculations, and this study reported the effective use of UTSA-16 for CO removal in H_2 purification, although these PSA simulations were not tested experimentally.

Another sub-category of MOFs with reports of size exclusion based gas separation are zeolitic imidazolate frameworks (ZIFs).[120,136] Experimental and computational studies have shown that this diverse category of MOFs have potential for size

exclusion based separations of various molecules including H_2, CO_2, N_2, CH_4 because of their small pore apertures.[120,137] As reported in a computational study, ZIF-68 and ZIF-69 may be suitable for CO_2/CO separation through differences in the rates of diffusion which allow for kinetic based separations.[120]

Another class of MOF structures exhibiting size exclusion based separation are molecular adjustable molecular sieves (MAMS).[117] MAMS correspond to MOF-based structures displaying both a permanent porosity for gases, and a degree of structural flexibility allowing pore/mesh size tuning by controlling the temperature at cryogenic temperatures tailored for gas separations. MAMS-1 (Ni_8(5-BBDC)$_6$(μ3-OH)$_4$ where 5-BBDC = 5-*tert*-butyl-1,3-benzenedicarboxylate) exhibits a tri-layered structure with hydrophilic channels, and separating the tri-layers are hydrophobic regions.[117] The hydrophilic channels of MAMS-1 act as an adjustable mesh, and this MOFs potential for adsorption and separation of CO, H_2, N_2, O_2, CH_4 as well as higher order hydrocarbons has been studied. The range of pore sizes of 3.0-3.4 Å at -196 °C permit purification of CO (and syngas in general) by selectively removing smaller sized impurities from the gas streams. Increasing the temperature to -160 °C did not significantly impact the uptake of CO (~0.6 mmol g^{-1}) at 1 bar, but resulted in N_2 selectivity with a 4-fold increase in the uptake of N_2 (2.5 mmol g^{-1}) because its kinetic diameter is 3.64 Å.

Another MOF capable of pore size tuning, which can be used for gas separation is Zn(ADC)(4,4‘-Bpe)0.5·xG (ADC = 4,4′-azobenzenedicarboxylate, 4,4′-Bpe = *trans*-bis-(4-pyridyl)ethylene, G = guest molecules).[118] The bidentate pillar-like linkers (4,4‘-Bpe) and long dicarboxylate linkers (ADC) produces a triply-interpenetrating framework with 1-D channels. This MOF readily adsorbs significant amounts of H_2 (2.79 mmol g^{-1})

while exhibiting minimal uptake of the larger CO and N_2 molecules (~0.5 mmol g^{-1}) at -196 °C and 1 bar.

2.5.7 *Current challenges and outlook in the use of MOFs for CO purification*

While the findings presented above highlight the potential of MOFs for CO/N_2 separation and syngas purification, a number of aspects call for further investigation to enhance MOFs competitiveness with existing technologies. From our review of the literature, four areas requiring further investigation are identified, these include: MOF stability, recyclability, performance testing under 'real' conditions and implementation into a CO purification process.

2.5.7.1 MOF stability

MOFs possessing unsaturated metal sites have proved to be the most effective for CO adsorption and CO/N_2 separation. However, this structural characteristic also contributes to MOF instability. These sites are often prone to water adsorption, particularly in the case of mono- and divalent metals, which can result in structural degradation of the MOF. There is also a substantial decrease in gas uptake when water molecules occupy these preferential adsorption sites.[138-143] HKUST-1 and a number of the M-MOF-74 analogues suffer from this detrimental effect and lead to a decline in performance.[144]

Studies of water adsorption on M-MOF-74 have shown a mechanism for water to dissociate to OH^- and H^+ at the metal centre, and thereby reportedly poisoning the sites, and irreversibly reducing the capacity of M-MOF-74.[139,144-150] Since the first experimental water isotherm was recorded for M-MOF-74,[140] further studies have disagreed with early suggestions that moderate exposure to water is not detrimental and that high capacity is retained. In any case, the stability of M-MOF-74 seems greatly

dictated by the metal centre of the MOF, with the stability trend of Co- > Ni- > Zn- > Mg-MOF-74 following the trend of these metals' reducing potential.[139,151] Not only does the presence of water affect the stability of M-MOF-74, long-term exposure to atmospheric oxygen was shown to have a similar effect; the strongly reducing metal centres are oxidised and the MOF irreversibly loses its capacity.[148,151]

Three routes have been proposed to enhance the stability of M-MOF-74: (i) substituting the oxygen atom in the organic ligand with sulphur to prevent H_2O dissociation,[152] (ii) protecting the unsaturated metal sites *via* binding with an organic molecule *e.g. N,N'*-dimethylethylenediamine[153] and (iii) substituting metal ions prone to oxidation (*e.g.* Mg^{2+}) with metals less vulnerable to oxidation or hydrolysis (*e.g.* Ni^{2+} and Co^{2+}).[154] Routes (ii) and (iii) are likely to change the overall gas uptake as well as the strength of adsorption. To date, none of these routes having been explored in the context of CO purification. Overall, a number of strategies are now available to enhance the stability of MOF structures, particularly towards moisture.[114,152-160]

The stability of Cu impregnated MOFs are also problematic because of the tendency of Cu^+ sites to oxidise to its unfavourable Cu^{2+} oxidation state. By performing Cu impregnation with vanadium for Cr-MIL-101, vanadium provided oxygen-resistance for the Cu^+ sites, as vanadium was slowly oxidised itself.[114] Cu^+/V impregnated Cr-MIL-101 maintained 92% of its original CO capacity after exposure in air for two weeks by employing this technique.

2.5.7.2 Recyclability

When it comes to long-term usage at scale, good adsorbents are characterised by: (i) high and sustained adsorption capacity and selectivity over multiple cycles and (ii) ease of regeneration involving minimal energy consumption. These properties are

dependent on the stability of the MOFs, the mechanisms of adsorption and the heat of adsorption involved.

When integrating a MOF in a given adsorption process, one needs to optimise the heat of adsorption so that it is high enough to allow the desired selectivity and uptake, but remains low enough so that it does not lead to an excessively energy intensive regeneration process. Such a delicate balance can only be found *via* a combination of process system modelling, molecular modelling and experimental testing. Such work has not been reported yet, at least not in the context of CO purification. Nevertheless, a number of molecular modelling and experimental studies have calculated the CO heat of adsorption for several MOFs. As seen in Table 2-4, MOFs possessing unsaturated metal sites for CO adsorption such as M-MOF-74, Fe_2Cl_2(BBTA), Fe_2Cl_2(BTDD) and Fe-BTTri exhibit the largest CO heats of adsorption, reaching up to 65 kJ mol^{-1} for Fe-BTTri.[97,111] When considering the M-MOF-74 analogues, it is possible to modulate the heat of adsorption *via* modification of the type of metal used. It is interesting to note that HKUST-1 exhibits lower heat of adsorption (~20 kJ mol^{-1}) than other MOFs involving similar adsorption mechanisms. This is linked to the weaker Cu^{2+}-CO interactions from the Cu-Cu paddlewheel based HKUST-1.[99] As seen in Table 2-4, when size exclusion based separation is the governing mechanism, low CO heats of adsorption are observed.

Cyclic studies have been reported for a few MOFs in the context of CO purification such as: HKUST-1, Rh-DUT-82, Fe-BTTri, Cu(AIP)(H_2O) and Cu impregnated Cr-MIL-101.[98,102,103,109,111,114,161] Regeneration was performed either *via* TSA or PSA, or a combination of the two with PTSA. Fe-BTTri was successfully recycled *via* a PTSA process showing no significant decrease in capacity after 10 cycles (Figure 2-5C).[111] For CO purification using Cu(AIP)(H_2O),[109] regeneration was performed *via* heating at

27 °C (adsorption was conducted at -191 °C). It was found that 85% and 94% enrichment was achieved after the 1st and 2nd cycles for 50:50 (*v:v*) CO:N_2. In the case of Rh-DUT-82,[98] a loss in capacity was observed after the first cycle and FTIR analyses confirmed the presence of residual CO that does not desorb fully until exposed to vacuum. Regeneration and stability tests produced encouraging results for the Cu impregnated Cr-MIL-101.[102,103,114] The CO capacity retained demonstrates facile regeneration with reversible Cu^+-CO binding.

2.5.7.3 Performance testing techniques

Overall, most studies on CO purification report static equilibrium adsorption measurements and have been conducted under conditions which are not necessarily representative of industrial settings. While equilibrium adsorption isotherms are valuable to compare and rank MOFs in terms of CO adsorption capacity and to calculate IAST selectivities, dynamic testing is a better indicator of performance at scale. From the dynamic measurement techniques used, it is possible to extract kinetic data[76] and also use the results to model the adsorption process system.[115,161] Furthermore, while single gas equilibrium adsorption measurements provide useful data for theoretical selectivity, multi-gas dynamic measurements can validate or dismiss the calculated selectivity. IAST selectivities are typically reported[128,129] and these involve performing prohibitively costly and lengthy experiments such as equilibrium sorption isotherms. Studies also report ideal selectivities, dividing the CO adsorbed amount by the impurity adsorbed amount, as seen in (Table 2-2 and Table 2-4). Although not perfect measures themselves, IAST selectivities are generally preferred over ideal selectivities as they represent gas mixtures more accurately.

The most common technique used for dynamic measurements is breakthrough column testing. CO/N_2 and CO/CO_2 breakthrough experiments were performed to

exhibit the dramatic improvement in CO/N_2 and CO/CO_2 separation upon Cu impregnation of Fe-MIL-100 and Cr-MIL-101.[100,105,112] The number of components in the gas mixtures have also varied with MOF testing, from single component CO breakthrough measurements[123] to CO_2:CO:O_2:N_2 quaternary mixtures[108] as well, but negligible CO adsorption was recorded in both cases. Breakthrough measurements with CO have also been recorded with CO_2 selective materials, amino-functionalised Ti-MIL-125[115] and ZIF-95 and ZIF-100.[136] Overall, there is a scarcity of dynamic breakthrough measurements in comparison to equilibrium sorption isotherms recorded. A significant number of the measurements including CO have focussed on CO_2 purification, and therefore have exhibited CO_2/CO selectivity. The best performing MOFs tested for CO breakthrough separation have been the Cu impregnated MOFs, however no breakthrough testing has been performed on the leading MOFs for CO/N_2 separation (*i.e* M-MOF-74, M-BTTri, M_2Cl_2(BBTA) and M_2Cl_2(BTDD))

CO diffusivity in MOF-5 and MOF-177 have been measured and compared to that of CO diffusivity in zeolites.[76] CO diffusivity was higher for the MOFs, especially MOF-5, than the zeolites. It was suggested that the larger pore sizes of the MOFs increased the CO diffusion rates.

Working capacity represents the amount of gas that can be captured and released during an adsorption-desorption cycle. This value is more representative than the adsorption capacity reported for a real-world performance, with regards to implementation into a PSA, TSA or VSA system. The working capacities of the MOFs are reported in a review of CO purification using MOFs.[1] For example, the M-MOF-74 group records particularly high CO uptake, however the MOF reaches near saturation at 0.3 bar and therefore a VSA system would be required for the CO purification

process.[97] MOFs that do no saturate at low pressure are favoured as they do not require a VSA system, as a PSA system results in lower expenditure.

2.5.7.4 CO purification implementation

While the performance metrics and material properties are crucial for appropriate adsorbent selection in an adsorption-based CO purification process, this purification must be considered in an industrial context. If a PSA or TSA unit is desired for CO purification, interactions between the sorbent and the other components of the gas stream must be considered, as discussed briefly in Section 2.5.7.1. CO separation from a raw syngas stream containing CO_2, CH_4, N_2, H_2, H_2S and H_2O in one step is most likely to be unrealistic for any sorbent, including MOFs. Indeed, MOFs have unsaturated metal sites that are therefore susceptible to adsorbing not only CO but also H_2O, CO_2 or H_2S for instance. Hence, additional steps may be needed prior to the CO purification step to remove these competitive species. There are limited MOF studies investigating multi-component syngas-like streams for CO purification; one such study has investigated CO enrichment from a binary stream ($CO:N_2$)[109] and another study investigates binary and ternary mixtures of CO, CO_2, and H_2.[115] Therefore the scarcity of knowledge on the effect of impurities (*e.g.* CO_2, H_2O, H_2S) in this area should be addressed to gain more insight into the CO purification process as a whole. Multi-component testing will indicate whether CO purification requires a multi-step process, and determine which CO separations can be reasonably targeted.

2.6 Conclusions and Research Gaps

This chapter presents an up-to-date summary and analysis of the technologies available today or currently under development for the purification of CO-containing streams, with an emphasis on CO/N_2 separation. Overall, the energy consumption and

poor stability of current technologies such as cryogenic distillation and absorption have led researchers to concentrate on adsorption technologies and the development of efficient CO adsorbents.

MOFs outperform activated carbon and zeolites and appear as a promising platform owing to their high metal density. While both chemisorption (or quasi-chemical sorption) and size exclusion based separation have been explored for CO purification using MOFs, the former route is the most effective so far and could be exploited in a temperature swing process. Within chemisorption (or quasi-chemical sorption), the most successful strategy to date is to use MOFs with unsaturated metal sites in order to favour selective CO-metal binding. MOFs containing a high density of unsaturated metal sites with a 1-D hexagonal pored topology (M-MOF-74, M_2Cl_2(BBTA), M_2Cl_2(BTDD)) have exhibited the best CO/N_2 separation ability. Chemical modification of MOFs through Cu impregnation techniques have drastically improved the CO/N_2 separation performance as well (Cu impregnated Fe-MIL-100 and Cu impregnated Cr-MIL-101). Moving forward, there is now a need to understand and quantify the actual value of MOFs for CO purification in an industrial context. To address this, a number of directions are worth exploring:

- Combining experimental and computational work at the molecular and process scale is necessary to allow a quick screening of potentially promising structures as well as an understanding of their performance at a process scale. To support this effort, experimental screening of a sub-set of promising MOFs is required to reliably evaluate the MOFs CO/N_2 separation ability.
- Equilibrium studies of CO adsorption in MOFs have provided the confidence to move to the next stage of testing, *i.e.* testing under ‘realistic’ conditions. Going beyond IAST selectivity calculations, experimental CO purification and dynamic

CO/N_2 separation tests of more complex CO-containing streams are required to get true selectivity data.

- Following the requirement for further dynamic testing, cyclic and regeneration CO testing of the most promising MOF candidates is required to test its structural, chemical and mechanical robustness. The regeneration conditions presented have scarcely been optimised and therefore exerting waste energy, therefore experimental testing is required to identify suitable conditions.
- The separation performance of the MOFs should be further investigated taking into account the nature of the syngas streams (*i.e* N_2 and CO_2 impurities) and the potential effects of the components on the MOF structures.
- Dynamic adsorption studies are also needed to obtain the kinetic data needed to model the performance of the materials at a process scale.
- Chemical modification should be explored and developed further for MOFs that already exhibit good CO/N_2 separation ability. To date, Cu impregnation has been performed solely on MOFs with high porosity but poor CO capacity and moderate CO/N_2 selectivity. Furthermore, greater analysis of the Cu impregnation and reduction procedure is required, which can be addressed by optimising the Cu reduction procedure and confirming Cu^+ sites and Cu^+-CO binding.

2.7 Research Objectives

From these conclusions and knowledge gaps, the overall objective of this project was to design and synthesize metal-organic frameworks for industrially relevant CO/N_2 separation.

The scope of the project was to: synthesize and test MOFs for CO/N_2 separation using high throughput screening; characterise and study the MOF properties that govern CO/N_2 separation; test the screened MOFs for dynamic CO/N_2 separation in a binary gas mixture; study the effect of varying levels of N_2 impurity upon CO purification ability; investigate the effect of CO_2 impurity upon CO purification ability in $CO:CO_2$ binary and $CO:N_2:CO_2$ ternary gas mixtures for comparison; record kinetic and thermodynamic data for CO/N_2 separation; develop new MOF materials using the knowledge gathered to improve CO purification.

2.7.1 *RO 1: To screen MOFs for CO/N_2 separation*

This objective aims to identify the best performing MOFs for CO/N_2 separation using high throughput testing techniques. The information extracted will also distinguish the structural and chemical features that govern CO purification.

2.7.2 *RO 2: To test the dynamic performance of the best performing MOFs for CO/N_2 separation*

This objective aims to evaluate the dynamic separation performance of the identified best performing MOFs from RO 1 for CO/N_2 using a binary gas mixture. This objective also explores the effect of varying N_2 impurity upon CO purification, while studying the effect of CO_2 impurity in a ternary $CO:N_2:CO_2$ stream to replicate industrial syngas composition. The cyclability of the MOFs must also be investigated in order to evaluate the MOF's lifetime.

2.7.3 *RO 3: To collect kinetic and thermodynamic data relevant for CO/N_2 separation*

This objective aims to provide kinetic and thermodynamic information of the best performing MOFs for CO/N_2 separation to assist in designing an adsorption process.

2.7.4 *RO 4: To design, synthesize and test new MOFs for CO/N_2 separation based on the knowledge collected*

This objective aims to improve MOF separation performance by enhancing its CO capacity and selectivity using the knowledge gained from RO 1 and RO 2. This approach aims to exploit the properties that governs the CO purification performance. In-depth *in-situ* characterisation is required for this objective to understand the chemical and mechanistic information of the new materials.

2.8 References

1 Evans, A., Luebke, R. & Petit, C. The use of metal–organic frameworks for CO purification. *Journal of Materials Chemistry A* **6**, 10570-10594, (2018).
2 Sholl, D. S. & Lively, R. P. Seven chemical separations: to change the world: purifying mixtures without using heat would lower global energy use, emissions and pollution--and open up new routes to resources. *Nature* **532**, 435-438, (2016).
3 Lieuwen, T., Yang, V. & Yetter, R. *Synthesis Gas Combustion: Fundamentals and Applications*. (CRC Press, 2009).
4 Wilhelm, D. J., Simbeck, D. R., Karp, A. D. & Dickenson, R. L. Syngas production for gas-to-liquids applications: technologies, issues and outlook. *Fuel Processing Technology* **71**, 139-148, (2001).
5 www.industry.airliquide.co.uk/carbon-monoxide
6 Mosa, T. & Taylor, G. T. *Method and apparatus for the manufacture of high purity carbon monoxide*, US Pat., 8,703,089, (2014).
7 Mosa, T. & Taylor, G. T. *Method and apparatus for the manufacture of high purity carbon monoxide*, US Pat., 9,567,226, (2017).
8 Dutta, N. N. & Patil, G. S. Developments in CO separation. *Gas Separation & Purification* **9**, 277-283, (1995).
9 Li, J.-R., Kuppler, R. J. & Zhou, H.-C. Selective gas adsorption and separation in metal–organic frameworks. *Chemical Society Reviews* **38**, 1477-1504, (2009).
10 Kuppler, R. J. *et al.* Potential applications of metal-organic frameworks. *Coordination Chemistry Reviews* **253**, 3042-3066, (2009).
11 Sumida, K. *et al.* Carbon Dioxide Capture in Metal–Organic Frameworks. *Chemical Reviews* **112**, 724-781, (2012).
12 Qiu, S., Xue, M. & Zhu, G. Metal-organic framework membranes: from synthesis to separation application. *Chemical Society Reviews* **43**, 6116-6140, (2014).
13 Li, B., Wang, H. & Chen, B. Microporous Metal–Organic Frameworks for Gas Separation. *Chemistry – An Asian Journal* **9**, 1474-1498, (2014).
14 Czaja, A. U., Trukhan, N. & Müller, U. Industrial applications of metal–organic frameworks. *Chemical Society Reviews* **38**, 1284-1293, (2009).
15 Frohning, C. D., Kohlpaintner, C. W. & Bohnen, H. W. *Carbon monoxide and synthesis gas chemistry*, Applied Homogeneous Catalysis with Organometallic Compounds, Second Edition, (2008).
16 Ramachandran, R. & Menon, R. K. An overview of industrial uses of hydrogen. *International Journal of Hydrogen Energy* **23**, 593-598, (1998).
17 Tijmensen, M. J. A., Faaij, A. P. C., Hamelinck, C. N. & van Hardeveld, M. R. M. Exploration of the possibilities for production of Fischer Tropsch liquids and power via biomass gasification. *Biomass and Bioenergy* **23**, 129-152, (2002).
18 Falbe, J. *Carbon monoxide in organic synthesis*. Vol. 10 (Springer Science & Business Media, 2013).
19 Franke, R., Selent, D. & Börner, A. Applied Hydroformylation. *Chemical Reviews* **112**, 5675-5732, (2012).
20 Weissermel, K. & Arpe, H. J. *Industrial Organic Chemistry*. (VCH, 1993).
21 LLP, M. I. Global Polyurethanes Market Segmented by Application, Industry and Geography Trends and Forecasts (2015-2020). (2016).

22 Haynes, A. *et al.* Promotion of Iridium-Catalyzed Methanol Carbonylation: Mechanistic Studies of the Cativa Process. *Journal of the American Chemical Society* **126**, 2847-2861, (2004).

23 Wakatsuki, K. Acetyls Chain - World Market Overview, in *APIC, Seoul.*

24 Song, C. in *Hydrogen and Syngas Production and Purification Technologies* 1-13 (John Wiley & Sons, Inc., 2009).

25 Torrence, G. P., Hendricks, J. D., Dickinson, D. D. & Aguilo, A. *Addition of hydrogen to carbon monoxide feed gas in producing acetic acid by carbonylation of methanol*, US Pat., 4,994,608, (1991).

26 Shenoy, T. A. *Cryogenic process for separating synthesis gas*, US Pat., 4,217,759, (1980).

27 Martin, J. R. *Separation of H_2, CO, and CH_4 synthesis gas with methane wash*, US Pat., 4,102,659, (1978).

28 Haik-Beraud, N., Hernandez, A., Marty, P. & Polster, B. *Process and apparatus for generating and purifying a syngas*, US Pat., 8,888,873, (2014).

29 Fabian, R. *Process for the extraction of carbon monoxide from gas streams*, US Pat., 4,478,621, (1984).

30 McNeil, B. A. & Scharpf, E. W. *Separation of carbon monoxide from nitrogen-contaminated gaseous mixtures also containing hydrogen and methane*, US Pat., 6,073,461, (2000).

31 Briglia, A., Court, P., Haik-Beraud, N., Hernandez, A. & Monereau, C. *Method And Apparatus For Producing Carbon Monoxide By Cryogenic Distillation*, US Pat., 9,410,738, (2009).

32 Rouquerol, J., Llewellyn, P. & Rouquerol, F. Is the BET equation applicable to microporous adsorbents. *Stud. Surf. Sci. Catal* **160**, 49-56, (2007).

33 Haase, D. J. & Walker, D. G. The COSORB Process. *Chemical Engineering Progress* **5**, 74-77, (1974).

34 Keller. A & R, S. The use of COSORB II to recover high purity Carbon Monoxide from a feed gas, in *AIChe Summer Meeting* (Denver, Colorado, 1988).

35 Zarca. G, Ortiz. I & A, U. Carbon Monoxide Separation By Reactive Absorption in Chlorocuprate(I)-Based Ionic Liquid, in *AIChE Annual Meeting* (Atlanta, USA, 2014).

36 Zarca, G., Ortiz, I. & Urtiaga, A. Kinetics of the carbon monoxide reactive uptake by an imidazolium chlorocuprate(I) ionic liquid. *Chemical Engineering Journal* **252**, 298-304, (2014).

37 Zarca, G., Urtiaga, A., Ortiz, I., Cañizares, P. & Rodrigo, M. A. Carbon monoxide reactive separation with basic 1-hexyl-3-methylimidazolium chlorocuprate(I) ionic liquid: Electrochemical determination of mass transport properties. *Separation and Purification Technology* **141**, 31-37, (2015).

38 Repper, S. E., Haynes, A., Ditzel, E. J. & Sunley, G. J. Infrared spectroscopic study of absorption and separation of CO using copper(i)-containing ionic liquids. *Dalton Transactions* **46**, 2821-2828, (2017).

39 Jacquemin, J., Husson, P., Majer, V. & Gomes, M. F. C. Low-pressure solubilities and thermodynamics of solvation of eight gases in 1-butyl-3-methylimidazolium hexafluorophosphate. *Fluid Phase Equilibria* **240**, 87-95, (2006).

40 Jacquemin, J., Costa Gomes, M. F., Husson, P. & Majer, V. Solubility of carbon dioxide, ethane, methane, oxygen, nitrogen, hydrogen, argon, and carbon monoxide in 1-butyl-3-methylimidazolium tetrafluoroborate between temperatures 283 K and 343 K and at pressures close to atmospheric. *Journal of Chemical Thermodynamics* **38**, 490-502, (2006).

41 Kumełan, J., Pérez-Salado Kamps, Á., Tuma, D. & Maurer, G. Solubility of the single gases H_2 and CO in the ionic liquid [bmim][CH3SO4]. *Fluid Phase Equilibria* **260**, 3-8, (2007).

42 Urukova, I., Vorholz, J. & Maurer, G. Solubility of CO_2, CO, and H_2 in the Ionic Liquid [bmim][PF6] from Monte Carlo Simulations. *Journal of Physical Chemistry B* **109**, 12154-12159, (2005).

43 Kumełan, J., Pérez-Salado Kamps, Á., Tuma, D. & Maurer, G. Solubility of the Single Gases Carbon Monoxide and Oxygen in the Ionic Liquid [hmim][Tf_2N]. *Journal of Chemical & Engineering Data* **54**, 966-971, (2009).

44 David, O. C., Zarca, G., Gorri, D., Urtiaga, A. & Ortiz, I. On the improved absorption of carbon monoxide in the ionic liquid 1-hexyl-3-methylimidazolium chlorocuprate. *Separation and Purification Technology* **97**, 65-72, (2012).

45 David, O. C., Gorri, D., Urtiaga, A. & Ortiz, I. Mixed gas separation study for the hydrogen recovery from H_2/CO/N_2/CO_2 post combustion mixtures using a Matrimid membrane. *Journal of Membrane Science* **378**, 359-368, (2011).

46 David, O. C., Gorri, D., Nijmeijer, K., Ortiz, I. & Urtiaga, A. Hydrogen separation from multicomponent gas mixtures containing CO, N_2 and CO_2 using Matrimid® asymmetric hollow fiber membranes. *Journal of Membrane Science* **419–420**, 49-56, (2012).

47 Zarca, G., Ortiz, I. & Urtiaga, A. Facilitated-transport supported ionic liquid membranes for the simultaneous recovery of hydrogen and carbon monoxide from nitrogen-enriched gas mixtures. *Chemical Engineering Research and Design* **92**, 764-768, (2014).

48 Zarca, G., Ortiz, I. & Urtiaga, A. Copper (I)-containing supported ionic liquid membranes for carbon monoxide/nitrogen separation. *Journal of Membrane Science* **438**, 38-45, (2013).

49 Gan, Q., Rooney, D., Xue, M., Thompson, G. & Zou, Y. An experimental study of gas transport and separation properties of ionic liquids supported on nanofiltration membranes. *Journal of Membrane Science* **280**, 948-956, (2006).

50 Gan, Q. *et al.* Theoretical and experimental correlations of gas dissolution, diffusion, and thermodynamic properties in determination of gas permeability and selectivity in supported ionic liquid membranes. *Advances in Colloid and Interface Science* **164**, 45-55, (2011).

51 Rouquerol, J., Rouquerol, F., Llewellyn, P., Maurin, G. & Sing, K. S. *Adsorption by powders and porous solids: principles, methodology and applications*. (Academic Press, 2013).

52 Helfferich, F. G. & Ruthven, D. M. Principles of adsorption & adsorption processes, by D. M. Ruthven, John Wiley & Sons, 1984, xxiv + 433 pp. *AIChE Journal* **31**, 523-524, (1985).

53 Grande, C. A., Lopes, F. V. S., Ribeiro, A. M., Loureiro, J. M. & Rodrigues, A. E. Adsorption of Off-Gases from Steam Methane Reforming (H_2, CO_2, CH_4, CO and N_2) on Activated Carbon. *Separation Science and Technology* **43**, 1338-1364, (2008).

54 Lopes, F. V. S. *et al.* Adsorption of H_2, CO_2, CH_4, CO, N_2 and H_2O in Activated Carbon and Zeolite for Hydrogen Production. *Separation Science and Technology* **44**, 1045-1073, (2009).

55 Delgado, J. A. *et al.* Adsorption and diffusion of H_2, CO, CH_4, and CO_2 in BPL activated carbon and 13X Zeolite: evaluation of performance in Pressure Swing Adsorption hydrogen purification by simulation. *Industrial & Engineering Chemistry Research* **53**, 15414-15426, (2014).

56 Hirai, H., Wada, K. & Komiyama, M. Active carbon-supported copper (I) chloride as carbon monoxide solid adsorbent. *Chemistry Letters* **12**, 361-364, (1983).

57 Gao, F., Wang, Y., Wang, X. & Wang, S. Selective CO adsorbent CuCl/AC prepared using $CuCl_2$ as a precursor by a facile method. *RSC Advances* **6**, 34439-34446, (2016).

58 Hirai, H., Komiyama, M. & Wada, K. Active carbon-supported aluminium copper chloride as water-resistant carbon monoxide adsorbent. *Chemistry Letters* **11**, 1025-1028, (1982).

59 Tamon, H., Kitamura, K. & Okazaki, M. Adsorption of carbon monoxide on activated carbon impregnated with metal halide. *AIChE Journal* **42**, 422-430, (1996).

60 Hirai, H., Wada, K. & Komiyama, M. Active carbon-supported copper (I) chloride as solid adsorbent for carbon monoxide. *Bulletin of the Chemical Society of Japan* **59**, 2217-2223, (1986).

61 Hirai, H., Wada, K. & Komiyama, M. Active carbon-supported aluminium copper (I) chloride as solid carbon monoxide adsorbent. *Bulletin of the Chemical Society of Japan* **59**, 1043-1049, (1986).

62 Huang, Y. *et al.* Preparation of CuCl@ AC with high CO adsorption capacity and selectivity from CO/N_2 binary mixture. *Adsorption* **21**, 373-381, (2015).

63 Ma, J., Li, L., Ren, J. & Li, R. CO adsorption on activated carbon-supported Cu-based adsorbent prepared by a facile route. *Separation and Purification Technology* **76**, 89-93, (2010).

64 Gao, F., Wang, Y. & Wang, S. Selective adsorption of CO on CuCl/Y adsorbent prepared using CuCl2 as precursor: Equilibrium and thermodynamics. *Chemical Engineering Journal* **290**, 418-427, (2016).

65 Iyuke, S. E. *et al.* Removal of CO from process gas with Sn–activated carbon in pressure swing adsorption. *Journal of Chemical Technology & Biotechnology* **75**, 803-811, (2000).

66 Xue, C., Hao, W., Cheng, W., Ma, J. & Li, R. Effects of pore size distribution of activated carbon (AC) on CuCl dispersion and CO adsorption for CuCl/AC adsorbent. *Chemical Engineering Journal* **375**, 122049, (2019).

67 Zhu, L.-q., Tu, J.-l. & Shi, Y.-j. Separation of $CO\text{-}CO_2\text{-}N_2$ gas mixture for high-purity CO by pressure swing adsorption. *Gas Separation & Purification* **5**, 173-176, (1991).

68 Kasuya, F. & Tsuji, T. High purity CO gas separation by pressure swing adsorption. *Gas Separation & Purification* **5**, 242-246, (1991).

69 Yeom, C. & Kim, Y. Mesoporous alumina with high capacity for carbon monoxide adsorption. *Korean Journal of Chemical Engineering*, (2017).

70 Cho, S. H. *et al. Adsorbent for selective adsorption of carbon monoxide and process for preparation thereof*, US Pat., 8,377,842, (2013).

71 Rabo, J. A., Francis, J. N. & Angell, C. L. *Selective adsorption of carbon monoxide from gas streams*, US Pat., 4,019,879, (1977).

72 Golden, T. C., Kratz, W. C. & Wilhelm, F. C. *Method for separation of carbon monoxide by highly dispersed cuprous compositions*, US Pat., 5,300,271, (1994).

73 Pillai, R. S., Sethia, G. & Jasra, R. V. Sorption of CO, CH_4, and N_2 in Alkali Metal Ion Exchanged Zeolite-X: Grand Canonical Monte Carlo Simulation and Volumetric Measurements. *Industrial & Engineering Chemistry Research* **49**, 5816-5825, (2010).

74 Sethia, G., Somani, R. S. & Chand Bajaj, H. Adsorption of carbon monoxide, methane and nitrogen on alkaline earth metal ion exchanged zeolite-X: structure,

cation position and adsorption relationship. *RSC Advances* **5**, 12773-12781, (2015).
75 Xie, Y. *et al.* Zeolites modified by CuCl for separating CO from gas mixtures containing CO_2. *Adsorption* **3**, 27-32, (1997).
76 Saha, D. & Deng, S. Adsorption Equilibria and Kinetics of Carbon Monoxide on Zeolite 5A, 13X, MOF-5, and MOF-177. *Journal of Chemical & Engineering Data* **54**, 2245-2250, (2009).
77 Egerton, T. A. & Stone, F. S. Adsorption of carbon monoxide by zeolite Y exchanged with different cations. *Journal of the Chemical Society, Faraday Transactions 1: Physical Chemistry in Condensed Phases* **69**, 22-38, (1973).
78 Egerton, T. A. & Stone, F. S. Adsorption of carbon monoxide by calcium-exchanged zeolite Y. *Transactions of the Faraday Society* **66**, 2364-2377, (1970).
79 Huang, Y.-Y. Selective adsorption of carbon monoxide and complex formation of cuprous-ammines in Cu (I) Y zeolites. *J Catal* **30**, 187-194, (1973).
80 Salama, T. M., Ahmed, A. H. & El-Bahy, Z. M. Y-type zeolite-encapsulated copper(II) salicylidene-p-aminobenzoic Schiff base complex: Synthesis, characterization and carbon monoxide adsorption. *Microporous and Mesoporous Materials* **89**, 251-259, (2006).
81 Sethia, G. *et al.* Equilibrium and Dynamic Adsorption of Carbon Monoxide and Nitrogen on ZSM-5 with Different $SiO_2/Al2O_3$ Ratio. *Separation Science and Technology* **45**, 413-420, (2010).
82 Triebe, R. W. & Tezel, F. H. Adsorption of nitrogen, carbon monoxide, carbon dioxide and nitric oxide on molecular sieves. *Gas Separation & Purification* **9**, 223-230, (1995).
83 Danner, R. & Wenzel, L. Adsorption of carbon monoxide-nitrogen, carbon monoxide-oxygen, and oxygen-nitrogen mixtures on synthetic zeolites. *AIChE Journal* **15**, 515-520, (1969).
84 Munusamy, K. *et al.* Sorption of carbon dioxide, methane, nitrogen and carbon monoxide on MIL-101(Cr): Volumetric measurements and dynamic adsorption studies. *Chemical Engineering Journal* **195–196**, 359-368, (2012).
85 Peng, J. *et al.* A supported Cu(I)@MIL-100(Fe) adsorbent with high CO adsorption capacity and CO/N_2 selectivity. *Chemical Engineering Journal* **270**, 282-289, (2015).
86 Janiak, C. & Vieth, J. K. MOFs, MILs and more: concepts, properties and applications for porous coordination networks (PCNs). *New Journal of Chemistry* **34**, 2366-2388, (2010).
87 Li, J.-R., Sculley, J. & Zhou, H.-C. Metal–Organic Frameworks for Separations. *Chemical Reviews* **112**, 869-932, (2012).
88 He, Y., Zhou, W., Qian, G. & Chen, B. Methane storage in metal-organic frameworks. *Chemical Society Reviews* **43**, 5657-5678, (2014).
89 Adil, K. *et al.* Gas/vapour separation using ultra-microporous metal-organic frameworks: insights into the structure/separation relationship. *Chemical Society Reviews* **46**, 3402-3430, (2017).
90 Bobbitt, N. S. *et al.* Metal-organic frameworks for the removal of toxic industrial chemicals and chemical warfare agents. *Chemical Society Reviews* **46**, 3357-3385, (2017).
91 Li, H. *et al.* Recent advances in gas storage and separation using metal–organic frameworks. *Materials Today*, (2017).

92 Eddaoudi, M. *et al.* Systematic Design of Pore Size and Functionality in Isoreticular MOFs and Their Application in Methane Storage. *Science* **295**, 469-472, (2002).
93 Guillerm, V. *et al.* A supermolecular building approach for the design and construction of metal-organic frameworks. *Chemical Society Reviews* **43**, 6141-6172, (2014).
94 Lu, W. *et al.* Tuning the structure and function of metal-organic frameworks via linker design. *Chemical Society Reviews* **43**, 5561-5593, (2014).
95 Li, J.-R. *et al.* Carbon dioxide capture-related gas adsorption and separation in metal-organic frameworks. *Coordination Chemistry Reviews* **255**, 1791-1823, (2011).
96 Wang, Y. & Zhao, D. Beyond Equilibrium: Metal–Organic Frameworks for Molecular Sieving and Kinetic Gas Separation. *Crystal Growth & Design* **17**, 2291-2308, (2017).
97 Bloch, E. D. *et al.* Reversible CO Binding Enables Tunable CO/H_2 and CO/N_2 Separations in Metal–Organic Frameworks with Exposed Divalent Metal Cations. *Journal of the American Chemical Society* **136**, 10752-10761, (2014).
98 Nickerl, G., Stoeck, U., Burkhardt, U., Senkovska, I. & Kaskel, S. A catalytically active porous coordination polymer based on a dinuclear rhodium paddle-wheel unit. *Journal of Materials Chemistry A* **2**, 144-148, (2014).
99 Chowdhury, P., Mekala, S., Dreisbach, F. & Gumma, S. Adsorption of CO, CO_2 and CH_4 on Cu-BTC and MIL-101 metal organic frameworks: Effect of open metal sites and adsorbate polarity. *Microporous and Mesoporous Materials* **152**, 246-252, (2012).
100 Li, Y.-X. *et al.* Incorporation of Cu(II) and its selective reduction to Cu(I) within confined spaces: efficient active sites for CO adsorption. *Journal of Materials Chemistry A* **6**, 8930-8939, (2018).
101 Karra, J. R. & Walton, K. S. Molecular simulations and experimental studies of CO_2, CO, and N_2 adsorption in metal− organic frameworks. *The Journal of Physical Chemistry C* **114**, 15735-15740, (2010).
102 Vo, T. K., Kim, J.-H., Kwon, H. T. & Kim, J. Cost-effective and eco-friendly synthesis of MIL-101(Cr) from waste hexavalent chromium and its application for carbon monoxide separation. *Journal of Industrial and Engineering Chemistry*, (2019).
103 Wang, Y. *et al.* $CuAlCl_4$ doped MIL-101 as a high capacity CO adsorbent with selectivity over N2. *Frontiers of Chemical Science and Engineering* **8**, 340-345, (2014).
104 Min Wang, Q. *et al.* Metallo-organic molecular sieve for gas separation and purification. *Microporous and Mesoporous Materials* **55**, 217-230, (2002).
105 Li, Y.-X. *et al.* Controlled Construction of Cu(I) Sites within Confined Spaces via Host–Guest Redox: Highly Efficient Adsorbents for Selective CO Adsorption. *ACS Applied Materials & Interfaces* **10**, 40044-40053, (2018).
106 Moreira, M. A. *et al.* Adsorption Equilibrium of Carbon Dioxide, Methane, Nitrogen, Carbon Monoxide, and Hydrogen on UiO-66(Zr)_$(COOH)_2$. *Journal of Chemical & Engineering Data*, (2019).
107 Rallapalli, P. *et al.* Sorption studies of CO_2, CH_4, N_2, CO, O_2 and Ar on nanoporous aluminum terephthalate [MIL-53 (Al)]. *Journal of Porous Materials* **18**, 205-210, (2011).

108 Duan, J. *et al.* High $CO_2/N_2/O_2/CO$ separation in a chemically robust porous coordination polymer with low binding energy. *Chemical Science* **5**, 660-666, (2014).

109 Sato, H. *et al.* Self-accelerating CO sorption in a soft nanoporous crystal. *Science* **343**, 167-170, (2014).

110 Reed, D. A. *et al.* A spin transition mechanism for cooperative adsorption in metal–organic frameworks. *Nature* **550**, 96-100, (2017).

111 Reed, D. A. *et al.* Reversible CO Scavenging via Adsorbate-Dependent Spin State Transitions in an Iron(II)–Triazolate Metal–Organic Framework. *Journal of the American Chemical Society* **138**, 5594-5602, (2016).

112 Kim, A.-R. *et al.* Creating high CO/CO_2 selectivity and large CO working capacity through facile loading of Cu(I) species into an iron-based mesoporous metal-organic framework. *Chemical Engineering Journal* **348**, 135-142, (2018).

113 Vo, T. K. *et al.* Highly CO selective Cu(I)-doped MIL-100(Fe) adsorbent with high CO/CO_2 selectivity due to π complexation: Effects of Cu(I) loading and activation temperature. *Microporous and Mesoporous Materials* **274**, 17-24, (2019).

114 Yin, Y. *et al.* Cuprous/Vanadium Sites on MIL-101 for Selective CO Adsorption from Gas Mixtures with Superior Stability. *ACS Sustainable Chemistry & Engineering* **7**, 11284-11292, (2019).

115 Regufe, M. J. *et al.* Syngas Purification by Porous Amino-Functionalized Titanium Terephthalate MIL-125. *Energy & Fuels* **29**, 4654-4664, (2015).

116 Deng, H. *et al.* Multiple Functional Groups of Varying Ratios in Metal-Organic Frameworks. *Science* **327**, 846-850, (2010).

117 Ma, S., Sun, D., Wang, X.-S. & Zhou, H.-C. A Mesh-Adjustable Molecular Sieve for General Use in Gas Separation. *Angewandte Chemie International Edition* **46**, 2458-2462, (2007).

118 Chen, B., Ma, S., Hurtado, E. J., Lobkovsky, E. B. & Zhou, H.-C. A Triply Interpenetrated Microporous Metal−Organic Framework for Selective Sorption of Gas Molecules. *Inorganic Chemistry* **46**, 8490-8492, (2007).

119 Ma, S., Wang, X.-S., Collier, C. D., Manis, E. S. & Zhou, H.-C. Ultramicroporous Metal−Organic Framework Based on 9,10-Anthracenedicarboxylate for Selective Gas Adsorption. *Inorganic Chemistry* **46**, 8499-8501, (2007).

120 Sirjoosingh, A., Alavi, S. & Woo, T. K. Grand-Canonical Monte Carlo and Molecular-Dynamics Simulations of Carbon-Dioxide and Carbon-Monoxide Adsorption in Zeolitic Imidazolate Framework Materials. *The Journal of Physical Chemistry C* **114**, 2171-2178, (2010).

121 Agueda, V. I. *et al.* Adsorption and diffusion of H_2, N_2, CO, CH_4 and CO_2 in UTSA-16 metal-organic framework extrudates. *Chemical Engineering Science* **124**, 159-169, (2015).

122 Rosi, N. L. *et al.* Rod Packings and Metal−Organic Frameworks Constructed from Rod-Shaped Secondary Building Units. *Journal of the American Chemical Society* **127**, 1504-1518, (2005).

123 Britt, D., Tranchemontagne, D. & Yaghi, O. M. Metal-organic frameworks with high capacity and selectivity for harmful gases. *Proceedings of the National Academy of Sciences* **105**, 11623-11627, (2008).

124 Valenzano, L., Civalleri, B., Sillar, K. & Sauer, J. Heats of Adsorption of CO and CO_2 in Metal–Organic Frameworks: Quantum Mechanical Study of CPO-27-M (M = Mg, Ni, Zn). *Journal of Physical Chemistry C* **115**, 21777-21784, (2011).

125 Valenzano, L. *et al.* Computational and Experimental Studies on the Adsorption of CO, N2, and CO2 on Mg-MOF-74. *The Journal of Physical Chemistry C* **114**, 11185-11191, (2010).
126 Valenzano, L. *et al.* Structure–activity relationships of simple molecules adsorbed on CPO-27-Ni metal–organic framework: In situ experiments vs. theory. *Catalysis Today* **182**, 67-79, (2012).
127 Chavan, S. *et al.* CO Adsorption on CPO-27-Ni Coordination Polymer: Spectroscopic Features and Interaction Energy. *The Journal of Physical Chemistry C* **113**, 3292-3299, (2009).
128 Myers, A. L. & Prausnitz, J. M. Thermodynamics of mixed-gas adsorption. *AIChE Journal* **11**, 121-127, (1965).
129 Cessford, N. F., Seaton, N. A. & Düren, T. Evaluation of Ideal Adsorbed Solution Theory as a Tool for the Design of Metal–Organic Framework Materials. *Industrial & Engineering Chemistry Research* **51**, 4911-4921, (2012).
130 Kim, H. *et al.* Effective CO_2 and CO Separation Using [M_2(DOBDC)] (M = Mg, Co, Ni) with Unsaturated Metal Sites and Excavation of Their Adsorption Sites. *ACS Applied Materials & Interfaces* **11**, 7014-7021, (2019).
131 Karra, J. R. & Walton, K. S. Effect of Open Metal Sites on Adsorption of Polar and Nonpolar Molecules in Metal−Organic Framework Cu-BTC. *Langmuir* **24**, 8620-8626, (2008).
132 Szanyi, J., Daturi, M., Clet, G., Baer, D. R. & Peden, C. H. F. Well-studied Cu-BTC still serves surprises: evidence for facile Cu^{2+}/Cu^{+} interchange. *Physical Chemistry Chemical Physics* **14**, 4383-4390, (2012).
133 St Petkov, P. *et al.* Defects in MOFs: A thorough characterization. *ChemPhysChem* **13**, 2025-2029, (2012).
134 Hou, X.-J., Li, H. & He, P. Theoretical investigation for adsorption of CO_2 and CO on MIL-101 compounds with unsaturated metal sites. *Computational and Theoretical Chemistry* **1055**, 8-14, (2015).
135 Horcajada, P. *et al.* Flexible Porous Metal-Organic Frameworks for a Controlled Drug Delivery. *Journal of the American Chemical Society* **130**, 6774-6780, (2008).
136 Wang, B., Cote, A. P., Furukawa, H., O'Keeffe, M. & Yaghi, O. M. Colossal cages in zeolitic imidazolate frameworks as selective carbon dioxide reservoirs. *Nature* **453**, 207-211, (2008).
137 Prakash, M., Sakhavand, N. & Shahsavari, R. H_2, N_2, and CH_4 Gas Adsorption in Zeolitic Imidazolate Framework-95 and -100: Ab Initio Based Grand Canonical Monte Carlo Simulations. *The Journal of Physical Chemistry C* **117**, 24407-24416, (2013).
138 Canivet, J., Fateeva, A., Guo, Y., Coasne, B. & Farrusseng, D. Water adsorption in MOFs: fundamentals and applications. *Chemical Society Reviews* **43**, 5594-5617, (2014).
139 Kizzie, A. C., Wong-Foy, A. G. & Matzger, A. J. Effect of Humidity on the Performance of Microporous Coordination Polymers as Adsorbents for CO_2 Capture. *Langmuir* **27**, 6368-6373, (2011).
140 Liu, J. *et al.* CO_2/H_2O Adsorption Equilibrium and Rates on Metal−Organic Frameworks: HKUST-1 and Ni/DOBDC. *Langmuir* **26**, 14301-14307, (2010).
141 Liu, J., Tian, J., Thallapally, P. K. & McGrail, B. P. Selective CO2 Capture from Flue Gas Using Metal–Organic Frameworks—A Fixed Bed Study. *Journal of Physical Chemistry C* **116**, 9575-9581, (2012).

142 Zang, J., Nair, S. & Sholl, D. S. Prediction of Water Adsorption in Copper-Based Metal–Organic Frameworks Using Force Fields Derived from Dispersion-Corrected DFT Calculations. *Journal of Physical Chemistry C* **117**, 7519-7525, (2013).
143 Grajciar, L., Bludský, O. & Nachtigall, P. Water Adsorption on Coordinatively Unsaturated Sites in CuBTC MOF. *Journal of Physical Chemistry Letters* **1**, 3354-3359, (2010).
144 Zuluaga, S. *et al.* Understanding and controlling water stability of MOF-74. *Journal of Materials Chemistry A* **4**, 5176-5183, (2016).
145 DeCoste, J. B. *et al.* The effect of water adsorption on the structure of the carboxylate containing metal–organic frameworks Cu-BTC, Mg-MOF-74, and UiO-66. *Journal of Materials Chemistry A* **1**, 11922-11932, (2013).
146 Han, S. S., Choi, S.-H. & van Duin, A. C. T. Molecular dynamics simulations of stability of metal-organic frameworks against H_2O using the ReaxFF reactive force field. *Chemical Communications* **46**, 5713-5715, (2010).
147 Tan, K. *et al.* Water interactions in metal organic frameworks. *CrystEngComm* **17**, 247-260, (2015).
148 Remy, T. *et al.* Selective Dynamic CO_2 Separations on Mg-MOF-74 at Low Pressures: A Detailed Comparison with 13X. *Journal of Physical Chemistry C* **117**, 9301-9310, (2013).
149 Schoenecker, P. M., Carson, C. G., Jasuja, H., Flemming, C. J. J. & Walton, K. S. Effect of Water Adsorption on Retention of Structure and Surface Area of Metal–Organic Frameworks. *Industrial & Engineering Chemistry Research* **51**, 6513-6519, (2012).
150 Tan, K. *et al.* Water Reaction Mechanism in Metal Organic Frameworks with Coordinatively Unsaturated Metal Ions: MOF-74. *Chemistry of Materials* **26**, 6886-6895, (2014).
151 Liu, J. *et al.* Stability Effects on CO2 Adsorption for the DOBDC Series of Metal–Organic Frameworks. *Langmuir* **27**, 11451-11456, (2011).
152 Sun, L., Miyakai, T., Seki, S. & Dincă, M. Mn_2(2,5-disulfhydrylbenzene-1,4-dicarboxylate): A Microporous Metal–Organic Framework with Infinite (−Mn–S−)∞ Chains and High Intrinsic Charge Mobility. *Journal of the American Chemical Society* **135**, 8185-8188, (2013).
153 McDonald, T. M. *et al.* Capture of Carbon Dioxide from Air and Flue Gas in the Alkylamine-Appended Metal–Organic Framework mmen-Mg_2(dobpdc). *Journal of the American Chemical Society* **134**, 7056-7065, (2012).
154 Jiao, Y. *et al.* Tuning the Kinetic Water Stability and Adsorption Interactions of Mg-MOF-74 by Partial Substitution with Co or Ni. *Industrial & Engineering Chemistry Research* **54**, 12408-12414, (2015).
155 Burtch, N. C., Jasuja, H. & Walton, K. S. Water Stability and Adsorption in Metal–Organic Frameworks. *Chemical Reviews* **114**, 10575-10612, (2014).
156 Cychosz, K. A. & Matzger, A. J. Water Stability of Microporous Coordination Polymers and the Adsorption of Pharmaceuticals from Water. *Langmuir* **26**, 17198-17202, (2010).
157 Wu, T. *et al.* Enhancing the stability of metal-organic frameworks in humid air by incorporating water repellent functional groups. *Chemical Communications* **46**, 6120-6122, (2010).
158 Jo, H. *et al.* Fine-Tuning of the Carbon Dioxide Capture Capability of Diamine-Grafted Metal–Organic Framework Adsorbents Through Amine Functionalization. *ChemSusChem* **10**, 541-550, (2017).

159 Decoste, J. B., Peterson, G. W., Smith, M. W., Stone, C. A. & Willis, C. R. Enhanced Stability of Cu-BTC MOF via Perfluorohexane Plasma-Enhanced Chemical Vapor Deposition. *Journal of the American Chemical Society* **134**, 1486-1489, (2012).
160 Tan, Y.-X., He, Y.-P. & Zhang, J. Tuning MOF Stability and Porosity via Adding Rigid Pillars. *Inorganic Chemistry* **51**, 9649-9654, (2012).
161 Silva, B. *et al.* H_2 purification by pressure swing adsorption using CuBTC. *Separation and Purification Technology* **118**, 744-756, (2013).

Chapter 3 Dynamic adsorption measurement techniques

3.1 Introduction

The performance of an adsorbent for dynamic separation of gas mixtures must be evaluated using dynamic adsorption measurement techniques. While single component equilibrium adsorption measurements provide useful information regarding adsorption capacity and theoretical selectivity, it is unable to accurately evaluate the separation performance of gas mixtures. Furthermore, kinetic data from dynamic measurements provides crucial information regarding the mass transfer of adsorption separation processes.

This chapter presents the background and theory of the two dynamic measurement techniques used in this study. Flux response technology was used for a high throughput screening procedure to identify the most promising MOFs for CO/N_2 separation. For measuring the CO/N_2 separation performance, a breakthrough column was employed with $CO:N_2$ mixture streams, which was also modified for diffusivity calculations.

3.2 Flux response technology

3.2.1 *Background*

Flux response technology (FRT) is an *in-situ* measurement technique that has mainly been used as a catalyst characterisation tool.[1] The instrument was initially built to be able to analyse a catalyst *in-situ* on the FRT instrument, instead of performing *ex-situ* analysis by comparing characterisation results before and after adsorption.

The concept of flux response was first explored for sorption-effect chromatography by monitoring the flow-rates after gas injection to probe the void space in the column.[2-4] Since then, FRT has been developed and employed for investigating catalytic reaction mechanisms[5-7] and kinetic data,[8-10] perturbation viscometry,[11-16] adsorption capacity[1,10] and surface area measurements.[1] FRT is a versatile technique capable of multiple applications, highlighted in studies presenting adsorption capacity and surface area measurements.[1] The functionality of FRT was also demonstrated with CO_2 diffusivity and adsorption capacity measurements.[10]

In the scope of this study, the application of FRT for dynamic adsorption capacity measurements. This technique provides high throughput screening for MOF performance with a small amount of material,[1] a useful advantage to possess when considering small scales of MOF synthesis. Here the theory and experimental procedure for dynamic capacity measurements on the FRT instrument are presented.

3.2.2 *Dynamic capacity measurements theory*

Adsorption capacity measurements through FRT are based on the pressure changes of the system. As adsorption takes place, the pressure of the system reduces and the flux response detected is attributed to the adsorption, and the reverse is true for desorption taking place.

An FRT experimental set-up replicates that of an electrical Wheatstone bridge assembly, where a system side and reference side are used as different legs of the bridge (Figure 3-1). The gas molecules represent electrons from the electrical configuration and the capillaries upstream and downstream represent the resistors.

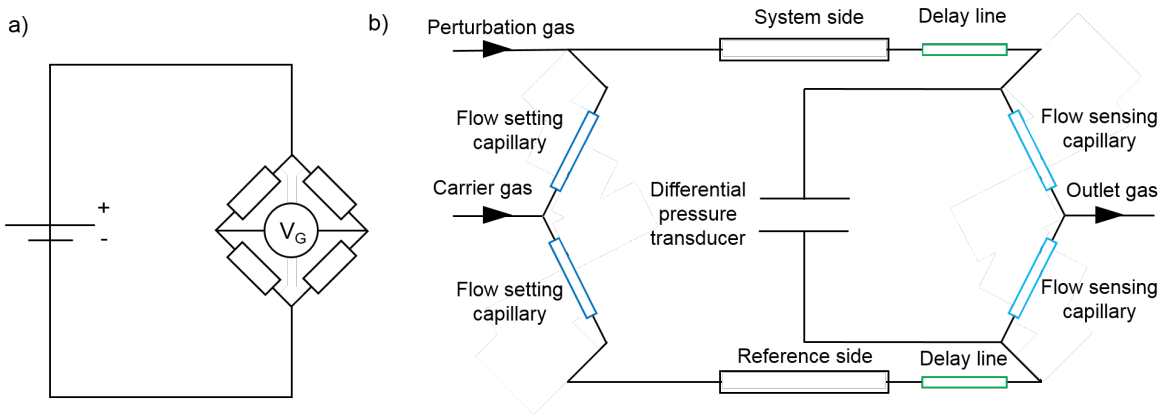


Figure 3-1. Schematic of the experimental configuration of flux response technology for an (a) electric Wheatstone bridge assembly and (b) pneumatic Wheatstone bridge assembly.

The perturbation gas entering the system side causes an imbalance of the bridge assembly due to pressure fluctuations from changes in flowrate and volume. The pressure difference between the system and reference sides are measured using a differential pressure transducer (DPT) and relays the signal as a change in voltage. The DPT can measure changes in flow-rates as small as 10^{-2} μL min^{-1}. A schematic of the FRT instrument is shown in Figure 3-2.

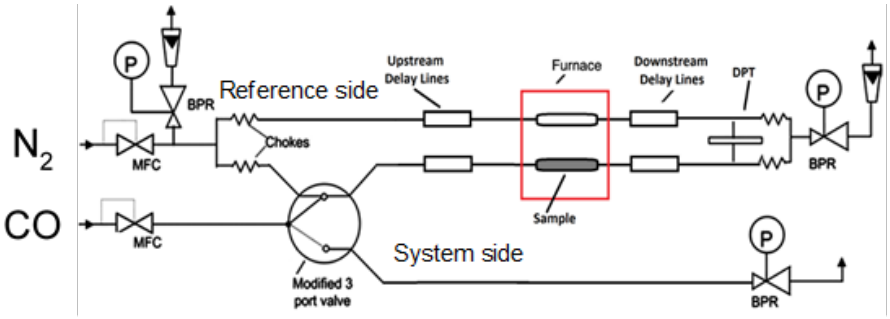


Figure 3-2. Schematic of flux response technology instrument for dynamic CO adsorption measurements. MFC = Mass-flow controller; BPR = Back-pressure regulator; DPT = Differential pressure transducer.

The flow setting capillaries (upstream) are set to provide a large pressure drop across these capillaries to ensure the carrier gas flow-rate is equal across both bridges to fix the pressure and flow-rate. The flow sensing capillaries (downstream) are set to provide a low pressure drop so that any small changes in pressure caused by perturbation are detected clearly by the DPT, as the pressure changes are minuscule in comparison the pressure of the system. The delay lines in the instrument extends the path length, delaying the DPT response time for clear resolution of the adsorption peak.

At the beginning of the measurement, a baseline is established with minimal pressure difference across the bridge, illustrated at t_1 in an example FRT profile in Figure 3-3. Upon switching to the perturbation gas (t_2), the DPT detects an instantaneous imbalance across the bridge because of the flow-rate and pressure change. A new baseline is established (t_2), and t_2-t_3 is the duration taken for the perturbation gas to travel to the sample in the system side.

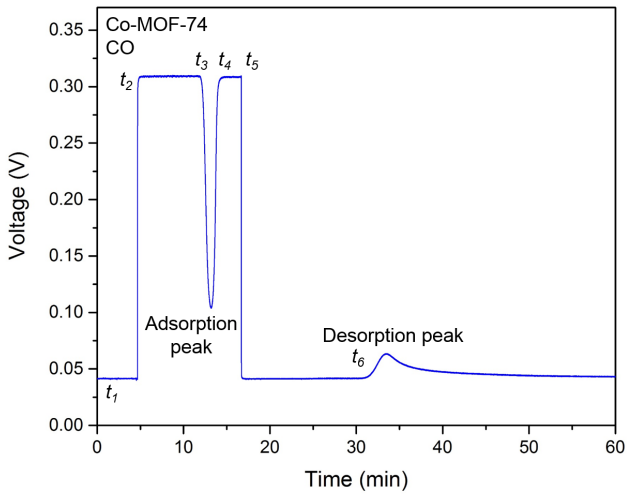


Figure 3-3. Flux response technology experimental profile of Co-MOF-74 (50:50 *v:v* CO:N_2) at 25 °C and 1 bar.

Upon adsorption taking place, a pressure drop occurs which results in a reduction in flow-rate and is relayed as an adsorption peak signal by the DPT (t_3-t_4). The signal returns back to the new baseline after saturation and the perturbation gas is switched off (t_5), resulting in a decrease in flow-rate and a return to the original baseline. The carrier gas induces desorption and a peak is observed because of the small increase in flow-rate from bound molecules desorbing (t_6). The desorption peak is broad in because of the difficulty in removing strongly bound molecules.

To analyse the flux response curve, both differential or integral analysis can be employed. Differential analysis is used when the Δp is very small, as observed in perturbation viscometry. During adsorption, integral analysis is employed because the flux response is large and finite perturbation is assumed while the viscosity remains unchanged. The pressure drop resulting from adsorption can be expressed using Hagen-Poiseuille's Law, which assumes the flow is laminar, viscous and incompressible.

$$\frac{dp_z}{dz} = -K_c \mu Q \quad (3\text{-}1)$$

Where p_z = change in pressure along distance (z) for a laminar flow, K_c = tube constant, μ = viscosity and Q = volumetric flow-rate.

When Eq 3-1 is combined with the assumptions of an ideal gas (Eq 3-2), the longitudinal pressure gradient is expressed as Eq 3-3:

$$Q = \frac{MRT}{p_z} \quad (3\text{-}2)$$

$$p_z \frac{dp_z}{dz} = -K_c \mu MRT \quad (3\text{-}3)$$

Where M = molar flow-rate, T = absolute temperature (in K), R = universal gas constant.

At low pressure, the viscosity of the gas is dependent on the temperature and independent of pressure. Therefore, pressure remains constant in Eq 3-3, and it is assumed temperature is constant, with factors providing Eq 3-4.

$$p_0^2 - P_{BPR}^2 = 2K\mu MRT \quad (3\text{-}4)$$

Where p = inlet pressure of the downstream flow detecting capillary at t_0, P_{BPR} = outlet pressure of the downstream flow detecting capillary and $K = K_c L$, where L = tube length.

With the assumption of small and finite perturbation, pressure increases to p_1 and the flow-rate increases to $M + m$. Changes in μ are negligible at this stage because of the extended path length of the delay lines providing a large system volume.

$$p_1^2 - P_{BPR}^2 = 2K\mu(M+m)RT \quad (3\text{-}5)$$

Subtracting Eq 3-4 from Eq 3-5 provides Eq 3-6.

$$P_1^2 - P_0^2 = 2K\mu mRT \quad (3\text{-}6)$$

Which can be factorised to Eq 3-7.

$$(p_1 - p_0)(p_1 + p_0) = 2K\mu mRT \quad (3\text{-}7)$$

Once the gas has travelled along the delay line and reaches the flow sensing capillaries, the pressure rises to p_2 because of a viscosity change ($\mu+\Delta\mu$).

$$p_2^2 - P_{BPR}^2 = 2K(\mu + \Delta\mu)(M+m)RT \quad (3\text{-}8)$$

Repeating the same procedure for producing Eq 3-7 using Eq 3-8 and Eq 3-5 provides Eq 3-9.

$$(p_2 - p_1)(p_2 + p_1) = 2K\Delta\mu(M+m)RT \quad (3\text{-}9)$$

Dividing Eq 3-9 by Eq 3-7 provides Eq 3-10.

$$\left(\frac{p_2-p_1}{p_1-p_0}\right)\left(\frac{p_2+p_1}{p_1+p_0}\right) = \left(\frac{M+m}{m}\right)\left(\frac{\Delta\mu}{\mu}\right) = R_{pert} \quad (3\text{-}10)$$

Where R_{pert} = ratio of the added perturbation gas.

It is assumed that the pressure differences (p_2-p_1 and p_1-p_0) are negligible relative to the pressure of the Wheatstone bridge system, therefore the ratio of the pressure changes ((p_2+p_1)/(p_1+p_0)) is considered unity, providing Eq 3-11.

$$\frac{p_2-p_1}{p_1-p_0} = \left(\frac{M+m}{m}\right)\left(\frac{\Delta\mu}{\mu}\right) = R_{pert} \quad (3\text{-}11)$$

The perturbation gas is denoted as species *i*, and the carrier gas is absent here. The mole fraction (X_i) is expressed below:

$$X_i = \frac{m}{M+m} \quad (3\text{-}12)$$

Therefore the number of moles adsorbed is shown to be proportional to the changes in flow-rate and pressure. Using this relationship, the integrated area of the adsorption peak in the FRT profile (Figure 3-3) is proportional to the number of moles adsorbed.

Peak integration was performed with aid of the curve fitting tool on Origin, and the peak area was subtracted from an area of the graph with a known quantity of flowing adsorbate moles after perturbation. The subtracted area provided the number of adsorbed moles from which the dynamic adsorption capacity could be determined. Depending on the interactions between the perturbation gas and the adsorbent, larger adsorption capacity resulted in larger pressure changes and peak area.

3.2.3 *Dynamic capacity measurements experimental*

For dynamic adsorption capacity measurements, in the context of this thesis, samples (~40 mg of dry sample) were sieved (80–120 *μm* size fraction) and loaded in a 4 mm ID quartz tube and packed using quartz wool. The column was pressurised and

sample activation was performed by flowing N_2 (10 mL min^{-1}) for 16 h and setting the temperature controller of the furnace to the desired activation temperature (indicated in the Section 5.2).

For analysis, the CO perturbation and N_2 carrier gas flow rates were set to 5 and 10 mL min^{-1}, controlled by Bronkhorst mass-flow controllers. The CO perturbation gas was switched using the 3-port valve and the differential pressure between the system and reference side was measured using a differential pressure transducer (manufactured by Furness Controls, model R.S.N 9411283), with data acquisition using a Data/Shuttle USB 54 system. 1/4" OD PFA tubing was used for the delay lines.

An adsorption peak was recorded along the new baseline due to the pressure response upon adsorption. After equilibration, the system side flow-rate was measured using a bubble flow-meter, and the CO perturbation gas was then switched off to induce desorption. An example of an FRT profile is shown in Section 3.2.2. The standard deviation for measurements on the instrument is ±5%, and error also arises from experimental variance of the MOF synthesis.

3.3 Breakthrough column analysis

3.3.1 *Background*

While FRT measures the adsorbent's dynamic capacity, its dynamic separation performance can be evaluated using a breakthrough column apparatus.[17,18] The breakthrough column represents a fixed-bed adsorption column used in a separation process and the response profile of this step input is the breakthrough curve (Figure 3-4).

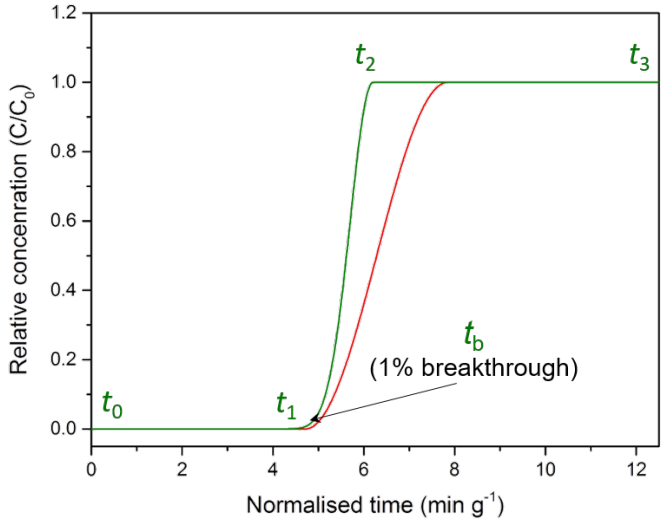


Figure 3-4. Example single component breakthrough curve profile of adsorbates exhibiting fast (green) and slow (red) sorption kinetics.

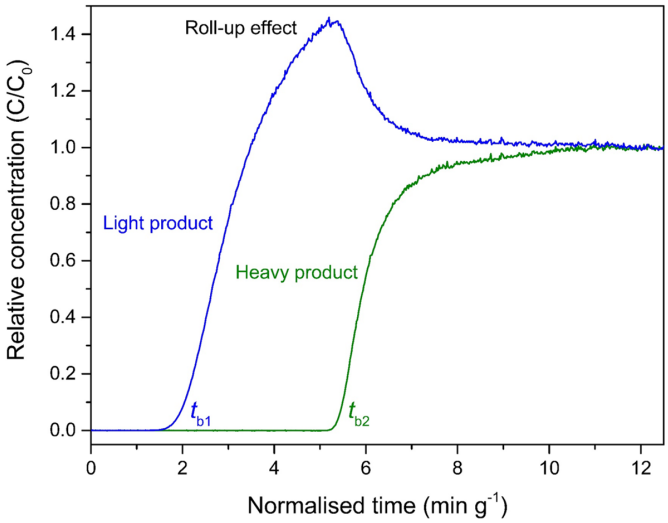


Figure 3-5. Example binary breakthrough curve profile of adsorbates with high (green) and low (blue) affinity to the adsorbate with differing breakthrough times (t_{b1} and t_{b2}).

Breakthrough measurements of one absorbable species with an inert carrier enables dynamic capacity measurements.[19,20] However, measurements with binary[21-27] and multi-component[28-30] gas mixtures of adsorbable species enable separation and selectivity measurements that replicate industrial conditions. The macroscopic conditions associated with industrial gas separation processes such as mass transfer, competitive adsorption, pressure and temperature changes are reflected more

accurately with dynamic breakthrough measurements than equilibrium based static measurements. Dynamic capacity measurements with varying levels of humidity have also been performed to explore the stability of MOF performance in the presence of water vapour.[31-33] Fundamental studies of breakthrough column measurements have investigated methods of improving the accuracy and reliability of measurements.[34-36] Computational studies have been performed to model the separation process to simulate a PSA system, using experimental data for validation.[28,37,38]

This study focusses on binary and multi-components gas separation measurements, recording breakthrough time, capacity and selectivity. The effect of varying the feed concentrations and impurity level was investigated, and the apparatus and experimental procedure was adapted for diffusivity measurements. Here the theory and experimental procedure for dynamic separation measurements on the breakthrough instrument and its modifications for diffusivity measurements are presented.

3.3.2 *Dynamic separation and breakthrough capacity measurements*

3.3.2.1 Theory

A breakthrough curve is an effluent adsorptive concentration profile detected at the outlet of an adsorbent bed recorded as a function of time (Figure 3-4). Breakthrough (t_1) occurs when the adsorbent bed becomes saturated with the adsorbate. Equilibrium is reached when the outlet concentration equals the inlet concentration (t_2-t_3 region). The main factor that governs the breakthrough time is the sorbent capacity, however numerous other kinetic and thermodynamic factors affect this measurement such as mass transfer, heat of adsorption, sorption rate and gas velocity. For binary or multicomponent gas mixtures, selectivity becomes a major factor. Therefore,

breakthrough time is a useful metric as a measurement of both sorption capacity and selectivity of an adsorbent.

The area above the breakthrough curve is proportional to the adsorption capacity at the time measured. The unsaturated zone lies at t_0-t_1, which is where the majority of the adsorption occurs. This zone represents the usable sorption capacity for a dynamic separation process. The mass transfer zone lies between t_1 *and* t_2 and provides kinetic information, governed by the diffusion rate and heat transfer. At t_2, the adsorbent bed is saturated and the saturation capacity (adsorption uptake when $C=C_0$ with the inlet feed) is measured at this point.

The 1% breakthrough capacity (t_b), adsorption uptake when $C/C_0 = 0.01$, is used as the dynamic capacity. An industrial adsorption cycle does not reach equilibrium and saturation capacity, and therefore breakthrough capacity is a more useful metric. Breakthrough capacity values close to the saturation capacity are favoured to maximise the usable sorption capacity, and this would be reflected with steep breakthrough curves with a small mass transfer zone (green curve in Figure 3-4). Slower sorption kinetics (red curve in Figure 3-4) result in longer cycle times and reduced breakthrough capacities. In binary breakthrough measurements (Figure 3-5), competitive adsorption of the two adsorbates result in differing breakthrough times based on their selectivity and capacity. This competitive binding also results in an overshot peak of the light product, which is known as a roll-up effect, due to the heavy product displacing the light product.

The adsorption capacity is determined by using a material balance calculation of the adsorbate in the packed column. While equations have been used to account for the pressure drop across the column,[39,40] numerous studies have ignored this and

deemed the pressure drop negligible.[35,41-43] As the pressure drop is small (less than 0.05 bar) and deemed negligible for our experimental set-up with the small amount of sample at atmospheric pressure, a material balance equation based from literature[17,18,41,42] was used for calculations for our experimental set-up (Eq 3-13), with the column's parameters illustrated in Figure 3-6.

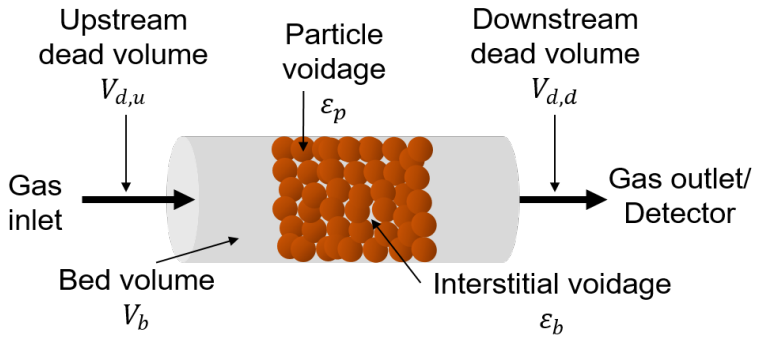


Figure 3-6. Schematic of breakthrough column.

$$\{V_{d,u} + V_{d,d} + V_b[\varepsilon_b + (1-\varepsilon_b)\varepsilon_p]\}c_t y_a + m_b q_a = \int_0^\infty (\dot{n}_i y_a - \dot{n}_o y_{a,o})dt \quad (3\text{-}13)$$

Where

$V_{d,u}$ Dead volume in the upstream pipework (m^3)

$V_{d,d}$ Dead volume in the downstream pipework (m^3)

V_b Volume of the bed containing the adsorbent (m^3)

ε_b Total interstitial voidage between the adsorbent particles of the bed (-)

ε_p Voidage inside the adsorbent particles (-)

c_t Total gas molar concentration (mol m^{-3})

m_b Mass of adsorbent within the bed (kg)

q_a Amount of adsorbate adsorbed on the surface of the adsorbent (mol kg^{-1})

y_a Mole fraction of adsorbate in the feed gas (-)

$y_{a,\,o}$ Mole fraction of adsorbate detected at the outlet (-)

$\dot{n}_i$ Molar flow of gas fed into the bed (mol min^{-1})

$\dot{n}_o$ Molar flow of gas out of the bed (mol min^{-1})

t Time (min)

An accurate measurement of the dead volume of the system ($V_{d,u}$, $V_{d,d}$, V_b) is required and material balance accounts for this (Eq 3-13). Therefore, a material balance using an inert gas is required for the dead volume measurement. It is assumed helium does not interact with the adsorbent and that the response time at the outlet is negligible compared to the duration of the breakthrough experiment.

Material balance of helium for the columns parameters (Figure 3-6) is shown in Eq 3-13 and substituted and rearranged into Eq 3-14 to provide Eq 3-15

$$\{V_{d,u} + V_{d,d} + V_b[\varepsilon_b + (1-\varepsilon_b)\varepsilon_p]\}c_t y_{\text{He}} = \int_0^{\infty}(\dot{n}_i y_{\text{He}} - \dot{n}_o y_{\text{He},o})dt \quad (3\text{-}14)$$

Where

y_{He} Mole fraction of helium in the feed gas (-)

$y_{\text{He},o}$ Mole fraction of helium detected at the outlet (-)

$$SC_{\text{a}} = \frac{\dot{n}_o y_a}{m_b}\int_{\text{t=0}}^{t_{at}\, y_{a,o}=y_a}\left(\frac{y_{\text{He},o}}{y_{\text{He}}} - \frac{y_{\text{a},o}}{y_a}\right)dt \quad (3\text{-}15)$$

Where SC_{a} = total adsorption uptake of the adsorbate when the feed and effluent flow-rates and compositions are equal at the outlet ($y_{a,\,o} = y_a$).

If the molar flow-rate of the adsorbate at the outlet cannot be measured, an approximation of the overall material balance (Eq 3-16) can be applied to Eq 3-15 to provide Eq 3-17.

$$\dot{n}_o \approx \dot{n}_i \frac{(1-y_a)}{(1-y_{a,o})} \quad (3\text{-}16)$$

$$SC_{\text{a}} = \frac{\dot{n}_i y_a}{m_b}\int_{\text{t=0}}^{t_{at}\, y_{a,o}=y_a}\frac{(1-y_{\text{a}})}{(1-y_{\text{a},o})}\left(\frac{y_{\text{He},o}}{y_{\text{He}}} - \frac{y_{\text{a},o}}{y_a}\right)dt \quad (3\text{-}17)$$

The breakthrough capacity (BC_a) was calculated at 1% breakthrough, when $\frac{y_{a,\,o}}{y_a}$ = 0.01 at the outlet, using the following equation:

$$BC_{\mathrm{a}} = \frac{\dot{n}_o y_{\mathrm{a}}}{m_b} \int_0^{t_{at}\,\frac{y_{\mathrm{a},\,o}}{y_a}=0.01} \left(\frac{y_{\mathrm{He},o}}{y_{\mathrm{He}}} - \frac{y_{\mathrm{a},o}}{y_a}\right) dt \quad (3\text{-}18)$$

The overall material balance (Eq 3-16) can also be applied to Eq 3-18 to produce the breakthrough capacity equivalent of Eq 3-17.

The adsorbate (*a*) can represent any gas species (a_1, a_2, a_3) which can be applied to ideal selectivity and separation factor calculations, which are important factors to consider for gas separation measurements using a breakthrough column.

Ideal selectivity (*IS*) at equilibrium was calculated using the following:

$$\mathrm{IS} = \frac{SC_{a_1}}{SC_{a_2}} \quad (3\text{-}19)$$

Separation factor (*SF*) was calculated using the following:

$$\mathrm{SF} = \frac{SC_{a_1} \big/ y_{a_1}}{SC_{a_2} \big/ y_{a_2}} \quad (3\text{-}20)$$

3.3.2.2 Experimental

The apparatus schematic and images of the home-built breakthrough column system are shown in Figure 3-7 and Figure 3-8, and the experimental procedure is outlined below.

Samples (~200 mg) were sieved (80–120 *μm* size fraction) and were loaded in a 4 mm ID quartz tube and packed using quartz wool. After loading the packed tube and pressurising the system (1 bar gauge pressure), sample activation was performed by flowing He (20 mL min^{-1}) for 16 h at the desired conditions using heating tape (Omega;

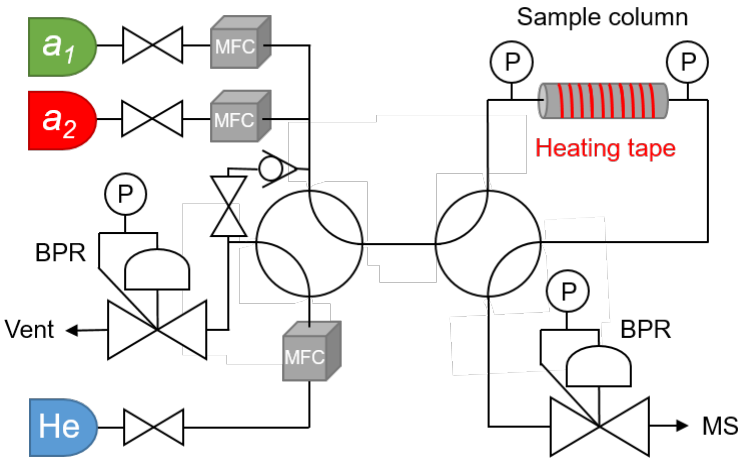


Figure 3-7. Schematic of breakthrough adsorption column instrument for CO/N_2 separation measurements. *a* = adsorbates, MFC = Mass-flow controller; BPR = Back-pressure regulator; MS = Mass spectrometer.

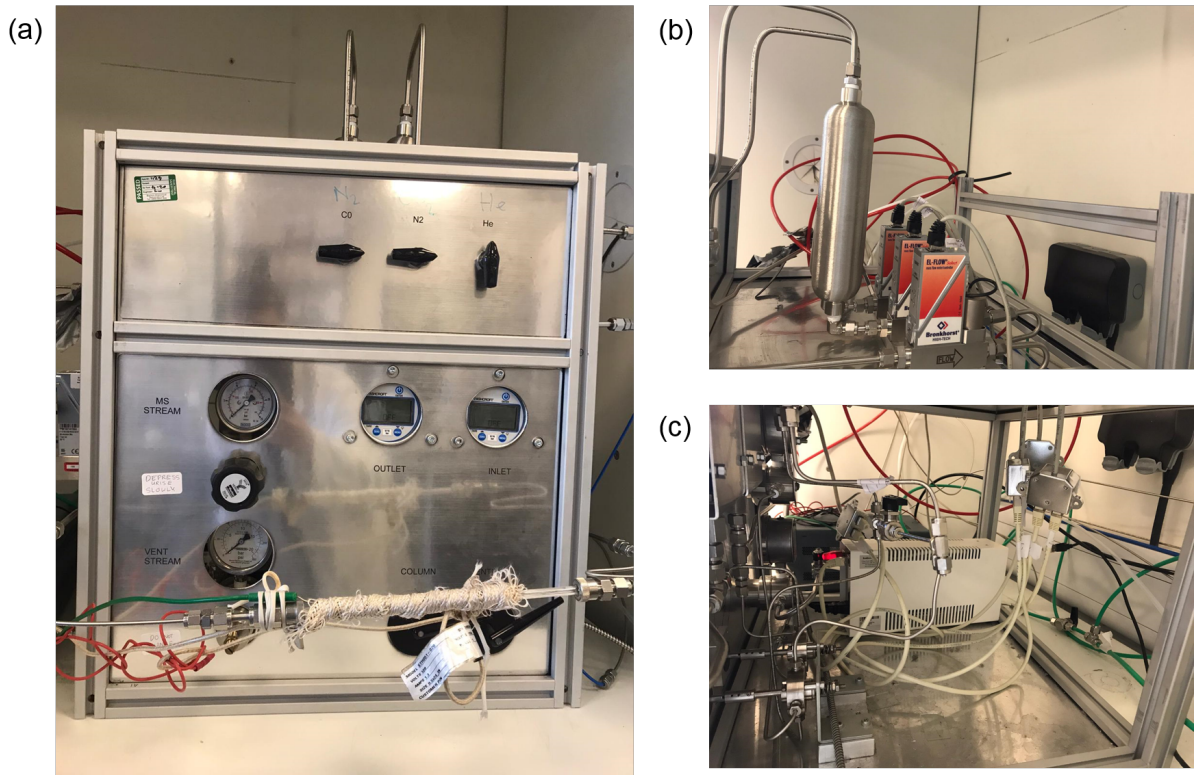


Figure 3-8. Images of the breakthrough adsorption column instrument for CO/N_2 separation measurements. (a) Front-view image displaying the column, back-pressure regulators, gauges and switches. (b) Side-view image displaying the mass-flow controllers and inlet gases. (c) Side-view image displaying power supply and the tubing from the inlet to the four-port switch valves to the outlet.

activation temperature indicated in Section 5.2), controlled by a temperature probe (RS components) and a Proportional-Integral-Derivative (PID) controller.

For analysis, the volumetric flow-rates (total flow rate of 20 mL min^{-1}) were set for the desired single component or binary mixture composition, and a back-pressure regulator was used to control and pressurise the column. The inlet flow-rates were controlled by Bronkhorst mass-flow controllers and the outlet flow-rate was monitored by a Bronkhorst mass-flow meter. The four-port switch valve was switched to send the single component or binary mixture to the sample column before reaching the MS detector at the outlet. Analysis of the outlet feed concentration was performed by an ESS GeneSys quadruople Mass Spectrometer (MS) 200, with data acquisition using a Quadstar 32-bit software. Digital pressure gauges at the inlet and outlet were used to monitor the pressure of the column. Hexagonal boron nitride (Saint Gobain, Tres BN) was used as a non-porous and non-adsorbing material to measure the dead volume of the instrument using He.

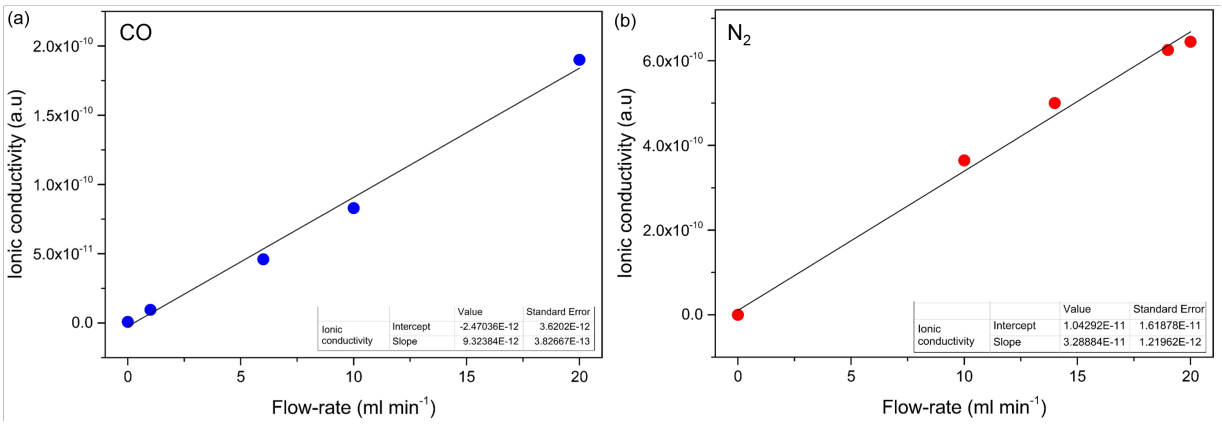


Figure 3-9. Calibration curves of the mass-spectrometer ionic conductivity signals relative to the inlet gas adsorbate flow rates of CO (left) and N_2 (right).

Before the breakthrough measurements, the ionic conductivity signal of the MS was recorded for each adsorbate MS peak signal and set as 0 ml min^{-1} for normalisation.

After breakthrough and saturation of the adsorbates (where inlet flow-rate = outlet flow-rate), the ionic conductivity signal for each adsorbate was recorded and set as the inlet flow-rate for each adsorbate, based off the total flow-rate and mole fractions used for the measurement. As the ionic conductivity signal has a linear relationship to the flow-rates measured, shown in the calibration curves in Figure 3-9, the MS signal was used to determine the breakthrough curves flow-rates and concentrations.

The breakthrough curves were normalised to eliminate the inlet dead volume time, so the plotted curves are a direct reflection of dynamic adsorption of the given sample. The relative concentration, C/C_0, on the *y*-axis was standardised to the mole fractions of the inlet feed. The standard deviation for measurements on the instrument is ±5%, and error also arises from experimental variance of the MOF synthesis.

3.3.3 *Diffusivity measurements*

Kinetic data can be extracted from breakthrough curve such as the diffusion rates and mass transfer during adsorption. The zero-length column (ZLC) method monitors the decay curve of the adsorbate concentration upon desorption with an inert carrier gas, developed for measuring diffusion time constants of adsorbates in porous materials.[44-47] The original ZLC model[44] operates on the certain assumptions (outlined in Section 3.3.3.1), and the model has been developed to account for deviations such as adsorbents with non-uniform crystallinity and crystal size distribution,[48] non-linear sorption isotherms[49,50] and variable outlet flow-rates.[51,52]

The breakthrough column was modified for ZLC[8,44] measurements for analysing diffusion coefficients which account for gas mixing. Dispersion and gas mixing that occurs in the system's dead volume makes it difficult to predict its effect in the breakthrough apparatus.[53] When there is significant dead volume, the mixing of the

gases exceeds the spreading of the concentration profile and does not replicate a desired true plug flow system.[36] The mass transfer and diffusion rate is affected by Taylor dispersion[54] of the adsorbate gases at the centre and walls of the tubing in the apparatus.

ZLC measurements to obtain CO and N_2 diffusivity coefficients of the tested MOFs were performed by modifying the breakthrough column and sample loading to replicate a ZLC apparatus.[44,47] While non-linear equilibrium sorption CO isotherms were observed with our MOFs, using the assumptions of the original ZLC method[44] as this has yielded diffusivity coefficients of the same order of magnitude as using a non-linear model.[49] Furthermore, using higher flow-rates of the inert carrier gas minimised the error of the measurements.[50]

3.3.3.1 Theory

The assumptions of the ZLC method[44-47] are as follows: spherical adsorbent particles, uniform crystallinity of the adsorbent, a linear equilibrium sorption isotherm, isothermal conditions, negligible pressure drop, a perfectly mixed gas phase, intracrystalline or microporous diffusion and that the carrier gas flow-rate is equal to the outlet flow-rate and remains constant. These assumptions provides a response curve expressed as the equation below[47]:

$$\frac{c}{c_0} = 2L \sum_{n=1}^{\infty} \frac{\exp\left(-\frac{\beta_n^2 Dt}{R^2}\right)}{[\beta_n^2 + L(L-1)]} \quad (3\text{-}21)$$

Where β_n is given by the roots of:

$$\beta_n \cot \beta_n + L - 1 = 0 \quad (3\text{-}22)$$

$$L = \frac{1}{3}\left(\frac{Fr^2}{KV_s D}\right) \quad (3\text{-}23)$$

c	Concentration of the adsorbate at any time
c_o	Initial concentration of the adsorbate
L	Dimensionless parameter
β_n	Dimensionless parameter
t	Time
F	Flow-rate of inert carrier gas
r	Adsorbent particle radius
K	Henry's constant (dimensionless)
V_s	Crystallographic volume of sample
D	Diffusivity coefficient

At the long time region of the sorption decay curve (Eq 3-21) can be expressed as the equation below, with the decay curve is reduced to the first term:

$$\frac{c}{c_0} = \frac{2L}{[\beta_n^2 + L(L-1)]} \exp\left(-\frac{\beta_n^2 Dt}{R^2}\right) \quad (3\text{-}24)$$

Therefore, the long decay curve can be plotted and can be used to determine the diffusivity coefficient when Eq 3-25 is plotted as *ln(c/c₀)* vs *t*, to provide the intercept (Eq 3-26) and slope (Eq 3-27).

$$ln\left(\frac{c}{c_0}\right) = ln\left(\frac{2L}{[\beta_n^2 + L(L-1)]}\right) - \frac{\beta_n^2 Dt}{R^2} \quad (3\text{-}25)$$

$$Intercept = ln\left(\frac{2L}{[\beta_n^2 + L(L-1)]}\right) \quad (3\text{-}26)$$

$$Slope = -\frac{\beta_n^2 D}{R^2} \quad (3\text{-}27)$$

3.3.3.2 Experimental

The apparatus schematic of the home-built breakthrough column system is shown in Figure 3-7, and the experimental procedure is outlined below. Samples (~30 mg) were sieved (80–120 *μm* size fraction) and were loaded in a 4 mm ID quartz tube and packed tightly using quartz wool. After loading the packed tube and pressurising the

system (1 bar gauge pressure), sample activation was performed by flowing He (15 mL min^{-1}) for 16 h at the desired temperature using heating tape.

For analysis, the adsorbate flow-rate was set to 15 mL min^{-1} and the back-pressure regulator was used to control and pressurise the column. The four-port switch valve was switched to send the single component adsorbate stream to the sample column before reaching the MS detector at the outlet. After breakthrough and saturation of the adsorbent bed (confirmed by monitoring the MS profile), the four-port switch valve was switched back to send the inert helium carrier gas to the column. The resulting desorption was monitored by the MS and mass flow-meter.

The resultant decay curve profile from the mass flow-meter is attributed to the desorption of the adsorbate and used for the graphical plot of Eq 3-25. Figure 3-10 shows the subsequent profiles of the graphs as Eq 3-25 was applied to obtain the diffusivity coefficient. Eq 3-26 and Eq 3-27 were solved analytically using Maple to calculate the diffusivity coefficient (K_D). The script for the software can be found in Appendix 1.

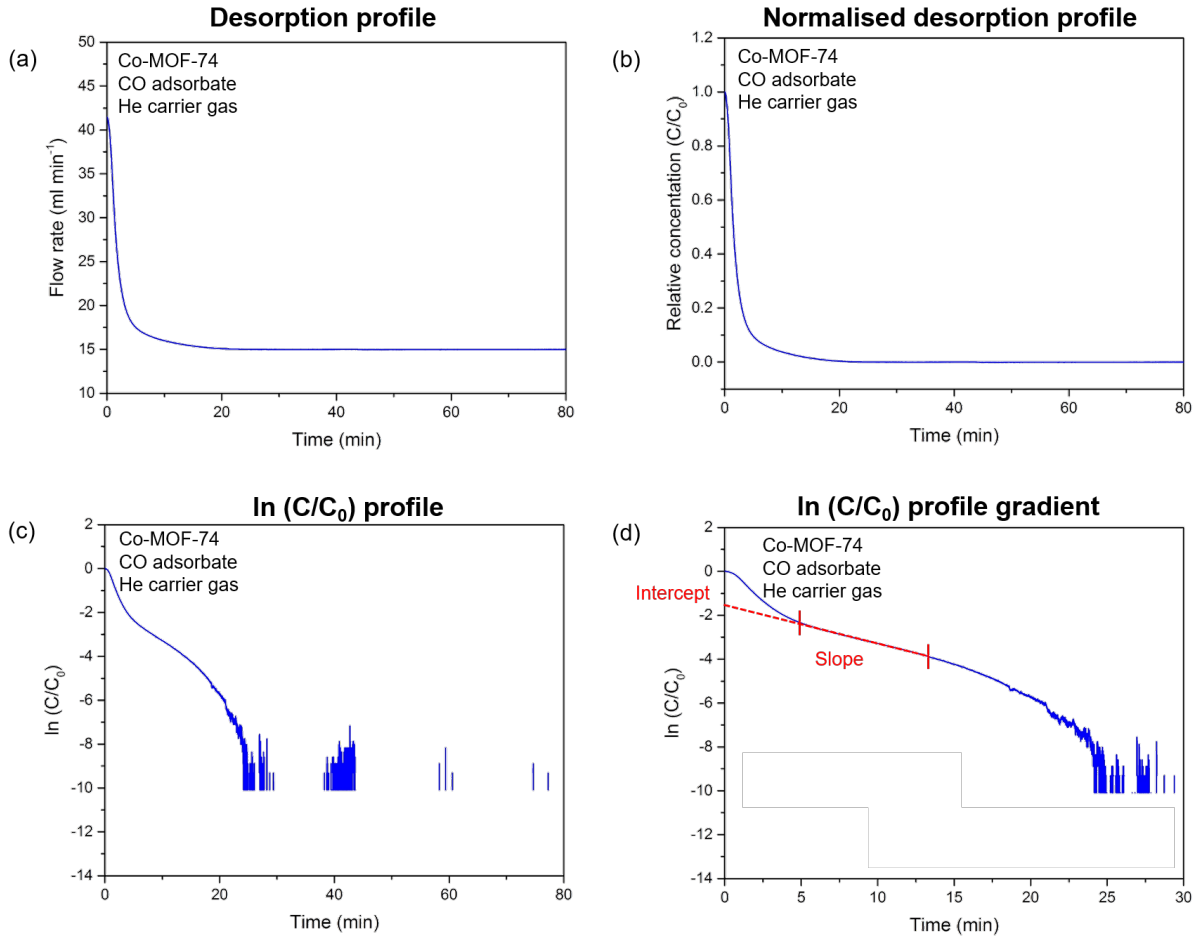


Figure 3-10. Desorption profiles of CO adsorbate with He inert carrier gas (15 mL min^{-1}) for $K_{D,\,CO}$ calculation at 25 °C through using the ZLC method.

3.4 References

1 Palmer, C., Sasegbon, A. & Hellgardt, K. In situ measurement of gas adsorption processes using Flux Response Technology. *Adsorption* **17**, 783-794, (2011).

2 Rathor, M. N., Buffham, B. A. & Mason, G. Determination of the volumes of void zones in packed chromatographic columns. *Journal of Chromatography A* **445**, 37-48, (1988).

3 Buffham, B., Mason, G. & Meacham, R. Sorption-effect chromatography. *Journal of Chromatographic Science* **24**, 265-269, (1986).

4 Buffham, B., Mason, G. & Meacham, R. Absolute gas chromatography. *Proceedings of the Royal Society of London. Series A: Mathematical and Physical Sciences* **440**, 291-301, (1993).

5 Buffham, B. A., Hellgardt, K., Heslop, M. J. & Mason, G. Remote sensing of the flux responses of a gas–solid catalytic micro-reactor. *Chemical Engineering Science* **55**, 1621-1632, (2000).

6 Buffham, B. A., Hellgardt, K., Heslop, M. J., Mason, G. & Richardson, D. J. Modelling and simulation of the flux responses of a gas–solid catalytic micro-reactor. *Chemical Engineering Science* **57**, 953-966, (2002).

7 Richardson, D. J., Hellgardt, K., Russell, P. A., Mason, G. & Buffham, B. A. Flux Response Analysis: A Study of Ammonia Decomposition Over Pt/Alumina. *Chemical Engineering Research and Design* **82**, 1397-1403, (2004).

8 Ruthven, D. M. & Eic, M. in *Perspectives in Molecular Sieve Science* Vol. 368 *ACS Symposium Series* Ch. 22, 362-375 (American Chemical Society, 1988).

9 Maguire, N. *et al.* Using temporal analysis of products and flux response technology to determine diffusion coefficients in catalytic monoliths. *Chemical Engineering Science* **87**, 224-233, (2013).

10 Sasegbon, A. & Hellgardt, K. Flux Response Technology (FRT) Applied in Zero Length Column Diffusivity and Adsorption Measurements. *Transport in Porous Media* **107**, 731-744, (2015).

11 Mason, G., Buffham, B. A., Heslop, M. J. & Zhang, B. Capillary viscometry by perturbation of flow and composition. *Chemical Engineering Science* **53**, 2665-2674, (1998).

12 Mason, G., Buffham, B. A., Heslop, M. J., Russell, P. A., Zhang, B. Perturbation viscometry of gas mixtures. Addition and removal of finite perturbations. *Chemical Engineering Science* **55**, 5747-5754, (2000).

13 Russell, P. A., Buffham, B. A., Mason, G. & Hellgardt, K. Measurement of the gradient of viscosity with composition of mixtures of non-ideal gases. *Chemical Engineering Science* **61**, 6604-6615, (2006).

14 Russell, P. A., Buffham, B. A., Mason, G., Richardson, D. J. & Heslop, M. J. Perturbation viscometry measurement of viscosity ratios for ternary gas mixtures and quantification of the errors. *Fluid Phase Equilibria* **215**, 195-205, (2004).

15 Russell, P. A., Buffham, B. A., Mason, G. & Heslop, M. J. The effect of very large perturbation flows on a perturbation viscometer. *Chemical Engineering Science* **60**, 2943-2954, (2005).

16 Richardson, D. J. *et al.* Viscosity of Binary Mixtures of Carbon Monoxide and Helium. *Journal of Chemical & Engineering Data* **53**, 303-306, (2008).

17 Helfferich, F. G. & Ruthven, D. M. Principles of adsorption & adsorption processes, by D. M. Ruthven, John Wiley & Sons, 1984, xxiv + 433 pp. *AIChE Journal* **31**, 523-524, (1985).

18 Yang, R. T. in *Gas Separation by Adsorption Processes* (ed Ralph T. Yang) 141-200 (Butterworth-Heinemann, 1987).

19 Britt, D., Tranchemontagne, D. & Yaghi, O. M. Metal-organic frameworks with high capacity and selectivity for harmful gases. *Proceedings of the National Academy of Sciences* **105**, 11623-11627, (2008).

20 Peterson, G. W., DeCoste, J. B., Fatollahi-Fard, F. & Britt, D. K. Engineering UiO-66-NH2 for Toxic Gas Removal. *Industrial & Engineering Chemistry Research* **53**, 701-707, (2014).

21 Li, Y.-X. *et al.* Controlled Construction of Cu(I) Sites within Confined Spaces via Host–Guest Redox: Highly Efficient Adsorbents for Selective CO Adsorption. *ACS Applied Materials & Interfaces* **10**, 40044-40053, (2018).

22 Kim, A.-R. *et al.* Creating high CO/CO_2 selectivity and large CO working capacity through facile loading of Cu(I) species into an iron-based mesoporous metal-organic framework. *Chemical Engineering Journal* **348**, 135-142, (2018).

23 Wang, B., Cote, A. P., Furukawa, H., O'Keeffe, M. & Yaghi, O. M. Colossal cages in zeolitic imidazolate frameworks as selective carbon dioxide reservoirs. *Nature* **453**, 207-211, (2008).

24 Britt, D., Furukawa, H., Wang, B., Glover, T. G. & Yaghi, O. M. Highly efficient separation of carbon dioxide by a metal-organic framework replete with open metal sites. *Proceedings of the National Academy of Sciences* **106**, 20637, (2009).

25 Munusamy, K. *et al.* Sorption of carbon dioxide, methane, nitrogen and carbon monoxide on MIL-101(Cr): Volumetric measurements and dynamic adsorption studies. *Chemical Engineering Journal* **195–196**, 359-368, (2012).

26 Shekhah, O. *et al.* Made-to-order metal-organic frameworks for trace carbon dioxide removal and air capture. *Nature Communications* **5**, 4228, (2014).

27 Yang, D.-A., Cho, H.-Y., Kim, J., Yang, S.-T. & Ahn, W.-S. CO_2 capture and conversion using Mg-MOF-74 prepared by a sonochemical method. *Energy & Environmental Science* **5**, 6465-6473, (2012).

28 Regufe, M. J. *et al.* Syngas Purification by Porous Amino-Functionalized Titanium Terephthalate MIL-125. *Energy & Fuels* **29**, 4654-4664, (2015).

29 Hao, H.-G. *et al.* Simultaneous Trapping of C_2H_2 and C_2H_6 from a Ternary Mixture of C2H2/C2H4/C2H6 in a Robust Metal–Organic Framework for the Purification of C2H4. *Angewandte Chemie* **130**, 16299-16303, (2018).

30 Qasem, N. A. A. & Ben-Mansour, R. Adsorption breakthrough and cycling stability of carbon dioxide separation from $CO_2/N_2/H_2O$ mixture under ambient conditions using 13X and Mg-MOF-74. *Applied Energy* **230**, 1093-1107, (2018).

31 Khabzina, Y. *et al.* Synthesis and Shaping Scale-up Study of Functionalized UiO-66 MOF for Ammonia Air Purification Filters. *Industrial & Engineering Chemistry Research* **57**, 8200-8208, (2018).

32 Coelho, J. A. *et al.* Stability of an Al-Fumarate MOF and Its Potential for CO_2 Capture from Wet Stream. *Industrial & Engineering Chemistry Research* **55**, 2134-2143, (2016).

33 Bozbiyik, B. *et al.* Stepped water isotherm and breakthrough curves on aluminium fumarate metal–organic framework: experimental and modelling study. *Adsorption* **23**, 185-192, (2017).

34 Hofman, P. S., Rufford, T. E., Chan, K. I. & May, E. F. A dynamic column breakthrough apparatus for adsorption capacity measurements with quantitative uncertainties. *Adsorption* **18**, 251-263, (2012).

35 Belmabkhout, Y., Pirngruber, G., Jolimaitre, E. & Methivier, A. A complete experimental approach for synthesis gas separation studies using static gravimetric and column breakthrough experiments. *Adsorption* **13**, 341-349, (2007).

36 Rajendran, A., Kariwala, V. & Farooq, S. Correction procedures for extra-column effects in dynamic column breakthrough experiments. *Chemical Engineering Science* **63**, 2696-2706, (2008).

37 Won, W., Lee, S. & Lee, K. S. Modeling and parameter estimation for a fixed-bed adsorption process for CO_2 capture using zeolite 13X. *Separation and Purification Technology* **85**, 120-129, (2012).

38 Casas, N., Schell, J., Pini, R. & Mazzotti, M. Fixed bed adsorption of CO_2/H_2 mixtures on activated carbon: experiments and modeling. *Adsorption* **18**, 143-161, (2012).

39 Hu, Z., Wang, Y., Shah, B. B. & Zhao, D. CO_2 Capture in Metal–Organic Framework Adsorbents: An Engineering Perspective. *Advanced Sustainable Systems* **3**, 1800080, (2019).

40 Hu, Z. *et al.* Ionized Zr-MOFs for highly efficient post-combustion CO_2 capture. *Chemical Engineering Science* **124**, 61-69, (2015).

41 Xiang, S. *et al.* Microporous metal-organic framework with potential for carbon dioxide capture at ambient conditions. *Nature Communications* **3**, 954, (2012).

42 Krishna, R. & Long, J. R. Screening Metal–Organic Frameworks by Analysis of Transient Breakthrough of Gas Mixtures in a Fixed Bed Adsorber. *Journal of Physical Chemistry C* **115**, 12941-12950, (2011).

43 Van Den Broeke, L. J. P. & Krishna, R. Experimental verification of the Maxwell-Stefan theory for micropore diffusion. *Chemical Engineering Science* **50**, 2507-2522, (1995).

44 Eic, M. & Ruthven, D. M. A new experimental technique for measurement of intracrystalline diffusivity. *Zeolites* **8**, 40-45, (1988).

45 Voogd, P., van Bekkum, H., Shavit, D. & Kouwenhoven, H. W. Effect of zeolite structure and morphology on intracrystalline n-hexane diffusion in pentasil zeolites studied by the zero-length column method. *Journal of the Chemical Society, Faraday Transactions* **87**, 3575-3580, (1991).

46 Ruthven, D. M. & Xu, Z. Diffusion of oxygen and nitrogen in 5A zeolite crystals and commercial 5A pellets. *Chemical Engineering Science* **48**, 3307-3312, (1993).

47 Brandani, S. & Ruthven, D. M. Analysis of ZLC desorption curves for gaseous systems. *Adsorption* **2**, 133-143, (1996).

48 Duncan, W. L. & Möller, K. P. The effect of a crystal size distribution on ZLC experiments. *Chemical Engineering Science* **57**, 2641-2652, (2002).

49 Brandani, S. Effects of nonlinear equilibrium on zero length column experiments. *Chemical Engineering Science* **53**, 2791-2798, (1998).

50 Brandani, S., Jama, M. A. & Ruthven, D. M. ZLC Measurements under non-linear conditions. *Chemical Engineering Science* **55**, 1205-1212, (2000).

51 Brandani, S. On the Chromatographic Measurement of Equilibrium Isotherms Using Large Concentration Steps. *Adsorption* **11**, 231-235, (2005).

52 Wang, H., Brandani, S., Lin, G. & Hu, X. Flowrate correction for the determination of isotherms and Darken thermodynamic factors from Zero Length Column (ZLC) experiments. *Adsorption* **17**, 687, (2011).

53 Joss, L. & Mazzotti, M. Modeling the extra-column volume in a small column setup for bulk gas adsorption. *Adsorption* **18**, 381-393, (2012).

54 Taylor Geoffrey, I. Dispersion of soluble matter in solvent flowing slowly through a tube. *Proceedings of the Royal Society of London. Series A. Mathematical and Physical Sciences* **219**, 186-203, (1953).

Chapter 4 Characterisation techniques

This chapter presents the characterisation techniques used throughout the studies to understand the structural and chemical properties of the MOFs synthesized. The techniques were used to verify successful synthesis and to gain insight about the nature of the materials. *In-situ* characterisation enabled us to further understand the MOF chemistry during activation and adsorption. Here the theory and experimental procedures used are presented.

4.1 MOF structure

4.1.1 *Textural parameters: N_2 sorption isotherms at -196 °C*

An adsorbent's textural parameters can provide important information regarding the adsorbent's structure and porosity. Pore sizes can be classified into three categories based on International Union of Pure and Applied Chemistry (IUPAC) definition[1]:

(i) pore widths exceeding ~500 Å are called macropores;

(ii) pore widths between 20 Å and 500 Å are called mesopores;

(iii) pore widths which do not exceed ~20 Å are called micropores.

Gas sorption isotherms of materials using N_2 at -196 °C or Ar at -186 °C can qualitatively determine the type of pores present by referring to the IUPAC isotherm recommendation (Appendix 2).[1] Furthermore, surface area, total pore volume, micropore volume and mesopore volume can be calculated from gas sorption analysis.

The volumetric technique measures the pressure change between the adsorbent sample chamber and manifold that occurs because of adsorption.[2] Once adsorption

has reached equilibrium, more of the adsorbate is dosed and this process is repeated systematically until saturation pressure has been reached. The amount of gas required to fill the sample chamber volume during the analysis (also known as effective void volume or dead volume) is also calculated for accurate porosity measurements. Helium is used as an inert probe gas for this measurement in the sample chamber.

For porosity analysis, N_2 adsorption and desorption isotherms were measured using a porosity analyser (Micromeritics 3Flex) at -196 °C. Prior to analysis, outgassing the sample at elevated temperature is required to remove any contaminants that may be physisorbing to the sample (*e.g.* H_2O, N_2, CO_2) and any trace solvent which was used during the synthesis and activation. The samples were initially outgassed by heating the samples up to a final vacuum of ~0.2 mbar for 16 h at 120 °C to remove the majority of the residual solvent. Subsequently, the samples were outgassed *in-situ* on the porosity analyser up to a final vacuum of ~0.003 mbar for 6 h for the stated activation temperature for each sample outlined in Section 5.2.

The sample surface area was calculated using the Brunauer-Emmett-Teller (BET) method.[3] The BET theory assumes that multi-layer adsorption occurs, with a monolayer forming first before the subsequent layers. Therefore, by knowing the monolayer capacity and N_2 diameter, the surface area can be determined. The BET surface area was calculated from the following equation[3]:

$$\frac{P}{V(P_0-P)} = \frac{1}{CV_m} + \frac{C-1}{CV_m}\left(\frac{P}{P_0}\right) \quad (4\text{-}1)$$

Where

P Equilibrium pressure (Pa)

P_0 Saturation pressure (Pa)

C BET constant (-)

V Quantity of gas adsorbed (cm^3)

V_m Quantity of gas adsorbed at the monolayer (cm^3)

The N_2 physisorption isotherms at -196 °C were plotted by the 3Flex software using a rearranged form of the BET equation (Eq 4-1) to provide the following relationship:

$$\frac{1}{v\left[\left(\frac{P_0}{P}\right)-1\right]} \; vs\left(\frac{P}{P_0}\right) \quad (4\text{-}2)$$

From which V_m (intercept) and C (slope) can be determined. The 3Flex software applied the Rouqureol criteria[4] which can be used for MOFs.[5] Generally, at least five data points were taken from the pressure range of P/P_0 = 0.05-0.035. V_m is inserted in Eq 4-3 to calculate the surface area.

$$S_{BET} = \frac{V_m \, L \, \sigma_{N_2}}{RT} \quad (4\text{-}3)$$

Where

S_{BET} BET surface area ($m^2\ g^{-1}$)
L Avogadro's constant (6.022 x 10^{23} mol)
σ_{N_2} Cross-sectional area of N_2 (0.162 nm^2)
R Universal gas constant (8.314 J K^{-1} mol^{-1})
T Standard Temperature (K)

The total pore volume was calculated using the total N_2 volume adsorbed at P/P_0 = 0.97 using the following equation:

$$V_{tot} = \frac{PV_{0.97}V_M}{RT} \quad (4\text{-}4)$$

Where

V_{tot} Total pore volume ($cm^3\ g^{-1}$)
P Standard Pressure (Pa)
$V_{0.97}$ Quantity adsorbed at P/P_0 = 0.97 ($cm^3\ g^{-1}$)
V_M Molar volume of N_2 at 196 °C (34.65 cm^3 mol^{-1})

The micropore volume was calculated using the Dubinin-Radushkevich method on the software.[6] Subsequently, the mesopore volume (V_{mes}) was calculated by subtracting the micropore volume from the total pore volume:

$$V_{mes} = V_{tot} - V_{mic} \quad (4\text{-}5)$$

Where

V_{mes} Mesopore volume ($cm^3\,g^{-1}$)
V_{mic} Micropore volume ($cm^3\,g^{-1}$)

4.1.2 *Crystalline structure- X-ray diffraction*

As MOFs self-assemble into ordered structures, these class of adsorbents are typically highly crystalline porous materials[7] which can be characterised by X-ray diffraction analysis. When the X-ray beam is directed onto the sample, the X-rays diffract between crystalline planes through constructive interferences. As the incident angle X-ray beam varies, characteristic diffraction patterns emerge that are unique to the structure and Bragg's law[8] can be used to calculate the space between the planes (d-spacing) using the equation below:

$$2d\,sin\theta = n\lambda \quad (4\text{-}6)$$

Where

d Interatomic spacing between the planes (nm)
θ Scattering angle of the incident beam (°)
n Positive integer (-)
λ Wavelength (nm)

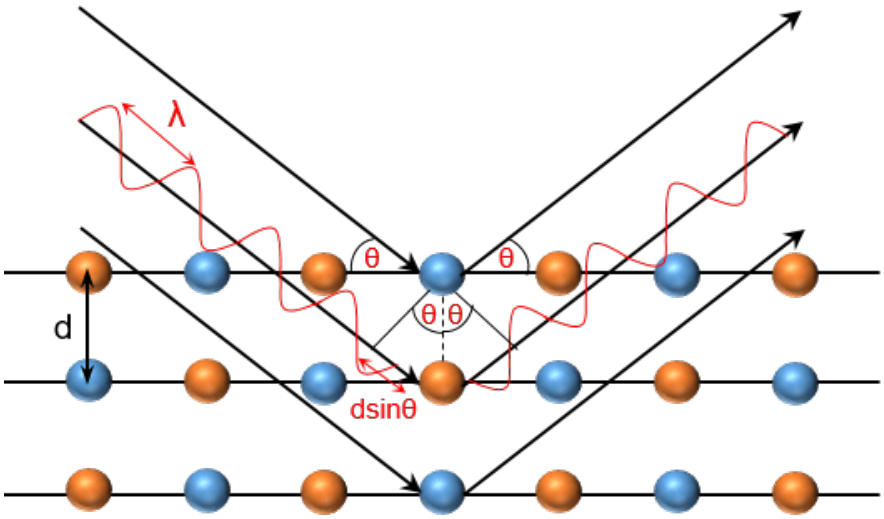


Figure 4-1. A schematic representation of Bragg's law with X-ray diffraction.

This bulk characterisation technique enables us to verify successful synthesis and activation by comparing the experimental diffraction pattern to the patterns obtained from either an XRD database,[9] simulated structure or from literature. Furthermore, XRD analysis also enables us to examine any structural changes after post-synthesis modification, by comparing to diffraction patterns of the precursors used and the material before modification.

X-ray diffraction measurements were performed using a PANalytical X'Pert PRO instrument in reflection mode using monochromatic Cu Kα radiation (λ = 1.54178 Å). For sample preparation, the powder samples were loaded onto a silicon diffraction plate and a glass slide was used to smoothen and produce a uniform surface. The diffraction plate was loaded onto a goniometer stage. The operating conditions included using an anode voltage of 40 kV and an emission current of 20 eV, and the X-ray beam was directed at angles ranging at 2θ = 5-50°. Measurements were recorded at ambient conditions.

By performing XRD measurements with increasing temperature, it was possible to test an adsorbent's thermal stability and robustness by monitoring its structural integrity upon heating. This procedure assists in selecting a suitable activation temperature that does not damage the material. The variable temperature X-ray diffraction (VT-XRD) measurements were performed by Mr Matthew Cummings, our collaborator at the University of Manchester. For the variable temperature powder X-ray diffraction VT-XRD measurements, a XRK 900 furnace stage (Anton-Parr) was used. Samples were heated to a predetermined temperature with a ramp rate of 1 °C min^{-1} and with a 10 min equilibration time. Samples collected under vacuum were maintained using a high vacuum Oerlikon Leybold Vacuum pump PT50 kit.

4.1.3 *Electronic structure: X-ray absorption fine structure*

X-ray absorption fine structure (XAFS) spectroscopy is a characterisation technique that provides structural and electronic information of a material through X-ray absorption. As the incident beam passes through the material, the detected photons (E) decrease in energy depending on factors that include the material density (ρ), atomic number (Z) and atomic mass (A), as expressed below (where μ is the absorption coefficient):

$$\frac{\mu}{\rho} \approx \frac{Z^4}{AE^3} \quad (4\text{-}7)$$

As absorption occurs, a characteristic peak (absorption edge) arises on the spectrum that exhibits information that can be extracted from two methods of analytical techniques: X-ray near-edge spectroscopy (XANES) and Extended X-ray absorption fine-structure spectroscopy (EXAFS).

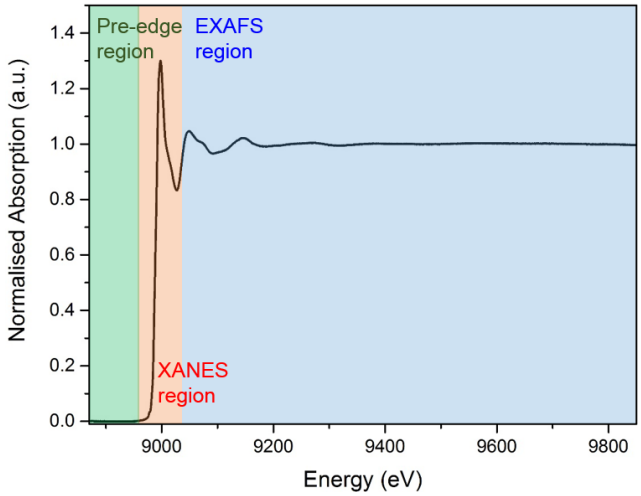


Figure 4-2. Ni-edge X-ray absorption fine structure spectrum of Ni-MOF-74.

XANES extracts chemical data of the element such as its oxidation state and coordination chemistry. The XANES region is comprised of the absorption edge and pre-edge region, as shown in Figure 4-2. No electrons are photoemitted in this region as the technique probes the transitions of the valence orbital. Therefore the electronic structure of the element includes information solely regarding the binding strength and electron delocalisation.

EXAFS can be used to extract physical data of the material such as the interatomic bond distances and coordination number. The EXAFS region is located after the absorption edge (Figure 4-2), and the photon energy detected is a result of the scattered photoelectrons. Information regarding the local structure is obtained regarding the geometry of the atoms, such as its coordination geometry and distance to neighbouring atoms.

In-situ XAFS measurements to analyse the Cu reduction procedure and metal-CO interactions were performed at B18 beamline at Diamond Light Source by myself, Dr Donato Decarolis and Mr Matthew Cummings, our collaborators at the University of Manchester. The experimental procedure is described in the subsections below.

4.1.3.1 Copper standards

The Cu standard used for the XAFS analysis were: CuO, $Cu(HCO_2)_2.4H_2O$, $Cu(NO_3)_2.4H_2O$ Cu_2O, $CuCl_2.2H_2O$, CuCl and Cu.

4.1.3.2 Sample preparation and activation

The samples, after appropriate dilution in boron nitride, were loaded into an open-ended capillary (ø = 3 mm, Length = 100 mm) and mounted on a catalysis testing station, with the capillary connected to gas lines. During the measurements, the samples were heated from room temperature to 250 °C under He atmosphere, stopping at 80 °C and 160 °C to collect higher quality spectra. After reaching the temperature of 250 °C, the atmosphere was changed to 10% CO in He and measurements were collected continuously until no changes of the Cu-edge XANES spectra could be observed. Samples were then brought down to room temperature and XAFS spectra were collected under a $CO:N_2$ atmosphere.

4.1.3.3 Data acquisition

XAFS data were acquired at Cu K edge (8.98 keV) for both samples and Ni K edge (8.33 keV) and Co K edge (7.71 keV), for 4-Cu@Ni-MOF-74 and 2-Cu@Co-MOF-74 respectively. Ni- and Co-edge measurements were performed in transmission mode, while fluorescence mode was required for Cu due to the low Cu amount in the sample. Unfortunately it was not possible to collect Cu-edge XAFS spectra under $CO:N_2$ atmosphere for the Cu@Co-MOF-74 due to experimental issues, but Co-edge XAFS measurements were obtained.

4.1.3.4 Data analysis

XAFS data processing and analysis was performed using the Athena and Artemis software from the Demeter IFEFIT package. Due to the high signal to noise ratio and

short acquisition range, only XANES information could be obtained from the Cu-edge data. For Ni and Cu, the resultant EXAFS data have been used to determine changes in structure of the MOF structure. The FEFF6 code was used to construct theoretical EXAFS signals, which included single-scattering contributions from atomic shells through the nearest neighboring atoms in the MOF. The *k*-range used for the fitting went from 3 to 10.634 $Å^{-1}$ and the *r*-range from 1.305 to 3.5 Å. The path degeneracy was kept constant in the fit and the amplitude reduction factor was fixed at 0.800. In particular, the path taken in exam are the M-O and M-M for all spectra, and M-C for the sample under CO atmosphere at room temperature.

4.2 MOF chemistry

4.2.1 *Bulk chemistry: Diffuse reflectance infrared Fourier transform spectroscopy*

Diffuse reflectance infrared Fourier transform spectroscopy (DRIFTS) is an analytical technique which transmits infrared energy and detects the scattered light to provide chemical and structural information of the analysed material.[10] While materials can either directly reflect or absorb IR radiation, DRIFTS detects the diffused energy which exits the sample at any angle relative to the incident beam. Since the radiation penetrates the sample, absorption data can be extracted from the analysis as well. The energy of the IR peaks observed provide structural environment regarding the chemical environment of the materials. This technique allows comparisons between different spectra to examine any structural change upon modification of the material.

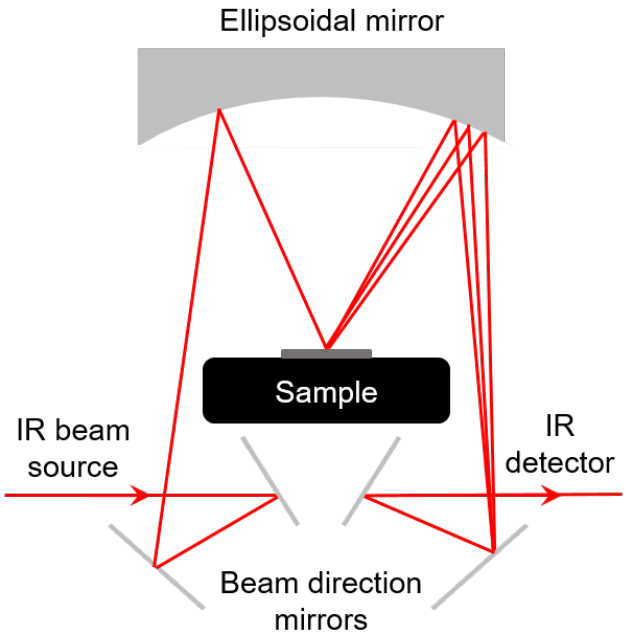


Figure 4-3. Schematic of a Diffuse reflectance infrared Fourier transform spectroscopy experimental set-up.

In-situ DRIFTS was used to study the metal-CO interactions of the MOFs under investigation. DRIFTS analysis was performed by Mr. Matthew Cummings and Dr. Donato Decarolis, our collaborators at the University of Manchester. Prior to analysis, the samples were degassed by heating the samples at ~0.2 mbar for 16 h at 120 °C. Sample activation was completed *in-situ* on the instrument with the desired conditions specific for each sample. After activation and cooling to room temperature, CO adsorption was performed using 10% CO in He, and was allowed to equilibrate until saturated. Following this, excess CO was purged from the cell using He. The IR spectrum was recorded with a Bruker Tensor 27 spectrometer using a liquid N_2 cooled mercury-cadmium-telluride (MCT) detector.

4.2.2 *Bulk chemistry: Inductively coupled plasma mass spectrometry*

Inductively coupled plasma mass spectrometry (ICP-MS) is a bulk analysis technique that detects the ion masses of a material using a mass spectrometer after ionisation

by a inductively coupled plasma.[11] During the analysis, the sample is turned into an aerosol and mixed with argon before exposure to the inductively coupled argon plasma from an electric current. The ions are directed to the mass spectrometer for ion detection in a high vacuum chamber. ICP-MS enables us to measure the elemental composition of the bulk material.

ICP-MS analysis was conducted using a Agilent Technologies 7900 ICP-MS. For sample preparation, the sample was digested in concentrated nitric acid (HNO_3) before being diluted to a 2% HNO_3 (aq) solution. An Agilent SPS4 Autosampler was used for high-throughput sample analysis with a 0.22 μm filter used to remove any remaining solid particles before analysis. Prior to analysis, the metal concentrations were calibrated using an Aristar ICP calibration standard containing 23 transition metals at 5, 20, 200, 500 and 1000 ppb concentration level. Yttrium was used as an internal standard to improve the accuracy and repeatability of the measurements. Three blanks (2% HNO_3) were prepared for analysis to eliminate any background noise. For each material analysed, three samples were prepared, and three measurements were performed on each solution prepared for error analysis.

4.2.3 *Surface chemistry: X-ray photoelectron spectroscopy*

X-ray photoelectron spectroscopy (XPS) is a surface analysis technique that uses X-ray radiation in vacuum to excite bound electrons of the analysed material for elemental characterisation.[12] As the electrons are photoemitted, the kinetic energy of the detected electrons are collected and can be used to determine the electron binding energy using the equation below[12]:

$$E_{binding} = E_{photon} - E_{kinetic} - \phi \quad (4\text{-}8)$$

Where

$E_{binding}$ Binding energy of the electron emitted (eV)

E_{photon} Photon energy of the X-ray beam, also known as *hv* (eV)

$E_{kinetic}$ Kinetic energy of the electron detected (eV)

ϕ Work function of the spectrometer (eV)

The number of electrons also collected at specific binding energies is quantified, plotting a spectrum of Binding Energy *vs* Intensity. This information allows us to measure the elemental composition at the surface and investigate the chemical states of the elements through characteristic peak shapes. Furthermore, this technique allows us to examine any shifts in peak energy from its original state, which may arise from modification from its original chemical environment.

XPS analysis was conducted using a Thermo Scientific K-Alpha$^+$ X-ray photoelectron spectrometer which is equipped with an MXR3 Al Kα monochromated X-ray source (*hv* = 1486.6 eV). Prior to analysis, the samples were degassed by heating the samples at ~0.2 mbar for 16 h at 120 °C. For sample loading, the samples were ground and mounted on the sample holder using conductive carbon tape. The X-ray gun power was set to 72 W (6 mA and 23 kV) and the operating pressure was set to 1x10^{-8} mbar. An electron flood gun was used to provide charge compensation. Before acquiring high-resolution data, a survey scan was performed using 200 eV pass energy, 0.5 eV step size and 100 ms (50 ms x2 scans) dwell times. High-resolution spectra were collected from the relevant electron shell of the elements under investigation using 20 eV pass energy and 0.1 eV step size. The adventitious carbon (C-C) peak position at 285.0 eV was used as reference to shift the XPS spectra to align with this value. XPS data analysis was performed using Thermo Avantage.

4.2.4 *Thermal analysis: Thermogravimetric analysis*

The thermal stability of an adsorbent could be examined by thermogravimetric analysis (TGA),[13] monitoring its mass loss with increasing temperature using a high precision balance (±0.0001 mg balance accuracy). The sample is loaded in an alumnia crucible that can resist high temperature, which is heated by a furnace controlled by a thermocouple built inside the crucible holder. This technique enables us to identify the thermal decomposition temperature, which assists in selecting a suitable activation temperature that does not damage the material.

Thermal stability analyses were conducted using a Netzsch TG209 F1 Libra thermogravimetrical analyser. Prior to analysis, a buoyancy measurement was conducted with an empty crucible under the same analysis conditions. Samples were initially outgassed by heating the samples up to a final vacuum of ~0.2 mbar for 16 h at 120 °C. Approximately 25 mg of sample was used in the analysis and loaded into the alumina crucible. The sample was heated from 30 °C to 900 °C at a ramp rate of 10 °C min^{-1} under N_2 gas flow (100 mL min^{-1}).

4.2.5 *Thermal analysis: Temperature programmed desorption*

Temperature programmed desorption (TPD) analysis is a technique which allows us to monitor the desorption profile upon heating.[14] The material is pre-saturated with the probe adsorbate and the amount of thermal energy required to induce desorption is an indication of the binding strength and enthalpy of adsorption. This technique also allows us to measure the rate of desorption and the adsorption capacity of the adsorbent, which is proportional to the integral of the curve. Furthermore, TPD also allows us to identify how many different types of binding sites are present, depending on the shape of the curve and the number of peaks observed.

CO TPD analysis was performed by Mr Russell Purves, our collaborator at BP (Saltend Chemicals Park). The measurements were carried out using a Micromeritics 2920 AutoChem II dynamic chemisorption analyser combined with an integrated thermal conductivity detector (TCD) and Cirrius 2 quadrupole mass spectrometer.

For the analysis, approximately 50 mg of sample was used and activated by heating from room temperature to 100 °C at a rate of 5 °C min^{-1} under flowing argon (30 mL min^{-1}) for 10 h. Next, the samples were heated from 100 °C to 250 °C at 5 °C min^{-1} under flowing argon (30 mL min^{-1}) and held for a further 6 h. Lastly, the samples were cooled to room temperature prior to being immediately subjected to CO TPD analysis. For the analysis, CO was loaded onto the samples by flowing 100% CO (30 mL min^{-1}) at room temperature for 2 h. CO desorption was carried out by heating the sample from room temperature to 250 °C at a rate of 5 °C min^{-1} under flowing argon (30 mL min^{-1}). CO desorption was continually monitored throughout by the TCD.

4.3 References

1 Thommes, M. *et al.* in *Pure and Applied Chemistry* Vol. 87, 1051 (2015).
2 Rouquerol, J., Rouquerol, F., Llewellyn, P., Maurin, G. & Sing, K. S. *Adsorption by powders and porous solids: principles, methodology and applications*. (Academic press, 2013).
3 Brunauer, S., Emmett, P. H. & Teller, E. Adsorption of Gases in Multimolecular Layers. *Journal of the American Chemical Society* **60**, 309-319, (1938).
4 Rouquerol, J., Llewellyn, P. & Rouquerol, F. Is the BET equation applicable to microporous adsorbents. *Stud. Surf. Sci. Catal* **160**, 49-56, (2007).
5 Gómez-Gualdrón, D. A., Moghadam, P. Z., Hupp, J. T., Farha, O. K. & Snurr, R. Q. Application of Consistency Criteria To Calculate BET Areas of Micro- And Mesoporous Metal–Organic Frameworks. *Journal of the American Chemical Society* **138**, 215-224, (2016).
6 Chen, S. G. & Yang, R. T. Theoretical Basis for the Potential Theory Adsorption Isotherms. The Dubinin-Radushkevich and Dubinin-Astakhov Equations. *Langmuir* **10**, 4244-4249, (1994).
7 Kaskel, S. *The Chemistry of Metal-Organic Frameworks, 2 Volume Set: Synthesis, Characterization, and Applications*. (Wiley, 2016).
8 Bragg William, H. & Bragg William, L. The reflection of X-rays by crystals. *Proceedings of the Royal Society of London. Series A, Containing Papers of a Mathematical and Physical Character* **88**, 428-438, (1913).
9 Allen, F. H. The Cambridge Structural Database: a quarter of a million crystal structures and rising. *Acta Crystallographica Section B: Structural Science* **58**, 380-388, (2002).
10 Settle, F. A. *Handbook of instrumental techniques for analytical chemistry*. (Prentice Hall PTR, 1997).
11 Thomas, R. *Practical Guide to ICP-MS: A Tutorial for Beginners, Third Edition*. (Taylor & Francis, 2013).
12 Briggs, D. & Grant, J. T. *Surface analysis by Auger and X-ray photoelectron spectroscopy*. (SurfaceSpectra, 2012).
13 Coats, A. W. & Redfern, J. P. Thermogravimetric analysis. A review. *Analyst* **88**, 906-924, (1963).
14 Ishii, T. & Kyotani, T. in *Materials Science and Engineering of Carbon* (eds Michio Inagaki & Feiyu Kang) 287-305 (Butterworth-Heinemann, 2016).

Chapter 5 Preliminary MOF screening

Aspects of the work presented in this chapter has been written in the form of a manuscript which has been accepted by Industrial & Engineering Chemistry Research.[1]

5.1 Introduction

Carbon monoxide (CO) is used an industrial reagent for chemical feedstock synthesis,[2] and therefore requires numerous purification steps to achieve the desired high purity (>99 mol%). N_2 concentration from the syngas stream which exceeds >1 mol% is problematic and contaminates the CO stream as an industrial reagent for it to be used in chemical feedstock synthesis. MOFs are promising candidates to be applied as adsorbents for industrially relevant CO/N_2 separation for CO purification to reduce energy consumption and costs of current technologies.[3-5] MOFs can selectively bind to CO through metal-CO interactions from its framework metal sites. When activated, these metal sites become coordinatively unsaturated which also forms π backbonding for reinforced CO binding. Therefore, the quantity and nature of these unsaturated unsaturated metal sites are important in the role of CO/N_2 separation. It is hypothesized that the best MOFs for CO/N_2 separation are structures that possess a high density of metal sites that have high affinity to CO. To date, multiple MOFs have been synthesized and tested for CO/N_2 separation application based on their ability to selectively bind to CO through their unsaturated metal sites.[6-10] However, no comprehensive study has investigated multiple MOFs with a consistent and systematic procedure to evaluate multiple MOFs performance for CO/N_2 separation.[3]

Along with the limited number of reports on MOFs for CO purification, there is a lack of dynamic studies with mixed gas streams. Yet, dynamic studies are critical to assess the large-scale viability of the adsorption process. For instance, kinetic diffusivity and mass transfer resistances are important considerations when designing an adsorbent bed for a process-system model for gas separations. Overall, among the few dynamic studies on CO separation, no pure MOFs demonstrate significant CO separation ability at ambient conditions.[11-15] Cu(AIP)(H_2O) exhibited good CO/N_2 separation at -153 °C while Fe-MIL-100 only displayed separation ability after Cu impregnation.[10,16]

This chapter screens several MOF structures for CO/N_2 separation using both static (*i.e.* CO and N_2 equilibrium isotherms) and dynamic measurements. FRT was employed to test the dynamic sorption behaviour as this technique only requires small amount of samples (10-20 mg).[17]

It was hypothesized that the nature of the metal centres would have a greater influence over the metal density and MOF textural parameters. Bloch *et al.* have previously cited the large variation of metal-CO binding strength based on the Irving-Williams series with different metal analogues.[6] The relationship between the metal density and structure's textural parameters can be interrelated. It was predicted that the surface interactions governed by the structure's porosity would have a weaker influence than the quantity of the unsaturated metal sites. From this study, the most promising MOFs were selected for further in-depth analysis.

5.2 Materials synthesis

A total of 14 MOFs were screened for CO/N_2 separation using equilibrium (CO and N_2 adsorption isotherms) and dynamic (CO FRT capacity, 50:50 *v:v* CO:N_2) measurements. The MOFs selected include: CuTDPAT, HKUST-1, MOF-505, PCN-

12, Cu-MFU-4L, Fe-MIL-100, Cr-MIL-101, Cu-MOF-74, Ni-MOF-74, Co-MOF-74, Ni_2Cl_2(BBTA), Co_2Cl_2(BBTA), Ni_2Cl_2(BTDD) and Co_2Cl_2(BTDD). These MOFs were chosen to represent structures of different classes of MOFs with unsaturated metal sites. A benchmark patented adsorbent used for CO/N_2 separation, Cu-Zeolite Y,[18] was also tested for comparison with the selected MOFs.

CuTDPAT, HKUST-1, MOF-505, PCN-12 and Cu-MFU-4L were chosen to investigate the effect of Cu sites upon CO/N_2 separation performance. Copper has been utilised in commercial absorption processes for CO purification.[5,19] CuTDPAT, HKUST-1, MOF-505 and PCN-12 all possess Cu-Cu paddlewheel metal nodes as part of these MOF structures, and were identified as promising MOF candidates by collaborators at the University of Cambridge who used molecular simulation for throughput MOF screening of the Cambridge Crystallographic Data Centre (CCDC) for CO/N_2 separation. Cu-MFU-4L was selected to study the effect of Cu^+ functionalisation, as Cu^+-CO interactions are stronger than Cu^{2+}-CO interactions. Fe-MIL-100 and Cr-MIL-101 were synthesized and tested to study the effect of a highly mesoporous structure.

M-MOF-74 (also known as CPO-27 and M_2(DOBDC) where H_2DOBDC = 2,5-dihydroxyterephthalic acid), M_2Cl_2(BBTA) (where H_2BBTA = 1H,5H-benzo(1,2-d:4,5-d')bistriazole) and M_2Cl_2(BTTD) (where H_2BTDD = bis-(1H-1,2,3-triazolo-[4,5-b],[4',5'-i])dibenzo-[1,4]-dioxin) were selected as MOFs that possess 1-D hexagonal pored topology. These isoreticular frameworks have different organic linkers that provide differing pore aperture sizes, which contributes to varying levels of metal density and quantity of unsaturated metal sites.

By studying Cu^{2+}-, Co^{2+}- and Ni^{2+}- analogues of M-MOF-74, it was possible to evaluate the performance of different metal sites. Cu-MOF-74 was also used as a Cu^{2+}-based

structure to compare the 1-D hexagonal pored topology and Cu-Cu paddlewheel based structures.

5.2.1 *Cu-Zeolite Y*

Cu-Zeolite Y was synthesized based on a previously reported experimental procedure[18] by an ion exchange method. Na-Zeolite Y was stirred in 200 mL of aqueous $Cu(NO_3)_2$ solution (0.5 M) for 4 days, with the solution replaced every 24 h. The exchanged zeolite was collected *via* filtration and washed briefly with H_2O to remove excess copper solution. The sample was dried resulting in a faintly blue powder. Copper exchange was confirmed using Energy Dispersive Analysis by X-ray (EDAX) which showed a 72% uptake, giving an assumed chemical formula of $Cu_{2.52}Na_{1.96}[Al_7Si_{17}O_{48}]$. This zeolite was synthesized by Mr Matthew Cummings, our collaborator at the University of Manchester. Sample activation for characterisation and testing was performed at 200 °C.

5.2.2 *CuTDPAT*

CuTDPAT was synthesized based on a previously reported experimental procedure.[20] 0.900 g of Na_6TDPAT (5,5',5''-(s-triazine-2,4,6-triyltriimino)triisophthalic acid hexasodium salt) – synthesized based on Ref [20] – 1.03 g copper(II) nitrate hemi(pentahydrate) ($Cu(NO_3)_2 \cdot 2.5H_2O$) and 124 mL DMF were combined in a 1 L Schott bottle and stirred until dissolved. 6 mL nitric acid (68%) was added to the solution and stirred further. The bottle was capped and heated in a convection oven for 7 days at 65 °C. The product was recovered by filtration and washed with DMF and MeOH. This MOF was synthesized by Mr Matthew Cummings, our collaborator at the University of Manchester. Sample activation for characterisation and testing was performed at 120 °C.

5.2.3 *HKUST-1*

HKUST-1 was synthesized based on a previously reported experimental procedure.[21] 2.30 g copper(II) nitrate hemi(pentahydrate) ($Cu(NO_3)_2 \cdot 2.5H_2O$) was dissolved in 16 mL DMF, 16 mL EtOH and 16 mL H_2O. 1.00 g H_3BTC (benzene-1,3,5-tricarboxylic acid) was dissolved in 16 mL DMF, 16 mL EtOH and 16 mL H_2O. Both solutions were combined and sonicated for 5 minutes before transferring to a 100 mL Schott bottle and heated in a convection oven for 16 h at 80 °C. After cooling, the product was recovered by filtration and washed with 100 mL of DMF, EtOH and H_2O. Sample activation for characterisation and testing was performed at 120 °C.

5.2.4 *MOF-505*

MOF-505 was synthesized based on a previously reported experimental procedure[22]. 0.307 g copper(II) nitrate hemi(pentahydrate) ($Cu(NO_3)_2 \cdot 2.5H_2O$), 0.104 g H_4BPTC (biphenyl-3,3′,5,5′-tetracarboxylic acid), 14 mL DMF, 7 mL H_2O and 2 mL hydrochloric acid (37%) were combined in a scintillation vial and sonicated until dissolved. The solution was heated in an oil bath for 24 h at 80 °C without stirring. The product was recovered by filtration while the solution was still hot and washed with warm DMF. This MOF was synthesized by Mr Matthew Cummings, our collaborator at the University of Manchester. Sample activation for characterisation and testing was performed at 120 °C.

5.2.5 *PCN-12*

PCN-12 was synthesized based on a previously reported experimental procedure.[23] 0.25 g copper(II) nitrate hemi(pentahydrate) ($Cu(NO_3)_2 \cdot 2.5H_2O$) and 0.1 g H_4MDIP (3,3′,5,5′-tetracarboxydiphenylmethane) were sonicated in 15 mL DMA until dissolved.

The solution was transferred to a 20 mL scintillation vial and was heated at 85 °C for 48 hr. The solution was allowed to cool to room temperature, and the resulting blue precipitate was washed with fresh DMA over 2 days. The blue precipitate was washed further with MeOH and DCM. The final product was collected after decanting the DCM and drying under N_2 flow. Sample activation for characterisation and testing was performed at 120 °C.

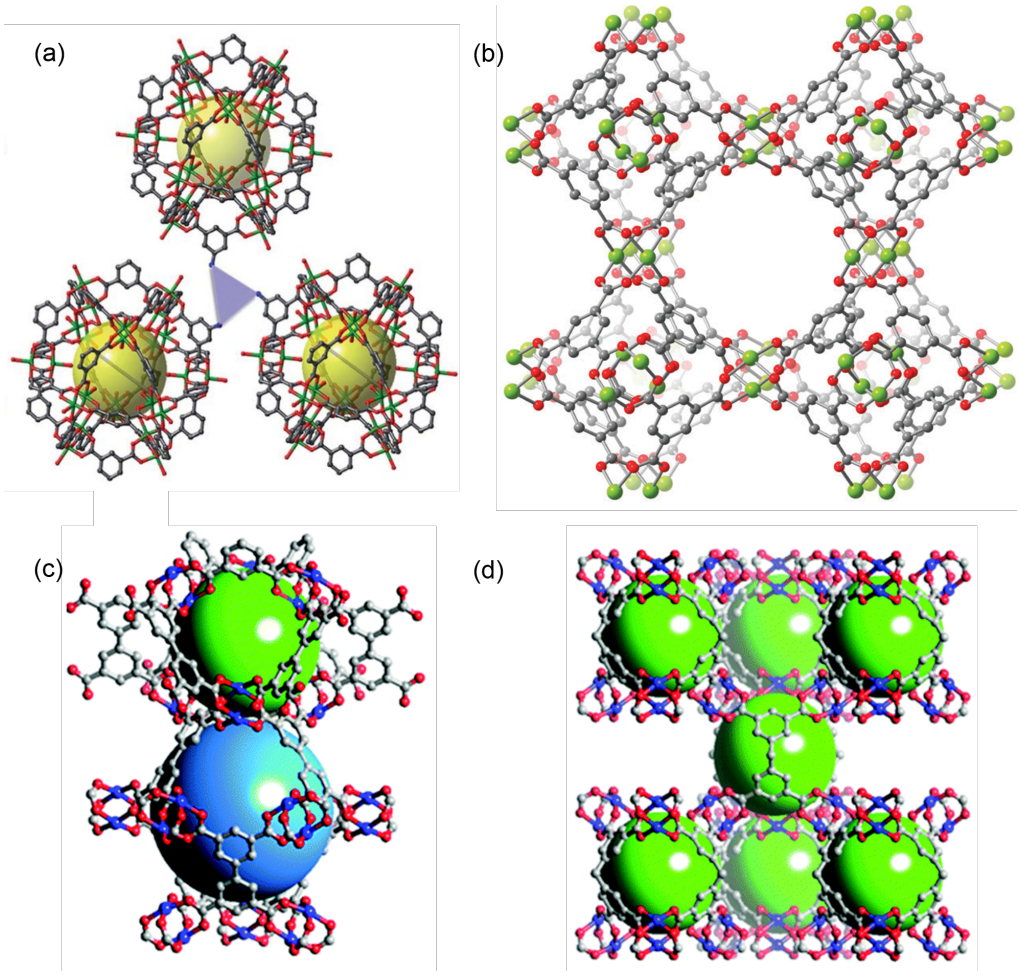


Figure 5-1. Structures of Cu-Cu paddlewheel MOFs: (a) CuTDPAT,[24] (b) HKUST-1,[25] (c) MOF-505[26] and (d) PCN-12.[26]

5.2.6 *Fe-MIL-100*

Fe-MIL-100 was synthesized based on a previously reported experimental procedure.[27] 0.09 g iron powder, 0.22 g H_3BTC (benzene-1,3,5-tricarboxylic acid) and 8 mL H_2O were added to a Teflon autoclave liner and stirred gently. 0.1 mL nitric acid (68%) and 0.05 mL hydrofluoric acid (48%) were added to the contents and the liner was inserted into the stainless steel autoclave and sealed. The autoclave and its contents were heated in a convection oven for 16 h at 150 °C. After cooling, the contents were recovered by filtration washing with H_2O and MeOH. Sample activation for characterisation and testing was performed at 150 °C.

5.2.7 *Cr-MIL-101*

Cr MIL-101 was synthesized based on a previously reported experimental procedure.[28] 4.00 g chromium(III) nitrate nonahydrate ($Cr(NO_3)_3 \cdot 9H_2O$), 1.60 g H_2BDC (benzene-1,4-dicarboxylic acid), 0.617 mL nitric acid (68%) and 50 mL H_2O were combined in a beaker and sonicated until dissolved. The contents were transferred into a Teflon liner and sealed inside a stainless steel autoclave. The autoclave and its contents were heated in a convection oven for 8 h at 220 °C. After cooling, the contents were recovered by centrifugation and washed with H_2O. After decanting the H_2O, DMF was added to the contents of the centrifuge tube and sonicated for 1 h before recovering through centrifugation. The product was then washed with 100 mL H_2O at 70 °C for 5 h, and then repeated with EtOH after recovering through centrifugation. The final product was recovered by centrifugation after the EtOH wash. Sample activation for characterisation and testing was performed at 120 °C.

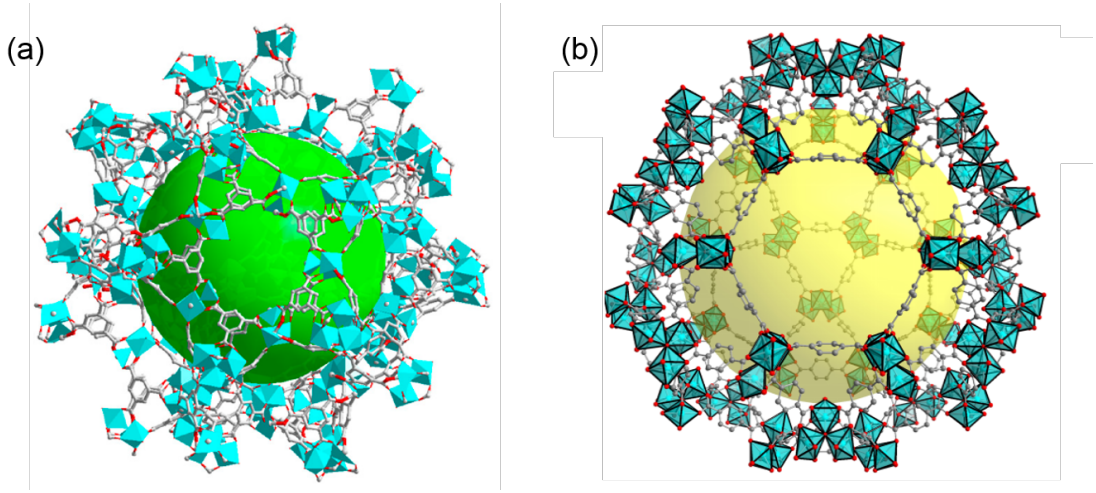


Figure 5-2. Structures of mesoporous MOFs: (a) Fe-MIL-100[29] and (b) Cr-MIL-100.[30]

5.2.8 *Cu-MFU-4L*

Cu-MFU-4L was synthesized based on a previously reported experimental procedure.[31,32] This method involves the synthesis of Zn-MFU-4L, which is ion exchanged to the Cu analogue. 0.768 g of H_2(BTDD) (bis(1H-1,2,3-triazolo[4,5-b],[4',5'-i])dibenzo[1,4] dioxin) was dissolved in 760 mL DMF at 130 °C and the solution was allowed to cool to room temperature. 7.81 g $ZnCl_2$ was dissolved into the solution while stirring. The solution was refluxed at 145 °C for 18 h and then cooled to room temperature. The powder was collected by filtration and washed with DMF, MeOH and DCM. The Zn was exchanged for Cu by heating Zn-MFU-4L in a solution of $CuCl_2$ in DMA for 24 h at 60 °C. The precipitate was washed with MeOH and DCM. 0.2 g of the recovered product was subsequently stirred in a lithium formate (0.2 M in MeOH) solution (60 mL) at room temperature for 1 h. The powder was collected by filtration and washed with MeOH and DCM. Inductively coupled plasma optical emission spectrometry (ICP-OES) analysis showed that 64.5% of the Zn sites of MFU-4L had been successfully exchanged to Cu giving an assumed framework chemical formula of $Zn_{1.78}Cu_{3.22}(O_2CH)_{0.78}(BTDD)_3$. Due to cluster coordination with its central Zn atom,

a total of 80.6% of the accessible unsaturated metal sites are Cu sites. This MOF was synthesized by Mr Matthew Cummings, our collaborator at the University of Manchester. Sample activation for characterisation and testing was performed at 120 °C.

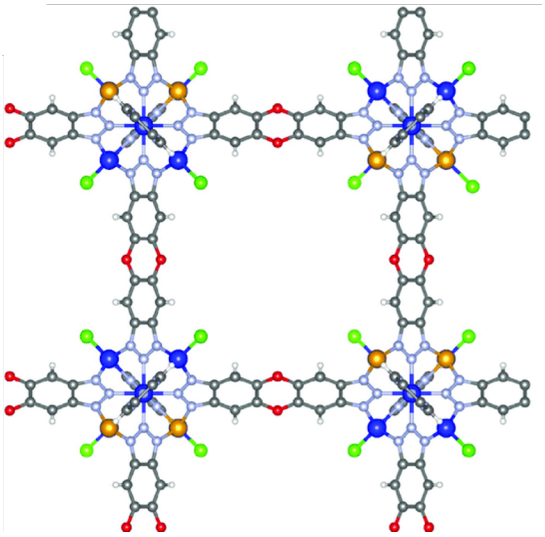


Figure 5-3. Structure of Cu-MFU-4L.[33]

5.2.9 *Cu-MOF-74*

Cu-MOF-74 was synthesized based on a previously reported experimental procedure[34] and modified for sample activation and scaled down for the reaction vessel used. 1.97 g copper(II) nitrate trihydrate ($Cu(NO_3)_2.3H_2O$), 0.73 g H_2DOBDC (2,5-dihydroxyterephthalic acid), 80 mL DMF and 4 mL IPA were combined in a beaker and sonicated until dissolved. The contents were transferred into a Teflon liner and sealed inside a stainless steel autoclave. The autoclave and its contents were heated in a convection oven for 18 h at 80 °C. After cooling, the contents were recovered and the supernatant was decanted and replaced by DMF. The product was soaked in DMF for 2 days, replaced with fresh DMF 4 times during this duration. The same procedure was repeated with MeOH. The final product was collected after decanting the MeOH

and drying under N_2 flow. Sample activation for characterisation and testing was performed at 250 °C.

5.2.10 *Ni-MOF-74*

Ni-MOF-74 was synthesized based on a previously reported experimental procedure[35] which was modified to increase product yield. 0.933 g nickel(II) acetate tetrahydrate ($Ni(OCOCH_3)_2 \cdot 4H_2O$), 0.373 g H_2DOBDC (2,5-dihydroxyterephthalic acid), 25 mL THF and 25 mL H_2O were combined in a beaker and sonicated until dissolved. The contents were transferred into a Teflon liner and sealed inside a stainless steel autoclave. The autoclave and its contents were heated in a convection oven for 3 days at 110 °C. After cooling, the contents were recovered and the supernatant was decanted and replaced by DMF. The product was soaked in DMF for 2 days, replaced with fresh DMF 4 times during this duration. The same procedure was repeated with MeOH. The final product was collected after decanting the MeOH and drying under N_2 flow. Sample activation for characterisation and testing was performed at 250 °C.

5.2.11 *Co-MOF-74*

Co-MOF-74 was synthesized based on a previously reported experimental procedure[36] and modified for sample activation and scaled down for the reaction vessel used. 1.07 g cobalt(II) nitrate hexahydrate ($Co(NO_3)_2 \cdot 6H_2O$), 0.357 g H_2DOBDC (2,5-dihydroxyterephthalic acid), 50 mL DMF, 50 mL EtOH and 50 mL H_2O were combined in a beaker and sonicated until dissolved. The contents were transferred to a 250 mL Schott bottle and heated in a convection oven for 66 h at 100 °C. After cooling, the contents were recovered and the supernatant was decanted and replaced by DMF. The product was soaked in DMF for 2 days, replaced with fresh DMF 4 times during this duration. The same procedure was repeated with MeOH. The

final product was collected after decanting the MeOH and drying under N_2 flow. Sample activation for characterisation and testing was performed at 250 °C.

5.2.12 *Ni_2Cl_2(BBTA)*

Ni_2Cl_2(BBTA) was synthesized based on a previously reported experimental procedure.[37] 0.1 g H_2(BBTA) (1H,5H- benzo(1,2-d:4,5-d′)bistriazole) was dissolved in 20 mL DMF in a 100 mL Schott bottle. 0.15 g of nickel(II) chloride hexahydrate ($NiCl_2 \cdot 6H_2O$) was dissolved in 20 mL MeOH and 8 mL hydrochloric acid (37%) to provide a blue solution. The solutions were combined into the Schott bottle and capped and heated for 3 days at 65 °C. After cooling, the product was recovered by filtration and washed with DMF and MeOH. The product was washed with MeOH for 3 days using soxhlet extraction. This MOF was synthesized by Mr Matthew Cummings, our collaborator at the University of Manchester. Sample activation for characterisation and testing was performed at 120 °C.

5.2.13 *Co_2Cl_2(BBTA)*

Co_2Cl_2(BBTA) was synthesized based on a previously reported experimental procedure.[37] 0.1 g H_2(BBTA) (1H,5H- benzo(1,2-d:4,5-d′)bistriazole) was dissolved in 20 mL DMF in a 100 mL Schott bottle. 0.15 g of cobalt(II) chloride hexahydrate ($NiCl_2 \cdot 6H_2O$) was dissolved in 20 mL MeOH and 0.2 mL hydrochloric acid (37%) to provide a blue solution. The solutions were combined into the Schott bottle and capped and heated for 3 days at 65 °C. After cooling, the product was recovered by filtration and washed with DMF and MeOH. The product was washed with MeOH for 3 days using soxhlet extraction. This MOF was synthesized by Mr Matthew Cummings, our collaborator at the University of Manchester. Sample activation for characterisation and testing was performed at 120 °C.

5.2.14 *Ni_2Cl_2(BTDD)*

Ni_2Cl_2(BTDD) was synthesized based on a previously reported experimental procedure.[38] 0.2 g H_2(BTDD) (bis(1H-1,2,3-triazolo[4,5-b],[4',5'-i])dibenzo[1,4] dioxin) was dissolved in 200 mL DMF in a 500 mL Schott bottle by stirring at heating at 110 °C. 0.357 g of nickel(II) chloride hexahydrate ($NiCl_2 \cdot 6H_2O$) was dissolved in 200 mL EtOH and 4 mL hydrochloric acid (37%). The solutions were combined into the Schott bottle and capped and heated for 10 days at 65 °C. After cooling, the product was recovered by filtration and washed with hot DMF and hot MeOH. This MOF was synthesized by Mr Matthew Cummings, our collaborator at the University of Manchester. Sample activation for characterisation and testing was performed at 120 °C.

5.2.15 *Co_2Cl_2(BTDD)*

Co_2Cl_2(BTDD) was synthesized based on a previously reported experimental procedure.[38] 0.2 g H_2(BTDD) (bis(1H-1,2,3-triazolo[4,5-b],[4',5'-i])dibenzo[1,4] dioxin) was dissolved in 200 mL DMF in a 500 mL Schott bottle by stirring at heating at 110 °C. 0.357 g of cobalt(II) chloride hexahydrate ($CoCl_2 \cdot 6H_2O$) was dissolved in 200 mL EtOH and 4 mL hydrochloric acid (37%). The solutions were combined into the Schott bottle and capped and heated for 10 days at 65 °C. After cooling, the product was recovered by filtration and washed with hot DMF and hot MeOH. This MOF was synthesized by Mr Matthew Cummings, our collaborator at the University of Manchester. Sample activation for characterisation and testing was performed at 120 °C.

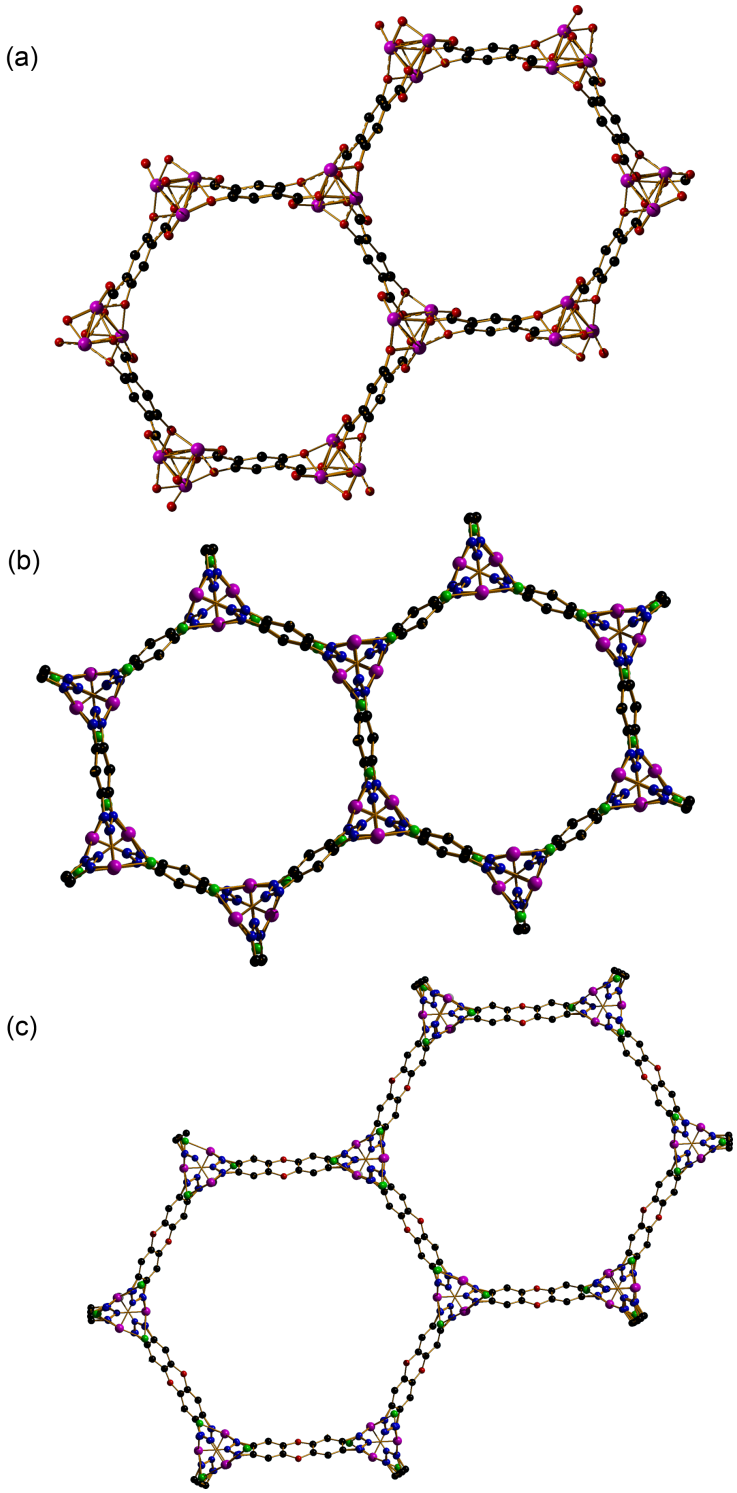


Figure 5-4. Structures of 1-D hexagonal pored MOFs: (a) M-MOF-74, M_2(BBTA) and (c) M_2(BTDD). Images produced by Mr Matthew Cummings (University of Manchester)

5.3 Materials characterisation

Prior to being tested, the successful synthesis of the MOFs and benchmark zeolite were confirmed using XRD and porosity measurements. The theory and experimental procedure of these characterisation techniques can be found in Section 4.1.

5.4 Materials testing

5.4.1 *Equilibrium testing*

For preliminary screening and an evaluation of the CO/N_2 separation performance of the selected MOFs and zeolite, CO and N_2 equilibrium adsorption isotherms were measured. Further selectivity values and enthalpy data was derived from these isotherms, outlined below.

5.4.1.1 Experimental procedure

The equilibrium adsorption isotherm measurements were performed by Mr Matthew Cummings, our collaborator at the University of Manchester. CO and N_2 isotherms (0-20 bar) were measured using a gravimetric gas sorption analyser (IGA-001 supplied by Hiden Isochema) under an ultra-high vacuum maintained with an oil and turbo pumping station. Samples (~100 mg of dry sample) were loaded into the analyser and degassed using an ultra-high vacuum according to synthesis and activation conditions indicated in Section 5.2 to provide the desolvated samples. Single component isotherms of CO and N_2 for all MOFs were measured at 25 °C. The experimental temperature of the measurements was controlled using a water bath circulator. A buoyancy correction was applied for each sample using the skeletal density calculated from a He (0-10 bar) isotherm at 25 °C. The buoyancy correction was calculated by the software provided by Hiden Isochema, IGASIM.

By fitting the single component CO and N_2 isotherms, the CO/N_2 Ideal Adsorbed Solution Theory (IAST) selectivities and CO and N_2 isosteric heat of adsorption (Q_{st}) values were calculated. Q_{st} calculations were performed for selected MOFs with CO and N_2 isotherm measurements at 10, 25 and 40 °C.

5.4.1.2 Ideal Adsorbed Solution Theory (IAST) selectivity calculations

An adsorption separation process requires information from gas adsorbate mixture isotherms, however these type of measurements are difficult and time-consuming.[39] Selectivity factor (S_{ads}) calculations have previously been applied for binary gas mixtures, which is the ratio of the number of moles adsorbed for each component at the partial pressure of their relative single component isotherms, as expressed in Equation 5-1.

$$S_{ads} = \frac{q_i/q_j}{p_i/p_j} \quad (5\text{-}1)$$

Where *q* is the number of adsorbed moles and *p* is the partial pressure, both for components *i* and *j*. However, this prediction is inaccurate with adsorbates that have large differences in binding energy and adsorbents with high-energy binding sites.[40]

Ideal Adsorbed Solution Theory (IAST) is a model which has been used to model the interaction of gases from their single component adsorption isotherm data to calculate its multicomponent selectivity for MOFs.[41,42] IAST is generally based on three assumptions: that the (i) adsorbent surface area is the same to all adsorbates, (ii) adsorbent is inert and (iii) the multicomponent gas mixture behaves as an ideal solution at constant spreading pressure and temperature.

Before performing the IAST calculations, two single component isotherms measured at the same temperature are required, and fitted to a model to perform the integration

required. There are no restraints on the model chosen, however the data over the pressure range measured should fit precisely. Commonly used analytical fittings are single site Langmuir (SL, Eq 5-2), Langmuir Freundlich (LF, Eq 5-3) and dual-site Langmuir Freundlich (DSLF, Eq 5-4) which are expressed below:

$$q = \frac{q_{\text{sat,A}} b_A P^{v_A}}{1 + b_A P^{v_A}} \quad (5\text{-}2)$$

$$q = \frac{q_{\text{sat}} b_n P^n}{1 + b_n P^n} \quad (5\text{-}3)$$

$$q = \frac{q_{\text{sat,A}} b_A P^{v_A}}{1 + b_A P^{v_A}} + \frac{q_{\text{sat,B}} b_B P^{v_B}}{1 + b_B P^{v_B}} \quad (5\text{-}4)$$

Where q is the number of adsorbed moles and q_{sat} is the total number of adsorbed moles of gas at saturation. In the DSLF equation, b and v are constants for the system and the subscript letters A and B represent the independent sites of the DSLF equation.

The equations are used to calculate the unknown values of the adsorbed mole fractions, gas phase mole fractions and spreading pressure (ψ) of the multicomponent gases.

As IAST assumes an ideal solution is present, Raoults Law can be applied to the gas and adsorbed phase, as shown in Eq 5-5 and 5-6 for components *i* and *j*:

$$\mathrm{P y_i = P_i^o x_i} \quad (5\text{-}5)$$

$$\mathrm{P y_j = P_j^o x_j} \quad (5\text{-}6)$$

Where P is the pressure, P^o is the pure component vapour pressure (at a specific temperature which is dependent on the spreading pressure), y and x are the mole fractions of the specified component in the gas and adsorbed phase and i and j are the components.

The spreading pressure, ψ, is determined from the pressure and amount adsorbed (*q*), and is calculated from the integration of equations and expressed as:

$$\psi_i = \int_0^{P_i^o} \frac{q(P)}{P} dP \quad (5\text{-}7)$$

$$\psi_j = \int_0^{P_j^o} \frac{q(P)}{P} dP \quad (5\text{-}8)$$

The IAST selectivity, S_{IAST}, is calculated by using these spreading pressure values and using the assumption that the mole fractions of components *i* and *j* equal unity in the gas phase (Eq 5-9). The selectivity equation is expressed as Eq 5-11.

$$y_i + y_j = 1 \quad (5\text{-}9)$$

$$\psi_i = \psi_j \quad (5\text{-}10)$$

$$S_{IAST} = \frac{P_1^o}{P_2^o} = \frac{x_i/x_j}{y_i/y_j} \quad (5\text{-}11)$$

5.4.1.3 Isosteric heat of adsorption (Q_{st}) calculations

From the analytical fittings of three pure single component isotherms measured at different temperatures (10, 25 and 40 °C), it was possible to calculate the heat of adsorption (Q_{st}) and entropy (ΔS) of the gas adsorption. The analytical fits provided the pressure values at specific loading which enabled the Van't Hoff equation[43] to be used to determine Q_{st} and ΔS:

$$\ln P = -\frac{\Delta H}{RT} + \frac{\Delta S}{R} \quad (5\text{-}12)$$

Where P is the pressure at the desired adsorption loading, T is temperature, R is the universal gas constant, ΔH is the isosteric heat of adsorption and ΔS is the change in entropy. A plot of ln(P) *vs* 1/T for each selected loading was then fitted with a linear fit, which enabled the Q_{st} and ΔS values to be extracted from the linear plot:

$$Q_{st} = -mR \quad (5\text{-}13)$$

$$\Delta S = -cR \quad (5\text{-}14)$$

Where m is the slope and c is the intercept of the plot.

5.4.2 *Dynamic testing*

The dynamic adsorption capacity measurements of the zeolite and selected MOFs were performed using FRT. The dynamic capacity calculations, fundamentals and theory of this technique are explained in Section 3.2.

5.4.2.1 Experimental procedure

The apparatus schematic (Figure 3-2), experimental procedure and an explanation of how the adsorption capacity was determined from the FRT profile (Figure 3-3) are all shown in Section 3.2. The activation conditions used are outlined in Section 5.2.

5.5 Results and discussion

5.5.1 *Materials characterisation*

The X-ray diffraction patterns of HKUST-1 and Ni-MOF-74 are shown in Figure 5-5, with simulated diffraction patterns to verify successful synthesis. The X-ray diffraction patterns of benchmark Cu-Zeolite Y and all the synthesized MOFs are shown in in the Appendix (Figure A3-1). The N_2 sorption isotherms at -196 °C for the Cu-Zeolite Y and synthesized MOFs are shown in Figure 5-6. The metal density (mol of coordinatively unsaturated metal sites per gram of adsorbent) and textural parameters derived from N_2 sorption isotherms at -196 °C for the benchmark Cu-Zeolite Y and synthesized MOFs are shown in Table 5-1.

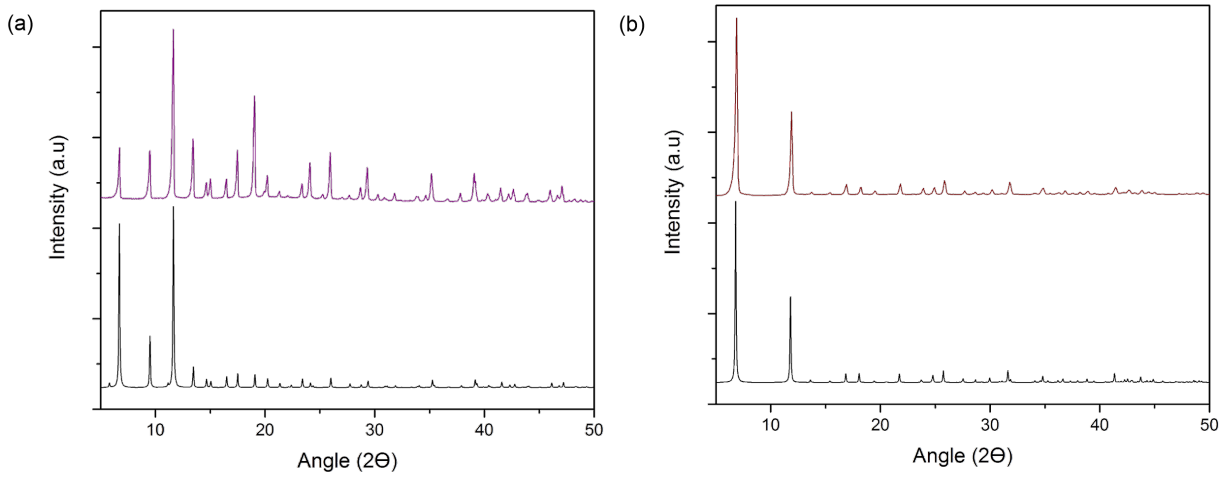


Figure 5-5. X-ray diffraction patterns of (a) HKUST-1 and (b) Ni-MOF-74. The simulated diffraction pattern of each structure is added on each panel for comparison, shown in black at the bottom of the panel.

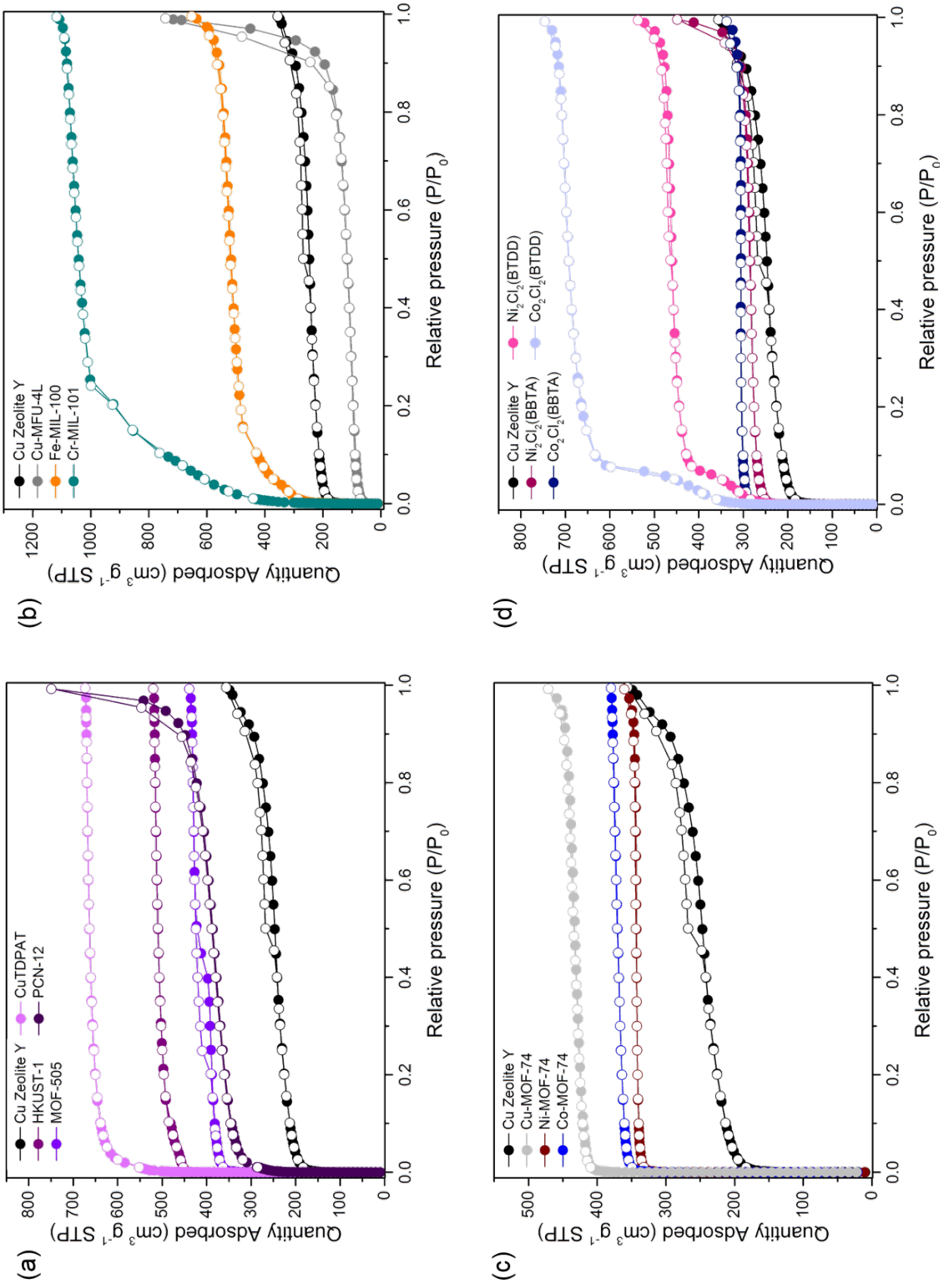


Figure 5-6. N_2 sorption isotherms at -196 °C of the: (a) Cu-Cu paddlewheel MOFs, (b) Cu^+-based MOF and mesoporous MOFs, (c) 1-D hexagonal pored M-MOF-74 structures and (d) 1-D hexagonal pored M_2Cl_2(BBTA) and M_2Cl_2(BTDD) structures. The isotherm for Cu-Zeolite Y is added on each panel for comparison.

Table 5-1. Metal density and textural parameters derived from N_2 sorption isotherms at -196 °C of the Cu-Zeolite Y and MOFs. (S_{BET} = BET surface area, V_{tot} = total pore volume, V_{mic} = micropore volume and V_{mes} = mesopore volume).

Materials	Metal density ($mmol_{metal}$ g^{-1}) *	S_{BET} (m^2 g^{-1})	V_{tot} (cm^3 g^{-1})	V_{mic} (cm^3 g^{-1})	V_{mes} (cm^3 g^{-1})	% Micropores
Benchmark adsorbent						
Cu-Zeolite Y	1.54†	852	0.55	0.37	0.18	67
Cu-Cu paddlewheel structure						
HKUST-1	4.96	1957	0.81	0.73	0.08	90
MOF-505	4.09	1586	0.68	0.60	0.08	88
CuTDPAT	3.50	2633	1.04	0.92	0.12	89
PCN-12	3.97	1415	0.72	0.53	0.19	74
Cu^{+} based structure						
Cu-MFU-4L	2.80±	347	1.15	0.14	1.01	12
Mesoporous structure						
Fe-MIL-100	4.88	1825	0.93	0.64	0.29	69
Cr-MIL-101	4.97	3579	1.73	1.14	0.59	66
1-D hexagonal pored M-MOF-74 structure						
Cu-MOF-74	3.90	1455	0.56	0.55	0.01	98
Ni-MOF-74	3.97	1427	0.58	0.53	0.05	91
Co-MOF-74	3.97	1520	0.59	0.58	0.01	97
1-D hexagonal pored M_2Cl_2(BBTA) structure						
Ni_2Cl_2(BBTA)	3.13	1103	0.48	0.42	0.06	88
Co_2Cl_2(BBTA)	3.13	1248	0.48	0.48	0	100
1-D hexagonal pored M_2Cl_2(BTDD) structure						
Ni_2Cl_2(BTDD)	2.55	1868	0.83	0.51	0.32	61
Co_2Cl_2(BTDD)	2.55	2270	1.16	0.65	0.51	56

* The desolvated adsorbent's general formula and crystallographic density was used to calculate the metal density (mol of coordinatively unsaturated metal sites per gram of adsorbent).

† Energy Dispersive Analysis by X-ray (EDAX) was performed by Mr Matt Cummings, which showed a 72% uptake to confirm copper exchange, giving an assumed chemical formula of $Cu_{2.52}Na_{1.96}[Al_7Si_{17}O_{48}]$.

± Inductively coupled plasma atomic emission spectroscopy (ICP-AES) was performed by Mr Matt Cummings which showed 64.5% of the MFU-4L Zn sites had been successfully exchanged to Cu to give an assumed framework chemical formula of $Zn_{1.78}Cu_{3.22}(O_2CH)_{0.78}(BTDD)_3$. Due to cluster coordination with its central Zn atom, a total of 80.6% of the accessible unsaturated metal sites are Cu sites.

5.5.2 *Equilibrium adsorption*

The CO and N_2 adsorption isotherms measured (25 °C, up to 20 bar) and plot of the IAST selectivities (50:50 *v:v* CO:N_2) of Cu-Zeolite Y and the MOFs are shown in Figure 5-7, Figure 5-8 and Figure 5-9. The CO/N_2 adsorption separation performance results (25 °C and 1 bar) of Cu-Zeolite Y and the MOFs are summarised in Table 5-2.

Ni-MOF-74 and Co-MOF-74 perform best among the selected MOFs, recording the highest CO equilibrium capacities (6.14 and 5.96 mmol g^{-1} for Ni-MOF-74 and Co-MOF-74). The Ni^{2+} and Co^{2+} ions of the M-MOF-74 structure has a strong affinity towards CO, as reported by Bloch *et al*.[6] Both the nature and density of these unsaturated metal sites result in near-saturation at very low pressure (~0.2 bar), as seen in Figure 5-7. The strong quasi-chemisorption interactions of Ni^{2+}-CO and Co^{2+}-CO result in minimal increase in CO uptake from the increasing physisorption from 1 to 20 bar (Figure 5-7). As Ni-MOF-74 and Co-MOF-74 N_2 uptake (Figure 5-8) increases up to 6.01 and 4.69 mmol g^{-1} at 20 bar, CO/N_2 selectivity (Figure 5-9) decreases. Therefore, despite possessing high CO capacity, its working capacity from 1-20 bar at 25 °C is low (Δq =1.01 and 1.39 mmol g^{-1} for Ni-MOF-74 and Co-MOF-74).

Ni-MOF-74 and Co-MOF-74 outperformed the benchmark Cu-Zeolite Y mainly because of its higher density of unsaturated metal sites (Table 5-1), but is also reinforced by the strong metal-CO interactions and high microporosity. Mg- and Fe-MOF-74 were not considered for this study due the greater stability of the Cu-, Ni- and Co-MOF-74 analogues.[44]

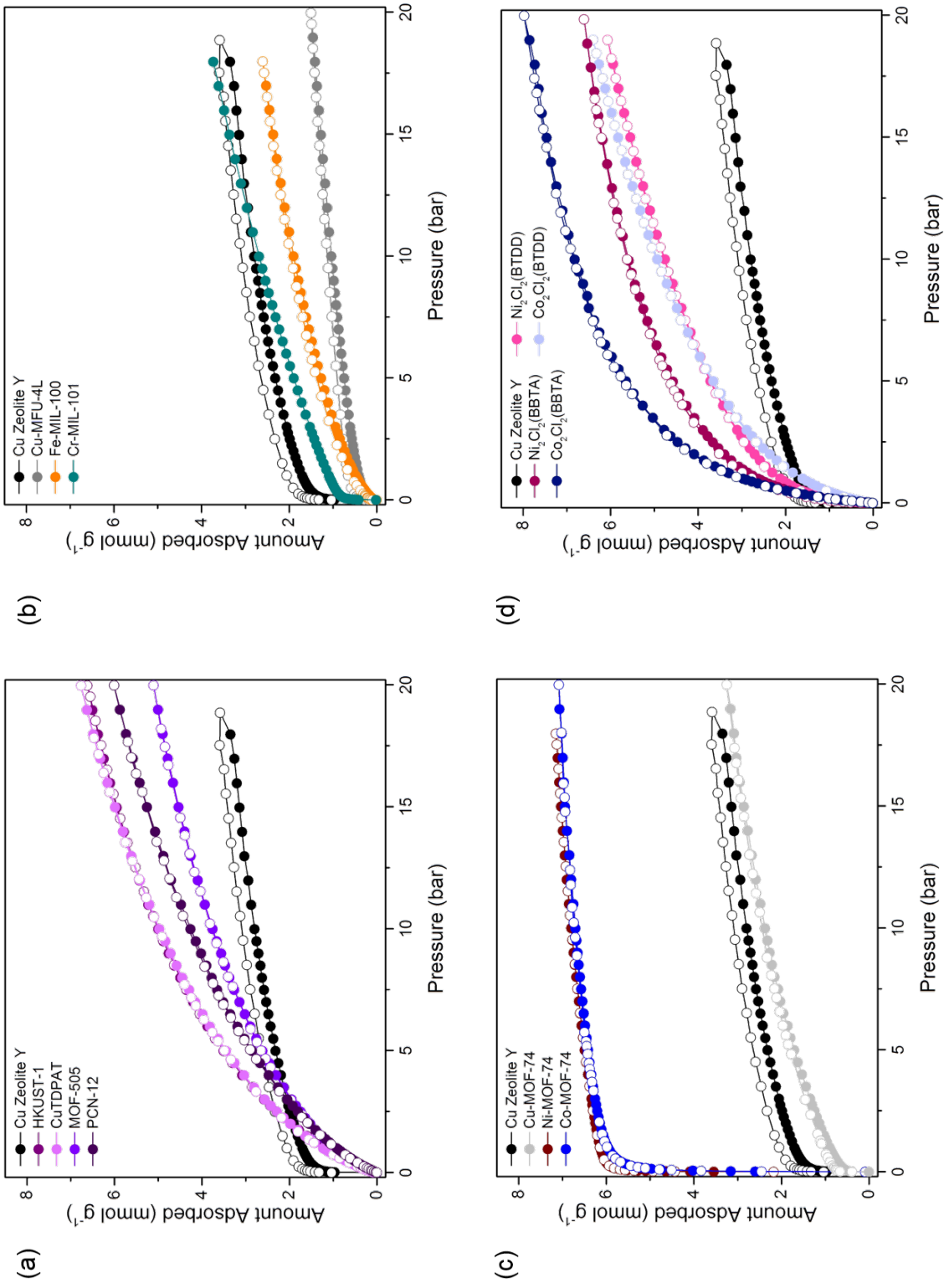


Figure 5-7. CO equilibrium sorption isotherms at 25 °C up to 20 bar using gravimetric gas sorption analysis of the: (a) Cu-Cu paddlewheel MOFs, (b) Cu^{+}-based MOF and mesoporous MOFs, (c) 1-D hexagonal pored M-MOF-74 structures and (d) 1-D hexagonal pored M_2Cl_2(BBTA) and M_2Cl_2(BTDD) structures. The isotherm for Cu-Zeolite Y is added on each panel for comparison.

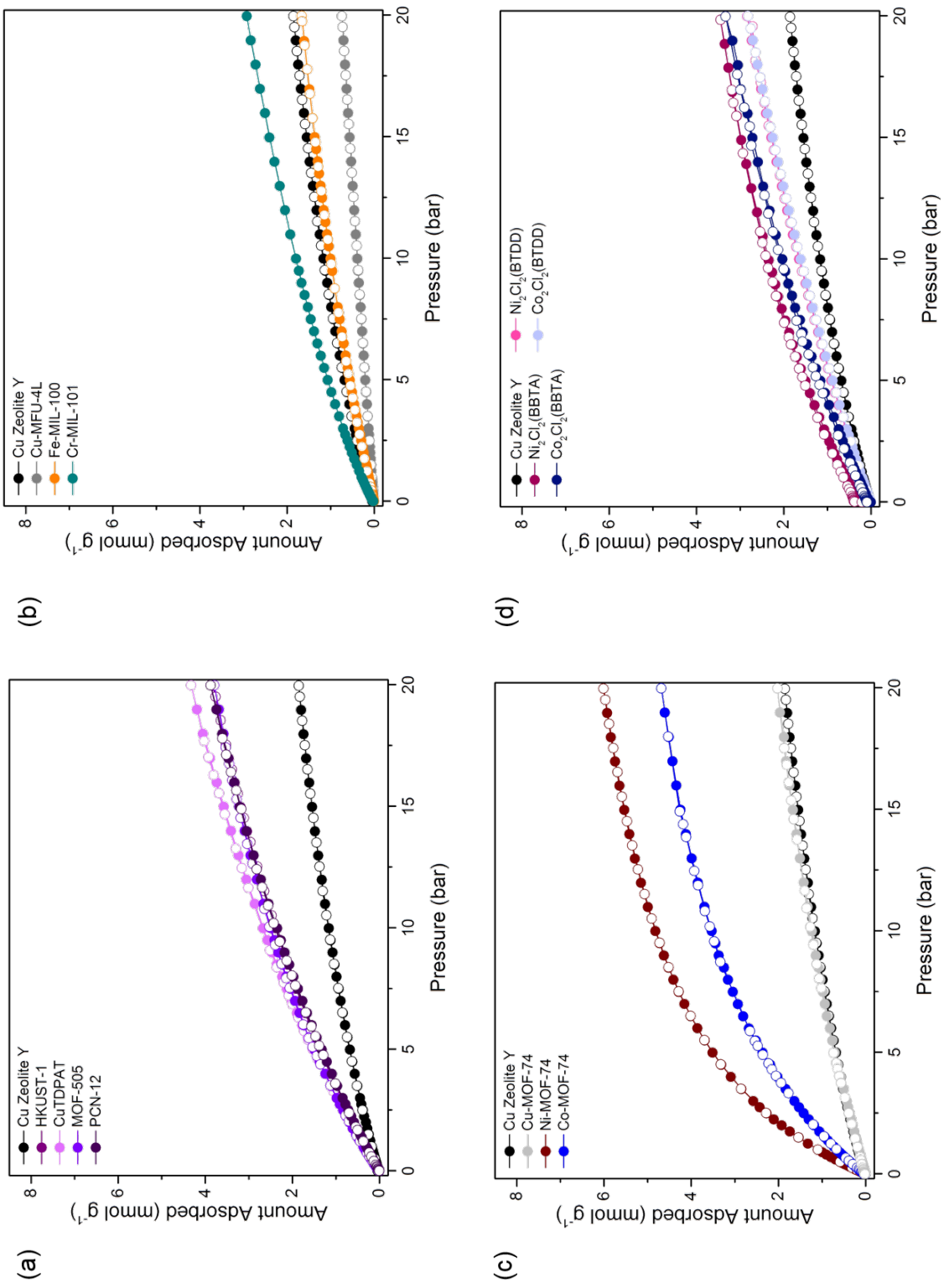


Figure 5-8. N_2 equilibrium sorption isotherms at 25 °C up to 20 bar using gravimetric gas sorption analysis of the: (a) Cu-Cu paddlewheel MOFs, (b) Cu^+-based MOF and mesoporous MOFs, (c) 1-D hexagonal pored M-MOF-74 structures and (d) 1-D hexagonal pored M_2Cl_2(BBTA) and M_2Cl_2(BTDD) structures. The isotherm for Cu-Zeolite Y is added on each panel for comparison.

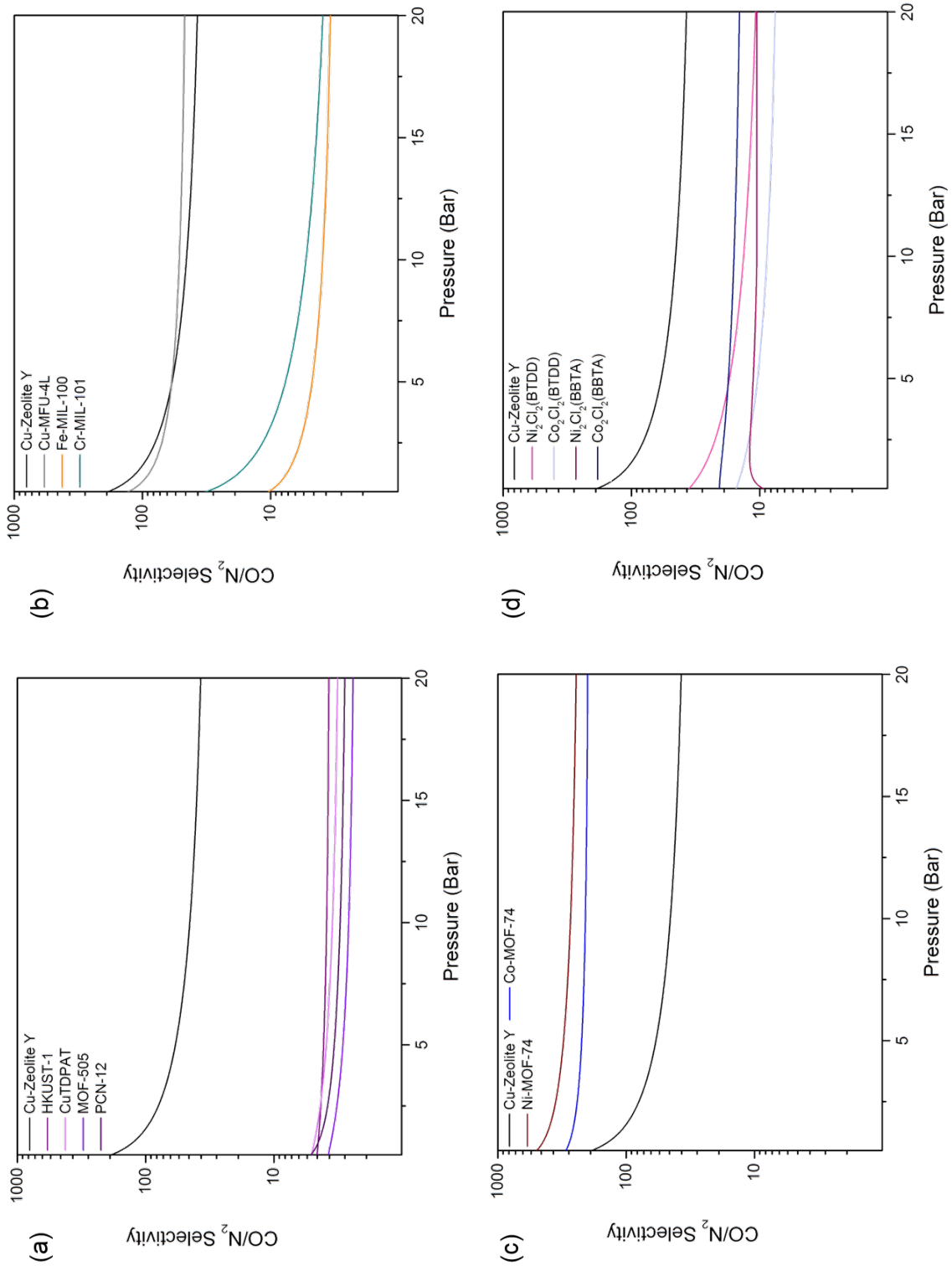


Figure 5-9. CO/N_2 (50:50 *v:v*) IAST selectivity at 25 °C up to 20 bar calculated from the CO and N_2 pure single component isotherms of: (a) Cu-Cu paddlewheel MOFs, (b) Cu^+-based MOF and mesoporous MOFs, (c) 1-D hexagonal pored M-MOF-74 structures and (d) 1-D hexagonal pored M_2Cl_2(BBTA) and M_2Cl_2(BTDD) structures. The isotherm for Cu-Zeolite Y is added on each panel for comparison.

Table 5-2. Summary of CO and N_2 equilibrium adsorption capacities, CO/N_2 IAST selectivity values (50:50 *v:v* CO:N_2) and dynamic CO uptake change values (50:50 *v:v* CO:N_2, obtained using the FRT instrument) at 25 °C and specified pressure.

Material	Dynamic testing (FRT) 0.5 bar	Equilibrium testing				
		1 bar			20 bar	
	CO uptake change (mmol g^{-1})	CO uptake (mmol g^{-1})	N_2 uptake (mmol g^{-1})	CO/N_2 (50:50 *v:v*) IAST selectivity*	CO uptake (mmol g^{-1})	N_2 uptake (mmol g^{-1})
Benchmark adsorbent						
Cu-Zeolite Y	0.84	1.70	0.19	260	3.46	1.85
Cu-Cu paddlewheel structure						
HKUST-1	0.18	1.16	0.32	5	6.62	3.83
MOF-505	0.30	0.97	0.37	4	5.11	3.79
CuTDPAT	0.46	1.23	0.34	5	6.77	4.32
PCN-12	0.12	0.92	0.30	5	6.01	3.88
Cu^{+} based structure						
Cu-MFU-4L	0.08	0.41	0.05	96	1.50	0.74
Mesoporous structure						
Fe-MIL-100	0.03	0.48	0.12	8	2.60	1.66
Cr-MIL-101	0.02	1.09	0.29	14	3.73	2.93
1-D hexagonal pored M-MOF-74 structure						
Cu-MOF-74	0.10	0.91	0.15	6†	3.25	2.02
Ni-MOF-74	3.05	6.14	1.09	446	7.15	6.01
Co-MOF-74	4.05	5.96	0.66	271	7.08	4.69
1-D hexagonal pored M_2Cl_2(BBTA) structure						
Ni_2Cl_2(BBTA)	1.03	2.62	0.57	11	6.61	3.45
Co_2Cl_2(BBTA)	1.12	2.97	0.29	20	7.98	3.33
1-D hexagonal pored M_2Cl_2(BTDD) structure						
Ni_2Cl_2(BTDD)	0.84	2.12	0.22	30	6.07	2.84
Co_2Cl_2(BTDD)	0.46	1.61	0.20	14	6.40	2.82

*IAST selectivity calculations are described in Section 5.4.1.2
† Denotes the ideal equilibrium selectivity calculation (Eq 3-19).

It is likely that the large CO/N_2 IAST selectivity values are inaccurate and overestimated, as it is difficult to accurately calculate the selectivity between two gases with large differences in polarities and binding energy.[42] With CO and N_2, the adsorbed phases become non-ideal. The issue is only overcome if one excludes the electrostatic interactions from the quadrupolar CO. However, these electrostatic interactions are responsible for the quasi-chemisorption forces which contributes largely to the CO

adsorption amount. This significant deviation from ideality with the IAST model at low pressure is highlighted further with M-MOF-74, resulting in IAST selectivity values of 446 and 271 for Ni-MOF-74 and Co-MOF-74 (Table 5-2, Figure 5-9).

The CO and N_2 isosteric heat of adsorption (CO and N_2 Q_{st}) values calculated from gas adsorption isotherms measured at 10, 25 and 40 °C for selected MOFs are shown in Table 5-3.

Table 5-3. CO and N_2 Q_{st} values of MOFs at low loading.

Material	**CO Q_{st} at low loading** (-kJ mol^{-1})	**N_2 Q_{st} at low loading** (-kJ mol^{-1})
HKUST-1	23.1	13.1
MOF-505	26.1	11.4
CuTDPAT	27.5	13.3
PCN-12	20.9	12.3
Ni-MOF-74	54.4	25.3
Co-MOF-74	43.8	19.4
Ni_2Cl_2(BBTA)	25.0	12.7
Co_2Cl_2(BBTA)	33.2	13.0
Ni_2Cl_2(BTDD)	39.1	12.9
Co_2Cl_2(BTDD)	32.9	12.1

The CO and N_2 Q_{st} plots, analytical fit and fitting parameters of the CO and N_2 isotherms at different temperatures and linear fit using the Van t'Hoff equation (Eq 5-12) for Ni-MOF-74 and Co-MOF-74 are shown in Appendix 4 as example calculations. The Q_{st} values at low loading (0-1 mmol g^{-1}) are presented due to anomalously high values at zero loading due to imperfect analytical fittings. The near-saturation of Ni-MOF-74 and Co-MOF-74 with CO observed at low pressure is reflected with the high heat of adsorption values calculated (Table 5-3) at low loading, as the Q_{st} values were calculated as -54.4 kJ mol^{-1} and -43.9 kJ mol^{-1}, respectively.

Cu-MOF-74 possesses the same structure and similar metal density and textural parameters as its Ni and Co analogues. Yet, its Cu^{2+} metal sites bind weakly to CO which results in low CO uptake and CO/N_2 ideal selectivity (Table 5-2, Figure 5-9). Analytical models used for Cu-MOF-74 did not provide a good fit for IAST calculations. Despite possessing a higher metal density, Cu-MOF-74 recorded lower uptake than the benchmark zeolite due to the presence of Cu^{+} ions in Cu-Zeolite Y. The stronger metal-CO interactions of CO result in a greater affinity towards CO than the Cu^{2+} unsaturated metal sites in Cu-MOF-74.

While the M-MOF-74 analogues provided a greater understanding upon the effect of the metal centres upon CO/N_2 separation, these analogues possess similar metal density and textural parameters. Therefore, M_2Cl_2(BBTA) and M_2Cl_2(BTDD) MOFs were used for further investigation as these 1-D hexagonal pored structures possess varying levels of metal density and porosity compared to M-MOF-74 (Table 5-1).

M-MOF-74 possesses the highest metal density of the 1-D hexagonal pored MOFs, and reducing the metal density in M_2Cl_2(BBTA) resulted in an expected decrease in CO capacity (2.62 and 2.97 mmol g^{-1} for Ni_2Cl_2(BBTA) and Co_2Cl_2(BBTA) *vs* 6.14 and 5.96 mmol g^{-1} for Ni-MOF-74 and Co-MOF-74 at 25 °C and 1 bar). While the H_2BBTA linker is a similar size to H_2DOBDC (M_2Cl_2(BBTA) pore window = 13 Å, M-MOF-74 pore window = 14 Å), the heavier Cl ions coordinated to M_2Cl_2(BBTA) reduces the metal density for both the Ni and Co analogues. Unlike M-MOF-74, higher pressures are required to saturate M_2Cl_2(BBTA) as CO uptake at higher pressure is governed to a larger degree by physisorption because of the weaker quasi-chemisorption forces relative to M-MOF-74. Therefore, M_2Cl_2(BBTA) possesses higher usable working capacity than M-MOF-74 from 1-20 bar at 25 °C.

The lowest metal density was attained by using the H_2BTDD organic linker (pore window = 23 Å) and resulted in the lowest CO uptakes of the 1-D hexagonal pored MOFs (2.12 and 1.61 mmol g^{-1} for Ni_2Cl_2(BTDD) and Co_2Cl_2(BTDD) at 25 °C and 1 bar). The coordinated Cl ions and larger organic linker resulted in a MOF structure with much lower crystallographic densities (0.76 and 0.74 g cm^{-3} for Ni_2Cl_2(BTDD) and Co_2Cl_2(BTDD), and 1.20 and 1.17 g cm^{-3} for Ni-MOF-74 and Co-MOF-74). As observed similarly with M_2Cl_2(BBTA), stronger physisorption results in higher CO uptake at elevated pressure.

The ratios of metal density and CO Q_{st} (Table 5-1) between M_2Cl_2(BTDD) and M-MOF-74 are similar, which reflects the influence of the quantity of unsaturated metal sites upon metal-CO binding. The low N_2 Q_{st} values of Ni_2Cl_2(BTDD) (-12.9 kJ mol^{-1}) and Co_2Cl_2(BTDD) (-12.1 kJ mol^{-1}) were expected for the highly mesoporous structures at low loading, while the higher M-MOF-74 N_2 adsorption uptake at low loading and pressure resulted in higher N_2 Q_{st} values (-23.5 and -19.4 kJ mol^{-1} for Ni-MOF-74 and Co-MOF-74)

The Cu-Cu paddlewheel based MOFs record lower CO uptake than Ni^{2+}- and Co^{2+}-based MOFs because of their weak Cu^{2+}-CO interactions. Their CO capacities are in line with that of Cu-MOF-74. Although the HKUST-1 metal density is greater than CuTDPAT (Table 5-1), CuTDPAT exhibits higher CO equilibrium capacity and CO/N_2 selectivity (Table 5-2). In fact, the trend of CO capacity follows the BET surface area, pore volume and micropore volume trends as opposed to the metal density. CuTDPAT recorded the highest BET surface area (2633 m^2 g^{-1}), while the least porous structure PCN-12 (1415 m^2 g^{-1}) recorded the lowest CO uptake at ambient conditions. At 20 bar, PCN-12 recorded higher CO uptake than MOF-505, which showcases the effect of the larger mesoporosity of PCN-12. The similar Q_{st} and CO/N_2 IAST selectivity

values of all the Cu-Cu paddlewheel structures also demonstrate the small influence of the metal density of Cu^{2+} sites.

Cu-MFU-4L recorded the lowest CO equilibrium capacity of all MOFs. The presence of Cu^{+} results in a high CO/N_2 IAST selectivity, however its active and accessible Cu^{+} content is low. The Fe^{3+} and Cr^{3+} ions present in Fe-MIL-100 and Cr-MIL-101 are also weakly binding to CO. This resulted in comparable equilibrium adsorption capacities (Table 5-2) to the Cu-Cu paddlewheel MOFs in spite of their higher metal densities.

5.5.3 *Dynamic adsorption*

In order to address the knowledge gap regarding the scarce number of studies measuring the CO dynamic capacity, FRT measurements were performed as a high throughput screening technique. The dynamic capacity results are shown in Table 5-2 alongside the equilibrium data. The dynamic CO capacity instrument is expressed as the change in adsorption upon release of the CO perturbation stream, as the samples are initially pre-saturated with the N_2 carrier gas with the FRT measurements.

The trends of the dynamic CO capacities largely follow the equilibrium capacities measured at the same conditions described in Section 5.5.2. Ni-MOF-74, Co-MOF-74, Ni_2Cl_2(BBTA) and Co_2Cl_2(BBTA) recorded higher CO dynamic capacities than Cu-Zeolite Y because of the strength of the Ni^{2+}-CO and Co^{2+}-CO binding mentioned in Section 5.5.2.

Ni_2Cl_2(BTDD) and Cu-Zeolite Y recorded the same dynamic capacity (0.84 mmol g^{-1}) despite Ni_2Cl_2(BTDD) possessing a higher equilibrium capacity. The measurements suggest that the equilibrium uptake of Cu-Zeolite Y is underestimated because of the poor sample activation (Cu^{2+} → Cu^{+} reduction) performed on the IGA. To replicate a flowing stream of CO for *in-situ* Cu reduction on the IGA, CO was manually cyclically

dosed and vented from the manifold to the sample cell. However, the FRT apparatus is able to flow CO as a continuous stream for sample activation for a greater degree of Cu^{2+} → Cu^{+} reduction. The dynamic capacity is not as high as anticipated because it is also possible that Cu^{2+} → Cu^{0} over reduction has occurred, which would result in a lower affinity to CO.

The Ni-MOF-74 dynamic capacity is lower than Co-MOF-74, despite Ni-MOF-74 possessing a higher equilibrium capacity. This observation is attributed to the exothermic heat released by M-MOF-74 during dynamic adsorption on the FRT apparatus. As there is no isothermal temperature regulation, the exothermic heat released during the short experimental duration impacts the sample's surroundings and raises the temperature. Ni-MOF-74 exhibits a higher CO heat of adsorption than Co-MOF-74 at low loading (-54.4 kJ mol^{-1} *vs* -43.9 kJ mol^{-1}), and therefore releases more heat upon adsorption, which reduces the dynamic CO uptake to a greater degree.

Alongside this observation, the FRT experimental set-up is accompanied with certain limitations that are responsible for deviations from expected values compared to the equilibrium data. Ideally under the same conditions, when the system has reached equilibrium after CO adsorption, the measured FRT capacity should equal the equilibrium capacity (Table 5-2). However, these values do not match for a number of reasons:

i) The CO partial pressure is 0.5 bar due to CO and N_2 mixing, rather than 1 bar which was the pressure of the equilibrium capacity measurements recorded.

ii) The range of the particles obtained by the sieves (80–120 μm) still results in experimental error with a potential uneven distribution of particle size despite sieving.

iii) It is difficult to replicate a consistent level of sample packing of the adsorbent bed for each sample, which leads to different degrees of pressure drop between the sample column and reference column.

iv) There are different methods of sample activation used, with ultra-high vacuum used for the gravimetric sorption analysis (equilibrium) and He and N_2 flow used for the FRT analysis (dynamic)

v) There is no isothermal temperature regulation.

Experimental variance from the synthesis also contributes a level of experimental error between the samples and measurements. Therefore, the FRT is mainly used as a high throughput dynamic testing technique to identify the best performing MOFs.

5.6 Conclusions

This chapter presents the synthesis, characterisation and preliminary screening and testing of MOFs for CO purification through CO/N_2 separation. After verifying successful synthesis through XRD analysis and N_2 BET sorption analysis at -196 °C, the MOFs equilibrium and dynamic capacities were measured using gravimetric sorption analysis and FRT. The results were compared to a benchmark adsorbent, Cu-Zeolite Y. The key findings are summarised below:

- The high CO capacities and selectivities recorded by the Ni^{2+}- and Co^{2+}-based MOFs confirm the hypothesis that the nature of the unsaturated metal sites is the most important property for CO/N_2 separation. Ni^{2+} and Co^{2+} exhibit the strongest metal-CO interactions of the metal centres tested.

- The density of unsaturated metal sites is the second most important property for CO/N_2 separation when the metal-CO interactions are governed by strong quasi-chemisorption forces (*i.e.* Ni^{2+}-CO and Co^{2+}-CO).
- However, when the metal-CO interactions are weak (*i.e.* Cu^{2+}-CO), the MOFs porosity of the textural parameters is the second most important property and governs the CO uptake.
- The discrepancies observed between the FRT and equilibrium capacity measurements are attributed to the experimental variance with the synthesis, differences in sample activation conditions between the instruments, and the pressure fluctuations associated with using the FRT instrument for adsorption measurements.
- The larger exothermic enthalpy of CO adsorption results in lower dynamic CO capacity than anticipated because of the increased temperature of the sample surroundings causing ‘desorption’ of the molecules.

5.7 References

1 Evans, A. D. *et al.* Screening Metal–Organic Frameworks for Dynamic CO/N_2 Separation Using Complementary Adsorption Measurement Techniques. *Industrial & Engineering Chemistry Research* **58**, 18336-18344, (2019).

2 Frohning, C. D., Kohlpaintner, C. W. & Bohnen, H. W. *Carbon monoxide and synthesis gas chemistry*. (2008).

3 Evans, A., Luebke, R. & Petit, C. The use of metal–organic frameworks for CO purification. *Journal of Materials Chemistry A* **6**, 10570-10594, (2018).

4 Dutta, N. N. & Patil, G. S. Developments in CO separation. *Gas Separation & Purification* **9**, 277-283, (1995).

5 Haase, D. J. & Walker, D. G. The COSORB Process. *Chemical Engineering Progress* **5**, 74-77, (1974).

6 Bloch, E. D. *et al.* Reversible CO Binding Enables Tunable CO/H_2 and CO/N_2 Separations in Metal–Organic Frameworks with Exposed Divalent Metal Cations. *Journal of the American Chemical Society* **136**, 10752-10761, (2014).

7 Karra, J. R. & Walton, K. S. Effect of Open Metal Sites on Adsorption of Polar and Nonpolar Molecules in Metal−Organic Framework Cu-BTC. *Langmuir* **24**, 8620-8626, (2008).

8 Reed, D. A. *et al.* A spin transition mechanism for cooperative adsorption in metal–organic frameworks. *Nature* **550**, 96-100, (2017).

9 Reed, D. A. *et al.* Reversible CO Scavenging via Adsorbate-Dependent Spin State Transitions in an Iron(II)–Triazolate Metal–Organic Framework. *Journal of the American Chemical Society* **138**, 5594-5602, (2016).

10 Sato, H. *et al.* Self-accelerating CO sorption in a soft nanoporous crystal. *Science* **343**, 167-170, (2014).

11 Duan, J. *et al.* High $CO_2/N_2/O_2/CO$ separation in a chemically robust porous coordination polymer with low binding energy. *Chemical Science* **5**, 660-666, (2014).

12 Regufe, M. J. *et al.* Syngas Purification by Porous Amino-Functionalized Titanium Terephthalate MIL-125. *Energy & Fuels* **29**, 4654-4664, (2015).

13 Wang, B., Cote, A. P., Furukawa, H., O'Keeffe, M. & Yaghi, O. M. Colossal cages in zeolitic imidazolate frameworks as selective carbon dioxide reservoirs. *Nature* **453**, 207-211, (2008).

14 Nickerl, G., Stoeck, U., Burkhardt, U., Senkovska, I. & Kaskel, S. A catalytically active porous coordination polymer based on a dinuclear rhodium paddle-wheel unit. *Journal of Materials Chemistry A* **2**, 144-148, (2014).

15 Britt, D., Tranchemontagne, D. & Yaghi, O. M. Metal-organic frameworks with high capacity and selectivity for harmful gases. *Proceedings of the National Academy of Sciences* **105**, 11623-11627, (2008).

16 Li, Y.-X. *et al.* Controlled Construction of Cu(I) Sites within Confined Spaces via Host–Guest Redox: Highly Efficient Adsorbents for Selective CO Adsorption. *ACS Applied Materials & Interfaces* **10**, 40044-40053, (2018).

17 Palmer, C., Sasegbon, A. & Hellgardt, K. In situ measurement of gas adsorption processes using Flux Response Technology. *Adsorption* **17**, 783-794, (2011).

18 Huang, Y.-Y. Selective adsorption of carbon monoxide and complex formation of cuprous-ammines in Cu (I) Y zeolites. *J Catal* **30**, 187-194, (1973).

19 Keller. A & R, S. in *AIChe Summer Meeting* (Denver, Colorado, 1988).

20 Luebke, R. *et al.* The unique rht-MOF platform, ideal for pinpointing the functionalization and CO_2 adsorption relationship. *Chemical Communications* **48**, 1455-1457, (2012).

21 Chui, S. S.-Y., Lo, S. M.-F., Charmant, J. P. H., Orpen, A. G. & Williams, I. D. A Chemically Functionalizable Nanoporous Material $[Cu_3(TMA)_2(H2O)_3]$n. *Science* **283**, 1148-1150, (1999).

22 Lin, X. *et al.* High Capacity Hydrogen Adsorption in Cu(II) Tetracarboxylate Framework Materials: The Role of Pore Size, Ligand Functionalization, and Exposed Metal Sites. *Journal of the American Chemical Society* **131**, 2159-2171, (2009).

23 Wang, X.-S. *et al.* Enhancing H_2 Uptake by "Close-Packing" Alignment of Open Copper Sites in Metal–Organic Frameworks. *Angewandte Chemie International Edition* **47**, 7263-7266, (2008).

24 Li, B., Chrzanowski, M., Zhang, Y. & Ma, S. Applications of metal-organic frameworks featuring multi-functional sites. *Coordination Chemistry Reviews* **307**, 106-129, (2016).

25 Murray, L. J., Dincă, M. & Long, J. R. Hydrogen storage in metal–organic frameworks. *Chemical Society Reviews* **38**, 1294-1314, (2009).

26 He, Y., Li, B., O'Keeffe, M. & Chen, B. Multifunctional metal–organic frameworks constructed from meta-benzenedicarboxylate units. *Chemical Society Reviews* **43**, 5618-5656, (2014).

27 Yoon, J. W. *et al.* Controlled Reducibility of a Metal–Organic Framework with Coordinatively Unsaturated Sites for Preferential Gas Sorption. *Angewandte Chemie International Edition* **49**, 5949-5952, (2010).

28 Zhao, T. *et al.* High-yield, fluoride-free and large-scale synthesis of MIL-101(Cr). *Dalton Transactions* **44**, 16791-16801, (2015).

29 Chen, G. *et al.* In Vitro Toxicity Study of a Porous Iron(III) Metal–Organic Framework. *Molecules* **24**, 1211, (2019).

30 Jeazet, H. B. T., Koschine, T., Staudt, C., Raetzke, K. & Janiak, C. Correlation of Gas Permeability in a Metal-Organic Framework MIL-101(Cr)–Polysulfone Mixed-Matrix Membrane with Free Volume Measurements by Positron Annihilation Lifetime Spectroscopy (PALS). *Membranes* **3**, 331-353, (2013).

31 Denysenko, D. *et al.* Elucidating Gating Effects for Hydrogen Sorption in MFU-4-Type Triazolate-Based Metal–Organic Frameworks Featuring Different Pore Sizes. *Chemistry – A European Journal* **17**, 1837-1848, (2011).

32 Denysenko, D., Grzywa, M., Jelic, J., Reuter, K. & Volkmer, D. Scorpionate-Type Coordination in MFU-4l Metal–Organic Frameworks: Small-Molecule Binding and Activation upon the Thermally Activated Formation of Open Metal Sites. *Angewandte Chemie International Edition* **53**, 5832-5836, (2014).

33 Weinrauch, I. *et al.* Capture of heavy hydrogen isotopes in a metal-organic framework with active Cu(I) sites. *Nature Communications* **8**, 14496, (2017).

34 Palomino Cabello, C., Gómez-Pozuelo, G., Opanasenko, M., Nachtigall, P. & Čejka, J. Metal–Organic Frameworks M-MOF-74 and M-MIL-100: Comparison of Textural, Acidic, and Catalytic Properties. *ChemPlusChem* **81**, 828-835, (2016).

35 Dietzel, P. D. C., Panella, B., Hirscher, M., Blom, R. & Fjellvåg, H. Hydrogen adsorption in a nickel based coordination polymer with open metal sites in the cylindrical cavities of the desolvated framework. *Chemical Communications*, 959-961, (2006).

36 Grant Glover, T., Peterson, G. W., Schindler, B. J., Britt, D. & Yaghi, O. MOF-74 building unit has a direct impact on toxic gas adsorption. *Chemical Engineering Science* **66**, 163-170, (2011).
37 Rieth, A. J. & Dincă, M. Controlled Gas Uptake in Metal–Organic Frameworks with Record Ammonia Sorption. *Journal of the American Chemical Society* **140**, 3461-3466, (2018).
38 Rieth, A. J., Tulchinsky, Y. & Dincă, M. High and Reversible Ammonia Uptake in Mesoporous Azolate Metal–Organic Frameworks with Open Mn, Co, and Ni Sites. *Journal of the American Chemical Society* **138**, 9401-9404, (2016).
39 Talu, O. Needs, status, techniques and problems with binary gas adsorption experiments. *Advances in Colloid and Interface Science* **76-77**, 227-269, (1998).
40 Mason, J. A., Sumida, K., Herm, Z. R., Krishna, R. & Long, J. R. Evaluating metal–organic frameworks for post-combustion carbon dioxide capture via temperature swing adsorption. *Energy & Environmental Science* **4**, 3030-3040, (2011).
41 Myers, A. L. & Prausnitz, J. M. Thermodynamics of mixed-gas adsorption. *AIChE Journal* **11**, 121-127, (1965).
42 Cessford, N. F., Seaton, N. A. & Düren, T. Evaluation of Ideal Adsorbed Solution Theory as a Tool for the Design of Metal–Organic Framework Materials. *Industrial & Engineering Chemistry Research* **51**, 4911-4921, (2012).
43 Chaires, J. B. Possible origin of differences between van't Hoff and calorimetric enthalpy estimates. *Biophysical Chemistry* **64**, 15-23, (1997).
44 Jiao, Y. *et al.* Tuning the Kinetic Water Stability and Adsorption Interactions of Mg-MOF-74 by Partial Substitution with Co or Ni. *Industrial & Engineering Chemistry Research* **54**, 12408-12414, (2015).

Chapter 6 CO/N_2 dynamic separation studies

Aspects of the work presented in this chapter has been written in the form of a manuscript which has been accepted by Industrial & Engineering Chemistry Research.[1]

6.1 Introduction

CO and N_2 equilibrium capacities and theoretical CO/N_2 selectivity values provide useful understanding of a MOF separation performance. However, the measurements are time-consuming and the static gas sorption experimental conditions are not realistic for large-scale industrial purification due to the unrepresentative gas mixtures, yet are currently widely used for CO separation studies.[2] Furthermore, the IAST values prove to be inaccurate with polar CO and non-polar N_2 molecules, especially at low pressure.[3] Therefore, dynamic CO/N_2 separation measurements are required for accurate selectivity and CO capacity values for a $CO:N_2$ mixture. While flux response technology is an effective throughput screening method for dynamic measurements, this technique is unable to perform separation measurements and has its shortcomings, as discussed in Section 5.5.3. For dynamic separation measurements, the CO and N_2 breakthrough times and capacities are dependent on both the CO and N_2 equilibrium capacities and CO/N_2 selectivity. Therefore, the CO breakthrough capacity is a measurement used to evaluate these equilibrium adsorption measurements as a single metric.

To date, there have been few studies on the dynamic CO separation performance of MOFs.[4-11] From these measurements, $CO:N_2$ breakthrough measurements of Rh-DUT-82 were performed, however no N_2 curves were presented to show the CO/N_2

separation performance. PCP-1[4] exhibited poor CO/N_2 separation ability in a multicomponent CO_2:CO:O_2:N_2 stream, while Fe-MIL-100[9] also showed similarly low CO breakthrough capacities for a CO:N_2 stream. Cu impregnated Fe-MIL-100 drastically improved the CO/N_2 separation performance.[9] Cu impregnation upon Fe-MIL-100 showcased high CO/N_2 IAST selectivity,[10] but only CO:CO_2 breakthrough measurements were performed and CO:N_2 mixtures were used solely for cyclability tests. CO:CO_2 breakthrough measurements have also been conducted on M-MOF-74 to demonstrate the reverse CO_2/CO selectivity of Mg-MOF-74 compared to the CO/CO_2 selectivity of Ni- and Co-MOF-74.[11] M_2Cl_2(BBTA) and M_2Cl_2(BTDD) structures have previously been reported for CO/N_2 separation,[12] however no dynamic separation studies were presented. IAST selectivity up to 1 bar was reported, as the focus was on the spin transition mechanism of Fe^{2+} for CO binding. To summarise, there have been no studies investigating the effect of N_2 impurity concentration on CO/N_2 separation ability.

This chapter investigates the CO/N_2 separation ability of the two best performing MOFs from the preliminary screening (Chapter 5); *i.e* Ni-MOF-74 and Co-MOF-74. By varying the inlet N_2 feed concentration, the effect of the impurity level upon CO breakthrough capacity, CO/N_2 selectivity and separation factor was studied. The effects of varying the metal density and pore size of the 1-D hexagonal pored structure were also investigated using M_2Cl_2(BBTA) and M_2Cl_2(BTDD) MOFs.

It was hypothesized that Co-MOF-74 would exhibit the best CO/N_2 separation ability because of its higher CO dynamic capacity recorded on the FRT instrument. Furthermore, it was expected that the M_2Cl_2(BBTA) and M_2Cl_2(BTDD) MOFs would be largely ineffective for CO/N_2 separation because of their lower metal density. It was

predicted that decreasing the level of N_2 impurity would result in higher breakthrough capacity and CO/N_2 selectivity, as this would increase the feed CO partial pressure.

6.2 Materials synthesis

A total of 6 MOFs were tested on the breakthrough column instrument for dynamic CO/N_2 separation. Details of the materials synthesis of the MOFs can be found in Section 5.2. The MOFs tested include Co-MOF-74, Ni-MOF-74, Ni_2Cl_2(BBTA), Co_2Cl_2(BBTA), Ni_2Cl_2(BTDD) and Co_2Cl_2(BTDD). A benchmark patented adsorbent used for CO/N_2 separation, Cu-Zeolite Y,[13] was also tested for comparison with the selected MOFs.

6.3 Materials testing

The dynamic breakthrough adsorption capacities of the selected MOFs and zeolite were performed using a breakthrough column instrument. The fundamentals and theory of this technique are explained in Section 3.2.2. The apparatus schematic (Figure 3-2) and experimental procedure are shown in Section 3.2.3. The inlet feed concentrations of the $CO:N_2$ binary mixture were set depending on the level of N_2 impurity used for investigation. The activation conditions used are outlined in Section 5.2. The full derivations and equations used for the CO breakthrough capacity, CO/N_2 selectivity and separation factor calculations are shown in Section 3.3.2.

6.4 Results and discussion

6.4.1 *Equimolar $CO:N_2$ breakthrough analysis*

Dynamic breakthrough adsorption testing on Cu-Zeolite Y, Ni-MOF-74 and Co-MOF-74 was initially performed using a 50:50 *v:v* $CO:N_2$ mixture at 25 °C and a total

pressure of 1 bar. Experiments were repeated 3 times for Co-MOF-74 for error analysis. Figure 6-1 displays the breakthrough curves of CO and N_2 for a normalised experimental sample mass for Cu-Zeolite Y, Ni-MOF-74 and Co-MOF-74.

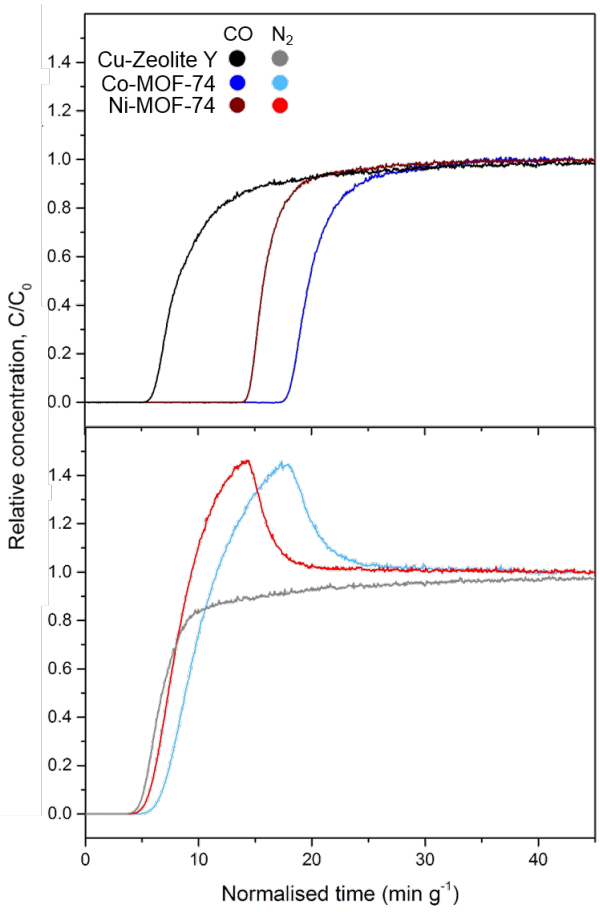


Figure 6-1. CO and N_2 breakthrough curves of Cu-Zeolite Y, Co-MOF-74 and Ni-MOF-74 for a 50:50 *v:v* CO:N_2 binary gas mixture measured on a breakthrough adsorption column instrument at 25 °C and 1 bar.

For the 50:50 *v:v* CO:N_2 mixture, N_2 breaks through first, as anticipated, for Cu-Zeolite Y (3.7 min g^{-1}), Ni-MOF-74 (4.0 min g^{-1}) and Co-MOF-74 (4.8 min g^{-1}) due to the weaker physisorption forces responsible for adsorption to non-polar N_2 (Figure 6-1). The calculated N_2 Q_{st} (Table 5-3) also accounts for this observation and the low N_2 breakthrough capacities (0.68 and 1.04 mmol g^{-1} for Ni-MOF-74 and Co-MOF-74, respectively). CO breakthrough capacities – 1.05, 4.49 and 5.40 mmol g^{-1} for Cu-

Zeolite Y, Ni-MOF-74 and Co-MOF-74, respectively – are expectedly higher than the N_2 breakthrough capacities due to the strong interactions between CO and the unsaturated metal sites.

Generally, the CO breakthrough curves are steeper than the N_2 curves due to the smaller mass transfer zone during dynamic adsorption, which indicates faster CO adsorption kinetics. The Type I shape of the Cu-Zeolite Y and M-MOF-74 CO isotherms (Figure 5-3) indicates a reduced mass transfer zone during dynamic adsorption with short equilibrium times.

The breakthrough adsorption measurements have partial pressures of 0.5 bar for both CO and N_2 for this mixture. The Cu-Zeolite Y CO breakthrough capacity (1.05 mmol g^{-1}) is lower than the equilibrium CO uptake measured at 0.5 bar and 25 °C (1.55 mmol g^{-1}, Figure 5-3). As with the $Cu^{2+} \rightarrow Cu^{+}$ reduction on the FRT, it is also possible that $Cu^{2+} \rightarrow Cu^{0}$ reduction has also occurred.

The Co-MOF-74 CO breakthrough capacity (5.40 mmol g^{-1}) is close to the equilibrium CO uptake measured at 0.5 bar and 25 °C (5.74 mmol g^{-1}, Figure 5-3). On the other hand, the Ni-MOF-74 CO breakthrough capacity (4.49 mmol g^{-1}) is much lower than its equilibrium adsorption uptake at 0.5 bar and 25 °C (6.04 mmol g^{-1}, Figure 5-3). This observation is attributed to the heat released by M-MOF-74 during dynamic adsorption on the breakthrough column, which is also exhibited with the FRT apparatus (discussed in Section 5.5.3). As there is no isothermal temperature regulation, the Co- and Ni-MOF-74 breakthrough times are short and the exothermic heat released raises the temperature of the sample's surrounding. Ni-MOF-74 exhibits a higher CO heat of adsorption than Co-MOF-74 (-54.4 kJ mol^{-1} *vs* -43.9 kJ mol^{-1}), and therefore releases

more heat upon adsorption, consequently reducing the dynamic CO uptake to a greater degree.

The M-MOF-74 CO breakthrough curves are steep, which is desirable for industrial processes. Steep breakthrough curves result in a larger amount of functional capacity that is close to the adsorbent saturation capacity, discussed in Section 3.3. The Ni-MOF-74 breakthrough curve is slightly steeper than the Co-MOF-74 curve observed in Figure 6-1, because of its faster CO adsorption kinetics and greater exothermic enthalpy change. The N_2 breakthrough time and capacity of Ni-MOF-74 is lower than anticipated when compared to its equilibrium capacity, also because of the heat released from CO adsorption inducing N_2 desorption.

After N_2 saturation, the Ni- and Co-MOF-74 N_2 breakthrough curves continue to climb above the initial N_2 inlet feed concentration C/C_0 and produce a roll-up effect (Figure 6-1). This effect occurs because of the incoming CO from the feed inlet continuing to adsorb, which desorbs the bound N_2 and produces a spike in N_2 concentration at the detector that exceeds the inlet feed concentration. This phenomenon is observed when there is competitive binding and significant adsorption uptake of the light product, as seen with N_2. This competitive behaviour is supported by the MOF's greater binding strength to CO over N_2, confirmed by the calculated Q_{st} values (Table 5-3).

The presence of Cu^{2+}, Cu^{+} and Cu^{0} sites of Cu-Zeolite Y are responsible for the different observations compared to M-MOF-74. No roll-up effect is observed with Cu-Zeolite Y (Figure 6-1) because of the lower CO uptake, the remaining Cu^{2+} sites of the zeolite contributes to N_2 sorption which reduces the number of sites for CO sorption. The Cu-Zeolite Y CO breakthrough curve is less steep than all the MOF breakthrough

curves and results in an undesired larger mass transfer zone. It is proposed that there is chemisorption to Cu^0 sites that have emerged from over reduction of Cu^+ upon heating, which slows the CO adsorption kinetics.

6.4.2 *Varying CO:N_2 compositions analysis*

The effect of varying the N_2 impurity level on the Co- and Ni-MOF-74 CO breakthrough capacity, CO/N_2 ideal selectivity and separation factor was investigated. The CO and N_2 breakthrough curves for Co- and Ni-MOF-74 at 25 °C and 1 bar are shown in Figure 6-2. The following CO:N_2 inlet feed compositions were selected: 5:95, 30:70, 50:50, 70:30, 95:5 (*v:v*). Experiments were repeated 3 times for Co-MOF-74 for error analysis.

While observing both Co- and Ni-MOF-74 breakthrough curves, the 5% CO feed concentration exhibits the longest breakthrough time (106.5 and 70 min g^{-1} for Co-MOF-74 and Ni-MOF-74). Yet, the CO breakthrough time of the 5% feed is very long, as the total exothermic enthalpy of CO adsorption and heat release across the column is dissipated over a long duration (approximately 21 min for ~200 mg of sample), and has minimal effect upon the temperature of the sample's surroundings.

The slow heat release results in the lowest overall experimental temperature increase upon CO breakthrough, from all of the CO concentrations tested. Large concentration feeds of CO (70 and 95%) exhibit similar breakthrough times (11.9 and 10.7 min g^{-1} for Co-MOF-74) and the steepest breakthrough curves. Indeed, the largest heat released during the quick saturation of the adsorbent bed contributes to faster kinetics. Ni-MOF-74 exhibits the same trends and behaviour as Co-MOF-74, albeit with shorter breakthrough times due to its larger exothermic enthalpy change (Table 5-3) and lower breakthrough capacity (Figure 6-2e).

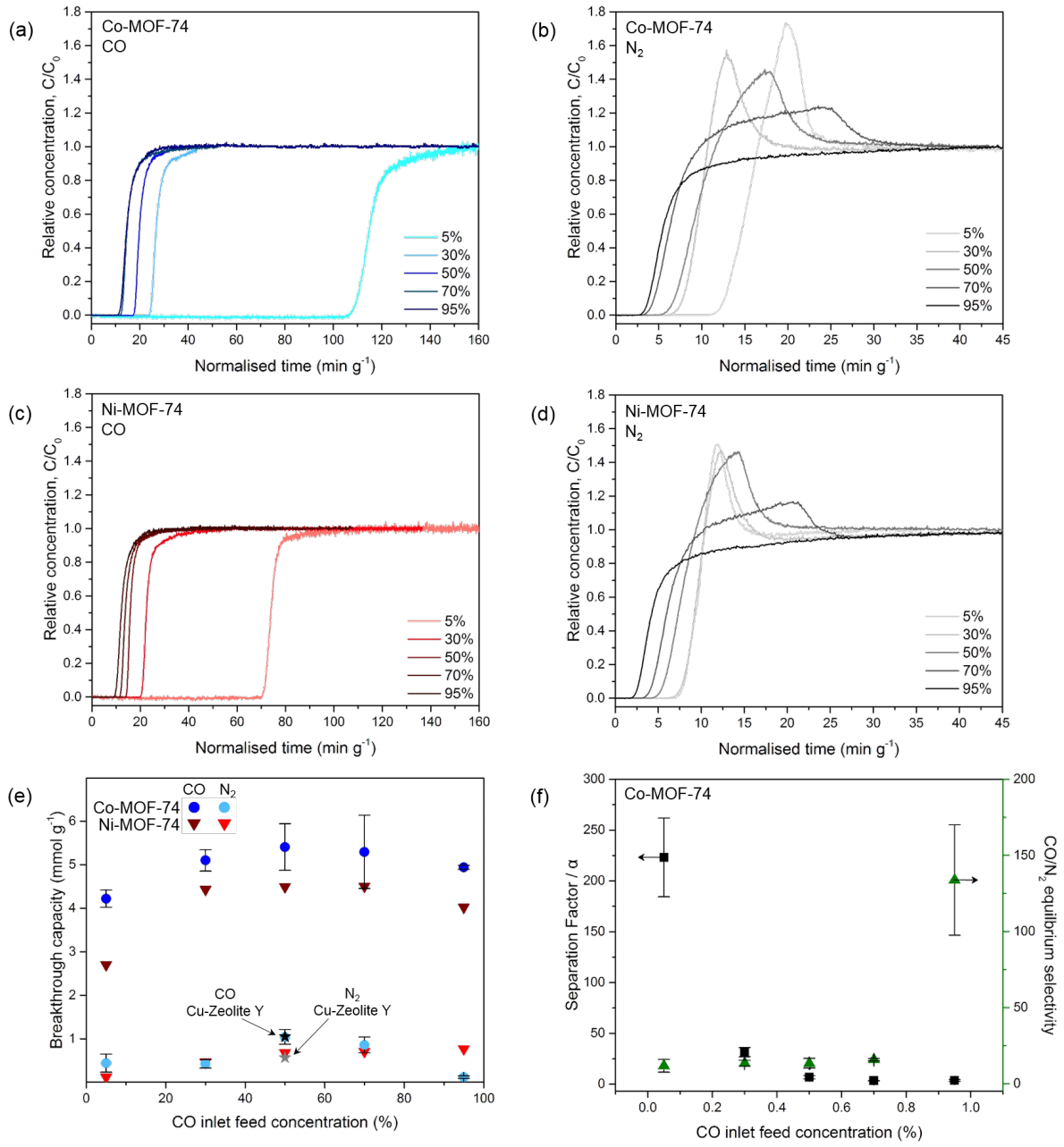


Figure 6-2. (a) CO and (b) N_2 breakthrough curves of a binary mixture (5:95, 30:70, 50:50, 70:30, 95:5 *v:v* CO:N_2 inlet feed concentration) for Co-MOF-74 at 25 °C and 1 bar. (c) CO and (d) N_2 breakthrough curves of a binary mixture (5:95, 30:70, 50:50, 70:30, 95:5 *v:v* CO:N_2 inlet feed concentration) for Ni-MOF-74 at 25 °C and 1 bar. (e) The CO and N_2 breakthrough capacities of Co-MOF-74 (circles) and Ni-MOF-74 (triangles) at varying inlet feed concentrations. The Cu-Zeolite Y breakthrough capacities at 50:50 *v:v* CO:N_2 are shown on the figure. (f) The separation factor (squares) and CO/N_2 equilibrium ideal selectivity (triangles) of Co-MOF-74 at varying inlet feed concentrations.

Figure 6-2 displays the Co-MOF-74 and Ni-MOF-74 N_2 breakthrough curves at varying CO:N_2 inlet feed concentrations and illustrates its influence upon the roll-up effect previously mentioned earlier (Figure 6-1). A characteristic of the roll-up effect is the overshooting peak of N_2 relative concentration after breakthrough, and its shape and broadness is dependent on the concentration of the competitively adsorbing CO which displaces the N_2. As seen in Figure 6-2b and Figure 6-2d with Co- and Ni-MOF-74, this peak becomes sharper and reaches a higher C/C_0 relative concentration with decreasing N_2 inlet feed concentration. The larger CO concentration front desorbs the weakly bound N_2 more readily due to the exothermic enthalpy change upon CO adsorption. The heat release generates a sharper decay of the overshot curve and faster N_2 desorption. As CO feed concentration decreases, the N_2 peak becomes broader and the decay slower because the heat dissipation is spread over a longer duration. The most dilute CO stream (5%) produces a negligible roll-up effect due to the small quantity of competitively adsorbing CO, which also induces minimal N_2 desorption.

Figure 6-2e displays the calculated breakthrough CO and N_2 capacities for Co- and Ni-MOF-74 with varying CO inlet feed concentrations at 25 °C and 1 bar. Co- and Ni-MOF-74 exhibit the same trends with varying inlet concentrations. At the 5% CO inlet feed concentration, the CO partial pressure (0.05 bar) is below its saturation point *i.e.* 0.2 bar (see Figure 5-3). This results in the lowest breakthrough capacities recorded at 25 °C and 1 bar (4.22 and 2.70 mmol g^{-1} for Co-MOF-74 for Ni-MOF-74). The breakthrough capacities at 30% CO inlet feed concentrations and above generally increase because of the stronger interactions operating at higher CO partial pressure.

Upon increasing the CO inlet feed concentration to 70% and above, the CO breakthrough capacity decreases below the 50% level. As explained above, the

exothermic CO adsorption during quick CO breakthrough at 75% and 90% CO concentration raises the temperature of the adsorbent bed. This results in lower uptakes than anticipated.

The N_2 breakthrough capacities are likely to be overestimated due to the roll-up effect phenomena (discussed in Section 6.4.1). Indeed, when CO breaks through after N_2, the quantity of displaced N_2 due to the incoming CO is not subtracted. However, due to the low N_2 partial pressure, this value is negligible. At 95% CO inlet feed concentration, the N_2 partial pressure is 0.05 bar, which results in the lowest N_2 breakthrough capacities. The N_2 breakthrough capacity at 5% CO inlet feed concentration provided the most accurate N_2 breakthrough capacity measurement, as the roll-up effect is limited due to the low CO concentration and longer heat dissipation. Two of the intermediate N_2 concentrations (50 and 70% CO inlet feed concentrations) resulted in the most significant overestimations of N_2 breakthrough capacities, as these compositions recorded notable N_2 uptake and a significant roll-up effect.

After CO and N_2 breakthrough are complete, and the outlet feed concentrations equal inlet feed concentrations, the adsorbent bed is in equilibrium with the binary gas mixture. At this point, it is possible to calculate the saturation capacity and calculate the CO/N_2 ideal selectivities and separation factors (α) at varying CO:N_2 compositions. Selectivity, alongside an adsorbent's capacity, is an important metric to consider in an adsorption separation process in order to optimise purity, recovery and number of cycles. Literature simulation studies have shown that a separation process must possess a separation factor above 3 to be viable[14] and maintain desired levels of purity of the targeted component.

As error analysis was performed on Co-MOF-74, selectivity and separation factor calculations were applied more reliably for this MOF. The CO/N_2 ideal selectivity values for Co-MOF-74 at 25 °C and 1 bar all exceed 11, while all separation factor values exceed 3 (Figure 6-2f, calculations shown in Eq 3-19 and 3-20). In addition, different correlations are observed with respect to increasing CO feed concentration. CO/N_2 selectivity at 95% CO feed concentration (134) is much larger than at more dilute CO concentrations (< 16). Its high selectivity is governed by the lower N_2 partial pressures, as increasing the CO partial pressures above 0.2 bar has a minor influence on CO/N_2 selectivity. Co-MOF-74 exhibits the greatest separation factor at 5% CO feed concentration (223). This observation is due to the long time taken for the dilute CO stream to saturate the bed, resulting in the largest difference in breakthrough times between N_2 and CO (2.6 and 106.5 min g^{-1}).

6.4.3 *1-D hexagonal pored MOF structure comparison*

The effect of varying the pore size and metal density upon the Ni- and Co-MOF-74 dynamic CO/N_2 separation performance was investigated by performing 50:50 *v:v* $CO:N_2$ breakthrough measurements (25 °C and 1 bar) on their M_2Cl_2(BBTA) and M_2Cl_2(BTDD) structural analogues. The CO and N_2 breakthrough curves are shown in Figure 6-3, alongside their equivalent CO breakthrough capacities and CO/N_2 selectivities.

Despite all structures possessing Ni^{2+} and Co^{2+} metal centres, M-MOF-74 exhibited larger CO breakthrough capacities than M_2Cl_2(BBTA) and M_2Cl_2(BTDD) because of their higher density of unsaturated metal sites. As seen in Figure 6-3a and b, Co-MOF-74 and Ni-MOF-74 possess the longest breakthrough times and largest capacities, as

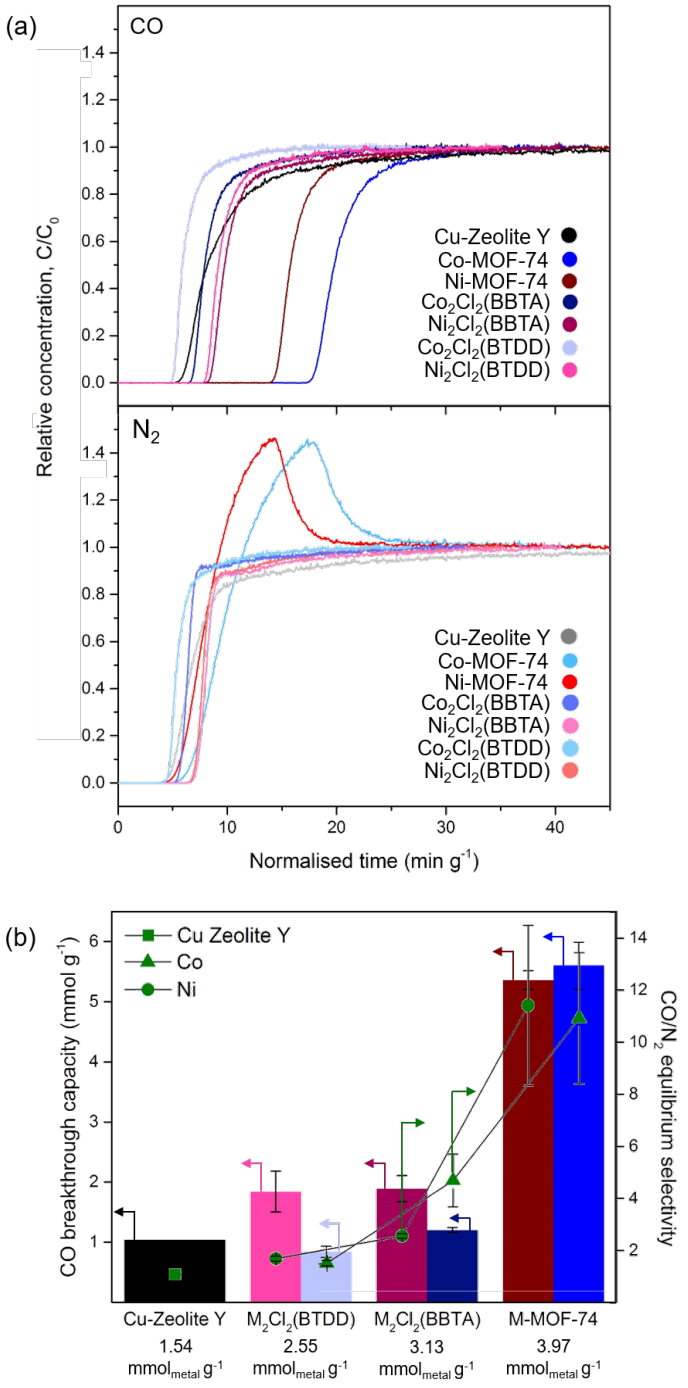


Figure 6-3. (a) CO and N_2 breakthrough curves, (b) CO breakthrough capacities and CO/N_2 ideal equilibrium selectivities of Cu-Zeolite Y, Co-MOF-74, Ni-MOF-74, Co_2Cl_2(BBTA), Ni_2Cl_2(BBTA), Co_2Cl_2(BTDD) and Ni_2Cl_2(BTDD) for a 50:50 *v:v* $CO:N_2$ binary gas mixture measured on a breakthrough adsorption column instrument at 25 °C and 1 bar.

expected from the large CO equilibrium adsorption capacities and IAST CO/N_2 selectivities (Table 5-2). The shorter CO breakthrough times of the M_2Cl_2(BBTA) and M_2Cl_2(BTDD) MOFs are reflected with their lower breakthrough capacities, as shown in Figure 6-3b. Overall, the Ni^{2+}-based MOFs exhibited the longest breakthrough times and largest breakthrough capacities, which indicates greater CO/N_2 dynamic separation performance with Ni^{2+}-centres compared to the Co^{2+}-centres. However, the M-MOF-74 analogues did not follow the same trend due to the high exothermic enthalpy of CO adsorption (Table 5-3) of Ni-MOF-74, associated with its larger quantity of unsaturated metal sites.

As the highly mesoporous M_2Cl_2(BTDD) structures performed similarly to the M_2Cl_2(BBTA) structures. It was deduced that the total pore volume resulting from the M_2Cl_2(BTDD) mesoporosity has a small influence upon CO/N_2 separation at atmospheric pressure. It is hypothesized M_2Cl_2(BTDD) CO/N_2 breakthrough separation at higher pressure would exhibit larger CO breakthrough capacity, CO/N_2 separation factor and selectivity. The low N_2 breakthrough capacities of these MOFs also resulted in no observable roll-up effect (explained in Section 6.4.1). The lower quantity of competitively binding CO and adsorbed N_2 adsorbed is responsible for this negligible effect.

The CO/N_2 selectivites of the M_2Cl_2(BBTA) MOFs are higher than the M_2Cl_2(BTDD) MOFs and Cu-Zeolite Y, indicating that the density of unsaturated metal sites impact the adsorbent's selectivity. The M-MOF-74 structures exhibit considerably higher CO/N_2 selectivities, however are much lower than the IAST values because of its overestimation with polar CO and non-polar N_2.[3]

The difference in activation procedures for Cu reduction using flowing CO (dynamic activation) and cycled CO (static activation) are exhibited with the similar breakthrough capacities of Cu-Zeolite Y and Co_2Cl_2(BBTA) and Co_2Cl_2(BTDD) MOFs (Figure 6-3b). The improved Cu reduction procedure on the FRT and breakthrough column instrument highlights the importance of generating Cu^+ sites, as the equilibrium adsorption uptake is underestimated due to inefficient activation and reduction.

6.5 Conclusions

This chapter presents the CO/N_2 separation ability of the two best performing MOFs from Chapter 5- Ni-MOF-74 and Co-MOF-74. The dynamic studies on the breakthrough column enabled us to evaluate these MOFs CO/N_2 separation performance while studying the effect of varying N_2 impurity level. Subsequently, the effect of varying the pore size and metal density of the M-MOF-74 structures was investigated by testing related 1-D hexagonal pored structures M_2Cl_2(BBTA) and M_2Cl_2(BTDD) on the breakthrough column. The key findings are summarised below:

- The highest dynamic CO capacity measured by a MOF on the FRT apparatus for single component measurements also resulted into the best CO/N_2 separation performance, as hypothesized.
- Significantly large exothermic enthalpy of adsorption resulted in reduced CO breakthrough capacity due to its greater heat release.
- The dynamic CO/N_2 separation performance is governed largely by the density of unsaturated metal sites. Higher pressures are required for CO/N_2 separation to capitalise on structures with larger total pore volume which result in larger working capacity.

- MOFs that possess a high density of unsaturated metal sites with strong π-complexation interactions resulted in favourable smaller mass transfer zones. The advantage of faster kinetics mean that the usable adsorption capacity in a process is close to the saturation capacity.
- MOFs with both a high density of unsaturated metal sites and strong metal-CO interactions reach saturation at low pressure. Therefore for these MOFs, a change in CO partial pressure does not impact selectivity as much as a change in N_2 partial pressure.
- The CO/N_2 selectivity values for a $CO:N_2$ mixture are much lower than the overestimated IAST CO/N_2 selectivity values with polar CO and non-polar N_2.
- Inaccurate Cu^+ reduction leads to lower CO capacity and slower sorption kinetics.
- With competitive binding between CO and N_2 and significant exothermic CO enthalpy of adsorption, it is difficult to accurately measure the N_2 capacity from a breakthrough binary mixture. The roll-up effect qualitatively shows the degree of N_2 desorption upon CO adsorption, relative to the inlet feed concentration.

6.6 References

1 Evans, A. D. *et al.* Screening Metal–Organic Frameworks for Dynamic CO/N_2 Separation Using Complementary Adsorption Measurement Techniques. *Industrial & Engineering Chemistry Research* **58**, 18336-18344, (2019).

2 Evans, A., Luebke, R. & Petit, C. The use of metal–organic frameworks for CO purification. *Journal of Materials Chemistry A* **6**, 10570-10594, (2018).

3 Cessford, N. F., Seaton, N. A. & Düren, T. Evaluation of Ideal Adsorbed Solution Theory as a Tool for the Design of Metal–Organic Framework Materials. *Industrial & Engineering Chemistry Research* **51**, 4911-4921, (2012).

4 Duan, J. *et al.* High $CO_2/N_2/O_2/CO$ separation in a chemically robust porous coordination polymer with low binding energy. *Chemical Science* **5**, 660-666, (2014).

5 Regufe, M. J. *et al.* Syngas Purification by Porous Amino-Functionalized Titanium Terephthalate MIL-125. *Energy & Fuels* **29**, 4654-4664, (2015).

6 Wang, B., Cote, A. P., Furukawa, H., O'Keeffe, M. & Yaghi, O. M. Colossal cages in zeolitic imidazolate frameworks as selective carbon dioxide reservoirs. *Nature* **453**, 207-211, (2008).

7 Nickerl, G., Stoeck, U., Burkhardt, U., Senkovska, I. & Kaskel, S. A catalytically active porous coordination polymer based on a dinuclear rhodium paddle-wheel unit. *Journal of Materials Chemistry A* **2**, 144-148, (2014).

8 Britt, D., Tranchemontagne, D. & Yaghi, O. M. Metal-organic frameworks with high capacity and selectivity for harmful gases. *Proceedings of the National Academy of Sciences* **105**, 11623-11627, (2008).

9 Li, Y.-X. *et al.* Controlled Construction of Cu(I) Sites within Confined Spaces via Host–Guest Redox: Highly Efficient Adsorbents for Selective CO Adsorption. *ACS Applied Materials & Interfaces* **10**, 40044-40053, (2018).

10 Kim, A.-R. *et al.* Creating high CO/CO_2 selectivity and large CO working capacity through facile loading of Cu(I) species into an iron-based mesoporous metal-organic framework. *Chemical Engineering Journal* **348**, 135-142, (2018).

11 Kim, H. *et al.* Effective CO_2 and CO Separation Using $[M_2(DOBDC)]$ (M = Mg, Co, Ni) with Unsaturated Metal Sites and Excavation of Their Adsorption Sites. *ACS Applied Materials & Interfaces* **11**, 7014-7021, (2019).

12 Reed, D. A. *et al.* A spin transition mechanism for cooperative adsorption in metal–organic frameworks. *Nature* **550**, 96-100, (2017).

13 Huang, Y.-Y. Selective adsorption of carbon monoxide and complex formation of cuprous-ammines in Cu (I) Y zeolites. *J Catal* **30**, 187-194, (1973).

14 Fu, Q. *et al.* R23/R22 Separation and Recovery Using the DIST-PSA Hybrid System. *Industrial & Engineering Chemistry Research* **56**, 331-341, (2017).

Chapter 7 Stability and impurity testing for CO/N_2 separation

Aspects of the work presented in this chapter has been written in the form of a manuscript which has been accepted by Industrial & Engineering Chemistry Research.[1]

7.1 Introduction

An adsorbent in an industrial gas separation process must maintain high adsorption capacity and selectivity over multiple cycles and require minimal energy for regeneration. To date, there have been scarce reports investigating MOF cyclability for CO purification, particularly in the context of CO/N_2 separation. While reporting CO isosteric heat of adsorption values (Table 2-4) provides useful insight for the energy requirements for MOF regeneration, few studies have performed cyclic testing. Among them, one can cite cyclic studies involving temperature swing (mild or at cryogenic conditions),[2,3] vacuum swing[4-7] or He purging.[8,9] In these MOF cyclability studies for CO/N_2 separation, the structural effects post-adsorption were not reported. An unstable adsorbent that deteriorates in performance would raise the cost of the separation process by requiring frequent sorbent renewal, as seen with COSORB.[10] By monitoring the adsorbent's textural parameters and structural integrity after testing its cyclability, it would be possible to observe any trends between these factors.

In addition to recyclability, the presence of impurities must be taken into account when implementing a new adsorbent technology. In the context of CO purification, besides N_2, other feed impurities may be present such as CH_4, CO_2, H_2S and H_2O. H_2S can be removed by wet scrubbing[11] or dry adsorption (using ACs),[12] H_2O by using

molecular sieves or a cold box,[13] excess CH_4 by distillation[14] and CO_2 by calcium looping,[15] chemical absorption[16] or a cold box.[13] Yet, ppm levels of CO_2 may still exist and could potentially compete for adsorption with CO. Indeed, CO_2 and CO undergo similar mechanisms for adsorption to unsaturated metal sites within MOFs. However, as the polarisability of CO_2 is higher than that of CO, this high level of competitive binding would detrimentally reduce CO capacity and selectivity. Different metal analogues of M-MOF-74 show different levels of affinity to CO over CO_2, with Mg-MOF-74 exhibiting CO_2/CO selectivity and Ni- and Co-MOF-74 exhibiting CO/CO_2 selectivity.[17] To date, post-synthesis modification has been employed to improve CO/CO_2 selectivity.[6,9,18] However, no study has investigated the effect of CO_2 impurity upon CO/N_2/CO_2 separation in a ternary stream. In fact, there have been no MOF studies testing multi-component streams specifically for CO purification.

This chapter investigates the cyclability of the two best performing MOFs for dynamic CO/N_2 separation at atmospheric pressure, established in Chapters 5 and 6: Ni- and Co-MOF-74. The optimum CO desorption temperature was identified for these MOFs in order to retain their CO/N_2 separation abilities. Thermogravimetric and X-ray diffraction analysis were used to monitor the MOFs structural integrity upon heating. Dynamic CO/N_2 separation was performed over multiple cycles, using the established regeneration temperature. Post-cyclic testing characterisation was used to observe the effect of CO adsorption and regeneration upon the MOFs structural integrity and porosity. It was hypothesized that high temperatures are required for CO desorption, a consequence of the large CO enthalpy of adsorption of Ni- and Co-MOF-74 (Table 5-3). This chapter also studies the effect of realistic trace level ppm CO_2 upon CO/N_2 separation in syngas streams using Ni-MOF-74 and Co-MOF-74. Firstly, CO/CO_2 dynamic separation was performed to compare the level of competitive binding with

CO/N_2 separation in binary streams. Subsequently, trace level CO_2 was introduced into the $CO:N_2$ stream to evaluate the CO separation performance in a $CO:N_2:CO_2$ ternary stream.

7.2 Materials synthesis

Co-MOF-74 and Ni-MOF-74 were tested on the breakthrough column instrument for cyclic CO/N_2 testing and dynamic CO/CO_2 and $CO/N_2/CO_2$ separation. Details of the materials synthesis of the MOFs can be found in Section 5.2.

7.3 Materials characterisation

Prior to being tested, a stable regeneration temperature was required. CO temperature programmed desorption (TPD, Section 4.2.5) analysis was used to monitor CO desorption upon heating and identify the temperature of complete CO desorption. Thermal gravimetric analysis (TGA, Section 4.2.4) and variable temperature X-ray diffraction analysis (VT-XRD, Section 4.1.2) were used to monitor the mass loss and structural integrity upon heating and identify the decomposition temperature. After the cyclic testing, post-CO adsorption characterisation was performed using XRD (Section 4.1.2) and porosity analysis (Section 4.1.1) to examine the structure's crystalline integrity and porosity.

7.4 Materials testing

The adsorption capacities of Co-MOF-74 and Ni-MOF-74 were performed using the following techniques: breakthrough column instrument (CO, N_2 and CO_2 dynamic capacity), gravimetric gas sorption analyser (CO and N_2 equilibrium capacity) and volumetric gas sorption analyser (CO_2 equilibrium capacity).

7.4.1 *Equilibrium testing*

7.4.1.1 Experimental procedure

The CO and N_2 equilibrium adsorption isotherm measurements were measured using a gravimetric gas sorption analyser. Full details of the theory and experimental procedure of this technique can be found in Section 5.4.1.1.

CO_2 equilbrium adsorption isotherm measurements up to 1 bar were performed on a volumetric gas sorption analyser (Micromeritics 3Flex) at 25 °C, using a water bath for temperature regulation. Prior to analysis, the samples were degassed by heating the samples at ~0.2 mbar for 16 h at 120 °C, and degassed *in-situ* on the gas sorption analyser at ~0.003 mbar for 6 h at 250 °C.

7.4.2 *Dynamic testing*

7.4.2.1 Experimental procedure

The fundamentals and theory of this technique are explained in Section 3.3. The apparatus schematic (Figure 3-7) and experimental procedure for breakthrough column testing are shown in Section 3.3.2. The activation conditions used are outlined in Section 5.2. The inlet feed concentrations of the CO:N_2, CO:CO_2 and CO:N_2:CO_2 mixtures were set depending on the level of N_2 and CO_2 impurity under investigation. Experiments were repeated 3 times for error analysis for both Ni-MOF-74 and Co-MOF-74 at all compositions. The full derivations and equations used for the CO breakthrough capacity and CO/N_2 and CO/CO_2 selectivity calculations are shown in Section 3.2.2. Thermal regeneration was performed in between adsorption cycles by heating at 190 °C and 180 °C for Ni-MOF-74 and Co-MOF-74 for 2 h with He flowing (20 mL min^{-1}).

7.5 Results and Discussion

7.5.1 *Thermal analysis of the MOF structural integrity*

Figure 7-1a and b exhibits the X-ray diffraction patterns of Ni-MOF-74 and Co-MOF-74 upon heating from 25 °C to 500 °C. Ni-MOF-74 analysis did not exhibit any change in the diffraction pattern until ~300 °C. A dramatic decrease in peak sharpness and intensity at 450 °C was observed, with full decomposition occurring between 450-500 °C, and no peaks visible at 500 °C. Based on the Ni-MOF-74 analysis, the same approach was repeated with fewer measurements at lower temperature for Co-MOF-74. No significant structural changes until ~325 °C was observed with Co-MOF-74. However, the peak intensities falls more sharply upon further heating from 325-425 °C, before decomposition at 450 °C.

Thermogravimetric analysis (Figure 7-1c) corroborates the M-MOF-74 decomposition behaviour, with a gradual decrease in weight loss up until ~430 °C for both MOFs. Complete structural collapse occurred at 530 °C and 575 °C for Ni-MOF-74 and Co-MOF-74, respectively. Water and methanol removal during MOF activation are responsible for the gradual mass loss of up to 300 °C. The mass loss from 300-430 °C is attributed to the thermal decomposition, which also resulted in CO, CO_2, and CH_4 evolution from the organic components of the MOFs.

7.5.2 *CO desorption temperature analysis*

TPD analysis (Figure 7-1d) exhibits full CO desorption at 190 °C and 180 °C for Ni-MOF-74 and Co-MOF-74 These temperatures were chosen for thermal regeneration. The CO T_{max} values quantified for Ni-MOF-74 and Co-MOF-74 are 95 °C and 90 °C, where T_{max} is the temperature of the quickest desorption rate. These Ni-MOF-74 values are higher due to its stronger metal-CO interactions, indicated by its larger CO

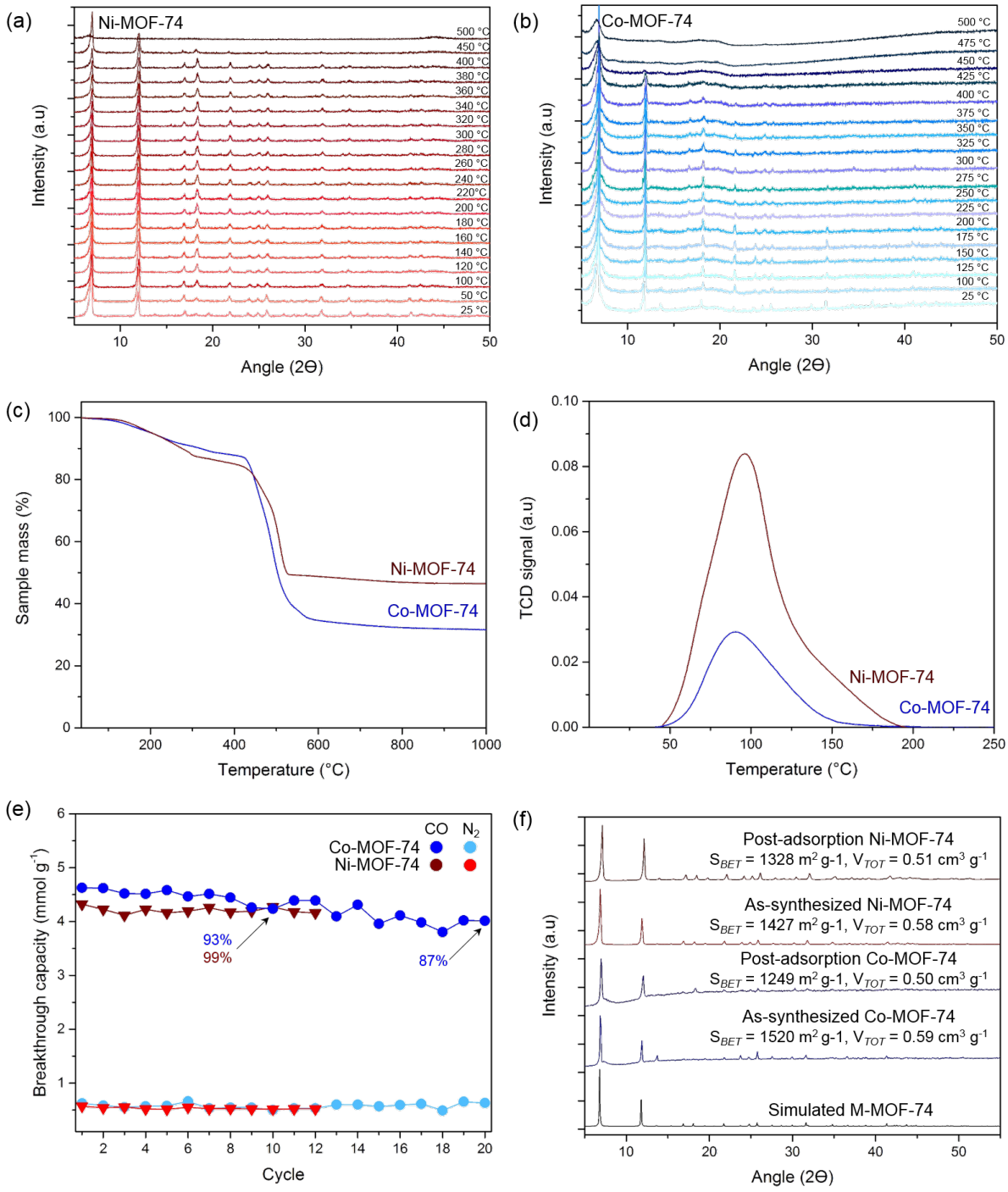


Figure 7-1. Variable-temperature X-ray diffraction patterns of (a) Ni-MOF-74 and (b) Co-MOF-74 from room temperature up to 500 °C. (c) Temperature Programmed CO desorption curve of Co-MOF-74 and Ni-MOF-74. (d) Thermogravimetric curve of Co-MOF-74 and Ni-MOF-74 under N_2 atmosphere. (e) Cyclic CO and N_2 breakthrough capacities of Co-MOF-74 (circles) and Ni-MOF-74 (triangles) for 50:50 *v:v* CO:N_2 feed mixture at 25 °C and 1 bar. Thermal regeneration was performed in between adsorption cycles by heating for 2 h at 190 °C and 180 °C for Ni-MOF-74 and Co-

MOF-74, respectively. (f) X-ray diffraction patterns and textural parameters of simulated M-MOF-74, as-synthesized and post-CO adsorption tested Co-MOF-74 (20 cycles) and Ni-MOF-74 (12 cycles).

enthalpy heat of adsorption (Table 5-3). The larger sample amount of Ni-MOF-74 used in the analysis resulted in a larger amount of CO adsorbed, which is proportional to the curve integral.

7.5.3 *Cyclic testing and post-CO adsorption characterisation*

The cyclic CO and N_2 breakthrough capacities calculated for Co-MOF-74 and Ni-MOF-74 are illustrated in Figure 7-1e. Co-MOF-74 only experienced a 13% loss of its original capacity after 20 adsorption/desorption cycles. It is proposed that this reduction in capacity is due to the frequency of the number of 2 h heating cycles. The regeneration temperature (180 °C) was comfortably lower than the decomposition temperature (~430 °C) observed in Figure 7-1c and therefore the temperature should not degrade the MOF. Moreover, full CO capacity was maintained after 5 cycles which indicates its robustness after these cycles. Further heating produces a slight loss in crystallinity and an 18% loss in porosity (Figure 7-1e).

It is hypothesized that as the MOF's structural integrity deteriorated over multiple heating cycles, the proportion of unsaturated metal sites become inaccessible and inactive, causing a lower CO capacity. Meanwhile, the N_2 breakthrough capacity remains steady over 20 cycles, indicating that the relatively high microporosity of the MOF results in sufficiently strong physisorbing surface interactions for N_2 adsorption. The decreased CO breakthrough capacity combined with the maintained N_2 breakthrough capacity results in a decrease in CO/N_2 ideal selectivity from 13 to 10.

As seen in Figure 7-1e, Ni-MOF-74 maintained high CO capacity, porosity (7% loss in BET surface area), structural integrity and CO/N_2 selectivity after 12 cycles.

Considering the partial collapse of the MOFs under thermal regeneration with the current temperatures, it is proposed that the heating duration is reduced to minimise the loss in CO capacity. Another option to maximise the MOFs lifetime would be to lower the regeneration temperature (*e.g.* ~160 °C). This would compromise between maintaining complete structural integrity and incomplete CO desorption.

7.5.4 *CO/CO_2 separation*

Dynamic breakthrough adsorption testing on Co-MOF-74 and Ni-MOF-74 was initially performed with 50:50, 95:5, 99:1 (*v:v*) CO:N_2 and CO:CO_2 inlet feed compositions to investigate the effect of competitive CO_2 impurity upon CO breakthrough capacity and selectivity. Figure 7-2 displays the Ni-MOF-74 and Co-MOF-74 CO, N_2 and CO_2 equilibrium adsorption isotherms at 25 °C up to 1 bar. The Ni-MOF-74 and Co-MOF-74 breakthrough capacities for CO:N_2 and CO:CO_2 mixtures are shown in Figure 7-3 alongside their CO ideal selectivities, and their breakthrough curves are shown in the Figure A5-1.

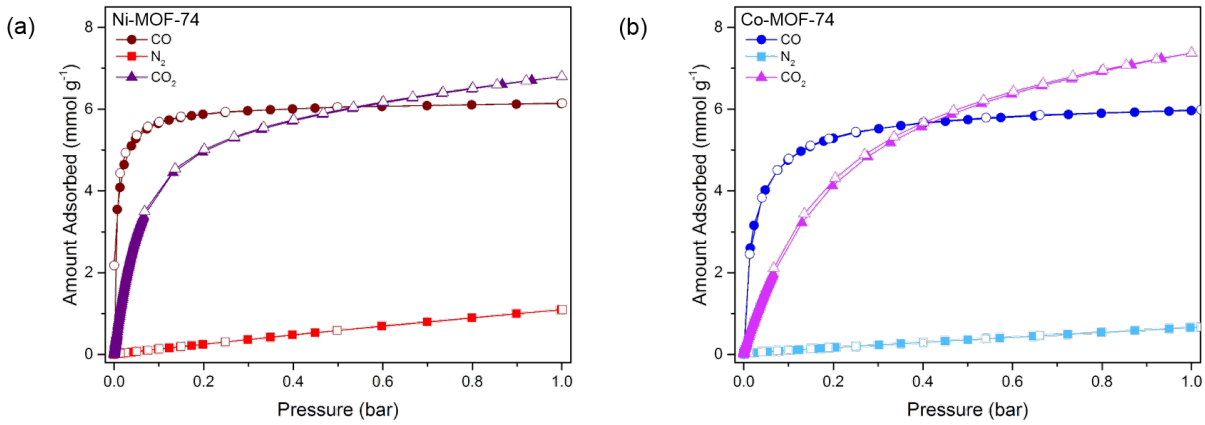


Figure 7-2. CO, N_2 and CO_2 equilibrium adsorption isotherms of (a) Ni-MOF-74 and (b) Co-MOF-74 at 25 °C up to 1 bar using volumetric gas sorption analysis.

The CO breakthrough capacities for all the tested compositions for CO:N_2 and CO:CO_2 were higher with Co-MOF-74 than Ni-MOF-74 because of smaller heat release upon

CO adsorption. Ni-MOF-74 and CO-MOF-74 exhibit smaller CO/CO_2 selectivity than CO/N_2 because the Ni^{2+} and Co^{2+} sites undergo strong π-complexation to CO.

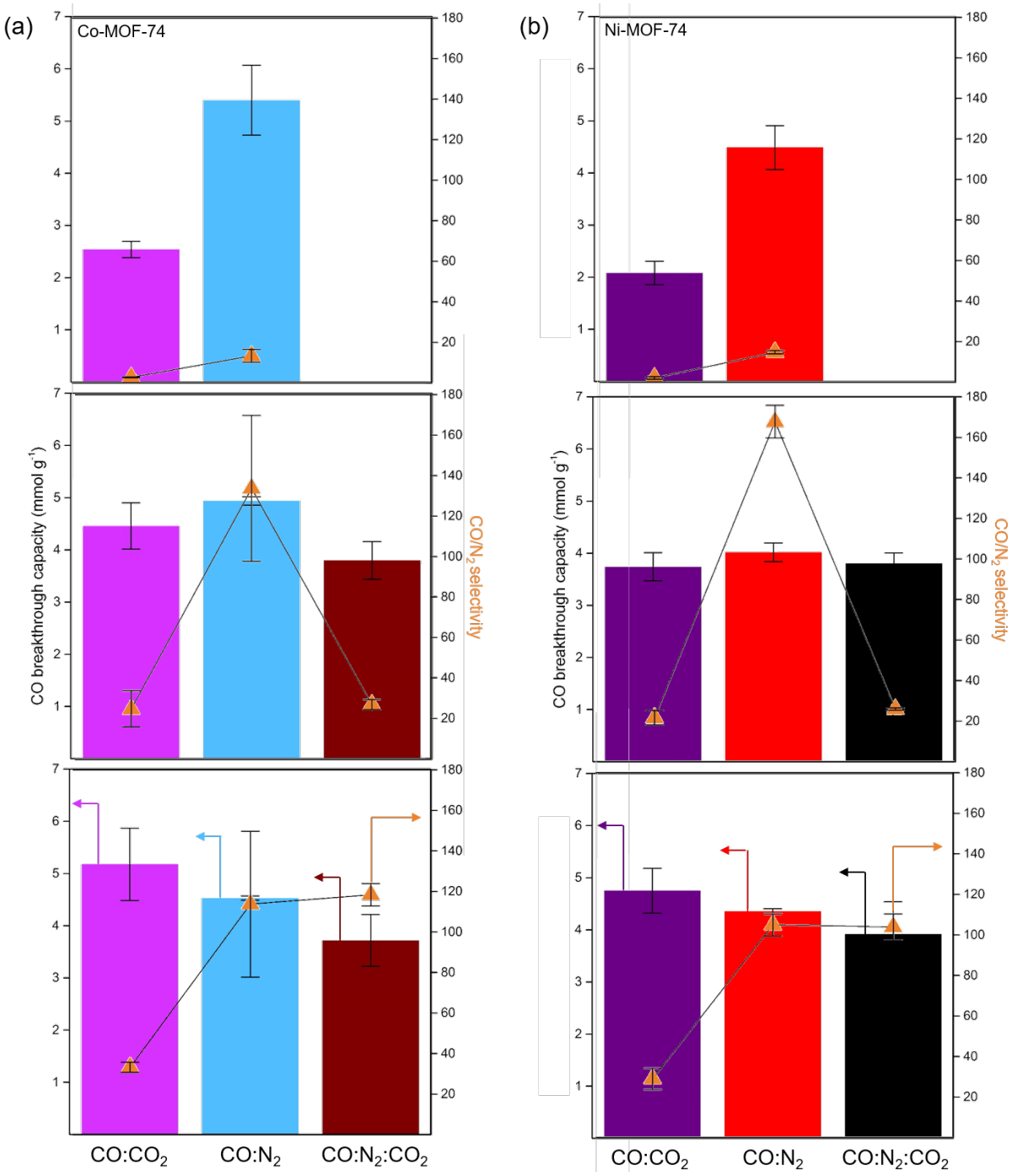


Figure 7-3. CO breakthrough capacities and CO/X (X = CO_2, N_2) ideal equilibrium selectivities of (a) Co-MOF-74 and (b) Ni-MOF-74 at 50% (top), 95% (middle) and 99% (bottom) CO inlet feed concentration of $CO:CO_2$, $CO:N_2$ and $CO:N_2:CO_2$ gas mixtures measured on a breakthrough adsorption column instrument at 25 °C and 1 bar.

For a 50:50 *v:v* CO:CO_2 mixture, similar CO and CO_2 breakthrough capacities for Ni-MOF-74 and Co-MOF-74 were observed. These capacities reflect the competitive level of polar CO and CO_2 molecules binding to the unsaturated metal sites, as the CO breakthrough capacity is much higher than with the CO:N_2 feed. The corresponding equilibrium capacities (Figure 7-2) at the same partial pressure are much higher than the breakthrough capacities, which demonstrates the detrimental effect of high CO_2 concentration. The CO:CO_2 feed also resulted in poor CO/CO_2 selectivity compared to CO/N_2 because of this CO reduced capacity.

When the CO_2 impurity level was reduced to 5% in the 95:5 *v:v* CO:CO_2 mixture, the CO breakthrough capacities were much higher and closer to the equilibrium capacities at the same partial pressure. The reduced CO_2 partial pressure resulted in higher CO/CO_2 selectivities than with 50% CO_2. However, these values were much lower than the CO/N_2 selectivities for a 50:50 *v:v* CO:N_2 composition as the MOF has a lower affinity to N_2 than CO_2. Decreasing the CO_2 concentration further to 1% for 99:1 *v:v* CO:CO_2 mixture increased the CO breakthrough capacities and CO/CO_2 selectivity further, but remained short of CO/N_2 selectivities.

Inverse trends with the CO breakthrough capacities was observed with decreasing CO_2 and N_2 impurity level. The CO capacity decreases as N_2 concentration decreases in the CO:N_2 feed, while the CO breakthrough capacity increases as the CO_2 impurity level decreases in the CO:CO_2 feed. There is less competitive CO and N_2 adsorption with 50% N_2 impurity in the CO:N_2 stream than with CO and CO_2 adsorption with the CO:CO_2 stream. At 50% CO_2 impurity, a larger amount of heat is released from CO and CO_2 adsorption, and this competitive adsorption reduces CO capacity and slows CO sorption. Therefore decreasing the CO_2 concentration to 5 and 1% reduces the exothermicity of the CO_2 adsorption, thereby raising the CO capacity. As N_2 adsorption

generates less heat than CO_2 adsorption, increasing CO concentration in a CO:N_2 mixture raises the heat of the surroundings without slowing CO sorption kinetics. The large exothermic CO enthalpy of adsorption reduces the CO capacity, and this effect and the repercussions for CO separation performance were discussed in detail in Section 6.4.2.

7.5.5 *CO/N_2/CO_2 separation*

While CO/CO_2 separation studies provided insight into the behaviour of competitively binding CO_2, ultimately this separation with high CO_2 concentration is not industrially relevant for MOFs. Therefore, ppm level CO_2 impurity was introduced into CO:N_2 for CO/N_2/CO_2 separation in a ternary stream. Dr Les Bolton from BP advised us that after CO_2 separation from syngas, 20-50 ppm CO_2 would be expected in the CO:N_2 stream. Dynamic breakthrough adsorption testing on Co-MOF-74 and Ni-MOF-74 with 95:5 (*v:v*) CO:N_2 inlet feed composition with 20 ppm CO_2 in the stream was performed. The same experimental procedure was repeated with 95:5 (*v:v*) CO:N_2 with 100 ppm CO_2. These ternary streams provided us with both low and extreme high CO_2 impurity level to compare with the binary CO:N_2 streams.

Figure 7-3a and b exhibit the CO breakthrough capacity and CO/N_2 ideal selectivities before (middle panels) and after (bottom panels) introduction of CO_2 impurity. When 20 ppm CO_2 was introduced, the CO/N_2 selectivity remained unaffected while the CO breakthrough capacity decreased for both Ni-MOF-74 and Co-MOF-74. Therefore, this trace level of CO_2 significantly impacts the MOFs CO capacity while having negligible impact on selectivity. The CO and N_2 breakthrough capacities are reduced to similar extents because of N_2 desorption upon CO breakthrough.

Increasing the CO_2 level to 100 ppm reduced the CO breakthrough capacity as well. However, this larger CO_2 concentration reduced the Ni-MOF-74 and Co-MOF-74 CO/N_2 selectivity when comparing the binary $CO:N_2$ and ternary $CO:N_2:CO_2$ streams. The five-fold increase of CO_2 concentration is significant enough to detrimentally reduce the CO capacity through competitive metal-CO_2 binding. A smaller quantity of bound N_2 is desorbed upon CO breakthrough, which results in lower CO/N_2 selectivity.

7.6 Conclusions

This chapter presents the cyclability of the two best performing MOFs, Ni-MOF-74 and Co-MOF-74. Thermal and CO desorption analysis enabled us to select the temperature for thermal regeneration. Post-adsorption characterisation was performed to study how cyclic CO adsorption/desorption affected the MOF structure. The effect of CO_2 impurity competitively binding with CO upon Ni-MOF-74 and Co-MOF-74 was investigated, firstly by performing CO/CO_2 dynamic breakthrough separation. Subsequently, realistic syngas $CO:N_2:CO_2$ ternary streams were replicated to study the effect of CO_2 impurity upon CO/N_2 separation. The key findings are summarised below:

- CO/N_2 separation ability is maintained after 5 cycles, however further regenerations decrease the CO capacity as structural deformation reduces the accessibility to the unsaturated metal sites and porosity. Therefore it is proposed a shorter regeneration time is required to maximise the MOF lifetime and CO/N_2 separation performance. Alternatively, the temperature could be decreased further to compromise between maximising the CO capacity and MOF lifetime.

- Full CO desorption was achieved at high temperature (+180 °C) as predicted, because of the MOFs high CO enthalpy of adsorption with the strong Ni^{2+}-CO and Co^{2+}-CO bonds.
- The CO/N_2 selectivity remained unaffected with low level of CO_2 impurity (20 ppm) in a syngas stream. CO and N_2 capacity were reduced to the same extent as N_2 was desorbed upon CO breakthough.
- When the CO_2 impurity level is increased to 100 ppm, CO/N_2 selectivity and CO capacity are reduced. The loss in performance severely diminishes its CO/N_2 separation ability, and shows that CO_2 concentration and partial pressure governs the CO/N_2 separation ability, as hypothesized.
- Increasing CO concentration in a $CO:CO_2$ feed does not reduce the CO breakthrough capacity as observed with $CO:N_2$ streams. High concentration of CO_2 (50%) in a binary stream increases the heat release and competitive level of CO and CO_2 adsorption, with lower CO_2 concentration (1 and 5%) slowing CO sorption kinetics and heat release. N_2 does not exhibit strong competitive adsorption to slow CO sorption and therefore does not provide the same trend.

7.7 References

1 Evans, A. D. *et al.* Screening Metal–Organic Frameworks for Dynamic CO/N_2 Separation Using Complementary Adsorption Measurement Techniques. *Industrial & Engineering Chemistry Research* **58**, 18336-18344, (2019).

2 Li, Y.-X. *et al.* Controlled Construction of Cu(I) Sites within Confined Spaces via Host–Guest Redox: Highly Efficient Adsorbents for Selective CO Adsorption. *ACS Applied Materials & Interfaces* **10**, 40044-40053, (2018).

3 Sato, H. *et al.* Self-accelerating CO sorption in a soft nanoporous crystal. *Science* **343**, 167-170, (2014).

4 Reed, D. A. *et al.* Reversible CO Scavenging via Adsorbate-Dependent Spin State Transitions in an Iron(II)–Triazolate Metal–Organic Framework. *Journal of the American Chemical Society* **138**, 5594-5602, (2016).

5 Wang, Y. *et al.* $CuAlCl_4$ doped MIL-101 as a high capacity CO adsorbent with selectivity over N2. *Frontiers of Chemical Science and Engineering* **8**, 340-345, (2014).

6 Vo, T. K., Kim, J.-H., Kwon, H. T. & Kim, J. Cost-effective and eco-friendly synthesis of MIL-101(Cr) from waste hexavalent chromium and its application for carbon monoxide separation. *Journal of Industrial and Engineering Chemistry*, (2019).

7 Yin, Y. *et al.* Cuprous/Vanadium Sites on MIL-101 for Selective CO Adsorption from Gas Mixtures with Superior Stability. *ACS Sustainable Chemistry & Engineering* **7**, 11284-11292, (2019).

8 Nickerl, G., Stoeck, U., Burkhardt, U., Senkovska, I. & Kaskel, S. A catalytically active porous coordination polymer based on a dinuclear rhodium paddle-wheel unit. *Journal of Materials Chemistry A* **2**, 144-148, (2014).

9 Kim, A.-R. *et al.* Creating high CO/CO_2 selectivity and large CO working capacity through facile loading of Cu(I) species into an iron-based mesoporous metal-organic framework. *Chemical Engineering Journal* **348**, 135-142, (2018).

10 Haase, D. J. & Walker, D. G. The COSORB Process. *Chemical Engineering Progress* **5**, 74-77, (1974).

11 Janssen, A. J. H., Ruitenberg, R. & Buisman, C. J. N. Industrial applications of new sulphur biotechnology. *Water Science and Technology* **44**, 85-90, (2001).

12 Feng, W., Kwon, S., Borguet, E. & Vidic, R. Adsorption of Hydrogen Sulfide onto Activated Carbon Fibers: Effect of Pore Structure and Surface Chemistry. *Environmental Science & Technology* **39**, 9744-9749, (2005).

13 Golden, T. C. & Barnes Jr, D. R. Synthesis gas drying and CO_2 removal. (1999).

14 Bligh, B. R. Process and plant for removing methane and argon from crude ammonia synthesis gas. U.S 4,549,890 (1985).

15 Hanak, D. P., Anthony, E. J. & Manovic, V. A review of developments in pilot-plant testing and modelling of calcium looping process for CO2 capture from power generation systems. *Energy & Environmental Science* **8**, 2199-2249, (2015).

16 Herzog, H. J. Peer Reviewed: What Future for Carbon Capture and Sequestration? *Environmental Science & Technology* **35**, 148A-153A, (2001).

17 Kim, H. *et al.* Effective CO2 and CO Separation Using $[M_2(DOBDC)]$ (M = Mg, Co, Ni) with Unsaturated Metal Sites and Excavation of Their Adsorption Sites. *ACS Applied Materials & Interfaces* **11**, 7014-7021, (2019).

18 Vo, T. K. *et al.* Highly CO selective Cu(I)-doped MIL-100(Fe) adsorbent with high CO/CO_2 selectivity due to π complexation: Effects of Cu(I) loading and activation temperature. *Microporous and Mesoporous Materials* **274**, 17-24, (2019).

Chapter 8 Thermodynamic and kinetic data

8.1 Introduction

The thermodynamic and kinetic properties of an adsorbent are important when implementing a material for gas separation processes.[1] While commonly reported metrics such as CO adsorption capacity and selectivity values are the principal measurements required, Henry's constant and diffusivity measurements provide fundamental information of adsorbent properties for process design simulations.

Henry's constant (K_H) provides thermodynamic data regarding the affinity to the adsorbate,[2] expressed in Eq 8-1:

$$P_i = K_H C \quad (8\text{-}1)$$

Where P_i is the partial pressure of the solute in the gas above the solution, K_H is the Henry's law constant and C is the concentration of the solute in the solution, at constant temperature. Henry's constant values indicate the affinity and strength of adsorption interaction, indicating if effective gas separation is feasible if there are large differences in magnitude between adsorbate K_H values.[3] To date there have been few studies presenting both $K_{H,\ CO}$ and $K_{H,\ N2}$ values for MOFs.[4-6] Isosteric heat of adsorption (Q_{st}) values have been the subject of more comprehensive thermodynamic data reporting for MOFs for CO separation (Table 2-4). Reporting $K_{H,\ CO}$ and $K_{H,\ N2}$ values would provide a quicker method of evaluating an adsorbent's CO/N_2 separation ability than calculating $Q_{st,\ CO}$ and $Q_{st,\ N2}$ values.

Diffusivity coefficient (K_D) measurements for adsorbent pore diffusion are important when considering a MOF for gas separation. By understanding the adsorbate's

diffusion behaviour and mass transfer during an adsorption separation process, it is possible to develop and optimise the separation. Slow diffusion rates and sorption kinetics result in longer adsorption cycles times and detrimentally reduce the time efficiency of the process. Fast diffusion rates are desired to maximise energy and cost efficiency, which are usually governed by the adsorbent's textural parameters. Diffusion studies of MOFs remain scarce in general, as highlighted in a review of computational MOF studies: "*One of the challenges in understanding diffusion of adsorbed molecules in MOFs is the lack of experimental data on diffusion in MOFs.*"[7] While this statement was made a decade ago, this still holds true with CO diffusion within MOFs. There have been few studies reporting $K_{D,\,CO}$ and $K_{D,\,N2}$ values,[6,8-10] with little discussion regarding the implications of the reported kinetic data.

In summary, there has been no thermodynamic or kinetic data presented for the leading MOFs for CO/N_2 separation (*i.e* M-MOF-74, M-BTTri, M_2Cl_2(BBTA) and M_2Cl_2(BTDD)) besides isosteric enthalpy of adsorption calculations. This knowledge gap requires addressing as these metrics are important for the industrial viability of these MOFs for implementation into a CO/N_2 separation process.

This chapter calculates the CO and N_2 Henry's law constant and diffusivity coefficient values for the two best performing MOFs for dynamic CO/N_2 separation at atmospheric pressure, *i.e*. Ni-MOF-74 and Co-MOF-74, as established from Chapter 5 and 6. The effect of different pore sizes and porosity upon K_H and K_D was investigated using related 1-D hexagonal pored MOF structures, M_2Cl_2(BTDD) and M_2Cl_2(BBTA). It was hypothesized that the varying pore windows would govern the K_D values, in particular with the larger pore windows of M_2Cl_2(BTDD). It was predicted that the CO and N_2 diffusivity would be comparable because of their similar kinetic diameter (3.76 Å for CO and 3.64 Å for N_2). The influence of the different textural parameters of Cu-Cu

paddlewheel MOFs upon K_H was also investigated. Overall, it was hypothesized that the $K_{H,\ CO}$ and $K_{H,\ N2,}$ values would follow the same trend as the CO and N_2 isosteric enthalpy of adsorption values previously reported (Table 5-3).

8.2 Materials synthesis

A total of 10 MOFs were selected for K_H and K_D measurements to obtain thermodynamic and kinetic data for these MOFs. Details of the materials synthesis of the MOFs can be found in Section 5.2. The MOFs tested include, Ni-MOF-74, Co-MOF-74, Ni_2Cl_2(BBTA), Co_2Cl_2(BBTA), Ni_2Cl_2(BTDD), Co_2Cl_2(BTDD), HKUST-1, CuTDPAT, PCN-12 and MOF-505.

8.3 Materials characterisation

The textural parameters of these MOFs were measured using porosity measurements (Section 4.1.1).

8.4 Materials testing

8.4.1 *Equilibrium testing*

CO and N_2 equilibrium adsorption isotherms were used for Henry's constant calculations and were measured using a gravimetric gas sorption analyser at 10, 25 and 40 °C. Full details of the theory and experimental procedure of this technique can be found in Section 5.4.1.1.

8.4.1.1 Henry's law constant calculations

Henry's law constant values were calculated by measuring the gradient of the CO and N_2 isotherms at low pressure, as this is the only region where Henry's law is applicable in an ideal solution.[11] Here, the low pressure molecule-surface forces are prominent

at the limit of zero loading (Henry's law region), and is expressed in the equation below:

$$K_H = \lim_{P \to 0} \left(\frac{q}{P}\right) = \lim_{P \to 0} \left(\frac{dq}{dP}\right) \quad (8\text{-}2)$$

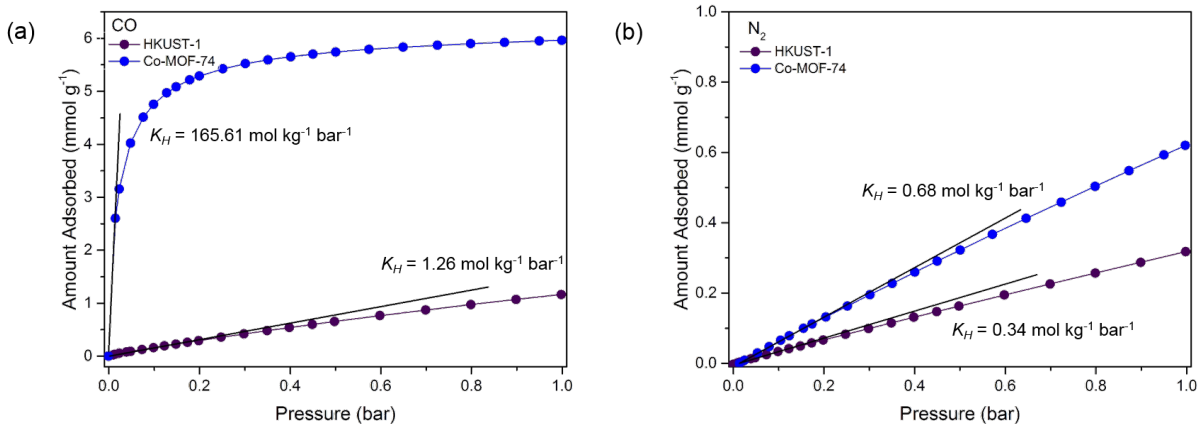


Figure 8-1. (a) CO and (b) N_2 equilibrium adsorption isotherms of HKUST-1 and Co-MOF-74 at 25 °C up to 1 bar with their corresponding Henry's law constant values labelled.

From Henry's Law (Eq 8-1), if the partial pressure of the gas over the solute is kept constant, then K_H is inversely proportional to the temperature of the system. This concept combines both Charles' law (Eq 8-3) and Boyle's law (Eq 8-4) when pressure is constant.

$$V \propto T \quad (8\text{-}3)$$

$$P \propto \frac{1}{V} \quad (8\text{-}4)$$

Where V = volume of the gas, P = pressure of the gas and T = temperature of the gas.

The application of K_H for selectivity measurements is theoretically similar to the Ideal Adsorbed Solution Theory (IAST) (discussed in Section 5.4.1.2), as both rely on ideal solutions.

8.4.1.2 Isosteric heat of adsorption calculations

From the analytical fittings of three pure single component isotherms measured at different temperatures (10, 25 and 40 °C), it was possible to calculate the heat of adsorption (Q_{st}). Full details of the theory, analytical fittings and the equation used to calculate Q_{st} can be found in Section 5.4.1.

8.4.2 *Dynamic testing*

Diffusivity coefficient values (K_D) were measured using the breakthrough column apparatus by monitoring the CO and N_2 desorption using a mass spectrometer and flow meter. Full details of the theory, experimental procedure, desorption curves and diffusivity coefficient calculations can be found in Section 3.3.3. 3 measurements were repeated of each sample and gas for error analysis.

8.5 Results and discussion

8.5.1 *1-D hexagonal pored MOFs K_H and K_D*

The K_H, K_D, BET surface area and metal density values of the 1-D hexagonal pored and Cu-Cu paddlewheel MOFs are shown in Table 8-1. The $Q_{st, CO}$ and CO/N_2 IAST selectivites of these MOFs can be found in Section 5.5.

The natural log plot of the K_H values measured from the CO and N_2 isotherms at 10, 25 and 40 °C as a function of inverse temperature is shown in Figure 8-2.

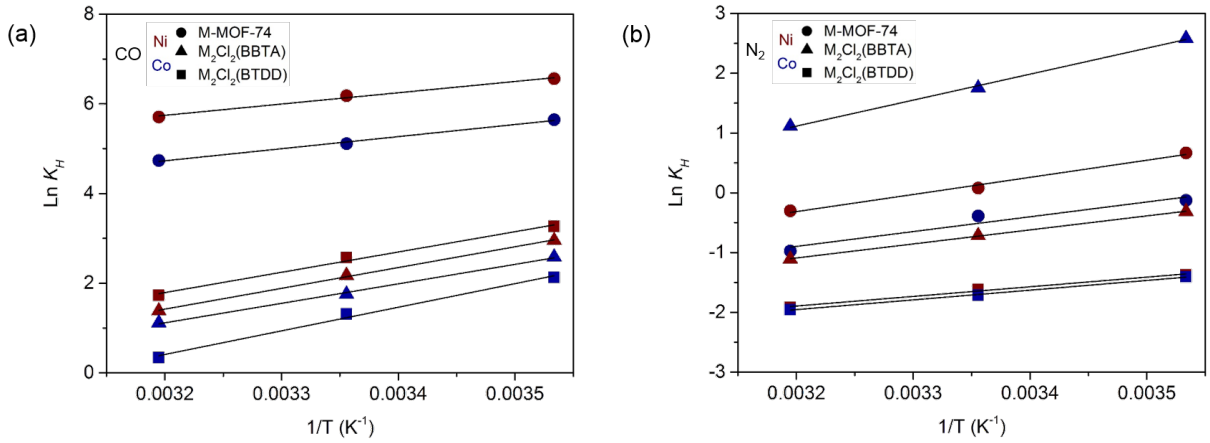


Figure 8-2. (a) CO and (b) N_2 Henry's law constant values as an inverse function of temperature over a range of 10-40 °C for Ni-MOF-74, Co-MOF-74, Ni_2Cl_2(BBTA), Co_2Cl_2(BBTA), Ni_2Cl_2(BTDD) and Co_2Cl_2(BTDD).

Table 8-1. Henry's law constants, diffusivity coefficent values, metal densities and textural parameters of 1-D hexagonal pored and Cu-Cu paddlewheel MOFs at 25 °C. (S_{BET} = BET surface area, Q_{st} = isosteric enthalpy of adsorption, K_H = Henry's law constant and K_D = diffusivity coefficient).

Materials	**Metal density** ($mmol_{metal}$ g^{-1}) *	**S_{BET}** (m^2 g^{-1})	**$K_{H,\ CO}$** (mol kg^{-1} bar^{-1})	**$K_{H,\ N2}$** (mol kg^{-1} bar^{-1})	**$Q_{st,\ CO}$** (kj mol^{-1})	**$K_{D,\ CO}$** (m^2 s^{-1})	**$K_{D,\ N2}$** (m^2 s^{-1})
1-D hexagonal pored M-MOF-74 structure							
Ni-MOF-74	3.97	1427	481.98	1.08	54.4	6.68	140.32
Co-MOF-74	3.97	1520	165.51	0.68	43.8	6.42	95.56
1-D hexagonal pored M_2Cl_2(BBTA) structure							
Ni_2Cl_2(BBTA)	3.13	1103	8.76	0.49	25.0	32.98	23.31
Co_2Cl_2(BBTA)	3.13	1248	5.77	0.25	33.2	28.17	44.65
1-D hexagonal pored M_2Cl_2(BTDD) structure							
Ni_2Cl_2(BTDD)	2.55	1868	6.82	0.20	39.1	24.05	435.71
Co_2Cl_2(BTDD)	2.55	2270	3.70	0.18	32.9	32.57	849.23
Cu-Cu paddlewheel structure							
HKUST-1	4.96	1957	1.26	0.34	23.1	-	-
MOF-505	4.09	1586	1.24	0.30	26.1	-	-
CuTDPAT	3.50	2633	1.39	0.35	27.5	-	-
PCN-12	3.97	1415	1.11	0.30	20.9	-	-

* The desolvated adsorbent's general formula and crystallographic density were used to calculate the metal density (mol of coordinatively unsaturated metal sites per gram of adsorbent).

Figure 8-2 exhibits inverse proportionality between the Henry's constant values and temperature, as anticipated from the equations shown in Section 8.4.1.1. The $K_{H,\ CO}$/ $K_{H,\ N2}$ and CO/N_2 IAST selectivity (Table 5-2) values are similar as anticipated, while the magnitude of $K_{H,\ CO}$ influences CO/N_2 selectivity greater than the magnitude of $Q_{st,\ CO}$. Figure 8-3a exhibits greater linearity between CO/N_2 IAST selectivity and $K_{H,\ CO}$ than with $Q_{st,\ CO}$, as the $K_{H,\ CO}/K_{H,\ N2}$ ratio is an indication of its affinity of the MOF, while the $Q_{st,\ CO}$ values are the strength of CO adsorption.

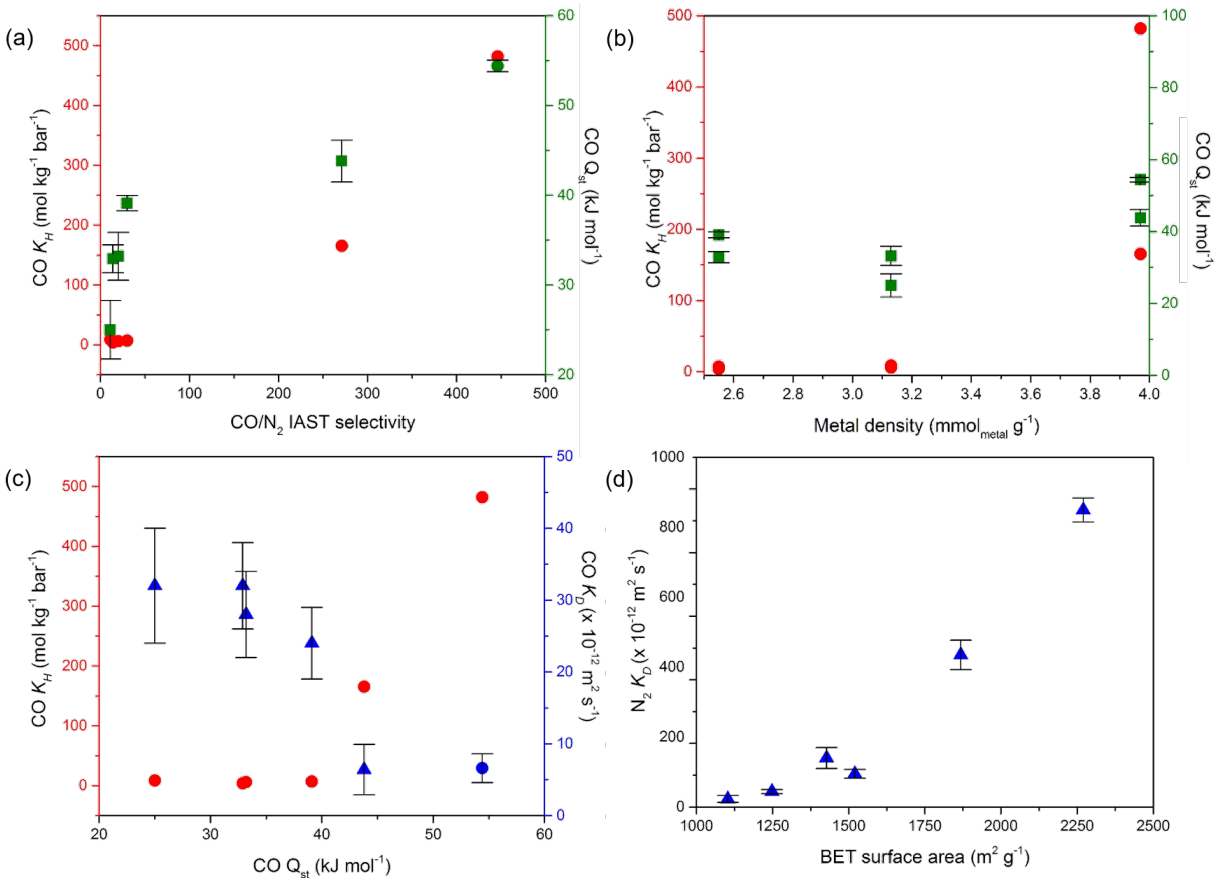


Figure 8-3. The 1-D hexagonal pored MOFs (a) CO Henry's law constant (25 °C) and CO Q_{st} values as a function of CO/N_2 (50:50 *v:v*) IAST selectivity. (b) CO Henry's law constant (at 25 °C) and $Q_{st,\ CO}$ values as function of metal density. (c) CO Henry's law constant (25 °C) and CO diffusivity coefficients (25 °C) values as a function of $Q_{st,\ CO}$. (d) N_2 diffusivity coefficient values as a function of BET surface area. 1 point (circle, triangle or square) represents one 1-D hexagonal pored MOF structure.

As shown in Figure 8-3b, both $K_{H,\ CO}$ and $Q_{st,\ CO}$ increase non-linearly with increasing metal density. The exponential increase in $K_{H,\ CO}$ and $Q_{st,\ CO}$ highlights the large difference in increasing metal density from 3.13 to 3.97 $mmol_{metal}\ g^{-1}$ with M_2Cl_2(BBTA) and M-MOF-74.

$K_{D,\ CO}$ values did not follow the trend of pore size, and the $K_{D,\ N2}$ values were larger than the $K_{D,\ CO}$ values overall. As seen in Figure 8-3c, $K_{D,\ CO}$ values decreased with increasing CO adsorption strength, reflected with $Q_{st,\ CO}$ on the *x*-axis. As the ZLC method uses the desorption curve with He purge, the stronger CO binding strength is responsible for the slower rates of kinetic desorption. Therefore kinetic measurements of the adsorption stage of the breakthrough curve are required for validation. However, due to the fast adsorption kinetics with these Ni^{2+}- and Co^{2+}-CO interactions, it is difficult to measure this on the breakthrough column apparatus. After He desorption for a long duration (~1 h), the samples were regenerated and there was further CO detected at the mass spectrometer upon heating.

Conversely, Figure 8-3d exhibits the $K_{D,\ N2}$ values increasing proportionally with increasing level of porosity, which is a consequence of the varying pore sizes of M-MOF-74, M_2Cl_2(BBTA) and M_2Cl_2(BTDD). Weak surface interactions of non-polar N_2 solely governs the adsorption strength, therefore N_2 diffusion is unaffected by the density of unsaturated metal sites. The large mesopore window of M_2Cl_2(BTDD) results in the fastest desorption kinetics as hypothesized.

8.5.2 *Cu-Cu paddlewheel MOFs K_H*

The effect of the textural parameters upon K_H of the Cu-Cu paddlewheel MOFs was also studied. The natural log plot of the K_H values measured from the CO and N_2 isotherms at 10, 25 and 40 °C as a function of inverse temperature are shown in Figure

8-4. $K_{D,\ CO}$ and $K_{D,\ N2}$ values were unable to be measured because of their low adsorption capacities.

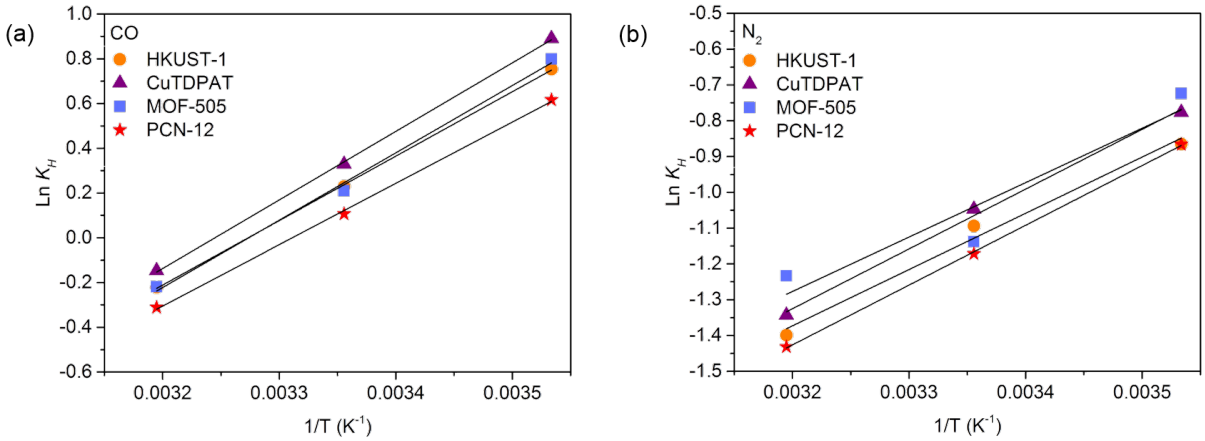


Figure 8-4. (a) CO and (b) N_2 Henry's law constant values as an inverse function of temperature over a range of 10-40 °C for HKUST-1, CuTDPAT, MOF-505 and PCN-12.

Figure 8-4 exhibits inverse proportionality between the Henry's constant values and temperature, as anticipated from the equations shown in Section 8.4.1.1. There were no correlations between the Cu^{2+} metal density and $K_{H,\ CO}$ (Figure 8-5a), further supporting the statement that porosity level has greater influence than the Cu^{2+}-CO adsorption strength in Cu-Cu paddlewheel MOFs in Section 5.5.2. Figure 8-5b shows that Cu-Cu paddlewheel MOFs affinity to CO and N_2 rely mainly on the MOFs porosity rather than the unsaturated metal sites.

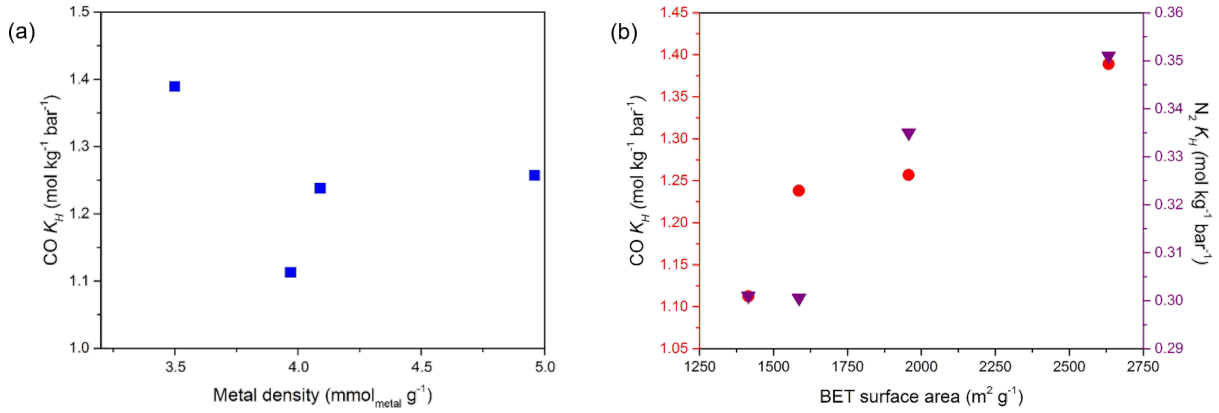


Figure 8-5. (a) CO and N_2 Henry's law constant values (25 °C) as a function of BET surface area and (b) CO/N_2 IAST selectivity as a function of N_2 Q_{st}. 1 point (circle, triangle or square) represents one 1-D hexagonal pored MOF structure.

8.6 Conclusions

This chapter presents the CO and N_2 Henry's law constant and diffusivity coefficient values for 1-D hexagonal pored MOFs and Cu-Cu paddlewheel MOFs. The study investigated the effect of varying the metal density upon $K_{H,\,CO,}$ and pore size window upon $K_{D.}$ The properties that govern the level of CO/N_2 selectivity and CO and N_2 binding strength were analysed. K_H measurements were also repeated with the Cu-Cu paddlewheel MOFs. The key findings are summarised below:

- The $K_{D,\,CO}$ and $K_{D,\,N2}$ values of the 1-D hexagonal pored MOFs were not similar despite both possessing similar kinetic diameter, proving differently from the hypothesis. However, $K_{D,\,N2}$ trends did follow the expected trend of the pore size governing the diffusivity, unaffected by the density of unsaturated metal sites. The largest pore size of the mesoporous structures resulted in the largest diffusivity coefficients.

- The $K_{D,\,CO}$ values followed the trend of CO heat of adsorption values, indicating that stronger metal-CO binding results in slower diffusion rates upon desorption.
- Both $K_{H,\,CO}$ and $Q_{st,\,CO}$ values of the 1-D hexagonal pored MOFs increase exponentially with the density of unsaturated metal sites.
- The affinity of the 1-D hexagonal pored MOFs to CO and N_2 calculated from the Henry's constant ($K_{H,\,CO}/K_{H,\,N2}$) is an indication of the CO/N_2 selectivity. CO isosteric heat of adsorption values does not provide the same insight as these values do not account for N_2 adsorption.
- The magnitude of the $K_{H,\,CO}$ and $K_{H,\,N2}$ values of the Cu-Cu paddlewheel MOFs are governed by the level of MOF porosity.

8.7 References

1 Rouquerol, J., Rouquerol, F., Llewellyn, P., Maurin, G. & Sing, K. S. *Adsorption by powders and porous solids: principles, methodology and applications*. (Academic Press, 2013).

2 Gaffney, J. & Marley, N. *General Chemistry for Engineers*. (Elsevier Science, 2017).

3 Li, J.-R., Kuppler, R. J. & Zhou, H.-C. Selective gas adsorption and separation in metal–organic frameworks. *Chemical Society Reviews* **38**, 1477-1504, (2009).

4 Evans, A., Luebke, R. & Petit, C. The use of metal–organic frameworks for CO purification. *Journal of Materials Chemistry A* **6**, 10570-10594, (2018).

5 Munusamy, K. *et al.* Sorption of carbon dioxide, methane, nitrogen and carbon monoxide on MIL-101(Cr): Volumetric measurements and dynamic adsorption studies. *Chemical Engineering Journal* **195–196**, 359-368, (2012).

6 Agueda, V. I. *et al.* Adsorption and diffusion of H_2, N_2, CO, CH_4 and CO_2 in UTSA-16 metal-organic framework extrudates. *Chemical Engineering Science* **124**, 159-169, (2015).

7 Keskin, S., Liu, J., Rankin, R. B., Johnson, J. K. & Sholl, D. S. Progress, Opportunities, and Challenges for Applying Atomically Detailed Modeling to Molecular Adsorption and Transport in Metal−Organic Framework Materials. *Industrial & Engineering Chemistry Research* **48**, 2355-2371, (2009).

8 Saha, D. & Deng, S. Adsorption Equilibria and Kinetics of Carbon Monoxide on Zeolite 5A, 13X, MOF-5, and MOF-177. *Journal of Chemical & Engineering Data* **54**, 2245-2250, (2009).

9 Sirjoosingh, A., Alavi, S. & Woo, T. K. Grand-Canonical Monte Carlo and Molecular-Dynamics Simulations of Carbon-Dioxide and Carbon-Monoxide Adsorption in Zeolitic Imidazolate Framework Materials. *Journal of Physical Chemistry C* **114**, 2171-2178, (2010).

10 Fallahi, F. & Mohammadi-Manesh, H. Molecular Dynamics Simulations of Carbon Monoxide Self-diffusion in the Nanoporous of the Cu-BTC. *Procedia Materials Science* **11**, 449-453, (2015).

11 Noorpoor, A. R. & Nazari Kudahi, S. Analysis and study of CO_2 adsorption on UiO-66/graphene oxide composite using equilibrium modeling and ideal adsorption solution theory (IAST). *Journal of Environmental Chemical Engineering* **4**, 1081-1091, (2016).

Chapter 9 Cu impregnation of MOF-74 to improve CO/N_2 and CO/CO_2 separations

The work presented in this chapter has been written in the form of a manuscript which has been accepted by RSC Advances.[1]

9.1 Introduction

To further improve MOFs' CO uptake, one can use metal impregnation for reinforced π–complexation from the 3d electrons to CO,[2] a method tested on ACs and zeolites.[2-12] This approach increases selectivity by decreasing the uptake of the undesired light product (*e.g.* N_2) whose affinity with the impregnated metal is low. Previous studies have demonstrated that it is favourable to initially perform Cu^{2+} impregnation before reducing to Cu^{+} which has stronger metal-CO interactions.[2-12] The Cu^{+} ions are prone to oxidation and reduction and are therefore not feasible for direct impregnation.

Impregnation has also been performed on MOFs to improve their CO separation performance. Cu^{+} metal sites have been incorporated on Fe-MIL-100, Cr-MIL-101 and HKUST-1 to improve CO/N_2, CO/H_2 and CO/CO_2 separation performance.[13-18] However, despite improving the CO purification ability, the CO capacity of Cu impregnated MOFs remains lower than most M-MOF-74 structures.[19] Interestingly, Cu impregnation of M-MOF-74 has never been reported. Provided the new Cu sites do not block the MOF metal sites, this approach would increase the number of sites available for interactions with CO, while decreasing the surface area/pore size available for adsorption of the lighter component, *i.e.* N_2. The combination of such effects should enhance CO uptake while increasing selectivity.

Cu impregnation, particularly Cu^{+} impregnation, is notably challenging due to the unstable nature of the metal species. Monitoring the state of the Cu sites becomes important to understand the adsorption mechanism. To date, there has been no *in-situ* analysis of the Cu^{2+} to Cu^{+} reduction procedure to monitor Cu^{+}, and there has been no confirmation of Cu^{+}-CO binding. X-ray photoelectron spectroscopy has been the sole characterisation technique used to confirm the presence of Cu^{+} by the absence of Cu^{2+} satellite peaks.[10,13] Yet, this approach can only evaluate the surface, and not the bulk, chemistry of the Cu-impregnated MOFs. Furthermore, the absence of Cu^{2+} satellite peaks may be caused by Cu^{2+} to Cu^{0} over reduction rather than the formation of Cu^{+}.

To achieve this, a systematic Cu impregnation study was performed on Ni-MOF-74 and Co-MOF-74, which were the best performing MOFs identified in Chapter 5 and 6. Cu^{+}-impregnated MOF-74 structures were synthesized in order to simultaneously use the metal-CO binding strength of the framework M^{2+} and introduce additional Cu^{+} ions. Cu impregnation was optimised and monitored *in-situ* the Cu^{2+} to Cu^{+} reduction process using X-ray absorption near edge structure (XANES) analysis. Cu^{+}-CO and M^{2+}-CO binding were verified using *in-situ* DRIFTS analysis and Cu@Ni-MOF-74 was tested for dynamic CO/N_2 and CO/CO_2 separation. This chapter investigates the Cu impregnation procedure of the two best performing MOFs from preliminary screening (Chapter 5); *i.e.* Ni-MOF-74 and Co-MOF-74 to enhance CO purification ability. The chapter provides fundamental insight into Cu^{+} impregnation and Cu^{+}-CO interactions of the MOFs.

9.2 Materials synthesis

Ni-MOF-74, Co-MOF-74 and Cu-MOF-74 were synthesized, and Cu impregnation on was performed the Ni and Co analogues. The synthesis routes for the parent MOFs are described in Section 5.2.

M-MOF-74 (M = Ni or Co) was subjected to Cu impregnation. The procedure, described below, depended on the Cu salt precursors used and the desired Cu impregnation level chosen.

For 200 mg of M-MOF-74, a total of 1.6 mL of Cu solution was used for this step and was kept constant for each synthesis. Aqueous solutions of the Cu salts were prepared by dissolving the salts in MeOH (for $CuCl_2$) or MeCN (for CuCl and $Cu(HCO_2)_2$) through sonication. The Cu concentration depended on the Cu loading desired using 1.6 mL Cu solution. For Cu impregnation procedures with two salt precursors (*e.g* $CuCl_2$ and $Cu(HCO_2)_2$), an equimolar solution was prepared.

The Cu solution and M-MOF-74 were sonicated in a 20 mL scintillation vial for 1 h, with the vial shaken by hand every 15 min to mix the suspension further. After sonication and allowing the suspension to settle, the excess solution was decanted and the remaining slurry was dried with flowing N_2 overnight. The solvent removal for MOF activation and reduction of the Cu^{2+} to Cu^{+} sites are referred to as separate procedures throughout (activation and reduction), with the conditions varying depending on the procedure desired. The Cu impregnated M-MOF-74 structures are labelled X-Cu@M-MOF-74, where M = Ni, Co, and X represents the ratio of Cu over Ni in the samples, rounded to the nearest integer.

9.3 Materials characterisation

The textural parameters of these MOFs were measured using porosity measurements (Section 4.1.1). The structural integrity of the MOFs upon impregnation and heating were assessed using XRD and VT-XRD (Section 4.1.2). The thermal stability of the MOFs was measured using TGA (Section 4.2.4). Elemental analysis of the MOFs was measured using ICP-MS (Section 4.2.2) and XPS (Section 4.2.3). *In-situ* characterisation of the Cu reduction procedure and analysis of the metal-CO interactions was performed by XANES analysis (4.1.3). DRIFTS analysis was also used to study the metal-CO interactions of the samples (Section 4.2.1).

9.4 Materials testing

The Cu impregnation and reduction procedure was optimised using flux response technology. This allowed us to calculate the dynamic CO adsorption capacity after *in-situ* Cu reduction and evaluate the Cu@M-MOF-74 CO purification performance. Binary CO/N_2 and CO/CO_2 adsorption measurements were conducted using a breakthrough apparatus to test the best performing Cu@Ni-MOF-74 sample.

9.4.1 *Dynamic testing conditions using flux response technology*

The dynamic adsorption capacity measurements of the MOFs were performed using flux response technology (FRT). The dynamic capacity calculations, fundamentals and theory of this technique are explained in Section 3.2.

9.4.1.1 Cu impregnation loading and Cu salt precursors analyses

For M-MOF-74 and Cu@M-MOF-74 (M = Ni or Co) activation and Cu^{2+} to Cu^{+} reduction, the samples were heated for 6 h at 250 °C with 10% CO (in He) flowing at 1 bar on the FRT instrument.

9.4.1.2 Cu reduction analysis

For Ni-MOF-74 activation and Cu^{2+} to Cu^{+} reduction, Ni-MOF-74 and Cu@Ni-MOF-74 samples were subjected to three different activation and Cu reduction procedures: i) heating at 250 °C with He flowing for 16 h, ii) heating at 250 °C with He flowing for 16 h, followed by heating at 250 °C for 6 h with 10% CO (in He) and iii) heating at 250 °C with 10% CO (in He) for *x* h (where *x* = 2, 6 and 16).

9.4.2 *Dynamic testing conditions using breakthrough column*

The dynamic breakthrough adsorption capacities of the MOFs were performed using a breakthrough column instrument. The fundamentals and theory of this technique are explained in Section 3.3. The apparatus schematic (Figure 3-7) and experimental procedure are shown in Section 3.3.2.2. Sample activation and Cu reduction was performed by flowing 10% CO in He with a total flow-rate of 20 mL min^{-1} for 6 h at 250 °C using heating tape. The full derivations and equations used for the CO breakthrough capacity and CO selectivity calculations are shown in Section 3.3.

9.5 Results and discussion

Ni-MOF-74 and Co-MOF-74 was impregnated with Cu and a systematic Cu impregnation study was performed, with the goal to produce an improved CO purification adsorbent. The findings are presented below.

9.5.1 *Characterisation of Cu impregnated samples*

Initially, the Cu@Ni-MOF-74 samples were synthesized using $CuCl_2$ and $Cu(HCO_2)_2$ as Cu precursors and used the results to optimise the Cu loading. $CuCl_2$, a commonly used precursor,[11-15] was selected because of its ability to be reduced to CuCl leading to strong Cu^{+}-CO π-complexation. $Cu(HCO_2)_2$ was selected due to its ability to

simultaneously behave as a reducing agent and a Cu^{+} source.[13,14] Upon heating, the decomposition of the formate ion produces H_2 for Cu^{2+} to Cu^{+} reduction.[20]

Ni-MOF-74 was initially impregnated with equimolar $CuCl_2$:$Cu(HCO_2)_2$ ratios while varying the Cu loading. ICP-MS and XPS analyses was used to quantify the loading (Table 9-1). ICP-MS probed the bulk Cu loading, while XPS measured the surface loading. The values from XPS analyses surpass those from ICP-MS since XPS is a surface characterisation technique. From the ICP-MS analysis, the estimated Cu loadings are 1.77, 3.50 and 7.07 %wt. and the samples are subsequently referred to as 2-, 4- and 7-Cu@Ni-MOF-74 throughout. These percentages represent the ratios of Cu over Ni in the samples.

Using XRD, it was confirmed that there was no major Cu aggregation of the Cu salt particles (Figure 9-1a).

Table 9-1. Metal loading quantities and textural parameters derived from the elemental analysis (XPS and ICP-MS) and N_2 sorption isotherms at -196 °C for the synthesized and Cu impregnated MOFs. The MOFs were loaded with equimolar solutions of $Cu(II)Cl_2$:$Cu(II)(HCOO)_2$. (S_{BET} = BET surface area, V_{tot} = total pore volume, V_{mic} = micropore volume and V_{mes} = mesopore volume).

Materials	**Bulk Cu loading*** (Cu:M % weight)	**Surface Cu loading†** (Cu:M % weight)	**Metal density±** (mmol $_{metal}$ $g^{-1}_{adsorbent}$)	S_{BET} (m^2 g^{-1})	V_{tot} (cm^3 g^{-1})	V_{mic} (cm^3 g^{-1})	V_{mes} (cm^3 g^{-1})
Ni-MOF-74	-	-	3.97	1427	0.58	0.53	0.05
2-Cu@ Ni-MOF-74	1.77	18.95	4.00	1259	0.49	0.48	0.01
4-Cu@ Ni-MOF-74	3.50	31.86	4.05	1047	0.43	0.40	0.03
7-Cu@ Ni-MOF-74	7.07	35.73	4.12	1036	0.44	0.40	0.04

* Calculated by using the ratio of µg L-1 concentrations of Cu and Ni measured by inductively coupled plasma mass spectrometry.
† Calculated by using the ratio of atomic percentage of Cu and Ni measured by X-ray photoelectron spectroscopy.
± The bulk Cu loading, desolvated adsorbent's general formula and crystallographic density was used to calculate the metal density (mol of coordinatively unsaturated metal sites per gram of adsorbent).

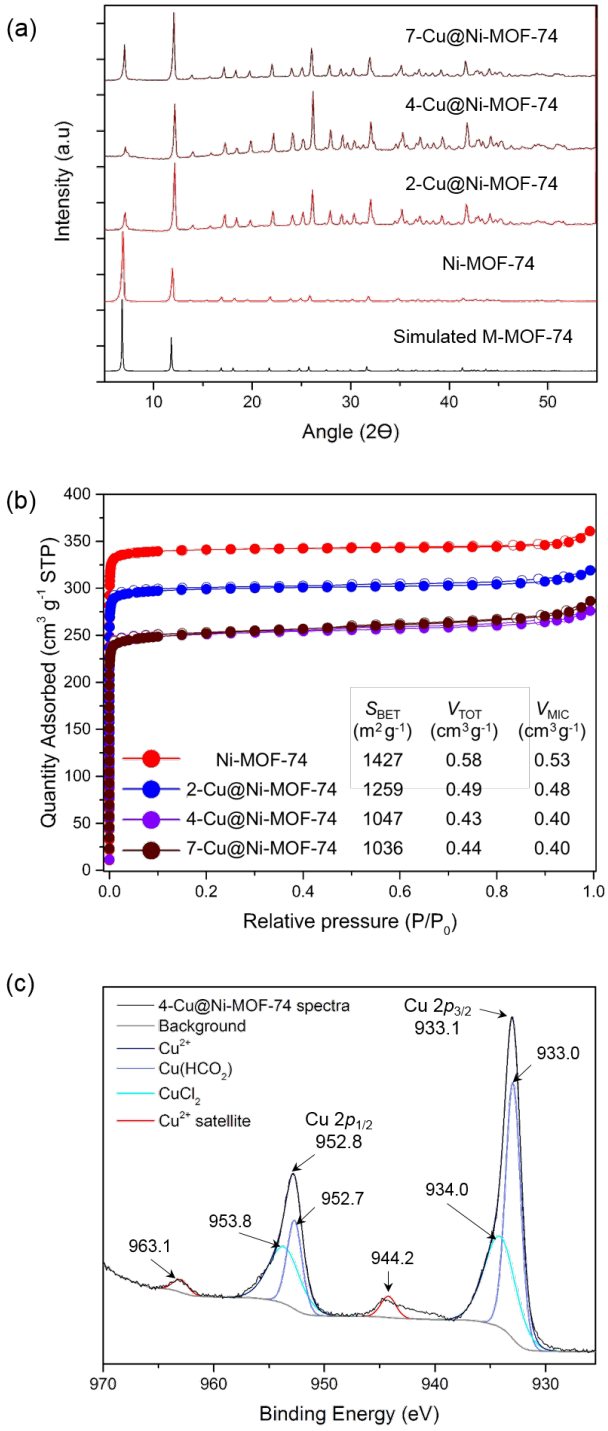


Figure 9-1. Characterisation of the Cu-impregnated MOFs: (a) X-ray diffraction patterns of simulated MOF-74, Ni-MOF-74, 2-Cu@Ni-MOF-74, 4-Cu@Ni-MOF-74 and 7-Cu@Ni-MOF-74. (b) N_2 sorption isotherms at -196 °C of Ni-MOF-74, 2-Cu@Ni-MOF-74, 4-Cu@Ni-MOF-74 and 7-Cu@Ni-MOF-74. The textural parameters derived from the isotherms are shown on the table. (c) Cu 2*p* spectra of 4-Cu@Ni-MOF-74. The deconvoluted Cu peaks and energy levels are shown alongside the characteristic Cu^{2+} satellites.

Porosity measurements allowed us to study the effect of impregnation on pore blocking of Ni-MOF-74 with increasing Cu amount (Figure 9-1b and Table 9-1). Increasing Cu loading reduced the BET surface area and pore volume as anticipated, due to the Cu sites inducing pore blocking and reducing accessibility to pores. As the Cu loading approximately doubled from 4- to 7-Cu@Ni-MOF-74, there was no additional reduction in porosity. This observation suggests that Cu accumulated on the external surface beyond 3.50% wt. Cu loading.

A reduction temperature that would not damage the Ni-MOF-74 and Co-MOF-74 structures was established using VT-PXRD (Figure 7-1a and b) and TG analyses (Figure 7-1c) in Section 7.5.1. Therefore, 250 °C was chosen for this study to maintain structure stability during the thermally-activated Cu reduction.

The oxidation state of surface Cu post activation and reduction was investigated using XPS. The full XPS survey of 4-Cu@Ni-MOF-74 is shown in Figure A6-1a. Figure 9-1c shows the XPS 2*p* spectra of 4-Cu@Ni-MOF-74. The reference 2*p* spectra of the Cu salts are presented in Figure A6-1b. The Cu 2*p* subshell is split into doublets: $2p_{3/2}$ and $2p_{1/2}$. The presence of $Cu(CHO_2)_2$ and $CuCl_2$ is confirmed by comparison against the spectra of the pure Cu salts. These peaks are assigned on the basis that the maximum Cu $2p_{3/2}$ and Cu $2p_{1/2}$ peaks of the $CuCl_2$ Cu 2*p* XPS spectra (Figure A6-1b) are more energetic than the $Cu(CHO_2)_2$ Cu 2*p* peaks. The negative charge of the oxygen formate ions is dispersed across two atoms and therefore the $CuCl_2$ chloride ions result in a slightly more energetic Cu 2*p* peaks. The small peaks at 944.2 and 963.1 eV in Figure 9-1c are due to the characteristic Cu^{2+} satellite peaks.[10] Their weak intensities result from Cu^{2+} reduction to Cu^{+} (or possibly Cu^{0}) facilitated by the heat treatment under vacuum during sample preparation. Overall, the XPS results indicate the possible reduction of Cu^{2+} to Cu^{+} but they are only representative of the surface

chemistry of the materials. The bulk chemistry of the materials is investigated later using XANES.

9.5.2 *Effect of Cu impregnation on CO adsorption*

Having produced Cu@Ni-MOF-74 and Cu@Co-MOF-74 samples of varying Cu loadings, the dynamic CO capacity was evaluated using flux response technology (FRT). This technique allowed us to activate and reduce the samples *in-situ* under flowing He or CO atmosphere prior to testing.

9.5.2.1 Cu loading analysis

The Cu@Ni-MOF-74 activation and Cu reduction conditions are outlined in Section 9.4.1.1, and their dynamic CO capacities (50:50 *v:v* CO:N_2) are presented in Figure 9-2a, 25 °C and 1 bar.

The uptakes of the bar plot are presented per gram of Ni-MOF-74 and Cu@Ni-MOF-74. Overall, Cu impregnation brings limited gains and appears to be detrimental over 3.50 %wt Cu loading, as the difference in values from unimpregnated Ni-MOF-74 falls within the ±5% standard deviation. The increased quantity of Cu induces pore blockage and reduces its capacity. Furthermore, some Cu^{2+} may remain and limit access to the more strongly binding Ni^{2+} unsaturated metal sites.

To accurately study the influence of the Cu loading, one must consider the increased metal density of the structure. Therefore, the CO uptake per mol of metal in the adsorbent was normalised, taking into account both the Cu loading and the Ni content (Table 9-1). These results demonstrate that increasing the Cu loading above 3.50%wt. is detrimental (Figure 9-2a).The normalised values show 4-Cu@Ni-MOF-74 achieves the highest CO uptake per gram of metal. This was identified as the optimised Cu loading for Ni-MOF-74.

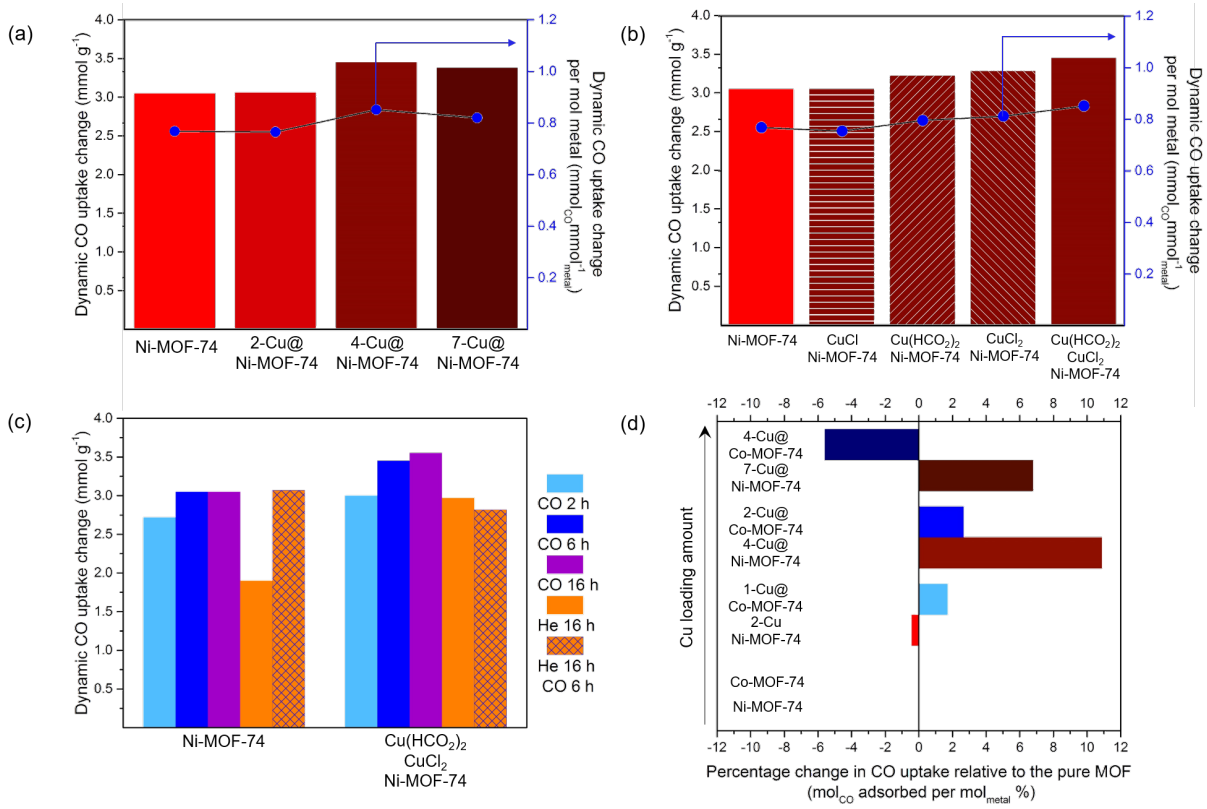


Figure 9-2. Dynamic CO capacities (50:50 *v:v* CO:N_2) measured at 25 °C and 1 bar on the FRT set-up. Thermal activation and Cu reduction was performed for 6 h at 250 °C with flowing 10% CO (in He) unless stated otherwise. The dynamic CO capacity per mol of metal was calculated using the measured values on the FRT and the Cu loading obtained from the ICP-MS analysis. (a) Dynamic CO capacities at varied Cu loadings using equimolar $CuCl_2$:$Cu(HCO_2)_2$ salt precursors. (b) Dynamic CO capacities using different Cu salts for impregnation. (c) Dynamic CO capacities using $CuCl_2$:$Cu(HCO_2)_2$ salts with thermal activation and Cu reduction performed using He or CO atmosphere. (d) Dynamic CO capacities of Cu@Ni-MOF-74 and Cu@Co-MOF-74 at varied Cu loadings using equimolar $CuCl_2$:$Cu(HCO_2)_2$ salt precursors.

9.5.2.2 Cu salt precursors analysis

After determining the optimum range of Cu loading, the effect of using different Cu salts for Cu impregnation was studied (*i.e.* $CuCl_2$, $Cu(HCO_2)_2$ and CuCl or a combination thereof) of Ni-MOF-74. The Ni-MOF-74 activation and Cu reduction conditions are outlined in Section 9.4.1.1. The dynamic capacities to the Cu loading was normalised to account for the small differences in Cu loading (3.17 to 3.95% wt.).

The results, presented in Figure 9-2b, show the presence of $CuCl_2$/$Cu(HCO_2)_2$ assists the reduction procedure, leading to the highest CO capacity, though only slightly. Impregnation with solely $Cu(HCO_2)_2$ produces the second highest CO capacity, indicating $CuCl_2$ is required as another source of Cu to improve CO capacity. The decomposed residual carbon of the formate precursor adds to the specific weight of the adsorbent. This fraction of the adsorbent mass did not contribute to CO adsorption. CuCl impregnation exhibited similar CO uptake to 'pure' Ni-MOF-74, and a small reduction in the normalised CO uptake. This result is due to Cu^+ to Cu^0 reduction upon heating with CO. To summarise, impregnation with a mixture of $CuCl_2$ and $Cu(HCO_2)_2$ leads to the highest CO uptake.

9.5.2.3 Cu reduction analysis

The activation and Cu reduction procedure through heat treatment was investigated using He and CO atmosphere for increasing durations (conditions outlined in 9.4.1.2). The analysis on the Cu@Ni-MOF-74 samples was conducted. The CO dynamic uptakes for the various activation and reduction procedures are shown in Figure 9-2c.

Activating Ni-MOF-74 under CO atmosphere produced a higher dynamic CO capacity than activating under He. It is hypothesized that at elevated temperatures, CO reacts with residual MeOH bound to the MOF, thereby increasing the number of unsaturated metal sites.[21] Activation *via* a combination of heating and CO flow led to the highest CO uptake for the equimolar $CuCl_2$:$Cu(HCO_2)_2$ impregnated sample. Overall, the results indicate that both He and CO behave as reducing agents to different degrees, and dictate the duration of heat treatment required. Following this study, Cu^{2+} to Cu^+ reduction *via* heating at 250 °C with 10% CO (in He) for 6 h was chosen as the activation and Cu reduction procedure for the subsequent experiments. These

conditions compromise between minimising the time of CO used at elevated temperature while maximising the amount of Cu^{+} generated.

9.5.2.4 Cu@Co-MOF-74 analysis

In this section Cu@Co-MOF-74 samples and the impact of Cu impregnation on CO uptake (Figure 9-2d) is discussed. Equimolar $CuCl_2$:$Cu(HCO_2)_2$ mixture was employed for impregnation. The ICP-MS analyses indicated Cu loading of 1.28, 2.42 and 4.22 wt%. The corresponding samples are referred to as 1-, 2- and 4-Cu@Ni-MOF-74. The CO uptakes were normalised to account for the variance in Cu loading. 1-Cu@Ni-MOF-74 and 2-Cu@Co-MOF-74 adsorbed similar amounts of CO, with marginal improvement compared to Co-MOF-74 (Figure 9-2d). Cu loading above 2.42 wt% was detrimental due to pore blocking and reduced accessibility to framework unsaturated metal sites for strong Co^{2+}-CO binding.

9.5.3 *In-situ Cu@M-MOF-74 XAFS characterisation*

XAFS experiments was conducted on the best performing Cu impregnated M-MOF-74 samples, *i.e.* 4-Cu@Ni-MOF-74 and 2-Cu@Co-MOF-74. The objectives were: (i) to further investigate the Cu reduction step since XPS only provided information on surface Cu sites, (ii) to assess the impact of the Cu impregnation on the states of the Ni and Co sites, (iii) to monitor changes in the Cu, Ni and Co sites upon CO adsorption.

9.5.3.1 XAFS analysis of the Cu species during the activation and reduction procedure

Here, the Cu oxidation process upon a progressive activation and reduction procedure was evaluated. The activation and reduction procedure consisted of progressive heating under He up to 250 °C, followed by a switch to a CO atmosphere and switching back to He, accompanied with cooling to 25 °C. The Cu-edge XANES spectra for 4-

Cu@Ni-MOF-74 are shown in Figure 9-3a and Figure A6-2a and b. Those for 2-Cu@Co-MOF-74 are shown in Figure A6-3.

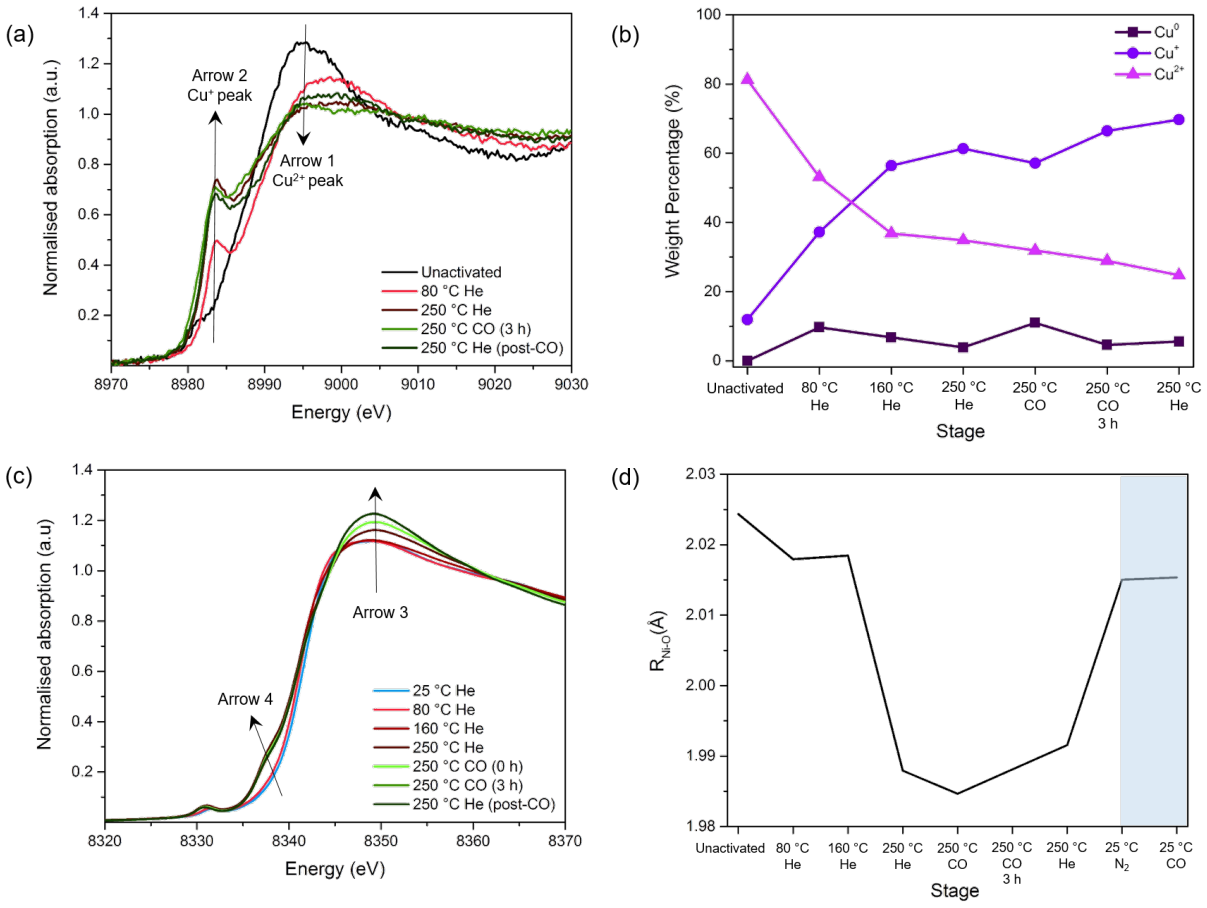


Figure 9-3. Study of the MOF activation and Cu reduction procedure of 4-Cu@Ni-MOF-74: (a) Cu-edge XANES spectra. Arrow 1 = Cu^{2+} peak; Arrow 2 = Cu^{+} peak. (b) Linear Combination Fit analysis of Cu species. (c) Ni-edge XANES spectra. (d) Ni-O bond lengths obtained by the EXAFS fit during the activation and Cu reduction procedure and analysis (shaded).

Here, the samples based on the Cu@Ni-MOF-74 sample (Figure 9-3a) are discussed first. Before activation/reduction, the peak at 8995 eV exhibits the characteristic intense white line of Cu^{2+} (*i.e.* intense absorption in the near-edge). As the temperature increases, the intensity of the white line decreases and is accompanied by the appearance of a feature at 8983.7 eV. This feature is attributed to the first transition peak of Cu^{+}, and is confirmed when its first derivative is overlaid with the CuCl

standard (Figure A6-4a). This observation indicates reduction from Cu^{2+} to Cu^{+} through the oxidation of the formate (9-1) proceeds at temperature as low as 80 °C.

$$Cu(COOH)_2 \leftrightarrow Cu^{+} + H^{+} + 2COO^{-} \quad (9\text{-}1)$$

By applying a linear combination fit in Athena, similar to that used by Lamberti *et al.*,[22] the percentage of each Cu species present (Cu^{2+}, Cu^{+} and Cu^{0}) was determined at various stages of activation and reduction using the spectra from the pure standards as references (Figure 9-3b). Overall, as the temperature increases, the amount of Cu^{+} increases while that of Cu^{2+} decreases. A pure flow of CO at 250 °C decreases markedly the amount of Cu^{+}. This observation is attributed to the formation of $[Cu^{+}(CO)n]_{+}$ adducts in the sample, as previously shown by Prestipino *et al*. and Yamashita *et al*. in the case of Cu^{+} in ZSM-5 and Cu-Zeolite Y.[23,24] However, as reduction proceeds the CO adduct decomposes and the Cu^{+} peak increases again. At the end of the reduction procedure, there is some Cu^{2+} species (24.4%) present but the majority of the copper is Cu^{+} (69.7%), with a small but significant amount of Cu^{0} (6%) due to over reduction. After the reduction procedure using CO, switching back to a He flow at 250 °C increases slightly the amount of Cu^{2+} while decreasing that of Cu^{+}. These changes are due to the oxidation of the Cu species caused by the desorption of residual CO on the Cu^{+}.

A similar analysis of the Cu^{+} evolution through the activation/reduction process was performed for the Cu impregnated Co-MOF-74 sample and similar conclusions are derived. Yet, the amount of Cu^{0} species present for this sample remains negligible (Figure A6-4b).

9.5.3.2 XAFS analysis of the Ni and Co species during the activation and reduction procedure

Following a greater understanding of the Cu reduction process, the interactions of the impregnate with the MOF metal centres was investigated. This study is important as Co^{2+} and Ni^{2+} centres strongly bind to CO. Any blockage or interference of these sites could be detrimental to the adsorption process. The Ni-edge XANES spectra of 4-Cu@Ni-MOF-74 and Co-edge XANES spectra of 2-Cu@Co-MOF-74 during the reduction process can be seen in Figure 9-3c and Figure A6-5a, respectively.

The following changes are observed as the temperature and the gas composition change: (i) an increase in the intensity of the white line position with a shift towards higher energies, (ii) the appearance of a pre-edge feature assigned to 1*s*-4p_z transition and (iii) an increase in intensity of the pre-edge feature with a shift towards lower energies assigned to 1*s*-3*d* transition. These observations are mostly coherent with the previously reported results regarding the pre-edge feature of the Ni- and Co-edge of the MOFs during heating.[25,26] During MOF activation, the symmetry changes from octahedral to square-pyramidal as the solvent and water molecules attached to the Ni^{2+} and Co^{2+} unsaturated metal sites desorb and provide accessibility for CO adsorption. This causes the removal of the degeneration of *p* levels and the loss of the inversion centre[25,26] and allows for the transition 1*s*-4p_z to appear,[27,28] as well as for the increase in intensity in the 1*s*-3*d* electronic transition which is forbidden in a perfect octahedral symmetry.[27,29]

9.5.3.3 EXAFS analysis of the Ni and Co species geometry during the activation and reduction procedure

EXAFS analysis was used to examine the geometry and bond lengths of the MOF structures during activation and Cu reduction. The results are presented in Figure 9-3d

and Figure A6-5b for 4-Cu@Ni-MOF-74 and Figure A6-6a for 2-Cu@Co-MOF-74. A decrease in the M-CO distance was observed upon heating, with further decrease upon introduction of CO. These contractions indicate a change in the MOF structure from an octahedral to square pyramidal geometry. The observations aligned with previous studies regarding the configuration of M-MOF-74.[26,30] This geometry change is due to release of trapped solvent molecules. Upon subsequent adsorption of N_2 and then CO, the structures revert back to the octahedral configuration.[26,30] A slight increase in bond length upon CO adsorption was observed because of the M^{2+}-CO π backdonation consequently weakens the M-O carboxylate bonds as the electrons are shared over an additional bond in the octahedral state.[31] To summarise, no unexpected trends of the framework geometry were observed, demonstrating no interference from the Cu species in the adsorption of CO on the Ni and Co sites.

9.5.3.4 XAFS analysis of the Cu species during CO adsorption

The focus of this section turns to monitoring the state of the Cu sites upon exposure to CO for adsorption. The results for the Cu-edge of 4-Cu@Ni-MOF-74 are presented in Figure 9-4a. After the activation and reduction step, N_2 adsorption causes a slight reoxidation of the Cu^+ species. This observation is similar to the effect of CO adsorption forming the $[Cu^+(CO)n]^+$ adduct and generating an increase in the Cu^+ peak, as previously mentioned.[23] These observations provide evidence of Cu^+-N_2 and then Cu^+-CO binding as the loss of electrons during oxidation occurs because of the new bond formations.

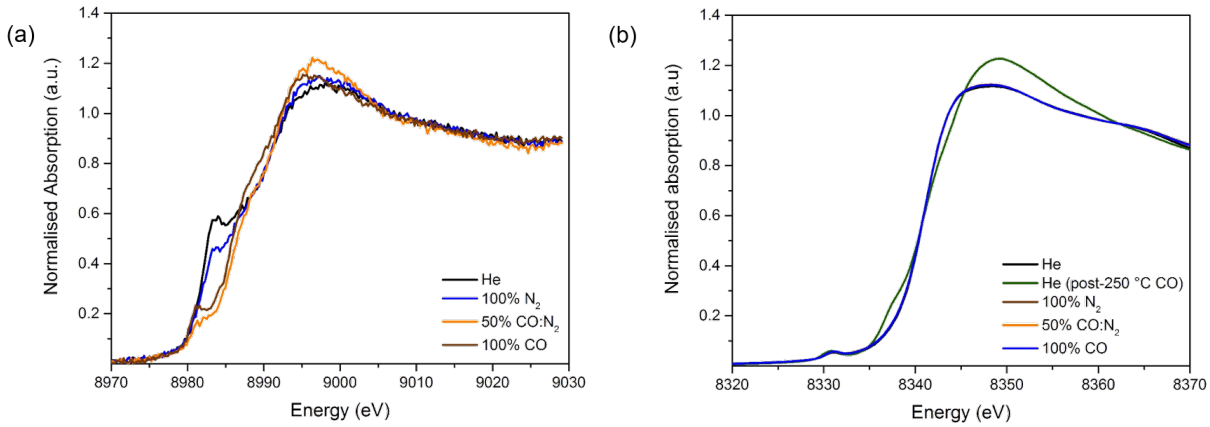


Figure 9-4. Study of CO adsorption upon 4-Cu@Ni-MOF-74: (a) Cu-edge XANES spectra. (b) Ni-edge XANES spectra.

9.5.3.5 XAFS analysis of the Ni and Co species during CO adsorption

Similarly to the study of the Cu sites, states of the Ni and Co sites upon CO adsorption are discussed. The results for 4-Cu@Ni-MOF-74 are presented in Figure 9-4b and those for 2-Cu@Co-MOF-74 in Figure A6-7a. The interaction of the MOF with N_2 immediately restores the O_h-like symmetry around the Ni^{2+} centre, as observed by the disappearance of the feature at 8338 eV and the decrease of the white line to intensity of the solvated material. This confirms Ni^{2+}-CO and Co^{2+}-CO binding and demonstrates the negligible effect of Cu impregnation upon the energy of Ni^{2+}-CO and Co^{2+}-CO interactions.

9.5.4 *In-situ Cu@M-MOF-74 DRIFTS characterization*

Diffuse reflectance infrared Fourier transform spectroscopy (DRIFTS) was used to further study the metal-CO interactions of both Ni and Cu of 4-Cu@Ni-MOF-74 and pure Ni-MOF-74 (Figure 9-5). The Cu^{2+}-CO interactions in Cu-MOF-74 was also monitored for comparison.

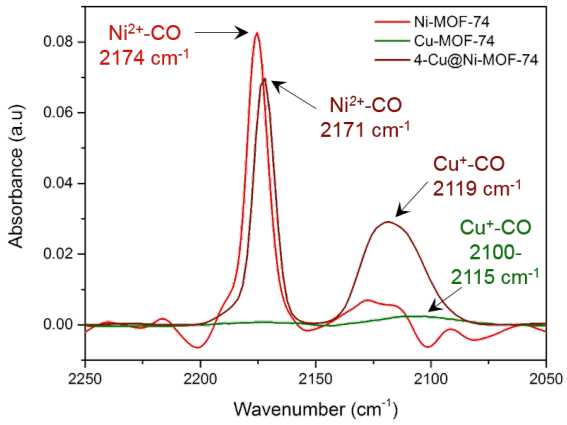


Figure 9-5. *In-situ* DRIFTS measurement of chemisorbed CO on Ni-MOF-74, Cu-MOF-74 and 4-Cu@Ni-MOF-74 at 25 °C and 1 bar. Each spectrum has been background corrected with respect to the instrument and sample holder.

The 4-Cu@Ni-MOF-74 sample is considered first. The Ni^{2+}-CO stretch appears at 2171 cm^{-1}, and corresponds to a non-classical interaction.[19] The spectrum shows that Cu^{+} impregnation left the framework Ni^{2+} sites unaffected and accessible to CO binding. This aligns with the findings from the XAFS study. A Cu-CO interaction at 2119 cm^{-1} is observed. A free CO stretch would be expected 2143 cm^{-1}, therefore the band at 2119 cm^{-1} indicates a classical Cu^{x+}-CO interaction.[32] This stretch is assigned to a $[Cu(CO)_1]^{+}$ adduct, previously observed in Cu-ZSM-5.[33] Ni-MOF-74 spectrum is similar to that of 4-Cu@Ni-MOF-74, minus the Cu-CO interactions. A small band is also observed at 2115-2130 cm^{-1} which is part of the background noise. The Cu-MOF-74 spectrum is more difficult to analyse due to the low intensity bands from the weakly binding Cu^{2+}-CO interactions (Figure A6-7b). The band from Cu^{2+}-CO interactions is less intense than that of Cu^{+}-CO interactions despite Cu-MOF-74 containing structural Cu^{2+} centres. This is due to the Cu^{2+} sites being prone to autroreduction to Cu^{+} at the external MOF surface.[34] The slight red shift of the Cu^{+}-CO band compared to 4-Cu@Ni-MOF-74 indicates weaker Cu^{+}-CO binding.

9.5.5 *Dynamic CO/N_2 and CO/CO_2 separation testing*

The dynamic separation performance of 4-Cu@Ni-MOF-74 for CO/N_2 and CO/CO_2 was tested using a dynamic breakthrough column apparatus. The results were compared to those of Ni-MOF-74 to evaluate the effect of Cu impregnation. The breakthrough curves for 50:50 *v:v* binary mixtures are shown on Figure 9-6.

For the 50:50 *v:v* $CO:N_2$ mixture (Figure A6-7b), N_2 breaks through first at similar times for both samples because of the weaker physisorption forces responsible for adsorbing to non-polar N_2. Upon CO breakthrough, the N_2 concentration exceeds the inlet feed concentration and produces a roll-up effect. The competitive binding with CO induces a spike in concentration as CO replaces the weakly adsorbed N_2 molecules. Cu impregnation resulted in an increased breakthrough capacity (from 4.07 to 4.49 mmol g^{-1}) and CO/N_2 selectivity at equilibrium after saturation (from 14 to 27). The increase in CO/N_2 separation performance is attributed to: (i) the increased number of unsaturated metal sites binding to CO and (ii) the lower porosity of the Cu impregnated samples reducing N_2 sorption.[13]

Introducing Cu^+ sites with no affinity to N_2 results in greater CO/N_2 selectivity. The same degree of improvement was not observed earlier with the FRT. Indeed, in the FRT tests, the sample is pre-saturated with N_2 before CO adsorption, and the instrument is unable to distinguish the CO selectivity and separation performance. Figure 9-6b exhibits similar breakthrough times for CO and CO_2 for Ni-MOF-74 because of similar binding strength between the unsaturated metal sites and polar CO and CO_2 adsorbates.

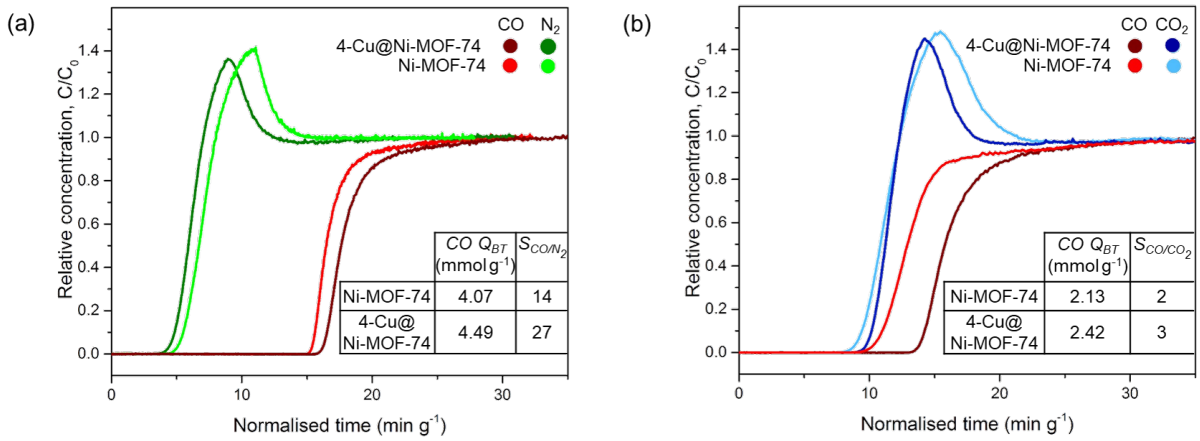


Figure 9-6. Breakthrough curves of Ni-MOF-74 and 4-Cu@Ni-MOF-74 for 50:50 v:v binary gas mixtures on a breakthrough adsorption column at 25 °C and 1 bar: (a) CO:N_2 mixture and (b) CO:CO_2 mixture. (*CO* Q_{BT} = CO breakthrough capacity, $S_{CO/X}$ = CO/X ideal selectivity at equilibrium where X = N_2, CO_2)

The CO breakthrough capacity is smaller than the amount in a CO:N_2 stream because of the MOFs greater affinity to CO_2 over N_2.[35] Cu impregnation improved the CO/CO_2 separation performance by increasing the number of Cu^+ unsaturated metal sites which undergo strong π-complexation to CO, but do not interact with CO_2 through this mechanism.[14] Therefore, both the CO breakthrough capacity and CO/CO_2 selectivity increased upon impregnation. Cu impregnation replaced the accessibility of Ni^{2+} unsaturated metal sites for CO and CO_2 binding with Cu^+ unsaturated metal sites solely for CO binding. CO/N_2 and CO/CO_2 separation performance was also improved after Cu impregnation of Fe-MIL-100 and Cr-MIL-101,[13-18] but was improved to a smaller degree with M-MOF-74 because of the highly active Ni^{2+} sites compared to Fe^{3+} and Cr^{3+}.

9.6 Conclusions

This chapter presents the synthesis, optimisation, characterisation and testing of the Cu impregnation and reduction procedure of Cu impregnated M-MOF-74 to enhance CO/N_2 and CO/CO_2 separation ability. After synthesis and optimisation of the Cu impregnation and reduction procedure using FRT, *in-situ* XANES analysis was performed to monitor the Cu species state and quantify the amount of desired Cu^+ throughout the procedure. XANES also enabled us to confirm Cu^+-CO binding and to verify that no changes in metal-CO interactions of the MOF occurred upon Cu impregnation. Finally, performed CO/N_2 and CO/CO_2 breakthrough measurements were performed to test the enhanced separation ability of Cu impregnated Ni-MOF-74 after impregnation. The key findings are summarised below:

- Cu impregnation of M-MOF-74 enhanced CO capacity and CO/N_2 and CO/CO_2 separation ability. Cu loading reduced the MOFs surface area and decreased N_2 sorption. The increased number of sites for π–complexation for CO adsorption reduced the number of available sites for CO_2 adsorption.
- CO at elevated temperature was used to reach the desired Cu^+ state, with the oxidation state confirmed using XANES. After the Cu reduction procedure, the majority of the Cu sites were in the Cu^+ state, while some Cu^{2+} remained and Cu^0 species were formed through over reduction as predicted.
- The Cu loading amount detrimentally reduces the CO capacity after a certain threshold as the Cu sites reduce accessibility to the active M^{2+} sites of M-MOF-74.
- Cu^+-CO binding was confirmed and there was no interference from the Cu species on CO adsorption on the Ni^{2+} and Co^{2+} sites of the MOF observed.

- $Cu(HCO_2)_2$ is required in the Cu impregnation procedure to enhance CO capacity and Cu reduction ability to Cu^+, as the formate ion decomposes to produce H_2 as a reducing agent upon heating.
- He and CO behave as reducing agents to different degrees, as Cu^{2+} to Cu^+ reduction occurs as low as 80 °C with He flowing at elevated temperature. CO is required to maximise the number of Cu^+ sites generated.

9.7 References

1 Evans, A. et al. Optimisation of Cu+ impregnation of MOF-74 to improve CO/N_2 and CO/CO_2 separations. *Accepted by RSC Advances*

2 Khan, N. A. & Jhung, S. H. Adsorptive removal and separation of chemicals with metal-organic frameworks: Contribution of π-complexation. *Journal of Hazardous Materials* **325**, 198-213, (2017).

3 Xie, Y. et al. Zeolites modified by CuCl for separating CO from gas mixtures containing CO_2. *Adsorption* **3**, 27-32, (1997).

4 Gao, F., Wang, Y. & Wang, S. Selective adsorption of CO on CuCl/Y adsorbent prepared using CuCl2 as precursor: Equilibrium and thermodynamics. *Chemical Engineering Journal* **290**, 418-427, (2016).

5 Hirai, H., Wada, K. & Komiyama, M. Active carbon-supported copper (I) chloride as carbon monoxide solid adsorbent. Chemistry Letters **12**, 361-364, (1983).

6 Hirai, H., Komiyama, M. & Wada, K. Active carbon-supported aluminium copper chloride as water-resistant carbon monoxide adsorbent. *Chemistry Letters* **11**, 1025-1028, (1982).

7 Hirai, H., Wada, K. & Komiyama, M. Active carbon-supported copper (I) chloride as solid adsorbent for carbon monoxide. *Bulletin of the Chemical Society of Japan* **59**, 2217-2223, (1986).

8 Hirai, H., Wada, K. & Komiyama, M. Active carbon-supported aluminium copper (I) chloride as solid carbon monoxide adsorbent. *Bulletin of the Chemical Society of Japan* **59**, 1043-1049, (1986).

9 Zhu, L.-q., Tu, J.-l. & Shi, Y.-j. Separation of $CO-CO_2-N_2$ gas mixture for high-purity CO by pressure swing adsorption. *Gas Separation & Purification* **5**, 173-176, (1991).

10 Huang, Y. et al. Preparation of CuCl@ AC with high CO adsorption capacity and selectivity from CO/N2 binary mixture. *Adsorption* **21**, 373-381, (2015).

11 Ma, J., Li, L., Ren, J. & Li, R. CO adsorption on activated carbon-supported Cu-based adsorbent prepared by a facile route. *Separation and Purification Technology* **76**, 89-93, (2010).

12 Gao, F. et al. Adsorption separation of CO from syngas with CuCl@AC adsorbent by a VPSA process. *RSC Advances* **8**, 39362-39370, (2018).

13 Peng, J. et al. A supported Cu(I)@MIL-100(Fe) adsorbent with high CO adsorption capacity and CO/N_2 selectivity. *Chemical Engineering Journal* **270**, 282-289, (2015).

14 Kim, A.-R. et al. Creating high CO/CO_2 selectivity and large CO working capacity through facile loading of Cu(I) species into an iron-based mesoporous metal-organic framework. *Chemical Engineering Journal* **348**, 135-142, (2018).

15 Vo, T. K. et al. Highly CO selective Cu(I)-doped MIL-100(Fe) adsorbent with high CO/CO2 selectivity due to π complexation: Effects of Cu(I) loading and activation temperature. *Microporous and Mesoporous Materials* **274**, 17-24, (2019).

16 Li, Y.-X. et al. Controlled Construction of Cu(I) Sites within Confined Spaces via Host–Guest Redox: Highly Efficient Adsorbents for Selective CO Adsorption. *ACS Applied Materials & Interfaces* **10**, 40044-40053, (2018).

17 Wang, Y. et al. $CuAlCl_4$ doped MIL-101 as a high capacity CO adsorbent with selectivity over N_2. *Frontiers of Chemical Science and Engineering* **8**, 340-345, (2014).

18 Yin, Y., Wen, Z.-H., Liu, X.-Q., Shi, L. & Yuan, A.-H. Modification of metal organic framework HKUST-1 with CuCl for selective separation of CO/H_2 and CO/N_2. *Journal of Porous Materials*, 1-7, (2018).

19 Bloch, E. D. et al. Reversible CO Binding Enables Tunable CO/H_2 and CO/N_2 Separations in Metal–Organic Frameworks with Exposed Divalent Metal Cations. *Journal of the American Chemical Society* **136**, 10752-10761, (2014).

20 Luidold, S. & Antrekowitsch, H. Hydrogen as a reducing agent: State-of-the-art science and technology. *JOM* 59**,** 20-26, (2007).

21 Matsumura, Y., Tanaka, K., Tode, N., Yazawa, T. & Haruta, M. Catalytic methanol decomposition to carbon monoxide and hydrogen over nickel supported on silica. Journal of Molecular Catalysis *A: Chemical* **152**, 157-165, (2000).

22 Lamberti, C. et al. Determination of the oxidation and coordination state of copper on different Cu-based catalysts by XANES spectroscopy in situ or in operando conditions. *Physical Chemistry Chemical Physics* **5**, 4502-4509, (2003).

23 Prestipino, C., Capello, L., D'Acapito, F. & Lamberti, C. Local structure of $[CuI(CO)2]^+$ adducts hosted inside ZSM-5 zeolite probed by EXAFS, XANES and IR spectroscopies. *Physical Chemistry Chemical Physics* **7**, 1743-1746, (2005).

24 Yamashita, H. et al. In-Situ XAFS, Photoluminescence, and IR Investigations of Copper Ions Included within Various Kinds of Zeolites. Structure of Cu(I) Ions and Their Interaction with CO Molecules. *Journal of Physical Chemistry* **100**, 397-402, (1996).

25 Bonino, F. et al. Local Structure of CPO-27-Ni Metallorganic Framework upon Dehydration and Coordination of NO. *Chemistry of Materials* **20**, 4957-4968, (2008).

26 Chavan, S. et al. CO Adsorption on CPO-27-Ni Coordination Polymer: Spectroscopic Features and Interaction Energy. *Journal of Physical Chemistry C* 113, 3292-3299, (2009).

27 Prestipino, C. et al. An in situ temperature dependent IR, EPR and high resolution XANES study on the NO/Cu+–ZSM-5 interaction. *Chemical Physics Letters* **363**, 389-396, (2002).

28 Estephane, J. et al. Structure and Enhanced Reactivity of Chromocene Carbonyl Confined inside Cavities of NaY Zeolite. *Journal of Physical Chemistry C* **113**, 7305-7315, (2009).

29 Prestipino, C., Solari, P. L. & Lamberti, C. EXAFS and XANES Investigation of the ETS-10 Microporous Titanosilicate. *Journal of Physical Chemistry B* **109**, 13132-13137, (2005).

30 Groppo, E. et al. In situ, Cr K-edge XAS study on the Phillips catalyst: activation and ethylene polymerization. *Journal of Catalysis* **230**, 98-108, (2005).

31 Bistoni, G. et al. How π back-donation quantitatively controls the CO stretching response in classical and non-classical metal carbonyl complexes. *Chemical Science* **7**, 1174-1184, (2016).

32 Strauss, S. H. Copper(I) and silver(I) carbonyls. To be or not to be nonclassical. *Journal of the Chemical Society, Dalton Transactions,* 1-6, (2000).

33 Hadjiivanov, K. I., Kantcheva, M. M. & Klissurski, D. G. IR study of CO adsorption on Cu-ZSM-5 and CuO/SiO_2 catalysts: σ and π components of the Cu+—CO bond. *Journal of the Chemical Society, Faraday Transactions* **92**, 4595-4600, (1996).

34 Drenchev, N. et al. Open Metal Sites in the Metal–Organic Framework CPO-27-Cu: Detection of Regular and Defect Copper Species by CO and NO Probe Molecules. *Journal of Physical Chemistry C* **122**, 17238-17249, (2018).

35 Dickey, A. N., Yazaydın, A. Ö., Willis, R. R. & Snurr, R. Q. Screening CO_2/N_2 selectivity in metal-organic frameworks using Monte Carlo simulations and ideal adsorbed solution theory. *The Canadian Journal of Chemical Engineering* **90**, 825-832, (2012).

Chapter 10 Conclusions and Outlook

10.1 Conclusions

This thesis presents the dynamic CO/N_2 separation performance of MOFs under industrially relevant conditions, and the method of designing novel MOFs for enhanced purification. From the literature, it was evident further dynamic CO/N_2 separation testing was required to provide a realistic insight into the industrial viability of the materials and complement the prominent equilibrium sorption data reported to date. Flux response technology and breakthrough column testing were employed to evaluate the dynamic CO/N_2 separation performance. From the MOFs synthesized, screened, designed, characterised and evaluated for CO/N_2 separation, the main conclusions are presented below:

In Chapter 5, preliminary screening of MOFs exhibiting CO/N_2 separation ability assisted in determining the key attributes responsible for an effective separation. It was found that the nature of the unsaturated metal sites of the MOFs mainly govern CO/N_2 separation ability, with Ni^{2+}- and Co^{2+}-based MOFs exhibiting the highest CO capacities and selectivities. The importance of the density of the unsaturated metal sites with strong metal-CO interactions was highlighted, however when these interactions are weak (*i.e* Cu^{2+}-CO), then the MOFs porosity governs the CO capacity at both low and high pressure.

Chapter 6 studied the effect of N_2 impurity upon CO/N_2 separation using the two best performing MOFs established; namely Ni-MOF-74 and Co-MOF-74, and their related 1-D hexagonal pored MOF structures, and it was found that the heat released from

the large CO enthalpy of adsorption detrimentally reduces the CO dynamic capacity with higher CO concentration streams of CO:N_2 mixtures. It was also found that CO/N_2 separation at elevated pressure is required to capitalise on their related 1-D hexagonal pored MOF structures (Ni_2Cl_2(BTDD) and Co_2Cl_2(BTDD)), which have greater porosity than Ni-MOF-74 and Co-MOF-74. Chapter 7 studied the effect of CO_2 impurity upon CO/N_2 separation, by investigating the effect of competitive CO_2 adsorption. The presence of low level CO_2 impurity (20 ppm) reduced the CO breakthrough capacity in a ternary CO:N_2:CO_2 mixture, but the CO/N_2 selectivity remained unaffected. Ni-MOF-74 and Co-MOF-74 recyclability was tested using thermal regeneration to replicate a temperature-swing adsorption process. It was discovered that CO/N_2 separation performance was maintained after 5 cycles. Shorter regeneration times or lower temperatures are required to compromise between maximising the MOF lifetime and working capacity, as there was a slight loss in performance and porosity after 20 cycles.

In Chapter 8, it was found that CO ($K_{D,\ CO}$) and N_2 ($K_{D,\ N2}$) diffusion rates upon desorption of the 1-D hexagonal pored MOFs followed different trends. The CO heat of adsorption governs the $K_{D,\ CO}$ values with materials with both a high density of unsaturated metal sites and strong metal CO-interactions, resulting in slower $K_{D,\ CO}$ diffusion rates upon desorption. $K_{D,\ N2}$ values were unaffected by the metal sites and were governed by pore size and porosity.

Chapter 9 combined the knowledge gained from literature and the key findings from the previous chapters to enhance the CO/N_2 separation performance of novel MOFs through post-synthesis chemical modification. By introducing auxiliary metal sites through Cu impregnation of M-MOF-74, CO capacity and CO/N_2 and CO/CO_2 selectivity was enhanced. The desired Cu^+ state was confirmed during the Cu

reduction procedure, and Cu^+-CO binding was also found not to impede metal-CO interactions from the MOF. The Cu impregnation and Cu reduction procedure was optimised and showed that $Cu(HCO_2)_2$ precursor and heating at 250 °C with CO assisted Cu reduction to the desired Cu^+ state.

Overall, the dynamic CO/N_2 separation performance of MOFs was improved upon impregnation. Dynamic testing with binary and ternary mixtures provided insight into the effect of N_2 and CO_2 impurity level upon CO purification ability of the MOFs to provide an industrial context for CO/N_2 separation.

10.2 Future work

While the CO/N_2 separation ability of MOFs has been enhanced in this thesis, implementation of these materials in an industrial setting is a long way ahead. To further progress in this direction, one needs to: improve the CO capacity and selectivity further to minimise the number of cycles and operating costs, synthesize MOFs into suitable structures for an adsorbent separation process and test MOFs using CO separation systems where the conditions are tailored to maximise their working capacities. Routes towards advancing these aspects are discussed below:

10.2.1 *To perform post-synthesis modification with MOFs with greater porosity*

While M-MOF-74 possesses high porosity, their related 1-D hexagonal pored MOF structures have characteristically higher porosity which can undergo larger Cu loading while maintaining the MOFs performance. Cu loading inside mesopores is less likely to induce pore blockage, and therefore would result in a higher CO capacity and an increase in CO recovery. CO and N_2 isotherm measurements of Cu impregnated MOFs with the correct Cu reduction procedure are also required for modelling the adsorbent bed in process system simulations.

10.2.2 *To develop MOF formulation for an adsorbent bed and to measure their material properties*

Currently, the MOFs are synthesized in powder form. Powders cannot be implemented in large-scale designs as they would lead to large pressure drops. Therefore, formulation of MOFs into pellets, beads or monolith is required. The bulk density of the material must be measured in order to assist with the simulations of the adsorbent bed and optimise the adsorption conditions of the process system. It will be useful to study the effects of Cu impregnation on the MOF density and particle size, and their impact on the MOF formulation.

10.2.3 *To develop an experimental breakthrough set-up to test different adsorption separation processes*

While the current configuration of the breakthrough column apparatus can replicate a temperature-swing adsorption system, the experimental set-up could be modified to replicate vacuum-swing adsorption and pressure-swing adsorption systems. By ensuring suitable pressure regulators, tubing and columns are in place to withstand high pressure, pressure-swing adsorption measurements can be performed to test the working capacities over larger pressure ranges to test a larger range of MOFs. The same objective is intended for vacuum-swing adsorption measurements by installing a vacuum source. Furthermore, thermal activation under vacuum represents more accurate activation conditions used in equilibrium sorption measurements for comparison.

Appendices

Appendix 1

Maple was used to solve the zero length column parameters to calculate the diffusivity coefficients. The code used to solve the calculations is shown below:

$Digits := 5$

$$Digits := \tag{1}$$

####### Enter Slope and Intercept Information Below. This is obtained from a linear fit of the longtime region of a semi-log $\left(\ln\left(\frac{C}{Co}\right) vs.\, t\right)$#########

######This worksheet will calculate the diffusion coefficient and Henrys constant for three runs.

$Slope1 :=$

$$Slope1 := \tag{2}$$

$$Intercept1 := \tag{3}$$

$Intercept1 :=$

########## Enter Sample and Experimental Information Below##############################

F=Flowrate $\frac{ml}{second}$

$F := \frac{}{60}$

$$F := \tag{4}$$

#Vs = sample volume in ml (cc)

$Vs :=$

$$Vs := \tag{5}$$

#r = particle radius (not crystallite radius) in meters

$r :=$

$$r := \tag{6}$$

#####Temperature in Centigrade

$ExpTemp :=$

$$ExpTemp := \tag{7}$$

####### Density in $\frac{g}{cc}$

$SorbentDensity :=$

$$SorbentDensity := \tag{8}$$

############### Calculations Below###

L is dimensionless constant

#B is a dimensionless constant

#H = Henrys Constant ----- Solving For this-- dimensionless

#D = Diffusion Coefficient -----Solving For this--- $\frac{meters^2}{second}$

#K is the time constant for the experiment, in literature used to determine if suitable for ZLC analysis

$Slope1 := \frac{-Bi^2 \cdot D1}{r^2} = Slope1$

$$Slope1 := \tag{9}$$

$Intercept1 := e^{Intercept1}$

$$Intercept_1 \tag{10}$$

$$Fofl1 := B1 - \cot(B1) + B1\cdot\cot^2(B1) + \frac{(2\cdot B1\cdot\cot(B1) - 2)}{B1\cdot Intercept1} = 0$$

$$Fofl1 := \tag{11}$$

$$B1 := fsolve(Fofl1, B1, B1 = 0 \ldots \pi)$$

(12)

########RESULTS###

Diffusion coefficient= $\frac{meters^2}{second}$

$$D1 := fsolve(Slope1, D1)$$

$$D1 := \tag{13}$$

####### Time Constants for diffusion must be less than 0.01 (s^{-1}) **for** ZLC experiments per ruthevenzeolites 1988.

$$K1 := \frac{D1}{r^2}$$

$$K1 := \tag{14}$$

Solving for Henrys Constant (H) (Dimensionless)

$$L1 := fsolve(B1\cdot\cot(B1) + L1 - 1 = 0, L1)$$

$$L1 := \tag{15}$$

$$H1 := fsolve\left(L1 = \frac{1}{3}\cdot\frac{F\cdot r^2}{H1\cdot Vs\cdot D1}, H1\right)$$

$$H1 := \tag{16}$$

##########Checks **for** Accuracy

$$fIntercept1 := \frac{2\cdot L1}{B1^2 + L1\cdot(L1 - 1)} = Intercept1$$

$$fIntercept1 := \tag{17}$$

$$L1 := \frac{1}{3}\cdot\frac{F\cdot r^2}{H1\cdot Vs\cdot D1}$$

$$L1 := \cdot \tag{18}$$

######### Conversion to Other Henrys Constant Units

$$TempKelvin := ExpTemp + 273.15$$

$$TempKelvin := \tag{19}$$

#######units= $\frac{mol}{Kg\cdot bar}$

####### $H1 := H1\cdot\frac{\frac{mmol(gas)}{ml(gas)\cdot Bar}}{\frac{ml(sorbent)}{g(sorbent)}} = \frac{Density(Sorbent)}{\frac{ml}{mmole(gas)}}$

$$H1 := H1\cdot\frac{SorbentDensity}{22.4\cdot\left(\frac{ExpTemp}{273.15}\right)}$$

$$H1 := \tag{20}$$

Appendix 2

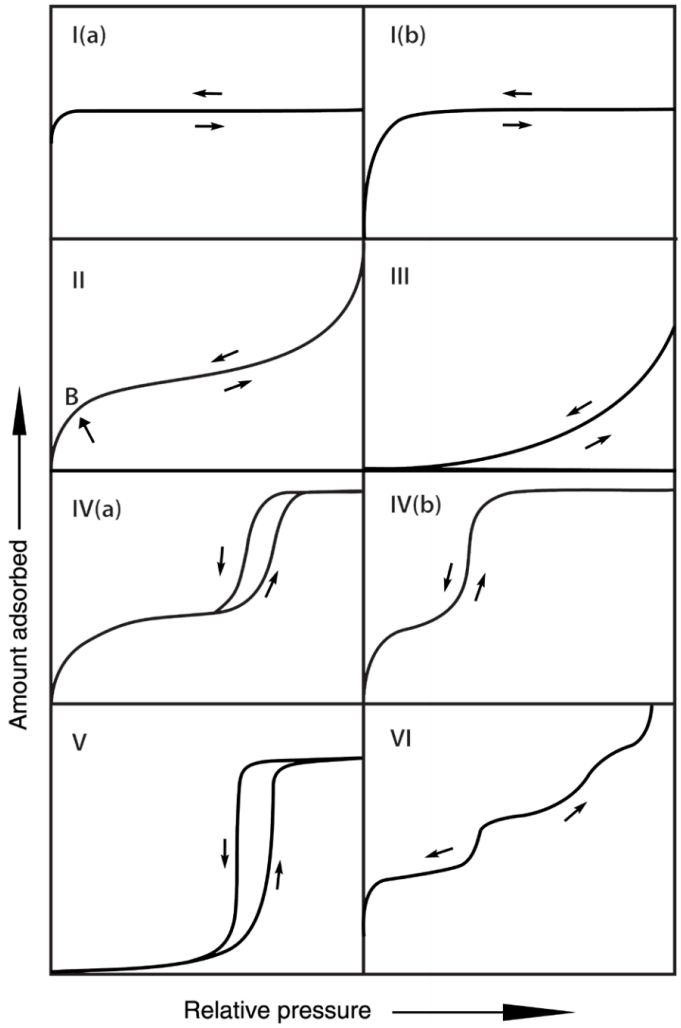


Figure A2-1. Classification of physisorption isotherms taken from IUPAC©, De Gruyter, 2015. (Thommes, M. *et al.* in *Pure and Applied Chemistry* Vol. 87, 1051 (2015)).

Appendix 3

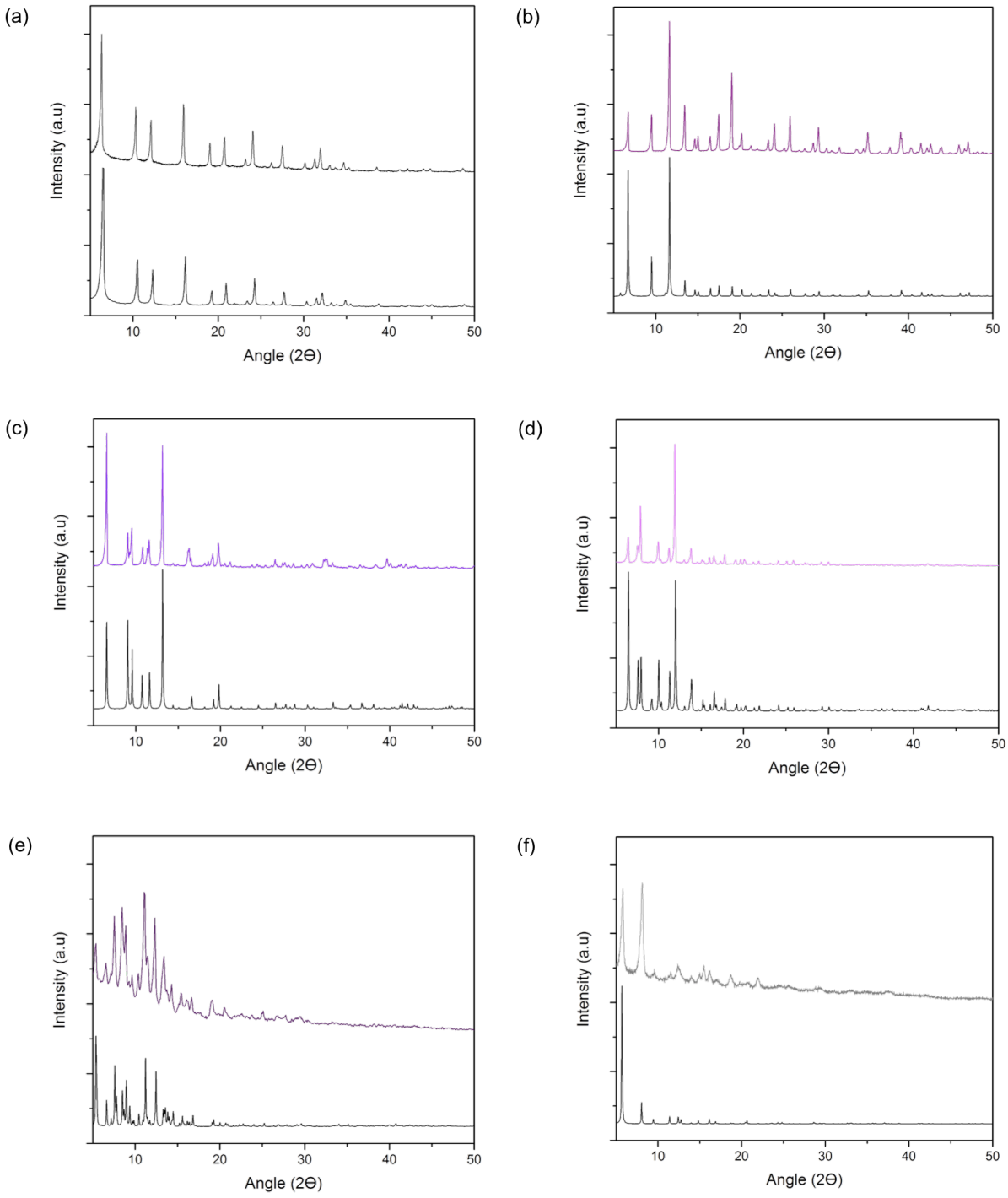


Figure A3-1. X-ray diffraction patterns of (a) Cu-Zeolite Y, (b) HKUST-1, (c) CuTDPAT, (d) MOF-505, (e) PCN-12 and (f) Cu-MFU-4L. The simulated diffraction pattern of each structure is added on each panel for comparison, shown in black at the bottom of the panel.

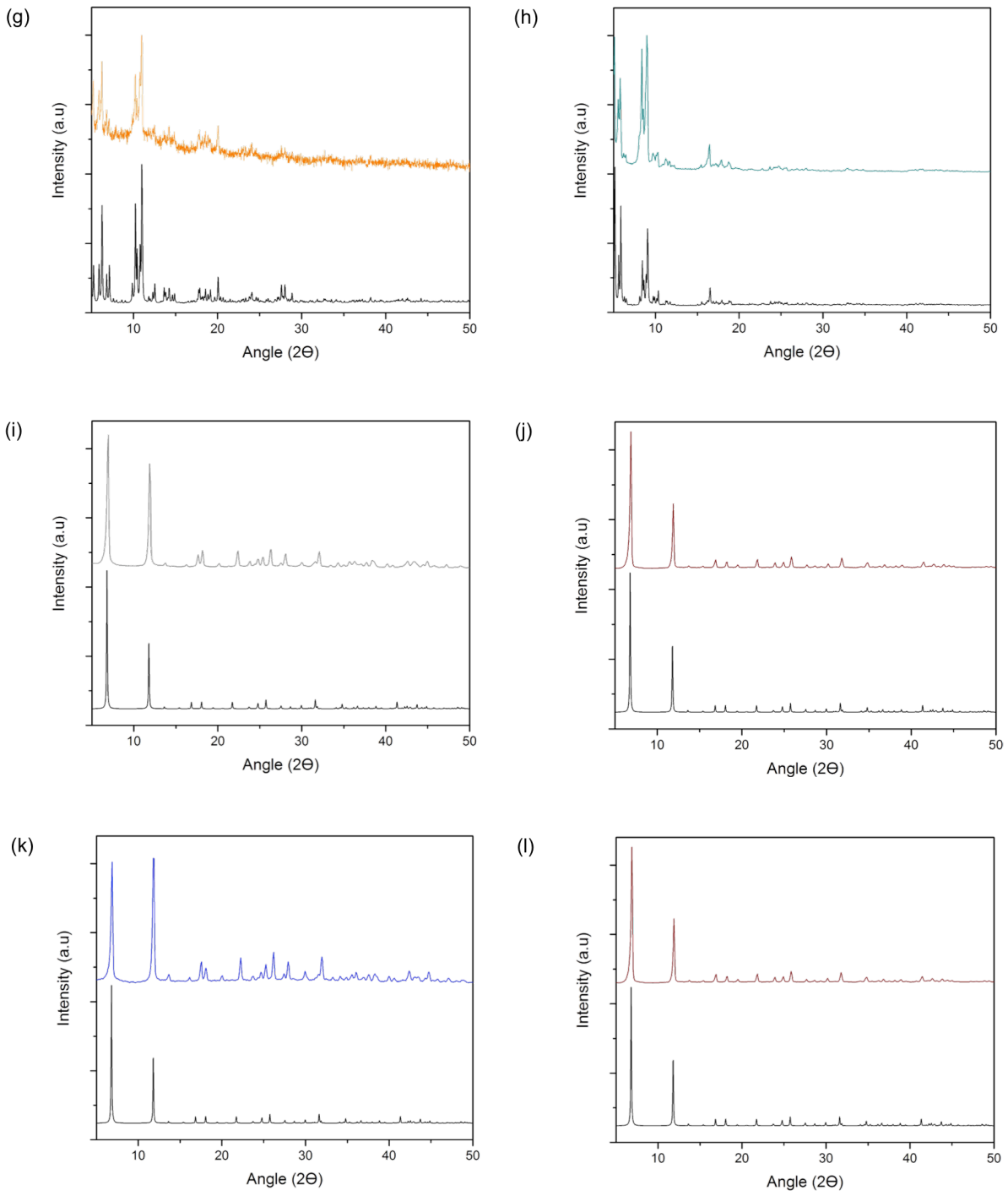


Figure A3-1. X-ray diffraction patterns of (g) Fe-MIL-100, (h) Cr-MIL-101, (i) Cu-MOF-74, (j) Ni-MOF-74, (k) Co-MOF-74 and (l) Ni_2Cl_2(BBTA). The simulated diffraction pattern of each structure is added on each panel for comparison, shown in black at the bottom of the panel.

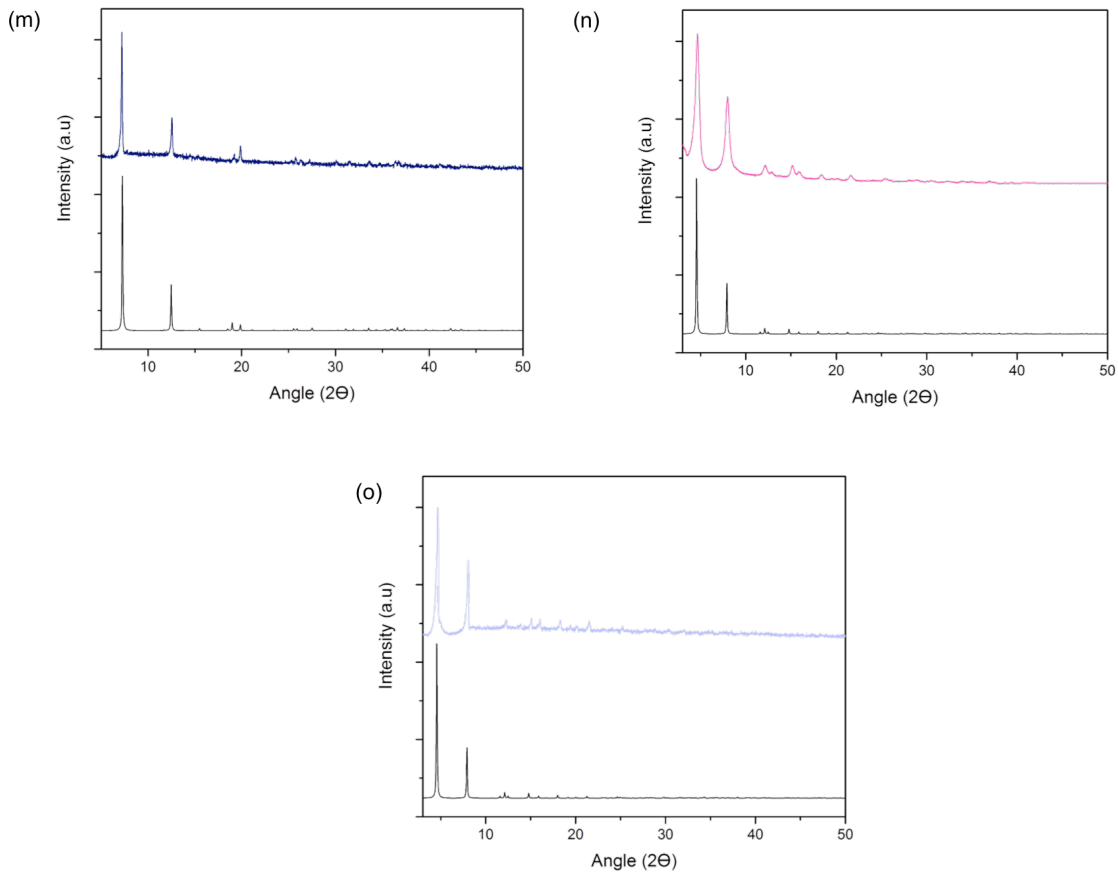


Figure A3-1. X-ray diffraction patterns of (m) Co_2Cl_2(BBTA), (n) Ni_2Cl_2(BTDD) and (o) Co_2Cl_2(BTDD). The simulated diffraction pattern of each structure is added on each panel for comparison, shown in black at the bottom of the panel.

Appendix 4

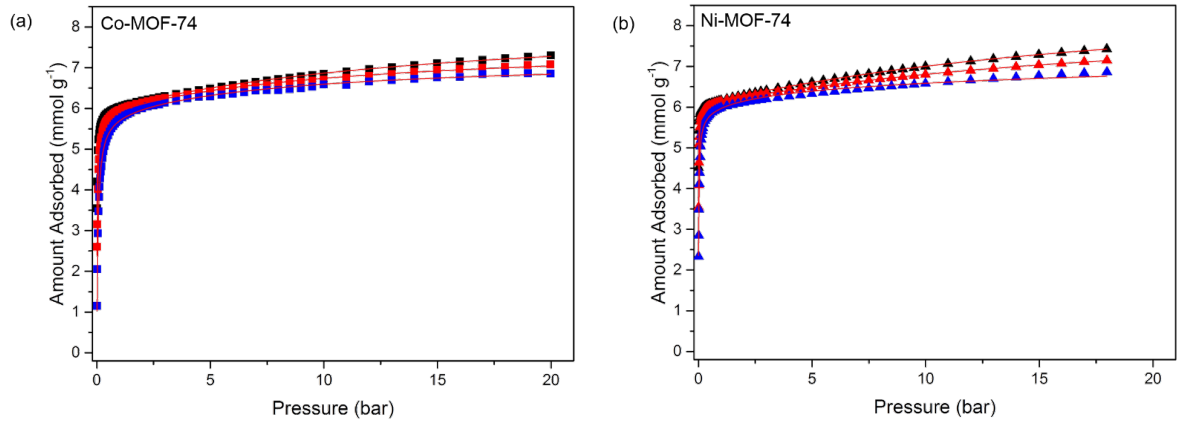


Figure A4-1. Fitting of the CO adsorption isotherms at 10 °C (black), 25 °C (red) and 40 °C (blue) for: (a) Co-MOF-74 (Dual-site Langmuir) and (b) Ni-MOF-74 (Dual-site Langmuir Freundlich) using gravimetric gas sorption analysis.

Table A4-1. Fitting parameters of CO adsorption isotherms at 10 °C, 25 °C and 40 °C for Co-MOF-74 using the Dual-site Langmuir equation.

Temperature (°C)	q_{satA}	b_A	q_{satB}	b_B
10	2.39466	0.06697	5.91101	110.25771
25	5.88165	47.33818	1.77509	0.09626
40	5.8276	18.96763	1.4511	0.12254

Table A4-2. Fitting parameters of CO adsorption isotherms at 10 °C, 25 °C and 40 °C for Ni -MOF-74 using the Dual-site Langmuir Freundlich equation.

Temperature (°C)	q_{satA}	b_A	v_A	q_{satB}	b_B	v_B
10	2.58155	0.03765	1.14273	6.12631	129.89133	0.7447
25	1.71065	0.02547	1.34279	6.20841	58.71764	0.77923
40	3.10612	194.38796	1.46022	3077.28658	0.00093633	0.08268

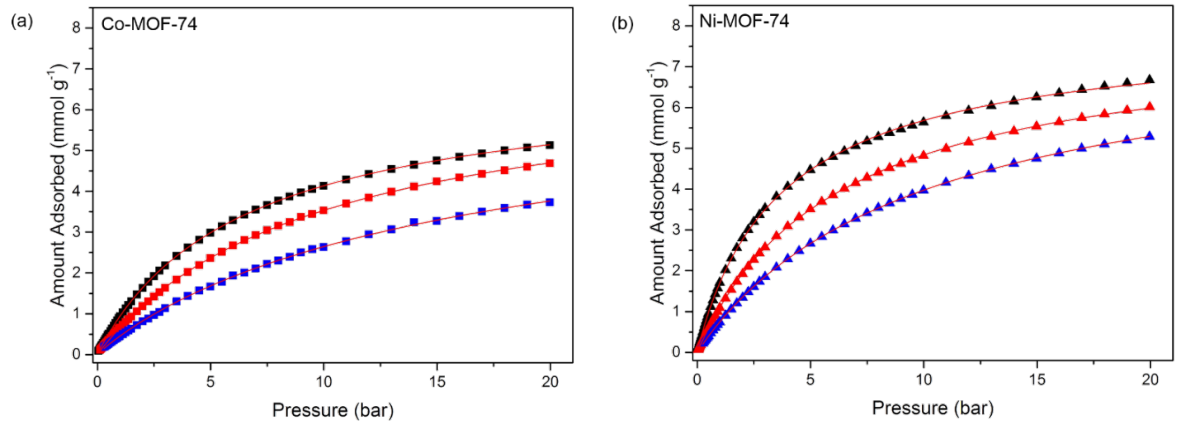


Figure A4-2. Fitting of the N_2 adsorption isotherms at 10 °C (black), 25 °C (red) and 40 °C (blue) for: (a) Co-MOF-74 (Single-site Langmuir Freundlich) and (b) Ni-MOF-74 (Single-site Langmuir Freundlich) using gravimetric gas sorption analysis.

Table A4-3. Fitting parameters of N_2 adsorption isotherms at 10 °C, 25 °C and 40 °C for Co-MOF-74 using the Dual-site Langmuir equation.

Temperature (°C)	q_{satA}	b_A	v_A
10	6.86475	0.15921	0.97912
25	7.06015	0.10296	0.98841
40	6.97793	0.06983	0.94161

Table A4-4. Fitting parameters of N_2 adsorption isotherms at 10 °C, 25 °C and 40 °C for Ni-MOF-74 using the Dual-site Langmuir equation.

Temperature (°C)	q_{satA}	b_A	v_A
10	7.95661	0.27332	0.96137
25	7.87837	0.16253	0.99107
40	8.04314	0.10274	0.97863

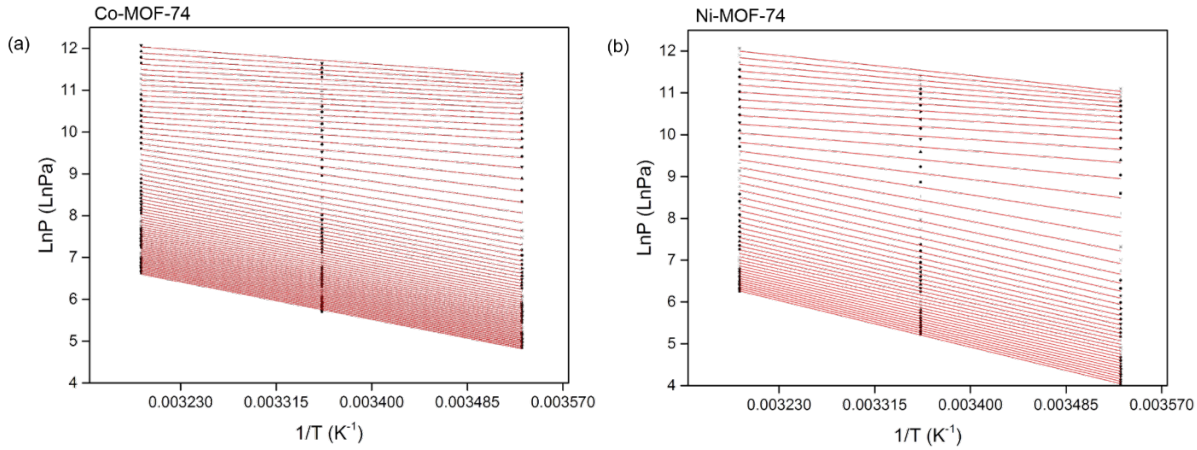


Figure A4-3. Linear fitting of 1/T *vs* LnP for CO to determine the isosteric heat of CO adsorption by the Van t'Hoff method for: (a) Co-MOF-74 and (b) Ni-MOF-74.

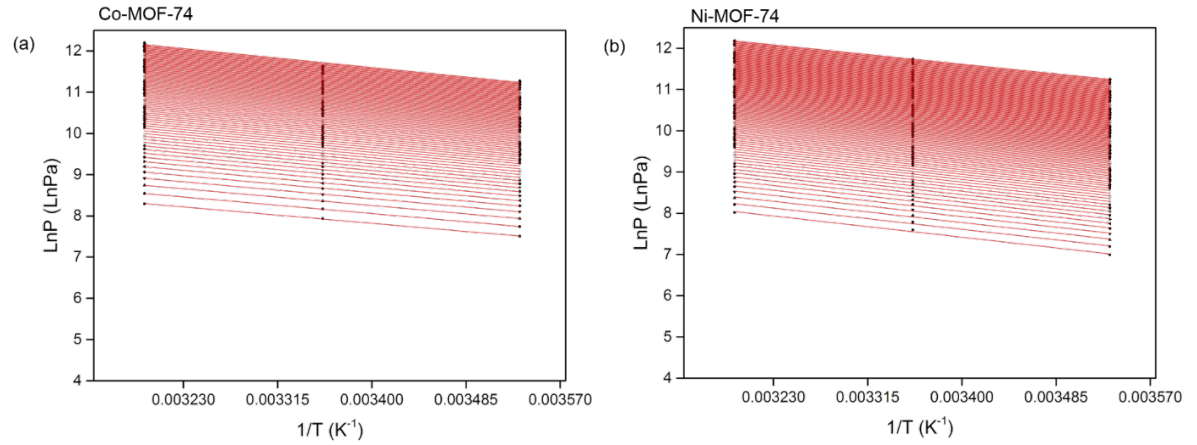


Figure A4-4. Linear fitting of 1/T *vs* LnP for N_2 to determine the isosteric heat of N_2 adsorption by the Van t'Hoff method for: (a) Co-MOF-74 and (b) Ni-MOF-74.

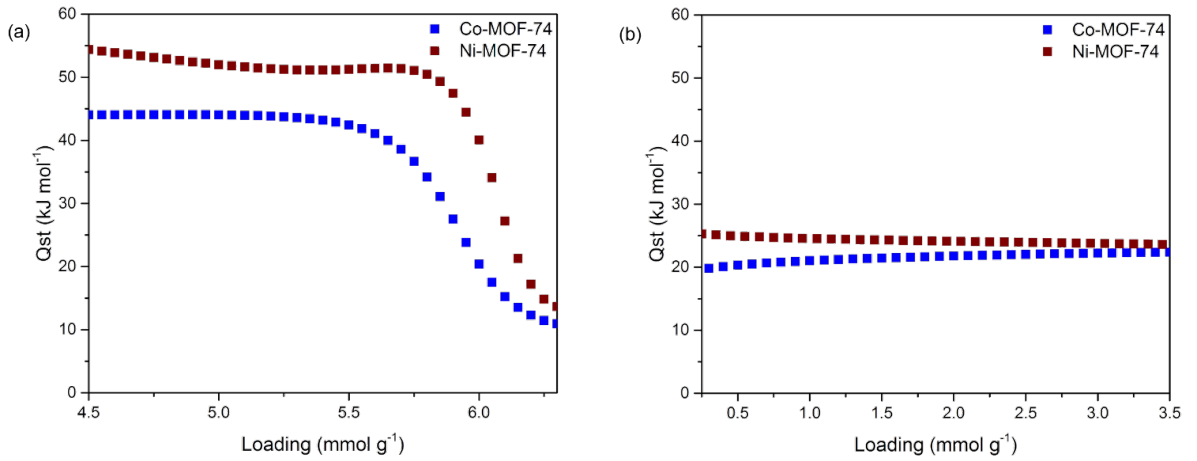


Figure A4-5. The (a) CO and (b) N_2 isosteric heat of adsorption of Co-MOF-74 and Ni-MOF-74.

Appendix 5

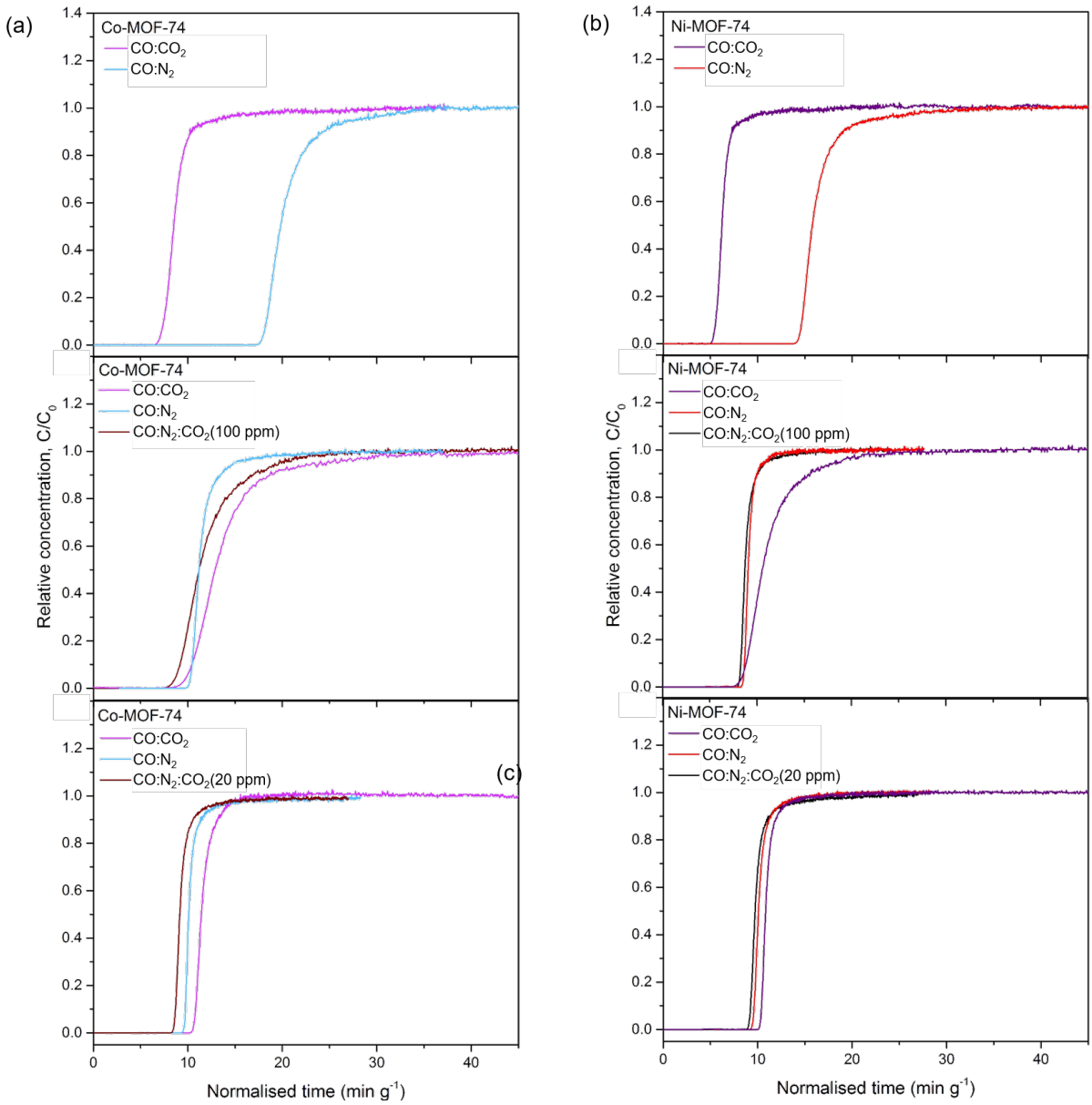


Figure A5-1. CO breakthrough curves of (a) Co-MOF-74 and (b) Ni-MOF-74 at 50% (top), 95% (middle) and 99% (bottom) CO inlet feed concentration of $CO:CO_2$, $CO:N_2$ and $CO:N_2:CO_2$ gas mixtures measured on a breakthrough adsorption column instrument at 25 °C and 1 bar.

Appendix 6

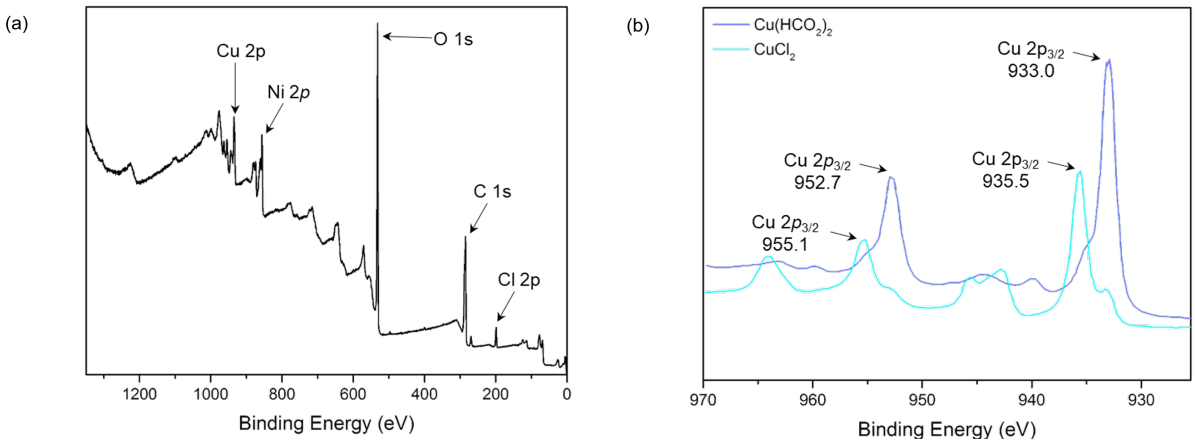


Figure A6-1. (a) Full XPS spectrum of 4-Cu@Ni-MOF-74. (b) Cu 2*p* spectra of the Cu impregnation salt precursors $Cu(HCO_2)_2$ and $CuCl_2$. The responsible Cu peaks and energy levels are shown on the figure.

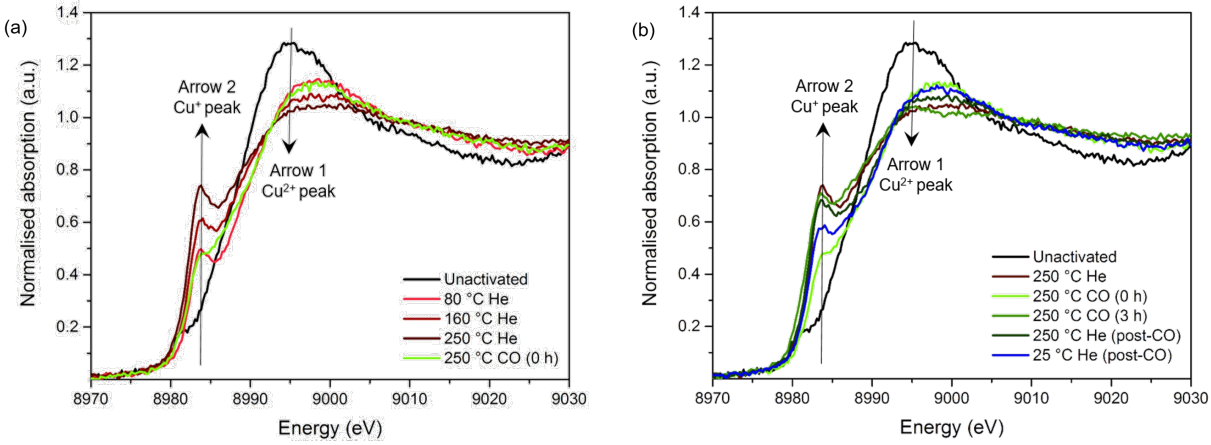


Figure A6-2. Cu-edge XANES spectra of 4-Cu@Ni-MOF-74 during the (a) initial activation procedure using He and switching to CO and (b) the Cu reduction procedure using CO. Indicated by arrows are the features for Cu^{2+} (Arrow 1) and Cu^{+} (Arrow 2) peaks.

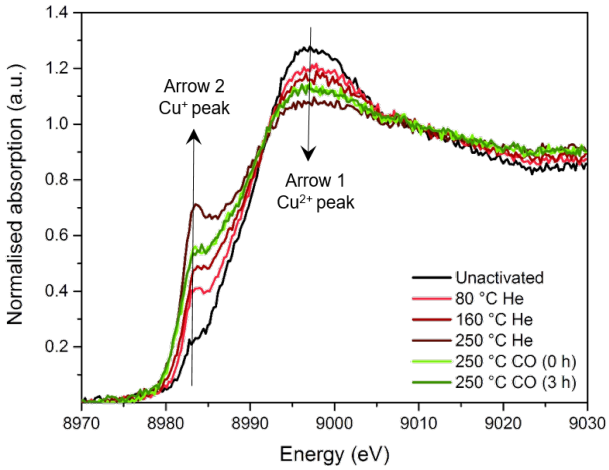


Figure A6-3. Cu-edge XANES spectra during the MOF activation and Cu reduction procedure of 2-Cu@Co-MOF-74. Indicated by arrows are the features for Cu^{2+} (Arrow 1) and Cu^{+} (Arrow 2) peaks.

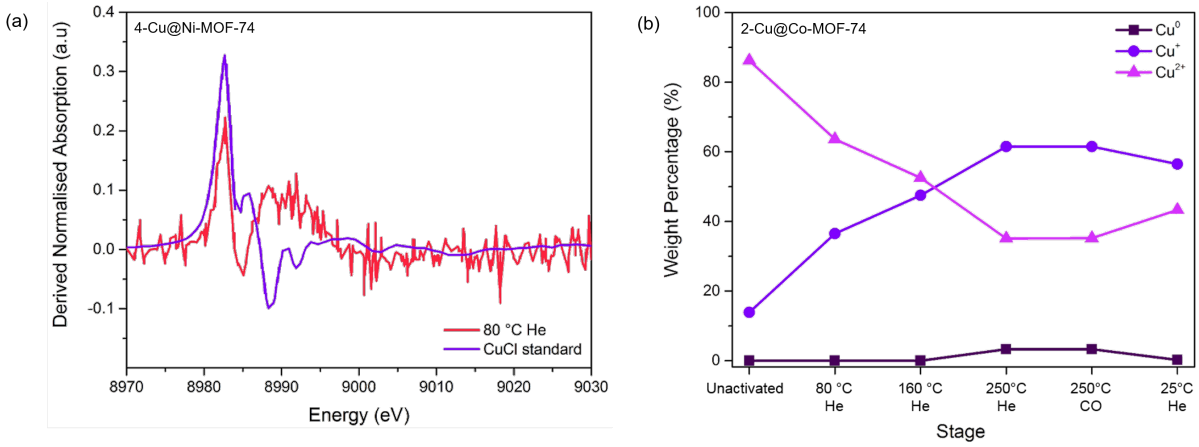


Figure A6-4. (a) First derivative of the Cu-Edge XANES spectra of CuCl and 4-Cu@Ni-MOF-74 at 80 °C under He atmosphere. (b) Linear Combination Fit analysis of Cu species in 2-Cu@Co-MOF-74 during the activation and reduction procedure.

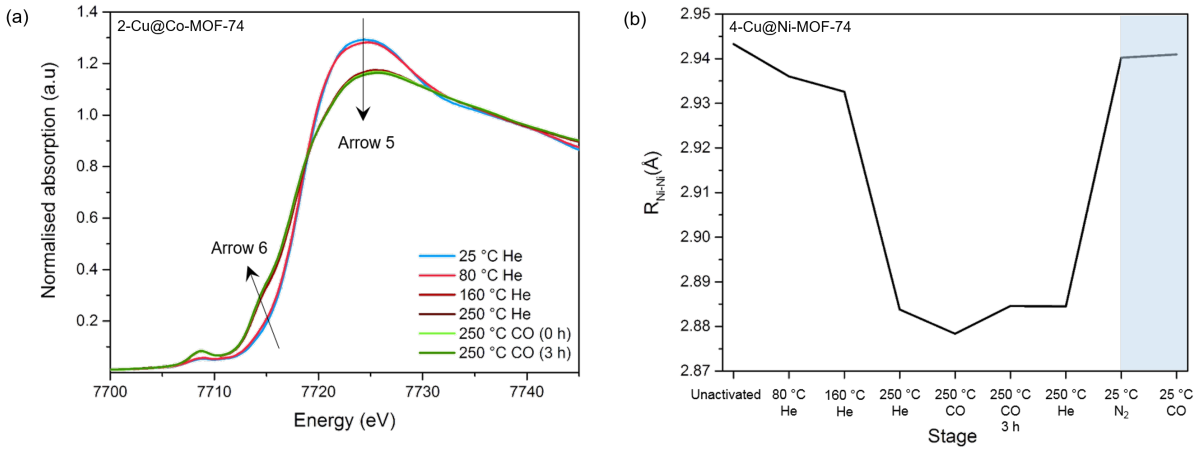


Figure A6-5. (a) Co-edge XANES spectra of 2-Cu@Co-MOF-74 during the MOF activation and Cu reduction procedure. Indicated by arrows are the features for the white line shift (Arrow 5) and 1s-4pz and 1s-3d transition (Arrow 6). (b) Ni-Ni bond of distance 4-Cu@Ni-MOF-74 as obtained by the EXAFS fit of the system at different temperature and atmosphere during the activation and reduction procedure and analysis (shaded).

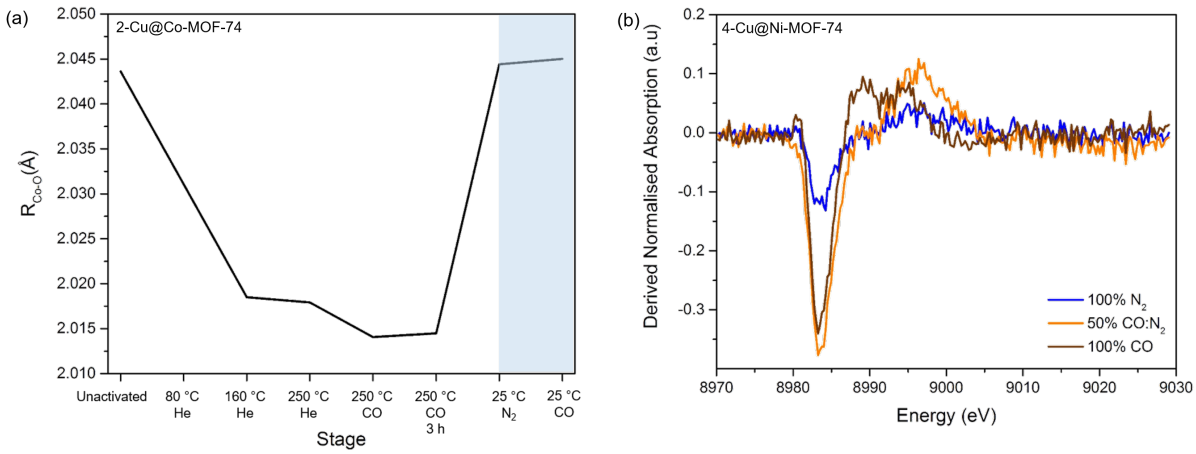


Figure A6-6. (a) Co-O bond of distance 2-Cu@Co-MOF-74 as obtained by the EXAFS fit of the system at different temperature and atmosphere during the activation and reduction procedure and analysis (shaded). (b) Cu-edge Δμ-XANES spectra 4-Cu@Ni-MOF-74 at 25 °C under N_2 and CO atmosphere after activation.

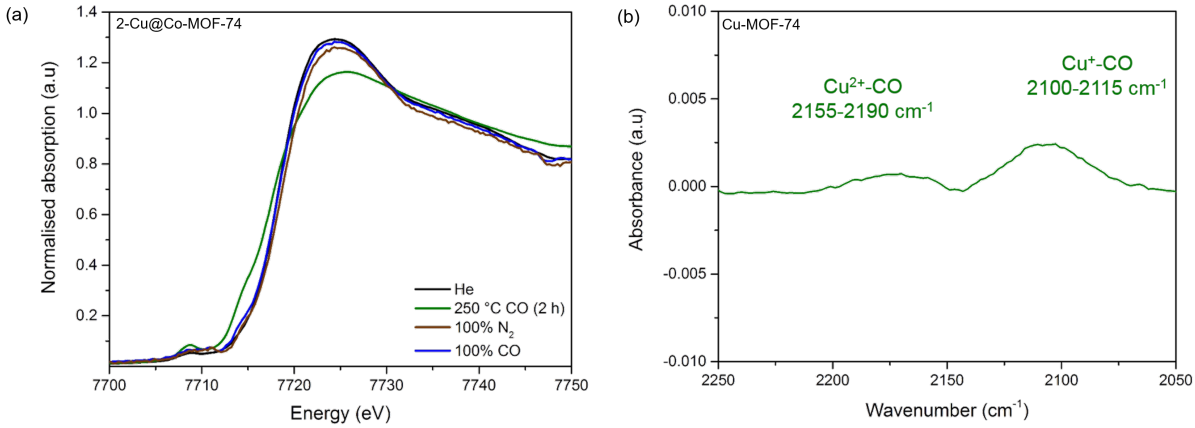


Figure A6-7. (a) Co-edge XANES spectra of 2-Cu@Co-MOF-74 at 25 °C under He atmosphere before activation and under N_2 and CO atmosphere after activation. The spectra during activation in CO atmosphere at 250 °C is shown in green. (b) *In-situ* DRIFTS measurement of chemisorbed CO on Cu-MOF-74 at 25 °C and 1 bar. The spectra has been background corrected with respect to the instrument and sample holder.

Rights and Permissions

A Evans, R Luebke, C Petit, “The use of metal–organic frameworks for CO purification,” Journal of Materials Chemistry A, 6, (2018), 10570-10594

Order Details

Journal of materials chemistry. A, Materials for energy and sustainability

Order detail ID:	72008052	**Permission Status:**	**Granted**
Order License Id:	4667000323725	**Permission type:**	Republish or display content
ISSN:	2050-7496	**Type of use:**	Thesis/Dissertation
Publication Type:	e-Journal	⊞ View details	
Volume:			
Issue:			
Start page:			
Publisher:	Royal Society of Chemistry		
Author/Editor:	Royal Society of Chemistry (Great Britain)		

Note: This item will be invoiced or charged separately through CCC's **RightsLink** service. More info **$ 0.00**

Evans, A. D. et al. “Screening Metal–Organic Frameworks for Dynamic CO/N2 Separation Using Complementary Adsorption Measurement Techniques.” Industrial & Engineering Chemistry Research 58, 18336-18344, (2019).

ACS Publications
Most Trusted. Most Cited. Most Read.

Screening Metal–Organic Frameworks for Dynamic CO/N2 Separation Using Complementary Adsorption Measurement Techniques

Author: Arwyn D. Evans, Matthew S. Cummings, Ryan Luebke, et al
Publication: Industrial & Engineering Chemistry Research
Publisher: American Chemical Society
Date: Oct 1, 2019

Copyright © 2019, American Chemical Society

PERMISSION/LICENSE IS GRANTED FOR YOUR ORDER AT NO CHARGE

This type of permission/license, instead of the standard Terms & Conditions, is sent to you because no fee is being charged for your order. Please note the following:

- Permission is granted for your request in both print and electronic formats, and translations.
- If figures and/or tables were requested, they may be adapted or used in part.
- Please print this page for your records and send a copy of it to your publisher/graduate school.
- Appropriate credit for the requested material should be given as follows: "Reprinted (adapted) with permission from (COMPLETE REFERENCE CITATION). Copyright (YEAR) American Chemical Society." Insert appropriate information in place of the capitalized words.
- One-time permission is granted only for the use specified in your request. No additional uses are granted (such as derivative works or other editions). For any other uses, please submit a new request.

BACK CLOSE WINDOW

Bloch, E. D. et al. “Reversible CO Binding Enables Tunable CO/H_2 and CO/N_2 Separations in Metal–Organic Frameworks with Exposed Divalent Metal Cations,” Journal of the American Chemical Society, 136, (2014),10752-10761



ACS Publications
Most Trusted. Most Cited. Most Read.

Title:	Reversible CO Binding Enables Tunable CO/H2 and CO/N2 Separations in Metal–Organic Frameworks with Exposed Divalent Metal Cations
Author:	Eric D. Bloch, Matthew R. Hudson, Jarad A. Mason, et al
Publication:	Journal of the American Chemical Society
Publisher:	American Chemical Society
Date:	Jul 1, 2014

Copyright © 2014, American Chemical Society

LOGIN

If you're a copyright.com user, you can login to RightsLink using your copyright.com credentials.

Already a RightsLink user or want to learn more?

PERMISSION/LICENSE IS GRANTED FOR YOUR ORDER AT NO CHARGE

This type of permission/license, instead of the standard Terms & Conditions, is sent to you because no fee is being charged for your order. Please note the following:

Sato, H. *et al.* “Self-accelerating CO sorption in a soft nanoporous crystal.” Science 343, (2014), 167-170



Science
AAAS

Title:	Self-Accelerating CO Sorption in a Soft Nanoporous Crystal
Author:	Hiroshi Sato,Wataru Kosaka,Ryotaro Matsuda,Akihiro Hori,Yuh Hijikata,Rodion V. Belosludov,Shigeyoshi Sakaki,Masaki Takata,Susumu Kitagawa
Publication:	Science
Publisher:	The American Association for the Advancement of Science
Date:	Jan 10, 2014

Copyright © 2014, Copyright © 2014, American Association for the Advancement of Science

Logged in as:
Arwyn Evans
Account #:
3001517171
LOGOUT

Order Completed

Thank you for your order.

This Agreement between Arwyn Evans ("You") and The American Association for the Advancement of Science ("The American Association for the Advancement of Science") consists of your license details and the terms and conditions provided by The American Association for the Advancement of Science and Copyright Clearance Center.

Your confirmation email will contain your order number for future reference.

Reed, D. A. *et al.* “Reversible CO Scavenging via Adsorbate-Dependent Spin State Transitions in an Iron(II)–Triazolate Metal–Organic Framework.” Journal of the American Chemical Society, 138, (2016), 5594-5602



Reed, D. A. *et al.* A spin transition mechanism for cooperative adsorption in metal–organic frameworks. Nature, 550, (2017), 96-100



Peng, J. *et al.* “A supported Cu(I)@MIL-100(Fe) adsorbent with high CO adsorption capacity and CO/N_2 selectivity,” Chemical Engineering Journal 270, (2015), 282-289.



Title: A supported Cu(I)@MIL-100(Fe) adsorbent with high CO adsorption capacity and CO/N2 selectivity

Author: Junjie Peng,Sikai Xian,Jing Xiao,Yan Huang,Qibin Xia,Haihui Wang,Zhong Li

Publication: Chemical Engineering Journal

Publisher: Elsevier

Date: 15 June 2015

Copyright © 2015 Elsevier B.V. All rights reserved.

Logged in as:
Arwyn Evans
Account #:
3001517171

LOGOUT

Order Completed

Thank you for your order.

This Agreement between Arwyn Evans ("You") and Elsevier ("Elsevier") consists of your license details and the terms and conditions provided by Elsevier and Copyright Clearance Center.

Li, B., Chrzanowski, M., Zhang, Y. & Ma, S. “Applications of metal-organic frameworks featuring multi-functional sites.” Coordination Chemistry Reviews 307, 106-129, (2016).

Your confirmation email will contain your order number for future reference.

License Number	4742531503334
License date	Jan 05, 2020

Printable Details

Licensed Content

Licensed Content Publisher	Elsevier
Licensed Content Publication	Coordination Chemistry Reviews
Licensed Content Title	Applications of metal-organic frameworks featuring multi-functional sites
Licensed Content Author	Baiyan Li,Matthew Chrzanowski,Yiming Zhang,Shengqian Ma
Licensed Content Date	Jan 15, 2016
Licensed Content Volume	307
Licensed Content Issue	n/a
Licensed Content Pages	24
Journal Type	S&T

Order Details

Type of Use	reuse in a thesis/dissertation
Portion	figures/tables/illustrations
Number of figures/tables/illustrations	1
Format	both print and electronic
Are you the author of this Elsevier article?	No
Will you be translating?	No

About Your Work

Title	Screening, developing and testing Metal-Organic Frameworks for industrially relevant CO/N2 separation
Institution name	Imperial College London
Expected presentation date	Sep 2019

Additional Data

Portions	Figure 25

Murray, L. J., Dincă, M. & Long, J. R. “Hydrogen storage in metal–organic frameworks.” Chemical Society Reviews 38, 1294-1314, (2009).

Dear Arwyn Evans,

Thank you for placing your order on Marketplace™.

Order Summary:
Order date: 05 Jan 2020
Order number: 1011891
No. of items: 1
Order total: 0.00 GBP

Billing Summary:
Payment method: Invoice
An invoice will be generated and emailed within 24 hours.

To view your order details, click the following link, sign in, and search for your order:
Manage Account.

Please do not reply to this message.

To speak with a Customer Service Representative, call +1-855-239-3415 toll free or +1-978-646-2600 (24 hours a day), or email your questions and comments to support@copyright.com.

Sincerely,

The CCC Marketplace Team

1. Chemical Society reviews — 0.00 GBP

Order license ID	Pending	**Publisher**	ROYAL SOCIETY OF CHEMISTRY
ISSN	1460-4744	**Portion**	Image/photo/illustration
Type of Use	Republish in a thesis/dissertation		

View Details — Print License

Order Total: 0.00 GBP

Total Items: 1 — Total Due: 0.00 GBP

He, Y., Li, B., O'Keeffe, M. & Chen, B. “Multifunctional metal–organic frameworks constructed from meta-benzenedicarboxylate units.” Chemical Society Reviews 43, 5618-5656, (2014).

Thank you for your order!

Dear Mr. Arwyn Evans,

Thank you for placing your order through Copyright Clearance Center's RightsLink® service.

Order Summary

Licensee:	Arwyn Evans
Order Date:	Jan 5, 2020
Order Number:	4742531503334
Publication:	Coordination Chemistry Reviews
Title:	Applications of metal-organic frameworks featuring multi-functional sites
Type of Use:	reuse in a thesis/dissertation
Order Total:	0.00 GBP

View or print complete details of your order and the publisher's terms and conditions.

Sincerely,

Copyright Clearance Center

1. Chemical Society reviews — 0.00 GBP

Order license ID	Pending	Publisher	ROYAL SOCIETY OF CHEMISTRY
ISSN	1460-4744	Portion	Image/photo/illustration
Type of Use	Republish in a thesis/dissertation		

View Details — Print License

Order Total: 0.00 GBP

Total Items: 1 — Total Due: 0.00 GBP

Jeazet, H. B. T., Koschine, T., Staudt, C., Raetzke, K. & Janiak, C. “Correlation of Gas Permeability in a Metal-Organic Framework MIL-101(Cr)–Polysulfone Mixed-Matrix Membrane with Free Volume Measurements by Positron Annihilation Lifetime Spectroscopy (PALS).” *Membranes* **3**, 331-353, (2013).

Dear Arwyn Evans,

Thank you for placing your order on Marketplace™.

Order Summary:
Order date: 05 Jan 2020
Order number: 1011896
No. of items: 1
Order total: 0.00 GBP

Billing Summary:
Payment method: Invoice
An invoice will be generated and emailed within 24 hours.

To view your order details, click the following link, sign in, and search for your order:
Manage Account.

Please do not reply to this message.

To speak with a Customer Service Representative, call +1-855-239-3415 toll free or +1-978-646-2600 (24 hours a day), or email your questions and comments to support@copyright.com.

Sincerely,

The CCC Marketplace Team

1. Dalton transactions — 0.00 GBP

Order license ID	Pending	Publisher	ROYAL SOCIETY OF CHEMISTRY
ISSN	1477-9234	Portion	Image/photo/illustration
Type of Use	Republish in a thesis/dissertation		

View Details — Print License

Order Total: 0.00 GBP

Total Items: 1 — Total Due: 0.00 GBP

Weinrauch, I. *et al.* “Capture of heavy hydrogen isotopes in a metal-organic framework with active Cu(I) sites.” *Nature Communications* **8**, 14496, (2017)

SPRINGER NATURE

Capture of heavy hydrogen isotopes in a metal-organic framework with active Cu(I) sites

Author: I. Weinrauch et al
Publication: Nature Communications
Publisher: Springer Nature
Date: Mar 6, 2017

Copyright © 2017, Springer Nature

Creative Commons

This is an open access article distributed under the terms of the Creative Commons CC BY license, which permits unrestricted use, distribution, and reproduction in any medium, provided the original work is properly cited.

You are not required to obtain permission to reuse this article.
To request permission for a type of use not listed, please contact Springer Nature